Marco Donà

ROLLING-BALL RUBBER-LAYER SYSTEM FOR THE LIGHTWEIGHT STRUCTURES
SEISMIC PROTECTION: EXPERIMENTATION AND NUMERICAL ANALYSES

UNIVERSITA' DEGLI STUDI
DI TRENTO

Doctoral School in
Engineering of Civil and Mechanical
Structural Systems

Marco Donà

# ROLLING-BALL RUBBER-LAYER SYSTEM FOR THE LIGHTWEIGHT STRUCTURES SEISMIC PROTECTION: EXPERIMENTATION AND NUMERICAL ANALYSES

April, 2015

Prof. Claudio Modena (Tutor)
Dr. Alan H. Muhr (Co-tutor)

Marco Donà

ROLLING-BALL RUBBER-LAYER SYSTEM FOR THE LIGHTWEIGHT STRUCTURES
SEISMIC PROTECTION: EXPERIMENTATION AND NUMERICAL ANALYSES

UNIVERSITA' DEGLI STUDI
DI TRENTO

Doctoral School in
Engineering of Civil and Mechanical
Structural Systems

Marco Donà

# ROLLING-BALL RUBBER-LAYER SYSTEM FOR THE LIGHTWEIGHT STRUCTURES SEISMIC PROTECTION: EXPERIMENTATION AND NUMERICAL ANALYSES

April, 2015

Prof. Claudio Modena (Tutor)
Dr. Alan H. Muhr (Co-tutor)

UNIVERSITA' DEGLI STUDI
DI TRENTO

Doctoral School in
Engineering of Civil and Mechanical
Structural Systems

Marco Donà

# ROLLING-BALL RUBBER-LAYER SYSTEM FOR THE LIGHTWEIGHT STRUCTURES SEISMIC PROTECTION: EXPERIMENTATION AND NUMERICAL ANALYSES

April, 2015

Prof. Claudio Modena (Tutor)
Dr. Alan H. Muhr (Co-tutor)

University of Trento
University of Brescia
University of Bergamo
University of Padova
University of Trieste
University of Udine
University IUAV of Venezia

Marco Donà (Ph. D. Student)

# ROLLING-BALL RUBBER-LAYER SYSTEM FOR THE LIGHTWEIGHT STRUCTURES SEISMIC PROTECTION: EXPERIMENTATION AND NUMERICAL ANALYSES

Prof. Claudio Modena (Tutor)
Dr. Alan H. Muhr (Co-tutor)

2015

UNIVERSITY OF TRENTO
Engineering of Civil and Mechanical Structural Systems - XXVII Cycle

Prof. Davide Bigoni (Ph. D. Head’s)

Final Examination 22/04/2015

Board of Examiners:

| | |
|---|---|
| Prof. Jiří Máca | (Czech Technical University in Prague) |
| Prof. Maria Rosaria Pecce | (University of Sannio in Benevento) |
| Prof. Daniele Zonta | (University of Trento) |
| Dr. Paolo Clemente | (UTPRA – ENEA CRE Casaccia) |
| Dr. Loris Vincenzi | (University of Modena and Reggio Emilia) |

© Marco Donà, 2015
All rights reserved

# SUMMARY

Protection of high-value building contents from seismic damage represents a worldwide challenging task. Artefacts, sophisticated medical and electrical equipment, high performance computer installations and other special contents have shown, in the last years, their high vulnerability both for high and moderate earthquakes. The lack of effective techniques, sufficiently developed for seismic risk mitigation of such objects, makes the seismic protection of contents a crucial issue.

An effective means to provide this protection is seismic isolation. The isolation techniques to be used for the content are not a mere extension of the ones used for civil structures, although the basic theories and concepts of seismic isolation are the same. Indeed, the following technical peculiarities have to be considered: the contents have masses orders of magnitude smaller than those characteristic of civil structures and, secondly, they are often very vulnerable and are not able to withstand even small seismic actions.

This thesis, that fits into this context, presents an innovative seismic isolation device for lightweight structures, named “RBRL” system, i.e. “Rolling-Ball Rubber-Layer”, and it is aimed at studying the dynamic behaviour of the system itself through numerical analyses and parametric experimentations, with the goals to get a sufficient comprehension of the system performance and its general numerical characterization. The device, invented by Alan Thomas at TARRC (“Tun Abdul Razach Research Centre”) comprises: a rolling-based bearing system, which allows any displacements in the horizontal plane; two rubber layers bonded to the steel tracks, which give an adequate damping to the rolling steel balls; some rubber springs, which ensure the recentering of the system through their elastic stiffness.

**Tutor**
Prof. Claudio Modena

**Co-Tutor**
Dr. Alan H. Muhr Alan Muhr

**Ph. D. Head’s**
Prof. Davide Bigoni

# SOMMARIO

La protezione del contenuto strutturale di elevato valore dal danneggiamento sismico è un compito impegnativo. Oggetti d'arte, strumentazioni elettriche e medicali sofisticate, installazioni di computer ad alta performance e altri contenuti speciali hanno mostrato, negli ultimi anni, la loro grande vulnerabilità, per terremoti sia di piccola che di grande intensità. La mancanza di tecniche effettive, sufficientemente sviluppate per la mitigazione del rischio sismico di tali oggetti, fa della protezione sismica del contenuto una questione cruciale.

Un mezzo efficace per fornire questa protezione è l'isolamento sismico. Anche se le teorie e i concetti base dell'isolamento sismico sono gli stessi, le tecniche di isolamento che devono essere utilizzate per il contenuto non sono una mera estensione di quelle usate per le strutture civili. Infatti bisogna considerare le seguenti peculiarità tecniche: i contenuti coinvolgono masse con ordini di grandezza minori rispetto a quelle delle strutture civili e, in secondo luogo, spesso sono molto vulnerabili, tali da non sopportare eventi sismici anche di bassa intensità.

Inserendosi in quest'ambito, questo lavoro di tesi vuole presentare un innovativo dispositivo di isolamento sismico per le strutture leggere, denominato sistema “RBRL” ossia “Rolling-Ball Rubber-Layer”, ed è indirizzato allo studio del comportamento dinamico dello stesso tramite analisi numeriche e sperimentazioni parametriche, con le finalità di comprenderne le caratteristiche prestazionali e giungere ad una generale caratterizzazione numerica dello stesso. Il dispositivo, inventato da Alan Thomas al TARRC (“Tun Abdul Razach Research Centre”), comprende: un sistema di appoggio su sfere in acciaio, che permette qualsiasi spostamento nel piano orizzontale; due fogli di gomma solidarizzati a piatti di acciaio, che forniscono un adeguato smorzamento alle sfere rotolanti; delle molle in gomma, che assicurano il ricentramento del sistema tramite la loro rigidezza elastica.

## DEDICATION

***Alla mia cara famiglia***
*“co-autrice” di quello che sono*

***… and to Valeria***
*because it is not possible*
*to live with only equations*

# ACKNOWLEDGEMENTS

*My first and utmost gratitude is to my tutors, Prof. Claudio Modena and Dr. Alan Muhr for their supervision and suggestions during my PhD study. Their generous encouragements and great enthusiasm have always stimulated me to face challenges with confidence. In particular the scientific competence and experience on rubber of Dr. Alan Muhr has been essential for the realization of this thesis.*

*My thanks go to Dr. Hamid Ahmadi, who never missed an opportunity to give me advice for my work and my life, and to all the staff of the TARRC engineering unit that kindly and patiently has helped me during my experimentation work at TARRC: Ian Stephens, Jean-Louis Poisson, John Kingston, Alan Harris, Robert Picken, Julia Gough, Judith Picken. The extensive discussions and close cooperation with them allowed me to get most of the result herein contained.*

*I would like to thank also Dr. Kamarudin Ab-Malek and Alberto Dusi, who have permitted the collaboration between University of Padova and TARRC.*

*I also wish to express my special thanks to Prof. Francesca da Porto and to all the friends and colleagues I met during the doctoral program, who have given with their efforts and enthusiasm a great contribution in this work, in particular Gabriele Granello and Giovanni Tecchio.*

*Marco Donà*
*April 2015, Padova, Italy*

## TABLE OF CONTENTS

**SUMMARY ........ I**
**SOMMARIO ........ III**
**ACKNOWLEDGEMENTS ........ VII**
**LIST OF FIGURES ........ XIII**
**LIST OF TABLES ........ XXVII**
**LIST OF SYMBOLS ........ XXIX**

**1 INTRODUCTION ........ 1**
- 1.1 Background and motivations ........ 1
- 1.2 Problem statement ........ 6
- 1.3 Aims and methods of the research ........ 7
- 1.4 Thesis organization ........ 9

**2 BACKGROUND OF SEISMIC ISOLATION FOR LIGHTWEIGHT STRUCTURES ........ 13**
- 2.1 Seismic vulnerability of content ........ 13
- 2.2 Motions of the rigid bodies and importance of base isolation ........ 20
- 2.3 Seismic isolation and energy dissipation: effects on the structures ........ 27
- 2.4 Issues of the traditional seismic devices for the content ........ 29
  - *2.4.1 Characteristics of the isolation devices and systems ........ 29*
  - *2.4.2 Elastomeric isolators ........ 32*
  - *2.4.3 Sliding isolators ........ 35*
- 2.5 Seismic isolation devices for lightweight structures ........ 37
  - *2.5.1 Roller or rail-type isolation devices ........ 37*
  - *2.5.2 Slider-type isolation devices ........ 40*
  - *2.5.3 Rolling-type isolation devices ........ 42*
  - *2.5.4 Other particular isolators for lightweight structures ........ 46*

**3 BACKGROUND OF RBRL SYSTEM AND RUBBER DYNAMIC BEHAVIOUR55**
- 3.1 RBRL isolation system ........ 55
  - *3.1.1 Previous research studies ........ 57*
  - *3.1.2 Highlights of the RBRL system behaviour ........ 58*
  - *3.1.3 Available numerical modelling ........ 59*
  - *3.1.4 Theory of Muhr et al. (1997) for rolling resistence on thin rubber layers: formulation and errors of assessment ........ 64*

3.2 Dynamic properties of rubber and viscoelastic linearization methods ......78
3.3 Shortcomings and need of further researches ......85

**4 NUMERICAL ANALYSES OF ECOEST PROJECT RESULTS AND APPLICATIONS OF ELVFD REPRESENTATION ......89**

4.1 Introduction ......89
4.2 Advantageous small-deflections behaviour of RBRL system ......90
4.3 ELVFD representation of system behaviour from ECOEST tests ......95
4.4 Guerreiro Model performance through ELVFD representation ......97
4.5 Proposal of a simplified model based on ELVFD representation ......100
4.6 Conclusions ......103

**5 PARAMETRIC CHARACTERIZATION TESTS ON RBRL SYSTEM: PROPOSAL OF A GENERAL DESIGN PROCEDURE ......105**

5.1 Introduction ......105
5.2 Characterization tests of the rubber compounds ......108
  *5.2.1 Dynamic tests and rubber dynamic properties ......110*
  *5.2.2 Creep tests and rubber relaxation moduli ......112*
5.3 Sinusoidal uniaxial tests on new RBRL devices: validation of the rolling friction theory of Muhr et al. (1997) ......117
  *5.3.1 Description of the tests ......117*
  *5.3.1 Results ......122*
5.4 Sinusoidal double-shear tests on recentering rubber springs ......129
  *5.4.1 Description of the tests ......129*
  *5.4.2 Results ......130*
5.5 Design procedure of the RBRL system: parametric investigation ......140
5.6 Conclusions ......144

**6 INVESTIGATIONS ON SMALL-DEFLECTIONS BEHAVIOUR OF RBRL SYSTEM: PROPOSAL OF A TIME-DOMAIN MODEL ......147**

6.1 Introduction ......147
6.2 Sinusoidal uniaxial tests on new RBRL devices: small-deflections behaviour ......148
  *6.2.1 Description of the tests ......148*
  *6.2.2 Results ......150*
6.3 Tests for the measurement of the pit geometric profiles ......180
  *6.3.1 Description of the tests ......180*

*6.3.2 Results ........ 185*
6.4 Sinusoidal uniaxial tests on ECOEST-project devices: dwell time influence ........ 199
*6.4.1 Description of the tests ........ 199*
*6.4.2 Results ........ 202*
6.5 Prediction of the peak forces and of the recovery effects of the rubber ........ 209
6.6 Proposal of a new time-domain prediction model for the RBRL system ........ 221
6.7 Conclusions ........ 232

**7 CONCLUSIONS AND FUTURE WORKS ........ 235**
7.1 General observations ........ 235
7.2 Innovative aspects of the research ........ 236
7.3 Future developments and recommendations for further research ........ 238

**REFERENCES ........ 241**
**APPENDIX A: ........ 251**

## LIST OF FIGURES

Fig. 1.1 a) Image of the Temple of Paestum in Capaccio (III c. BC). b) Scheme of the mechanism to protect the Temple by the earthquake: base of sand and gravel inserted between the foundation and the ground (image from Martelli, 2010). ... 3

Fig. 1.2 a) Touaillon's original patent, Feb. 1870. b) Cooper's original patent, Mar. 1870.3

Fig. 1.3 Comparison of the number of buildings seismically isolated between the most active countries - data of September 2013 (image from Martelli et al., 2014). .... 5

Fig. 1.4 Number of Italian buildings seismically isolated during years (image from Martelli et al., 2014). .......... 5

Fig. 1.5 Typical cost breakdown in building construction, according to Taghavi & Miranda (2003), for three different occupancies (image from FEMA E-74, 2011). ............ 6

Fig. 2.1 a) Destruction of Saturnino Gatti statue (National Museum of Abruzzo in L'Aquila, April 6, 2009); b) overturning of a decorative statue in a private garden (San Felice Sul Panaro, May 21-29, 2012). Images from Borri & De Maria, 2013 a,b. .......... 16

Fig. 2.2 a) Destruction of some showcases and b) damage of pottery exhibited at Nias Heritage Museum, after the seismic event of Indonesia in March 28, 2005 (Neurohr, 2005). .......... 16

Fig. 2.3 Damage to the non-structural components and contents of the Veteran Hospital (a) and Shiu-Tuan Hospital (b) (from Soong & Yao, 2000). .......... 17

Fig. 2.4 a) General purpose cabinet, unanchored, at General Hospital of Haiti. b) Control wiring conduit damage after 2010 Haitian quake (PGA=0.21g). (From Goodno et al., 2011). .......... 19

Fig. 2.5 a) Metal-enclosed load interrupter switchgear (MELIS) equipment at the U.S. Embassy. b) and displacement due to the 2010 Haitian quake (PGA=0.16g). (From Goodno et al., 2011). .......... 19

Fig. 2.6 a) Electrical cabinets overturned by 1999 Izmit earthquake –magnitude 7.4- Turkey (photos of NISEE Izmit Collection). b) Rail mounted transformer slipped off rails by 2010 Haiti earthquake –magnitude 7- Port-au-Prince (photos of Eduardo Fierro, BFP Engineers). (From FEMA E-74, Jan. 2011). .......... 20

Fig. 2.7 Representation of the rocking phenomena for a slender rigid block (Housner, 1963). .......... 22

Fig. 2.8 a) Cumulative probability distribution functions for maximum rotation $\theta_{MAX}$ . b) Overturning probability. Different values of R and H/B investigated, for rigid blocks subjected to an ensemble of horizontal and vertical ground motion. (Yim et al., 1980). .......... 24

Fig. 2.9 Overturning criteria for rigid bodies (from Ishiyama, 1984). ............................. 25
Fig. 2.10 Effects of the seismic isolation in terms of spectral acceleration (a) and displacement (b) (from Symans, 2004). ............................................................ 29
Fig. 2.11 Effects of the seismic isolation with different response spectra (from Symans, 2004)............................................................................................................ 29
Fig. 2.12 Ideal force-displacement loops of: a) isolators made of elastomeric material and steel; b) sliding isolators (from Dolce et al., 2010). .......................................... 31
Fig. 2.13 Ideal force-displacement loops of auxiliary devices based on: a) hysteresis of some metals; b) friction; c) superelastic properties of shape memory materials; d) viscous behaviour; e) quasi-linear or viscoelastic behaviour (from Dolce et al., 2010)............................................................................................................ 31
Fig. 2.14 a) Image of a High Damping Rubber Bearing (HDRB). b) Typical hysteresis loops of a HDRB isolator obtained by dynamic tests at increasing shear strain amplitude $\gamma$ (from FIP Industriale S.p.A., 2015). ............................................. 34
Fig. 2.15 a) Image of the Lead Rubber Bearing (LRB). b) Typical hysteresis loops of a LRB isolator obtained by dynamic tests at increasing shear strain amplitude $\gamma$ (from FIP Industriale S.p.A., 2015)................................................................... 34
Fig. 2.16 a) Image of a curved surface slider or friction pendulum system (FPS) device. b) Relative hysteresis loop (from FIP Industriale S.p.A., 2015)........................ 36
Fig. 2.17 Seismic isolation device used at the Getty Villa (from Lowry et al., 2007). ....... 38
Fig. 2.18 a) Application of the isolator in situ (Getty Villa); b) application on the Agrigento Youth (http://www.getty.edu)............................................................................ 38
Fig. 2.19 Roller-Type Isolation Device: a) image; b) schematic drawing (from Ueda et al., 2004)............................................................................................................ 40
Fig. 2.20 Installation of the Roller-Type Isolation device at the base of: (a) “Burghers of Calais” by Auguste Rodin at National Western Art Museum at Tokyo; (b) showcases at Gifu Modern Museum at Gifu prefecture (from Ueda et al., 2004).40
Fig. 2.21 a) DCCSS isolator. b) Setup used for shaking table tests (from Berto et al., 2013)............................................................................................................ 41
Fig. 2.22 a) Statue “Prigione Barbuto” by Michelangelo. b),c) Finite Element Model of the statue, with the stress field, for the case without b) and with c) seismic isolation (from Baggio et al., 2013). ................................................................... 41
Fig. 2.23 a) Sectioned view of the BNC device. b) Perspective views of the isolation system with BNC devices for the isolation of a showcase (from Erdik et al., 2010)............................................................................................................ 43
Fig. 2.24 BNC geometry and corresponding restoring laws (from Kesti et al., 2010)....... 43
Fig. 2.25 Museum items at the Istanbul Archaeological Museums (from Erdik et al., 2010).44
Fig. 2.26 a) Exploded perspective view of SDI-BPS device; b) related force-displacement

hysteresis loop (from Tsai et al., 2010). ........................................................ 46
Fig. 2.27 Movements of a SDI-BPS device under service and seismic loadings (from Tsai et al., 2010). ................................................................................................ 46
Fig. 2.28 Scheme of the Rolling Double Pendulum device (from De Canio, 2012). ......... 47
Fig. 2.29 Principal parts of the isolation system. a) Global view of the device. b) Internal view of the upper base (from De Canio, 2012)................................................ 47
Fig. 2.30 a) Forces acting in the internal anchoring cables, before and after the installation of the new isolation system: a) "Bronzo A", the "Young"; b) "Bronzo B", the "Old" (from De Canio & Modena, 2013). ................................................................. 48
Fig. 2.31 "Wire-Rope" or "Steel Cable Dampers" device. Images from: a) Demetriades et al., 1993 and b) Alessandri et al., 2014. ......................................................... 49
Fig. 2.32 Installation of the seismic isolation system with Wire-Rope devices at the base of a HV circuit breakers in a power plant (from Alessandri et al., 2014). ........... 50
Fig. 2.33 a) GIS 3-Dimensional Finite Element model. b) RBRL isolation device (see next Chapter for more details about this device, in particular Tab. 3.1). ................... 51
Fig. 2.34 a) GIS top acceleration and b) GIS top displacement (Tolmezzo earthquake, 1976, PGA 0.35g). Comparison between fixed base and isolated base solution.52
Fig. 2.35 RoGlider seismic isolator: a) image (from http://www.robinsonseismic.com) and b) section (from Robinson et al., 2006). ........................................................ 53
Fig. 3.1 Combined package of RBRL bearing and recentering springs as used for REEDS and ECOEST projects, by Donà et al. (2014). .................................... 56
Fig. 3.2 Simplified representation of the RBRL system (from Guerreiro et al. 2007)...... 56
Fig. 3.3 Schematic hysteresis loop for isolation system comprising rolling-ball dissipative-layer isolators and springs (from Cook et al., 1997). ....................... 59
Fig. 3.4 a) Rubber spring analytical model, b) track surface friction model, c) analytical model of the indentation effects, by Guerreiro et al. (2007). ............................ 61
Fig. 3.5 Force-displacement response results comparison using the Guerreiro Model and for the seismic input of Northridge Kagel Canyon - monoaxial (+3dB), by Guerreiro et al. (2007). ....................................................................................... 62
Fig. 3.6 Complex stiffness and loss tangent results, both versus relative displacement amplitude, for the systems used in the sinusoidal shaking table tests carried out at ISMES, Bergamo, 2000 (from Muhr & Bergamo, 2010). .............................. 64
Fig. 3.7 Possible schemes, with the position of balls and rubber layers, for experimental determination of rolling resistance; n indicates the number of balls in one layer.65
Fig. 3.8 Schematic plot of reduced friction ratio versus reduced rubber thickness (Eq.(3.28), Muhr et al., 1997). ......................................................................... 70
Fig. 3.9 Parametric schematic plots of rolling friction ratio μ, scaled using α, versus dimensionless ratio of rubber layer thickness to ball radius (Eqs.(3.28),(3.16)).

W/ER$^2$ is the stress parameter (Muhr et al., 1997). .......................................... 70
Fig. 3.10 Tests setup for measuring rolling forces (Muhr et al., 1997). ........................... 72
Fig. 3.11 Experimental results for steady-state rolling friction coefficient, versus ratio of rubber layer thickness to ball radius, for three different values of W/R$^2$ (Muhr et al., 1997). ........................................................................................ 73
Fig. 3.12 Comparison of theory for the plateau value of μ (Eq. (3.16)) with experimental results, for steady-state rolling resistance as a function of load (Muhr et al., 1997). ........................................................................................ 73
Fig. 3.13 New calculation of the theoretical plot of reduced friction ratio versus reduced rubber thickness (Eq. (3.28)). ......................................................................... 75
Fig. 3.14 New calculation of the theoretical plots of rolling friction ratio μ, scaled using α, versus dimensionless ratio of rubber layer thickness to ball radius (Eqs. (3.28),(3.16)). W/ER$^2$ is the stress parameter. ................................................. 75
Fig. 3.15 New calculation of the theoretical plot of reduced friction ratio versus reduced rubber thickness (Fig. 3.13), represented for a smaller range of abscissa values, compatible with the experimentation. ............................................................. 76
Fig. 3.16 Comparison between the predicted values of μ (lines), by theory of Muhr et al. (1997), and the experimental data (dots), reported here through the digitalization of Fig. 3.11. α value to get the best fitting is reported for each stress level (W/R$^2$) considered. ........................................................................................ 76
Fig. 3.17 Theoretical plot of reduced friction ratio versus reduced rubber thickness (Eq. (3.28)), for lubricated condition. ...................................................................... 77
Fig. 3.18 Theoretical plots of rolling friction ratio μ, scaled using α, versus dimensionless ratio of rubber layer thickness to ball radius (Eqs. (3.28), (3.16)), for lubricated condition. W/ER$^2$ is the stress parameter. ....................................................... 77
Fig. 3.19 Kelvin model ........................................................................................ 80
Fig. 3.20 Sinusoidal stress response $\tau(t)$ to an imposed sinusoidal shear strain $\gamma(t)$ for a viscoelastic material. ........................................................................ 80
Fig. 3.21 Stress response $\tau(t)$ to an initial constant strain $\gamma_0$ for a viscoelastic material.80
Fig. 3.22 Dynamic shear properties of rubbers A (unfilled) and B (filled) used for the RBRL devices in the ECOEST project. Rubber B shows Payne effect (from Guerreiro et al., 2007). ........................................................................ 82
Fig. 3.23 Hysteresis loops showing non-linear behaviour typical of filled rubber at high strain and illustrating: a) Secant method; b) Skeleton curve method (from Ahmadi & Muhr, 1997). ........................................................................ 85
Fig. 4.1 a) View of the two test set-ups used in the ECOEST experimentation: a) Mass Down and b) Mass Up configuration (from Guerreiro et al., 2007). .................. 91
Fig. 4.2 a) Mass Up configuration with indication of the transducers (A = accelerations; D

= displacements). b) Relative fixed-base model analyzed in OpenSees for comparisons. ........ 91
Fig. 4.3 a) Acceleration and b) displacement response spectra of the ground motion selected for the tests with Mass Up configuration, as recorded at the table ( $\zeta$ = 5%). ........ 92
Fig. 4.4 a) Top(“T”)-bottom(“B”) slab accelerations a[g] and b) drifts θ [%] between the two slabs versus peak table acceleration from ECOEST results, for the isolated-base case, compared with the simulated fixed-base case (“Fixed”) (≈ sliding isolator for small seismic intensity), for Northridge_PCKC different-scaled earthquakes (K= -12, -6, -4, -3, 0 dB). ........ 93
Fig. 4.5 As Fig. 4.4, for Tolmezzo different-scaled earthquakes (K= -12, -6, 0, +3, +5 dB). ........ 93
Fig. 4.6 As Fig. 4.4, for Faial different-scaled earthquakes (K= -12, -6, 0, +3, +3 dB). .. 94
Fig. 4.7 As Fig. 4.4, for EC8(05) different-scaled earthquakes (K= -15, -12, -9, -6, -3 dB).94
Fig. 4.8 As Fig. 4.4, for EC8(02) different-scaled earthquakes (K= -12, -9, -9, -7, -6 dB). For these tests a combination of rolling tracks A (low damping) – B (high damping) was used. ........ 94
Fig. 4.9 Equivalent linear viscoelastic parameters obtained from ECOEST sinusoidal tests at 5Hz: a) $K^{/}$ $K^{//}$, b) δ. ........ 97
Fig. 4.10 Force-displacement loops obtained for AA tracks during the ECOEST project and compared with equivalent linear viscoelastic representations a) amplitudes up to 5 mm b) amplitudes up to 15 mm. ........ 97
Fig. 4.11 Comparison of directly measured and modelled force-displacement plots for NorthridgePCKC: a) 0 dB; b) –12 dB. ........ 98
Fig. 4.12 Force-disp. loops from Guerreiro model for selected amplitudes and frequencies. ........ 99
Fig. 4.13 a) $K^{/}$, b) $K^{//}$ from the Guerreiro model for all the amplitudes and frequencies analysed. ........ 99
Fig. 4.14 Author’ proposal for a new simple “no-updating” model. ........ 101
Fig. 4.15 Force-disp. loops from author model for selected amplitudes and frequencies.102
Fig. 4.16 Comparison of the ELVFD parameters, which describe the non-linear dynamic behaviour of the RBRL device, calculated by Guerreiro Model, Author Model and sinusoidal tests of the ECOEST project for different sinusoidal amplitudes: a) storage stiffness $K^{/}$; b) loss stiffness $K^{//}$; c) complex stiffness K*; d) loss angle δ. ........ 103
Fig. 5.1 Some images of the principal realization phases of the RBRL devices at TARRC. ........ 107
Fig. 5.2 Cylindrical double shear test piece that shows the nominal thickness of the

rubber disc (darker colour) sandwiched between three metal pieces (from Ahmadi et al., 2008). 108
Fig. 5.3 a) Production of the test pieces for the rubber characterization. b) View of the three test pieces used in the double shear tests. c) Test setup using Instron 1271 servo hydraulic test machine (the specimen is not yet placed in the loading rig). d) Images from test execution. 109
Fig. 5.4 Dynamic shear properties of rubber compounds (A, A+,A-) by Harmonic (a) and Secant (b) linearization method – influence of strain level at 1 Hz frequency. 110
Fig. 5.5 Dynamic shear properties of rubber compounds (A, A+,A-) by Harmonic (a) and Secant (b) linearization method – influence of frequency for a 5% strain. 111
Fig. 5.6 Dynamic shear properties of rubber compounds (A, A+,A-) by Harmonic (a) and Secant (b) linearization method – influence of frequency for a 10% strain. 112
Fig. 5.7 a) Schematic drawing of the creep test setup; b) installation of the test piece (view of the LVDT transducer); c) application of the load through an hydraulic jack minimizing the load oscillations; d) general view of the setup during the creep tests; e) comparison of the residual strain, between specimens A+ and A-, just finished the test. 113
Fig. 5.8 Creep plots for all the specimens tested. 115
Fig. 5.9 Temperatures measured during the creep tests for the specimens A and A+. 115
Fig. 5.10 Relaxation moduli for all the compounds tested, calculated by the creep test results of Fig. 5.8. 116
Fig. 5.11 Setup of the sinusoidal uniaxial tests to verify the theory of Muhr et al. (1997): a) schematic drawing, b) photo. c), d) Images from running tests (with additional weight). 120
Fig. 5.12 Planning of the tests execution order and balls position: rubber A, layer thickness 1.5 mm 121
Fig. 5.13 a), b) Images of balls positioning. Images of rubber tracks, lower (c) and upper (d), after running some (c) / all (d) tests associated with that RBRL device. 122
Fig. 5.14 a) Example of force (F)-displacement (D) loop, for the second sinusoidal cycle, for the case: A, t=2mm, D=20mm, $W/ER^2=3$. b) The same, in terms of friction coefficient μ (=F/Wg). The quadrants are numbered following the rolling of the balls. 123
Fig. 5.15 Comparison, for the compound A, of the rolling friction values (μ) obtained by the tests and the theory, for different values of the thickness/radius ratio (t/R). (a) Stress parameters ($W/ER^2$) from 0.4 to 2.0 (b) Tests with higher stress parameters: 3.0 and 4.0. 124
Fig. 5.16 Comparison, for the compound A+, of the rolling friction values (μ) obtained by the tests and the theory, for different thickness/radius ratios (t/R) and stress

parameters ($W/ER^2$). 125
Fig. 5.17 Comparison, for the compound A-, of the rolling friction values (μ) obtained by the tests and the theory, for different thickness/radius ratios (t/R) and stress parameters ($W/ER^2$). 125
Fig. 5.18 Semi-permanent rolling tracks after a test with rubber A and stress parameter 4. 126
Fig. 5.19 Complete theory in terms of (t/R), for rubber A, calibrated from experimentation. 126
Fig. 5.20 a) $g$ parameter (see Eq. (5.5)) needed to scale the hysteretic parameter value, calculated as α=π·sinδ, to have the best fitting between theory and test results. b) Comparison, for rubber A+ and A-, between the values of the parameter $g$ obtained by tests and the ones calculated by Eq. (5.6), in which compound A is the reference one. 127
Fig. 5.21 a) Values of the hysteretic parameter α considering the classic definition: α=π·sinδ. b) α values calibrated from tests to have the best fitting with the theory (Eq. (5.5)). 127
Fig. 5.22 Theoretical μ values, calibrated through the experimentation, for each compound (A+, A, A-) and stress parameter ($W/ER^2$) analyzed, on an adequate range of t/R ratios. 128
Fig. 5.23 a) Schematic drawing and b) image of the double shear test setup for the behaviour characterization of the recentering rubber springs. c),d) Images from quasi-static test for spring ϕ30 at 150 mm of deflection. 129
Fig. 5.24 Tested recentering rubber springs; diameter (ϕ), from left to right: 50, 40, 30 mm. 130
Fig. 5.25 Hysteretic loops from the sinusoidal tests with same frequency,1 Hz, and different amplitudes; diameters of the springs tested: 30, 40, 50 mm. Values for one spring. 131
Fig. 5.26 Hysteretic loops from the sinusoidal tests with same amplitude,75 mm, and different frequencies; diameters of the springs tested: 30, 40, 50 mm. Values for one spring. 131
Fig. 5.27 ELVFD parameters from sinusoidal tests at the same frequency,1 Hz. Comparison between the Harmonic and Secant linearization methods. Values for one spring. 132
Fig. 5.28 ELVFD parameters from sinusoidal tests at the same amplitude, 75 mm. Comparison between the Harmonic and Secant linearization methods. Values for one spring. 133
Fig. 5.29 Force-deflection plots from quasi-static tests; diameters of the springs tested: 30, 40, 50 mm. Values for one spring. 134
Fig. 5.30 a) Secant stiffness and b) tangent stiffness plots calculated from the results of the quasi-static tests (Fig. 5.29). Values for one spring. 134

Fig. 5.31 Comparison between the storage stiffness $K^{/}$, from dynamic tests, and the secant one $K_{sec}$, from quasi-static tests. The stiffness finally considered derives from $K^{/}$ values until 75 mm, and from $K_{sec}$ values for higher deflections (as indicated by the dashed lines)........................................................................ 135
Fig. 5.32 Nonlinear dependence of the stiffness $K^{/}$ on deflection. Values obtained by the ones of Fig. 5.31 subtracting the initial values of stiffness $K^{/}$ associated with each diameter. ................................................................................................ 136
Fig. 5.33 Prediction of the storage stiffness values $K^{/}$, using Eq. (5.13), and comparison with the experimental values for the diameters 30, 40 and 50 mm. ................ 137
Fig. 5.34 Nonlinear dependence of the tangent stiffness $K_{tan}$ of the springs on deflection.138
Fig. 5.35 Prediction of the tangent stiffness values $K_{tan}$, using Eq. (5.15), and comparison with the experimental values for the diameters 30, 40 and 50 mm. ................ 138
Fig. 5.36 Tangent stiffness calculated by the experimental results, compared with the one proposed in the Guerreiro et al. (2007) Model for the RBRL device, relatively to the recentering springs system used in the ECOEST Project (4 spring, diameter 30 mm)........................................................................................................ 139
Fig. 5.37 Prediction of the storage stiffness values $K^{/}$, using Eq. (5.13). ...................... 141
Fig. 5.38 Design displacement response spectra from EC8 (2004), assuming a spectrum of “type 1”, a ground of “type B” and a bedrock acceleration of 0.15 [g]. ........ 143
Fig. 6.1 μ-disp loops. Rubber A, t=2mm, D=25mm, $W/ER^2$=1.2, constant max. velocity.151
Fig. 6.2 μ-disp loops. Rubber A, t=2mm, D=25mm, $W/ER^2$=1.2, constant frequency. . 152
Fig. 6.3 Envelopes of μ-disp loops. Rubber A, t=2mm, D=25mm, $W/ER^2$=1.2. ........... 153
Fig. 6.4 Comparisons of μ-disp loops - 1st cycle. Rubber A, t=2mm, D=25mm, $W/ER^2$=1.2. ............................................................................................ 153
Fig. 6.5 Comparisons of μ-disp loops - 2nd cycle. Rubber A, t=2mm, D=25mm, $W/ER^2$=1.2. ............................................................................................ 154
Fig. 6.6 Comparisons of μ-disp loops - 3rd cycle. Rubber A, t=2mm, D=25mm, $W/ER^2$=1.2. ............................................................................................ 154
Fig. 6.7 μ-disp loops. Rubber A, t=2mm, D=25mm, $W/ER^2$=2. ................................. 157
Fig. 6.8 Comparisons of μ-disp loops – 1st cycle. Rubber A, t=2mm, D=25mm, $W/ER^2$=2.158
Fig. 6.9 Comparisons of μ-disp loops – 2nd cycle. Rubber A, t=2mm, D=25mm, $W/ER^2$=2. ............................................................................................... 158
Fig. 6.10 μ-disp loops. Rubber A+, t=2mm, D=25mm, $W/ER^2$=1.2. ............................. 159
Fig. 6.11 Comparisons of μ-disp loops–1st cycle. Rubber A+, t=2mm, D=25mm, $W/ER^2$=1.2. ............................................................................................ 160
Fig. 6.12 Comparisons of μ-disp loops–2nd cycle. Rubber A+, t=2mm, D=25mm, $W/ER^2$=1.2. ............................................................................................ 160
Fig. 6.13 μ-disp loops. Rubber A-, t=2mm, D=25mm, $W/ER^2$=1.2. .............................. 161

Fig. 6.14 Comparisons of μ-disp loops–1st cycle. Rubber A-, t=2mm, D=25mm, $W/ER^2$=1.2. ........ 162

Fig. 6.15 Comparisons of μ-disp loops–2nd cycle. Rubber A-, t=2mm, D=25mm, $W/ER^2$=1.2. ........ 162

Fig. 6.16 $K^{/}$, $K^{//}$, $K^*$, δ vs ampl. Rubber A, t=2mm, D=25mm, $W/ER^2$=1.2, constant velocity. ........ 165

Fig. 6.17 $K^{/}$, $K^{//}$, $K^*$, δ vs ampl. Rubber A, t=2mm, D=25mm, $W/ER^2$=1.2, constant frequency ........ 165

Fig. 6.18 $K^{/}$, $K^{//}$, $K^*$, δ vs amplitude. Rubber A, t=2mm, D=25mm, $W/ER^2$=1.2, 1st cycle.166

Fig. 6.19 $K^{/}$, $K^{//}$, $K^*$, δ vs amplitude. Rubber A, t=2mm, D=25mm, $W/ER^2$=1.2, 2nd cycle.166

Fig. 6.20 μ_max vs displacement. Rubber A, t=2mm, D=25mm, $W/ER^2$=1.2. a) Different cycles, all at 1 Hz; b) comparison of constant frequency (1 Hz) and velocity (31 mm/s) results for first cycles. ........ 167

Fig. 6.21 Comparison of $K^{/}$, $K^{//}$, $K^*$, δ vs amplitude, for the values of the stress parameter W* analyzed. Case: rubber A, t=2mm, D=25mm _ 2nd cycle. ........ 168

Fig. 6.22 Comparison of $K^{/}$, $K^{//}$, $K^*$, δ vs amplitude, for the values of the ball diameter D analyzed. Case: rubber A, t=2mm, $W/ER^2$=1.2 _ 2nd cycle. ........ 169

Fig. 6.23 Comparison of $K^{/}$, $K^{//}$, $K^*$, δ vs amplitude, for the values of the rubber thickness t analyzed. Case: rubber A, D=25mm, $W/ER^2$=1.2 _ 2nd cycle. ........ 170

Fig. 6.24 Comparison of $K^{/}$, $K^{//}$, $K^*$, δ vs amplitude, for the different rubbers (A-, A, A+) analyzed. Case: t=2mm, D=25mm, $W/ER^2$=1.2 _ 2nd cycle. ........ 171

Fig. 6.25 Comparison of $\mu_{max}$ vs displacement, for the values of the stress parameter W* analyzed. Case: rubber A, t=2mm, D=25mm _ 1st cycle. ........ 174

Fig. 6.26 Comparison of $\mu_{max}$ vs displacement, for the values of the ball diameter D analyzed. Case: rubber A, t=2mm, $W/ER^2$=1.2 _ 1st cycle. ........ 174

Fig. 6.27 Comparison of $\mu_{max}$ vs displacement, for the values of the rubber thickness t analyzed. Case: rubber A, D=25mm, $W/ER^2$=1.2 _ 1st cycle. ........ 174

Fig. 6.28 Comparison of $\mu_{max}$ vs displacement, for the different rubbers (A-, A, A+) analyzed. Case: t=2mm, D=25mm, $W/ER^2$=1.2 _ 1st cycle. ........ 175

Fig. 6.29 $\mu_{peak}$, relative displacement $\Delta_{peak}$ and secant stiffness $K_{peak}$ plotted versus the stress parameter $W/ER^2$. Case: rubber A, t=2mm, D=25mm. ........ 176

Fig. 6.30 $\mu_{peak}$, relative displacement $\Delta_{peak}$ and secant stiffness $K_{peak}$ plotted versus the diameter D of the ball. Case: rubber A, t=2mm, $W/ER^2$=1.2. ........ 177

Fig. 6.31 $\mu_{peak}$, relative displacement $\Delta_{peak}$ and secant stiffness $K_{peak}$ plotted versus the thickness t of the rubber layer. Case: rubber A, D=25mm, $W/ER^2$=1.2. ........ 178

Fig. 6.32 $\mu_{peak}$, relative displacement $\Delta_{peak}$ and secant stiffness $K_{peak}$ plotted versus the type of the rubber. Case: t=2mm, D=25mm, $W/ER^2$=1.2. ........ 179

Fig. 6.33 Samples used to measure the geometric profiles of the pits: a) painting with

Chemlok_220 (bonding agent) after sandblasting of the steel plates; b) samples finished. .......... 180
Fig. 6.34 Setup for the first phase of the test: application of the load on the samples for 25h. .......... 181
Fig. 6.35 a) Scheme and b) image of the setup for the measurement of the geometric profiles of the pits. .......... 182
Fig. 6.36 Details of the setup (a) for the measurement of the pit profiles: b) non-contacting capacitance probe and c) needle probe at the two ends of the aluminium alloy bar. d) View of a pit after some measures (the lines shown the measurement directions). .......... 183
Fig. 6.37 Comparison of the geometric profiles of the residual indentation for the case of rubber A, D=25mm, t=2mm, for different values of the stress level (W*=1.2, 2, 3). .......... 186
Fig. 6.38 Geometric profiles of Fig. 6.37 with the indication of the relative indenter. ..... 186
Fig. 6.39 Comparison of the geometric profiles of the residual indentation for the case of rubber A, D=25mm, W*=2, for different thicknesses of the rubber layer (t=1.5, 2, 3 mm). .......... 187
Fig. 6.40 Geometric profiles of Fig. 6.39 with the indication of the relative indenter. ..... 187
Fig. 6.41 Comparison of the geometric profiles of the residual indentation for the case of rubber A, t=2mm, W*=3, for different values of the ball diameter (D=15, 20, 25).188
Fig. 6.42 Geometric profiles of Fig. 6.41 with the indication of the relative indenters. ... 188
Fig. 6.43 Comparison of the geometric profiles of the residual indentation for the case of rubber A+, D=25mm, for different combinations of stress level (W*=1.2, 2) and thickness of rubber layer (t=1.5, 2, 3 mm). .......... 189
Fig. 6.44 Geometric profiles of Fig. 6.43 with the indication of the relative indenter. ..... 189
Fig. 6.45 Comparison of the geometric profiles of the residual indentation for the case of rubber A-, D=25mm, for different combinations of stress level (W*=1.2, 2) and thickness of rubber layer (t=1.5, 2, 3 mm). .......... 190
Fig. 6.46 Geometric profiles of Fig. 6.45 with the indication of the relative indenter. ..... 190
Fig. 6.47 Different shape of the profile of the residual indentation: a) recovery of the rubber at the same velocity (typical for rubber A+, and A with W*<2); b) recovery of the rubber with different velocities inside the pit, slower in the central part (typical for rubber A-). .......... 191
Fig. 6.48 a) Maximum residual indentations by tests, after a dwell time of the load of 25 hours, for the case of rubber A and different values of t/R and W/ER$^2$. The same results are reproduced in the figures b), c), d) for the different values of rubber layer thickness analyzed. .......... 192
Fig. 6.49 Maximum residual indentations by tests, after a dwell time of the load of 25

hours, for different values of t/R and W/ER$^2$, and for the case of rubber A+ (a) and A- (b). ........ 192
Fig. 6.50 a) Maximum indentations under load given by Waters' equations (Eqs. (6.6) and (6.7)), considering the Young's modulus (t=0) and the one relaxed after 25 hours (t=25h), for the case of rubber A and different values of t/R and W/ER$^2$. The same results are reproduced in the figures b), c), d) for the different values of rubber layer thickness analyzed. ........ 195
Fig. 6.51 Maximum indentations under load given by Waters' equations (Eqs. (6.6) and (6.7)), considering the Young's modulus (t=0) and the one relaxed after 25 hours (t=25h), for different values of t/R and W/ER$^2$, and for the case of rubber A+ (a) and A- (b). ........ 195
Fig. 6.52 a) Comparisons between test results and values calculated by Eq. (6.12) for the maximum residual indentation, for the case of rubber A and different values of t/R and W/ER$^2$. The same results are reproduced in the figures b), c), d) for the different values of rubber layer thickness analyzed. ........ 197
Fig. 6.53 Comparisons between test results and values calculated by Eq. (6.12) for the maximum residual indentation, for different values of t/R and W/ER$^2$, and for the case of rubber A+ (a) and A- (b). ........ 197
Fig. 6.54 Estimate of the maximum residual indentation $d_R$ through the Eq. (6.12), after a dwell time of the load of 25 hours, for the rubber A and for a certain range of t/R and W/ER$^2$. ........ 198
Fig. 6.55 Estimate of the maximum residual indentation $d_R$ through the Eq. (6.12), after a dwell time of the load of 25 hours, for the rubber A+ and for a certain range of t/R and W/ER$^2$. ........ 198
Fig. 6.56 Estimate of the maximum residual indentation $d_R$ through the Eq. (6.12), after a dwell time of the load of 25 hours, for the rubber A- and for a certain range of t/R and W/ER$^2$. ........ 199
Fig. 6.57 μ-disp loops. Case: rubber tracks A-A, W = 250 N, $t_{dw}$ = 24 h, 2nd cycle. ........ 203
Fig. 6.58 μ-disp loops. Case: rubber tracks B-B, W = 250 N, $t_{dw}$ = 24 h, 2nd cycle. ........ 204
Fig. 6.59 Comparison of $K^{/}$, $K^{//}$, K*, δ vs amplitude, for the different rubber tracks considered: A-A, A-B and B-B. Case: $t_{dw}$ = 24 hours, max. vel. = 31 mm/s, 2nd cycle. ........ 205
Fig. 6.60 Semi-permanent rolling tracks on the rubber layer B. Case B-B, $t_{dw}$=24 h, W=250 N: a) before the test (the semi-permanent rolling tracks visible derive from the previous test with W=150 N); b) afer the test. ........ 206
Fig. 6.61 Comparison of $K^{/}$, $K^{//}$, K*, δ vs amplitude, for the different dwell times of the load considered: 6, 24 and 96 hours. Case: tracks A-A, W = 250 N, max. vel.= 31 mm/s, 2nd cycle. ........ 206

Fig. 6.62 Dependence of $K^{/}$, $K^{//}$, $\delta$ and $\mu_{max}$ on the logarithm of the dwell time, for amplitudes up to 5 mm (balls inside pits). Case: tracks A-A, W = 250 N, max. vel.= 31 mm/s, 2nd cycle. ........ 207

Fig. 6.63 Comparisons of $K^{/}$ and $K^{//}$ of the RBRL device with rubber A, t = 2mm, D = 25 mm between the cases of: sinusoidal shaking-table test performed at 5 Hz during ECOEST project ($W^* \approx 1.3$), new sinusoidal test on the same ECOEST device and with similar W* (after 15 years from its production), new sinusoidal tests on a new RBRL device (produced at TARRC for this PhD Project) with values of W* of 1.2 and 1.6. ........ 208

Fig. 6.64 Same dependence of the ratio $\mu_{peak}/\mu_{roll}$ (a) and $d_R/d_W$ (b) on the parameter t/R. The values of $\mu_{peak}$ were obtained by sinusoidal tests performed with same $W/ER^2$ and rubber A, presented in section 6.2. ........ 210

Fig. 6.65 Different dependence of the ratio $\mu_{peak}/\mu_{roll}$ (a) and $d_R/d_W$ (b) on the stress parameter $W/ER^2$. The values of $\mu_{peak}$ were obtained by sinusoidal tests performed on the same device with rubber A, t = 2 mm, D = 25 mm, presented in section 6.2. ........ 210

Fig. 6.66 Interpolating function $f_a$ according to Eq. (6.16). ........ 212

Fig. 6.67 Interpolating function $f_b$ according to Eq. (6.17). ........ 212

Fig. 6.68 Estimate of $\mu_{peak}$ according to empirical Eq. (6.18) and comparison of the values with the experimental ones. ........ 213

Fig. 6.69 Comparison that shows the same dependence of the ratio $\mu_{peak}/\mu_{roll}$ and of the function $f_a$ (shown in Fig. 6.66) on the parameter t/R. ........ 213

Fig. 6.70 Dependence of the estimated values of $\mu_{peak}$ on the load dwell time, according to Eq.(6.18), for different stress levels and for the case of rubber A, t = 2 mm and D = 25 mm. Overlap of the $\mu_{peak}$ values gathered by the sinusoidal tests presented in section 6.4 on the associated ECOEST device (A, t = 2mm, D = 25 mm). ........ 214

Fig. 6.71 Dependence of the estimated values of $\mu_{peak}$ on the load dwell time, according to Eq.(6.18), for different stress levels and for the case of rubber A-, t = 2 mm and D = 25 mm. ........ 214

Fig. 6.72 Dependence of the estimated values of $\mu_{peak}$ on the load dwell time, according to Eq.(6.18), for different stress levels and for the case of rubber A+, t = 2 mm and D = 25 mm. ........ 215

Fig. 6.73 Estimate of $\mu_{peak}$, according to Eq.(6.18), for rubber A, D = 25 mm and different combinations of the parameters $W/ER^2$ and t/R. Each of these combinations is characterized by the same value of $\mu_{roll}$ according to the theory of Muhr et al. (1997). ........ 215

Fig. 6.74 a), b) Effects of the recovery of the rubber on the maximum rolling friction $\mu_{max}$

due to the roll-out of the balls from their pits. c), d) Interpolating equations for the functions $f_1$(Ampl.) and $f_2$(time) necessary to apply the equation Eq. (6.20). .. 218
Fig. 6.75 Estimate of the recovery effects of the rubber on $\mu_{max}$, according to Eq. (6.20).218
Fig. 6.76 a), b) Effects of the recovery of the rubber on the maximum rolling friction $\mu_{max}$ due to the roll-out of the balls from their pits. c), d) Interpolating equations for the functions $f_1$(Ampl.) and $f_2$(time) necessary to apply the equation Eq. (6.20). .. 219
Fig. 6.77 Estimate of the recovery effects of the rubber on $\mu_{max}$, according to Eq. (6.20).219
Fig. 6.78 a), b) Effects of the recovery of the rubber on the maximum rolling friction $\mu_{max}$ due to the roll-out of the balls from their pits. c), d) Interpolating equations for the functions $f_1$(Ampl.) and $f_2$(time) necessary to apply the equation Eq. (6.20). .. 220
Fig. 6.79 Estimate of the recovery effects of the rubber on $\mu_{max}$, according to Eq. (6.20).220
Fig. 6.80 Modelling of the steady-state rolling resistance. ........................................... 222
Fig. 6.81 Theoretical μ values, calibrated through the experimentation (Ch. 5), for each compound (A+, A, A-) and stress parameter ($W/ER^2$) analyzed, for an adequate range of t/R. ........................................................................................ 223
Fig. 6.82 Hysteretic loops from the sinusoidal tests (Ch. 5) with same amplitude,75 mm, and different frequencies; diameters of the springs tested: 30, 40, 50 mm. Values for one spring. ........................................................................ 225
Fig. 6.83 Prediction of the tangent stiffness $K_{tan}$ values using Eq. (5.15), proposed again in Eq.(6.21), for different diameters of the spring: 30, 40 and 50 mm. ............ 225
Fig. 6.84 a) Non-linear elastic behaviour for the presence of the initial depression under the ball. b) Tangent stiffness calculated from the non-linear μ-disp behaviour of plot a). Results from a sinusoidal test performed at 65 mm amplitude and 0.5 Hz frequency, on the RBRL device assumed as reference (A, t=2mm, D=25mm, W*=1.2). ........................................................................................ 227
Fig. 6.85 Influence of the pits on the rolling friction resistance for small displacements of the balls. Test at 65 mm and 0.5 Hz, on the reference RBRL device............. 228
Fig. 6.86 a) Envelopes of the μ-disp loops of the tests with constant velocity (v=31mm/s) and constant frequency (f=1Hz), for the reference RBRL device, presented in section 6.2. The points represent the non-linear elastic μ-disp behaviour inside the pit, and were obtained by scaling the values of Fig. 6.84 a) by the ratio of the $\mu_{peak}$ values. b) Related tangent stiffnesses. ................................................. 229
Fig. 6.87 Influence of the pits on the rolling friction resistance for small displacements of the balls. Test at 65 mm and 0.5 Hz, on the reference RBRL device............. 229
Fig. 6.88 Proposal of a time-domain model for the RBRL isolation system. .................. 230
Fig. 6.89 Comparison of the real μ-disp loops (no recentering springs) with those predicted by the model..................................................................... 231

# LIST OF TABLES

Tab. 3.1 Summary of earlier studies done by TARRC and collaborating research centres on RBRL device, from Donà et al. (2014). .......... 57

Tab. 5.1 Geometric characteristics of the test pieces. .......... 108

Tab. 5.2 Forces used in the creep tests. .......... 113

Tab. 5.3 Parameters to calibrate a discrete Prony series (Ahmadi et al., 2008). .......... 115

Tab. 5.4 Summary of the parameters for the rubber compounds (from dynamic test). . 118

Tab. 5.5 Tests planning for rubber compound A. .......... 118

Tab. 5.6 Tests planning for rubber compound A-. .......... 119

Tab. 5.7 Tests planning for rubber compound A+. .......... 119

Tab. 5.8 Double shear tests carried out on the recentering rubber springs. .......... 130

Tab. 5.9 Static stiffness $K_{st}$ values, according to Eqs. (5.9)-(5.10), for the various diameters. .......... 135

Tab. 5.10 Initial value of the storage stiffness, $K_{init}^{/}$, and nonlinear dependence of the tangent stiffness on the deflection, $\Delta K_{\tan}\left(D\right)$, for the various diameters $\phi_i$ tested. .......... 139

Tab. 5.11 Rolling friction for rubber A calculated from stipulated values of thickness ratio t/R and selected stress parameter values $W/ER^2$ using the theory of Muhr et al. (1997), experimentally calibrated. .......... 141

Tab. 5.12 Values of μ and K needed to obtain a RBRL isolation system able to provide the relative isolation periods and damping ratios, considering the design spectrum above. The highlighted values of μ are the ones more compatible with a rubber of type A. .......... 143

Tab. 6.1 Sinusoidal input of the tests and characteristics of the output data. Every step was spaced from the previous one by 8 seconds to recreate the undisturbed conditions. .......... 149

Tab. 6.2 Load conditions for test sequences using the sinusoidal input given in Tab. 6.1.149

Tab. 6.3 Characteristics of the tests carried out: combinations of the stress parameter W*, thickness t of the rubber layer and diameter D of the balls for the different rubber compounds. .......... 184

Tab. 6.4 Principal characteristics of the rubber compounds used in the tests. .......... 194

Tab. 6.5 Tests performed on the devices used in the ECOEST project (1999). .......... 200

Tab. 6.6 First sinusoidal input, with amplitudes from 1 to 5 mm (corresponding to balls rocking inside their pits). .......... 201

Tab. 6.7 Sinusoidal inputs subsequent to the one of Tab. 6.6, with amplitudes from 6 to

70 mm. ........................................................................................................ 201

Tab. 6.8 Theoretical μ values for rubber A, calculated for selected values of t/R and W/ER$^2$ using the theory of Muhr et al. (1997), experimentally calibrated. ....... 223

Tab. 6.9 $K_{init}^{/}$ and $\Delta K_{\tan}(D)$ for the various diameters $\phi_i$ of the rubber spring tested.225

Tab. 6.10 Interpolating equations of the non-linear μ-disp behaviour and of the associated tangent stiffness plotted in Fig. 6.84. ............................................................ 227

## LIST OF SYMBOLS

| | | |
|---|---|---|
| · | **D** | diameter of the ball (or steel sphere) |
| · | $\mathbf{d_R}$ | residual indentation on rubber layer after unloading (spherical indentor of infinite stiffness) |
| · | **DRS** | displacement response spectrum |
| · | $\mathbf{d_W}$ | elastic indentation on rubber layer under load (spherical indentor of infinite stiffness) |
| · | **E** | Young’s modulus |
| · | **ELVFD** | Equivalent Linear Viscoelastic Frequency-Domain parameters (or representation) |
| · | **G** | shear modulus |
| · | $\mathbf{H_0}$ | parameter of Prony series (or negative slope value of the relaxation modulus versus ln(t)) |
| · | **K** | stiffness (in general) |
| · | **K*** | dynamic complex stiffness |
| · | $\mathbf{K^{/}}$ | storage stiffness |
| · | $\mathbf{K^{//}}$ | loss stiffness |
| · | $\mathbf{K_{peak}}$ | stiffness associated with $\mu_{peak}$ |
| · | **M** | mass |
| · | **PGA** | Peak Ground Acceleration |
| · | **R** | radius of the ball (or steel sphere) |
| · | **S** | stress relaxation rate or creep rate |
| · | **SDOF** | Single Degree Of Freedom |
| · | **T** | period of oscillation |
| · | **t** | thickness of the rubber layer (or rubber track) |
| · | **W** | load per ball (of the RBRL device) |
| · | **W*** | Stress parameter ($W/ER^2$) |

---

### Greeks

| | | |
|---|---|---|
| · | $\boldsymbol{\alpha}$ | hysteresis parameter |
| · | $\boldsymbol{\delta}$ | loss angle |
| · | $\boldsymbol{\Delta}_{\mathbf{peak}}$ | displacement associated with $\mu_{peak}$ |
| · | $\boldsymbol{\zeta}$ | damping ratio |
| · | $\boldsymbol{\mu}$ | rolling friction |
| · | $\boldsymbol{\mu}_{\mathbf{f}}$ | sliding friction |
| · | $\boldsymbol{\mu}_{\mathbf{max}}$ | maximum rolling friction of a μ-displacement loop |
| · | $\boldsymbol{\mu}_{\mathbf{peak}}$ | peak value of the rolling friction among the μ-displacement loops of a sinusoidal test with increasing amplitude |
| · | $\boldsymbol{\mu}_{\mathbf{roll}}$ | steady-state rolling friction |
| · | $\boldsymbol{\phi}$ | diameter of the recentering spring |

# 1 INTRODUCTION

## 1.1 Background and motivations

The effort to provide seismic protection of structures is certainly not new: probably the first evidence dates back to the half of the II millennium BC, as shown by the Massive Trojan Walls elevated above a layer of compacted soil specifically made over the bedrock (Giovannardi & Guisasola 2013, Clemente 2010). Carl Blegen, the archaeologist who was responsible for the Trojan Walls excavations in the 1930s, supposed that the ancient designers wanted to protect the structure from earthquakes through this “cushion of earth”, which was supposed to behave as a shock absorber between the foundations and the rocks.

Other evidences, dating back to 2500 years ago, are given by several Greek temples built above alternated layers of charcoal and fleeces of wool (Giovannardi & Guisasola 2013, Clemente 2010, Martelli 2010). A famous example is the Temple of Artemis, also known as the Temple of Diana, which was located in Ephesus: it was one of the Seven Wonders of the Ancient World. This temple was erected upon layers of wool and carbon, as described by Pliny the Elder in his masterpiece Naturalis Historia:

*“Graecae magnificentiae vera admiratio exstat templum Ephesiae Dianae CXX annis factum a tota Asia. In solo id palustri fecere, ne terrae motus sentiret aut*

*hiatus timeret, rursus ne in lubrico atque instabili fundamenta tantae molis locarentur, calcatis ea substravere carbonicus, dein velleribus lanae." (N.H., XXXVI,95).*

Other examples are the Temple of Heraion in Samo (VII-VI c. BC), again erected above alternated layers of charcoal and fleeces of wool, the Temple of Athena in Ilion (III c. BC) and the Temple of Paestum in Capaccio (III c. BC), both elevated on a base of sand and gravel (see Fig. 1.1). The same techniques were also known and experienced in the American continent, as shown by the walls of Cuzco in Perù (XIII c.) or the monastery of Santa Catalina in Arequipa (XVI c.), which were constructed upon a layer of sand and stone.

But the first examples of proper seismic isolation systems appear more recently. To the best of the author's knowledge, the isolation system proposed by Jules Touaillon in 1870 was the first to be patented (Tsai, 2012): this consisted of a rolling-based bearing system, between the base of the superstructure and its foundation, with balls placed between spherical concave surfaces as shown in Fig. 1.2 a). Some days later, Almond F. Cooper patented a base isolation system consisting of some rubber isolators (India-rubber buffers) placed under the walls of the building and above the foundation curbs, as represented in Fig. 1.2 b). In 1891, Kouzou Kawai proposed in the "Journal of Architecture and Building Science" a base isolation system consisting of alternating layers of concrete and tree trunks, to be realized at the level of the foundation plan of the structure to improve its seismic performance (Giovannardi & Guisasola 2013); the idea was similar to those undertaken in the ancient times, as seen above. Another isolation system worth noticing is the one patented by Jacob Bechtold in the 1906: a rigid plate to be placed between the upper structure and a pillow of rigid balls, to decouple the motion of the structure from the one of the ground. A few years later, in 1909, Jhoannes A. Calantarientes patented a sliding mechanism, consisting of a talc layer inserted between the building and its foundation, to reduce the friction and allow the superstructure to slide during an earthquake (Izumi, 1988).

Despite these first patents registered at the turn of the 20th century, the passive control technique of seismic isolation has developed rapidly only in the last 30-40 years. This is proved by the several studies and scientific publications on the topic which started to appear from the end of the 1970s, such as: Derham et al. 1977 and 1985, Tyler 1977, Robinson 1982, Derham 1983, Zayas et al. 1987, Costantinou et al. 1988, Uang and Bertero 1990, Kelly 1990 and 1991, and many others.

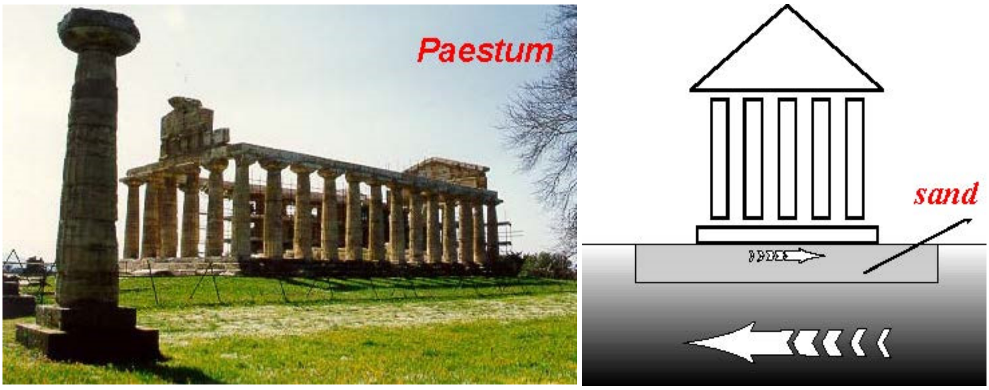
Paestum
sand

a) b)

*Fig. 1.1 a) Image of the Temple of Paestum in Capaccio (III c. BC). b) Scheme of the mechanism to protect the Temple by the earthquake: base of sand and gravel inserted between the foundation and the ground (image from Martelli, 2010).*

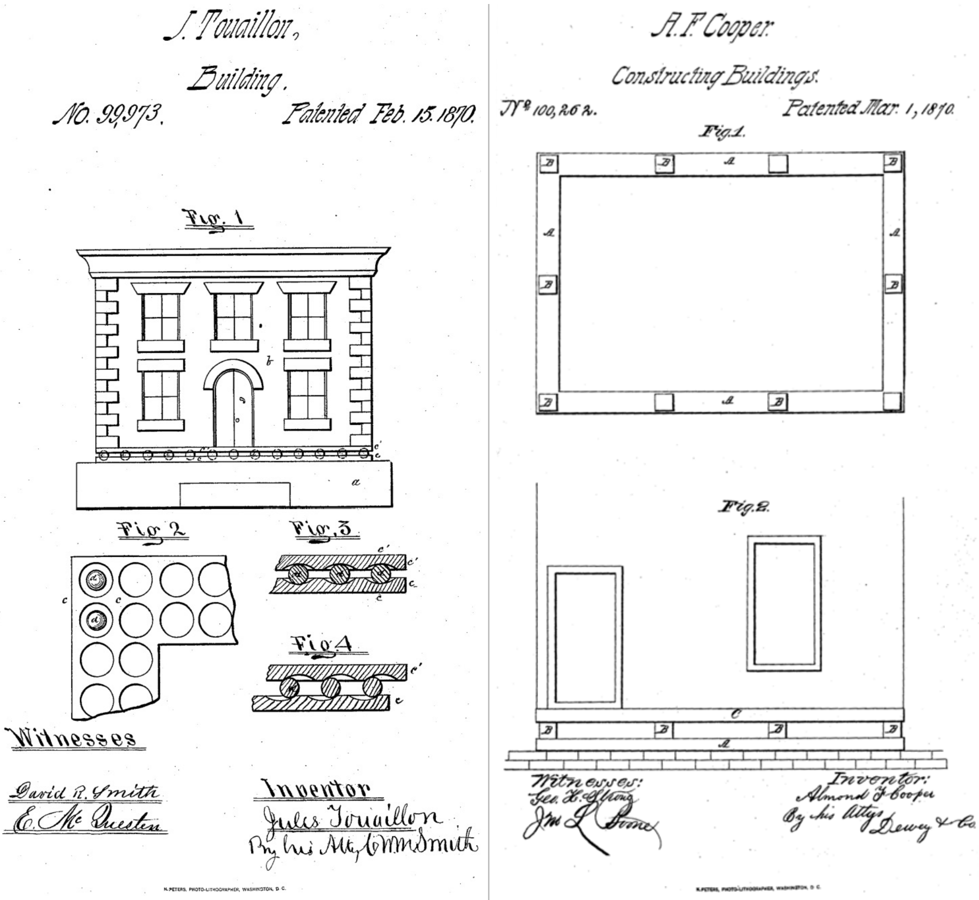
J. Touaillon,
Building.
No. 99,973.
Patented Feb. 15, 1870.
Fig. 1
Fig. 2
Fig. 3
Fig. 4
Witnesses
David R. Smith
E. McQuesten
Inventor
Jules Touaillon
By his Atty C. M. Smith
A. F. Cooper
Constructing Buildings.
No. 100,262.
Patented Mar. 1, 1870.
Fig. 1.
Fig. 2.
Witnesses:
Inventor:
Almond F. Cooper
By his Attys Dewey & Co.

a) b)

*Fig. 1.2 a) Touaillon's original patent, Feb. 1870. b) Cooper's original patent, Mar. 1870.*

The isolation technique allows the decoupling of the structure motion from the ground motion, by inserting structural elements with low horizontal stiffness ("isolators"): in this way the energy entering the structure is reduced, and the deformation is localized in the isolators. The principal characteristics of a seismic isolation device and system, and the principal modern techniques to seismically isolate a structure will be presented later in the next chapter.

To date, more than 23,000 structures located in over 30 countries have been protected by passive anti-seismic systems (Martelli et al., 2014), mainly through the techniques of seismic isolation and energy dissipation. Fig. 1.3 shows the number of buildings seismically isolated in the most active countries, while Fig. 1.4 shows the evolution of the use of isolation systems in Italy.

The use of these systems is increasing everywhere, and its extension in each country is strongly affected by the seismicity level as well as by the design rules of the country itself. For example, in some countries (such as Japan or USA) the isolation system is considered by the design codes as an additional safety measure, resulting in significant additional costs for the construction, while in others (such as Italy) the codes authorize to take into account a partial reduction of the seismic forces due to the benefits of the isolation system.

Passive anti-seismic systems, and in particular isolation systems, have been applied to new and existing civil and industrial structures of all kinds: from strategic and public structures to high risk plants, such as nuclear reactors and chemical installations, and also to residential buildings and private houses.

It is worth noting that, while in the last decades several studies and applications have involved seismic isolation of structures ("casing"), the isolation of content has lagged behind the trend.

Furthermore, isolation has not become the dominant means of seismic protection of structures: most structural engineers seek to prevent catastrophic failure through provision of adequate ductility and strength, which leaves the content and functionality of the structure vulnerable to earthquakes. Direct application of seismic isolation to content is thus needed, if its seismic protection is required and other approaches, such as anchorage, are not practicable or adequate.

The lack of effective techniques, which are sufficiently developed and applicable for the seismic risk mitigation of lightweight objects, make the seismic protection of contents a crucial and worldwide issue.

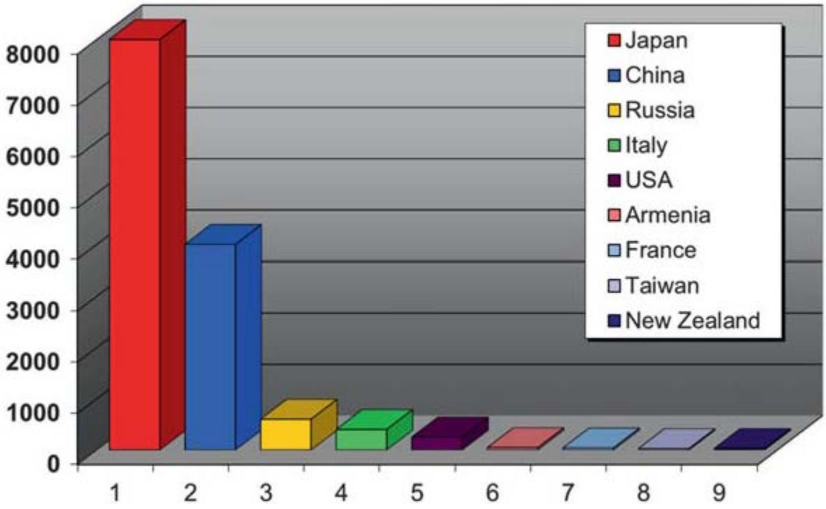

*Fig. 1.3 Comparison of the number of buildings seismically isolated between the most active countries - data of September 2013 (image from Martelli et al., 2014).*

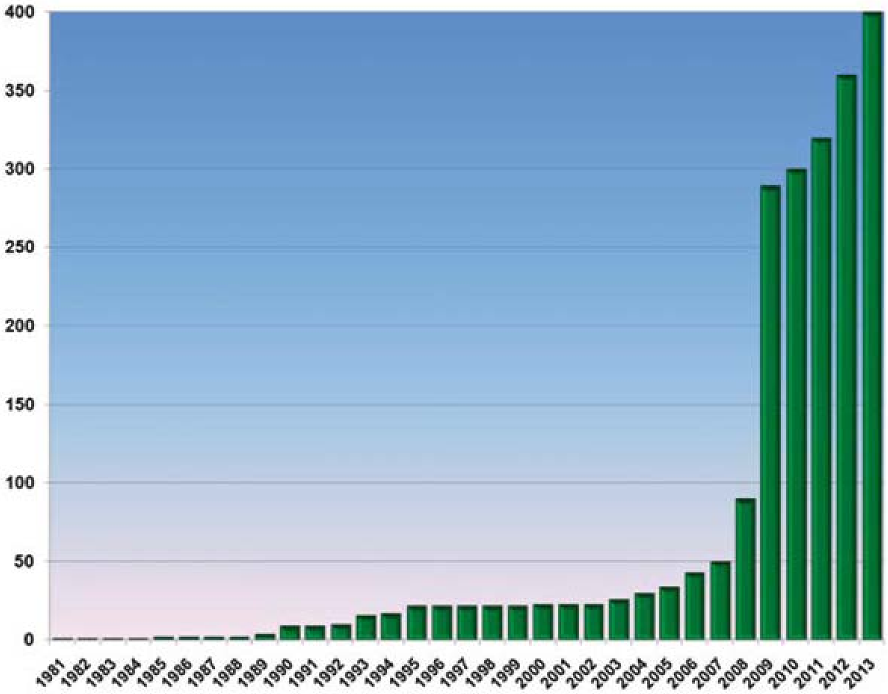

*Fig. 1.4 Number of Italian buildings seismically isolated during years (image from Martelli et al., 2014).*

## 1.2 Problem statement

Although the basic theories and concepts of seismic isolation are the same, the isolation techniques to be used for the content are not a mere extension of the ones used for civil structures. Indeed, the following technical peculiarities have to be considered: the contents have masses orders of magnitude smaller than those characteristic of civil structures and, secondly, they are often very vulnerable and are not able to withstand even small seismic actions.

Another main issue is given by the value of the content objects, sometimes much greater than that of the structure in which they are. Some data from Taghavi & Miranda (2003), reported in Fig. 1.5, illustrate the typical investment in structural framing, non-structural components and building contents, for three common types of commercial construction: office, hotel and hospital. Clearly the investment in non-structural components and building contents is far greater than that for structural components and framing (Whittaker & Soong 2003, FEMA E-74 2011).

The value of the content objects might be high not only from an economical point of view, e.g. for special medical or industrial equipment, but also from a cultural or historical one: this is the case for museum contents and art objects in general. The need to prevent or mitigate the devastating effects of earthquakes on cultural heritage assets is acute for countries in which this heritage is concentrated, and which suffer the highest seismic risk level: such as the case of Italy, and many other sites in the Mediterranean basin. Awareness of this issue has recently grown in Italy too, as a result of the quakes of Umbria-Marche (1997), l'Aquila (2009) and Emilia (2012).

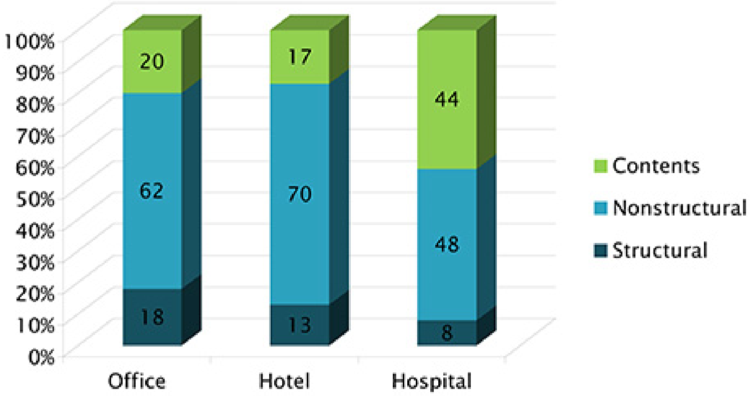

*Fig. 1.5 Typical cost breakdown in building construction, according to Taghavi & Miranda (2003), for three different occupancies (image from FEMA E-74, 2011).*

## 1.3 Aims and methods of the research

The thesis presents an innovative device for seismic isolation of lightweight structures, named “Rolling-Ball Rubber-Layer” (RBRL) system, and it is aimed at studying the dynamic behaviour of the system itself through numerical analyses and parametric experimentations. The principal goal is to get sufficiently comprehensive data on the performance of the system, to enable the creation of a time-domain model of its behaviour for quantifying its efficacy through time-history analyses.

The device, invented by Alan Thomas at TARRC (“Tun Abdul Razach Research Centre”, a Research and Promotion Centre of the Malaysian Rubber Board, located in Hertford, UK) comprises: a rolling-based bearing system, which allows any displacements in the horizontal plane; two rubber layers bonded to the steel tracks, which give an adequate damping to the rolling steel balls; some rubber springs, which ensure the recentering of the system through their elastic stiffness.

Numerical analyses, including also Time-History simulations in OpenSees, were performed on the results of the ECOEST Project, an extensive experimental study involving diverse shaking-table tests (Guerreiro et al., 2007); these show effectiveness of the RBRL system for moderate-high intensity earthquakes and also an advantageous behaviour, if compared to the alternative of a sliding system, for small intensity earthquakes. The equivalent linearized viscoelastic frequency-domain (ELVFD) representation is introduced and used to describe the RBRL system behaviour as tested in the ECOEST Project.

A parametric experimentation with sinusoidal uniaxial tests has been carried out changing the principal device parameters that control its behaviour, i.e. the rubber type, the thickness of the rubber layers, the ball diameter and the stress parameter for each ball, to validate the theory presented by Muhr et al. (1997): this provides the adimensional rolling resistance of steel balls, under a vertical load, on steel tracks covered with a thin rubber layer.

The viscoelastic properties of the rubber (creep phenomena) and the dwell time of the load lead to the creation of an initial indentation or pit on the rubber tracks, corresponding to the original position of the steel balls: this is an important peculiarity of the system, responsible for its advantageous dynamic response for small seismic intensities. Thus, a new parametric experimentation has been performed, comprising sinusoidal uniaxial tests and direct measurements of the geometric profiles of the pits, to understand and model the device behaviour for small oscillations, for which either the balls remain inside their pits or in the transition phase from their initial position to steady-state rolling.

Further tests have been conducted on the RBRL systems used in the ECOEST Project and produced 15 years ago: the devices without the recentering springs, with different rubber compounds (high and low damping) and different dwell times of the static configuration, and the single rubber springs with different geometric configurations have been tested. Useful information has been thus gathered, for the influence of the dwell time on the small-deflection behaviour of the device and for the dynamic behaviour of the springs.

All the numerical analyses and experimentations performed, needed for the characterisation of the device dynamic behaviour, have been finalized into the proposal of:

- a simplified design procedure, starting from chosen values of the isolation period and damping ratio and leading to the determination of all the device parameters, for a specific design spectrum and vertical load considered;
- a new numerical model, for the seismic response prediction of the RBRL system through non-linear numerical analyses in the Time-Domain.

A model is a prerequisite for the prediction of the system behaviour, and hence necessary to quantify the efficacy of the system for seismic mitigation and achieve design objectives. Since there is considerable uncertainty regarding both the actual strong motion and the response behaviour of the structure to be protected, the need is for a robust model that is easy to fit to the measured characteristics of the system and to implement numerically, and that captures the essence of behaviour, rather than for a very elaborate model that captures every detail. We shall restrict attention here to uniaxial behaviour.

The experimental campaign described in this work, together with the RBRL devices production, has been carried out at TARRC in collaboration and under the scientific guidance of Dr. Alan H. Muhr.

## 1.4 Thesis organization

The principal contents of each chapter are briefly presented here below.

Chapter 1
*Introduction*

Chapter 2
*Background of seismic isolation for lightweight structures*

The issue of the seismic vulnerability of the contents of a building is deepened, in particular considering three principal such categories: artefacts, special medical equipment and electrical equipment.

A background about the possible motions of a rigid object only rested on a horizontal rigid plane, which is moving, is presented; in particular, the highlights about the rocking phenomenon are reported. Also relative to the dynamic behaviour of the objects of the content, the seismic isolation technique is presented as an effective solution to reduce the seismic risk of these lightweight structures.

The effects of the passive anti-seismic systems on structures, through the techniques of seismic isolation and energy dissipation, are explained. Subsequently, the principal characteristics of an isolation device and the technologies available to date to seismically isolate civil structures are illustrated, together with the principal issues that made these technologies unsuitable for lightweight structures and content.

Finally, a state of the art review of isolators specifically studied and designed to seismically protect lightweight structures is presented, describing the principal characteristics of the isolators themselves and showing their applications.

Chapter 3
*Background of RBRL system and rubber dynamic behaviour*

A state of the art review of the RBRL system is presented. The device is described in its components and functions and a summary of the history of the tests carried-out on the device to date is provided. In addition, the principal information about the modelling of the RBRL system is reported.

The concepts and formulation of a very interesting theory, given by Muhr et al. in 1997, are presented. This theory provides the equivalent rolling friction coefficient for the rolling of a steel ball over a thin rubber layer, given the principal parameters that influence the behaviour of the device: type of rubber compound, thickness of rubber layer, diameter of ball, stress parameter. The results form Muhr et al. (1997) are reported and then discussed.

The dynamic properties of the rubber together with a brief overview of viscoelasticity are presented, the RBRL system being based on the rubber behaviour. Subsequently, the principal linearization methods for the Equivalent Linearized Viscoelastic Frequency-Domain (ELVFD) representation are shown: this representation is generally used to describe the non-linear behaviour (amplitude dependence) of filled rubber. In this thesis project only unfilled rubbers have been considered for the rolling tracks of the RBRL device; however, the ELVFD parameters have been presented because these will be used to describe the non-linear behaviour of the RBRL system itself for small displacements, where the stiffness and damping of the device highly depend on the deflection amplitude despite the unfilled rubber.

Chapter 4

*Numerical analyses of ECOEST project results and applications of ELVFD representation*

Some numerical analyses performed on results from the ECOEST Project (1999), an extensive experimental study involving diverse shaking-table tests (Guerreiro et al., 2007), are presented. These analyses, including time-history simulations in OpenSees, besides confirming the effectiveness of the RBRL system for moderate-high intensity earthquakes, proved its efficacy in the reduction of excitation of the first mode of the isolated structure for small seismic events, despite its being very much stiffer when the deflections across the isolators are smaller than about 5 mm.

The ELVFD representation is used to describe the behaviour of the RBRL system as tested in the ECOEST Project. ELVFD parameters are then used, together with the force-displacement loops, to compare the properties of the actual RBRL system with two different time-domain models: the one given in Guerreiro et al. (2007) and a new simplified one proposed here.

The new simplified time-domain model is described: it gives a better representation of the behaviour of the RBRL system than the Guerreiro model. It is based on the ELVFD parameters and requires 2 or 3 iterations for the prediction of the small-deflections behaviour of the device, through the value updating of these parameters. However, this model represents a conceptual model: further investigations and tests are necessary to better understand the performance of the system, in particular for the small oscillations, and thus to provide a more comprehensive and generalizable time-domain model.

Chapter 5

*Parametric characterization tests on RBRL system: proposal of a general design procedure*

A parametric experimentation on new RBRL devices produced at TARRC, carried out changing the principal device parameters that control behaviour, is here presented; the parameters investigated are: rubber compound, thickness of rubber layers, diameter of ball and stress parameter per ball. 153 tests in total were performed, from which the steady-state rolling friction ratios were measured. This experimentation was needed to verify the usefulness of the theory of Muhr et al. (1997), which was proved, and subsequently to calibrate the hysteresis parameter α for each rubber tested, which is a key parameter in this theory. The result obtained could be important at two different levels:

- one more general, related to technological and scientific research in the rubber field, for which this theory could be a useful tool;
- one more specific, related to modelling of the rolling friction force for the RBRL device in steady-state conditions.

The characterization tests of the rubbers used in this experimentation are also presented, together with their mechanical properties.

A further parametric test carried out on the recentering rubber springs of the RBRL system, involving different diameters of the spring, is shown; the springs are a fundamental component of the isolation system, since they alone provide its stiffness – and hence recentering capability – in the steady-state rolling phase.

Finally a design procedure for the RBRL system is given, considering the results gathered by the experimentations presented and using the theory of Muhr et al. (1997). This procedure allows the determination of all the device parameters, for a specific design spectrum and vertical load, by choosing the values of isolation period and damping ratio.

Chapter 6

*Investigations on small-deflections behaviour of RBRL system: proposal of a time-domain model*

The viscoelastic properties of the rubber together with the dwell time of the load, lead to the creation of an initial indentation or pit in the rubber layers, corresponding to the original steel spheres position: this peculiarity is responsible of the advantageous dynamic response of the system for small seismic intensities.

Three different experimentations are presented and discussed in this chapter, all addressed to the characterization of the device behaviour for small deflections, namely with balls rocking in their pits or rolling in the transition phase between the initial static configuration and the free rolling.

- The first experimentation consisted of some parametric sinusoidal monoaxial tests on new RBRL devices, produced at TARRC specifically for this purpose: the force-displacement behaviour for small deflections was investigated, considering device with diverse parameters and different imposed sinusoidal motions; a time of dwelling of the load of 25 hours was allowed to elapse before the tests.
- The second one consisted of some direct measurements, immediately after unloading, of the pit geometric profiles and of the maximum residual indentations. For this experimentation new smaller samples were produced, with the same characteristics of the rubber tracks as for the RBRL devices. An empirical equation is proposed to estimate the maximum residual indentation, based on the test conditions and on the viscoelastic properties of the rubber.

Subsequently, comparing the results of these two experimentations, another useful empirical relation is provided between the maximum residual indentation and the peak rolling friction for the roll-out of the balls from their pits.

- The last experimentation described is related to sinusoidal monoaxial tests on the same RBRL devices used for the ECOEST Project, thus with rubber tracks of type A, low damping, and B, high damping, moulded in 1999. Different dwell times of the load in its static configuration were considered. These tests proved the good performance of the RBRL device also after 15 years from the moulding of the rubber tracks, and showed interesting results for the high-damping compound (B) as well as for the influence of the dwell time on the behaviour of the device for small deflections.

Finally, a Time-Domain model for the prediction of the non-linear behaviour of the RBRL system is presented.

Chapter 7

*Conclusions and future works*

# 2 BACKGROUND OF SEISMIC ISOLATION FOR LIGHTWEIGHT STRUCTURES

## 2.1 Seismic vulnerability of content

While in the last decades the main studies and applications performed in the field of seismic isolation were aimed toward the isolation of structures, in the last few years attention was also dedicated to the protection of the contents, since they may have an extremely high value, sometimes even more than the structure in which they are contained. This different perspective represents a new worldwide challenge. The technical challenge is that the contents are generally lightweight.

As mentioned above, the value of the contents may be relevant, and it is worth noting that it may be true not only from a merely economic point of view, but also from the perspectives of cultural or historical merit, such as museum content and art objects in general, or of their essential function, as in the case of special medical or infrastructure equipment that needed to ensure integrity for example of the electricity or communications network.

The isolation of the structures in which such contents are settled may not always be sufficient to prevent their seismic damage, because of the higher level of vulnerability of the contents compared to that of the structure. For example, in the case of buildings provided with seismic isolators with passive control, and settled in areas with high seismic exposure level such as Turkey, Japan, California and some

Italian regions, the isolators tend to be over dimensioned to low intensity earthquakes, that are more frequent than the design one. In this case, the elastomeric devices might present too high stiffness, transmitting a relevant portion of the seismic energy to the content. Considering sliding devices, they could present too high break-away force such that the entire seismic action might be transferred to the structure, as in the case of a fixed base, further amplified by the building seismic response.

So, if the seismic protection of the content is required, and other techniques such as anchorage are not sufficient or appropriate, seismic base isolation is needed. For the aim, it is possible to recalibrate seismic devices typically used in civil engineering (Berto et al., 2013), in order to apply them on the lightweight content directly, exploiting the fact that this technology and scientific knowledge are already well known and established. An alternative to the recalibration is the creation of new devices, specifically for the isolation of lightweight structures.

Although the basic theories and concepts of the seismic isolation are the same, the isolation techniques to be used for the content are not a mere extension of the ones used for civil structures. Indeed, the following technical peculiarities have to be considered:

- lightweight structures are often very vulnerable, even for small seismic actions, since they often are merely supported on the base without possibility to be anchored (because of architectural or preservation requirements); this lead to the necessity to design a base isolation considering the possible rocking/overturning and sliding phenomena;
- the contents involve masses orders of magnitude smaller than those characteristic of civil structures, whereas the demand for relative displacement is not likewise scaled down, and the combination may fall outside the range feasible with a conventional isolator suitable for large masses;
- besides being technically proficient, the isolation systems at the base of items of content have to observe conservation and aesthetic requirements too.

Some considerations regarding the importance of seismic protection for three of the main categories of lightweight structures, artefacts, medical and electrical equipment, are reported below.

- Artefacts

The importance to prevent or mitigate the devastating effects of earthquakes on cultural heritage assets is really acute for countries in which this heritage is concentrated, that often correspond to the ones with highest seismic exposure level: it’s the case of Italy, other many sites in the Mediterranean basin, almost all the Central America and Asiatic countries. The awareness to this issue has recently grown in Italy too, as a result of the quakes of Umbria-Marche (1997), l’Aquila (2009) and Emilia (2012).

Following are reported the main known intervention methods, for seismic risk mitigation of the artefacts, with particular attention to the performed interventions on the exhibited items of the antiquities collection of the Getty Museum (Lowry et al., 2007 and 2008):

- a first approach consists of the lowering of the centre of gravity of the object, by changing the relationship between height and base or adding weight. Some examples are adding sand in vases, or bricks or other loads in the bottom of pedestals or cabinets, or anchoring on heavier objects. This solution is easy, but sometimes is not feasible or could threaten the object preservation because of the damage that an excess load could cause;
- another approach, that leads to some advantages, consists of the anchoring of the objects by different support mounts that integrate them in the structure; however this solution implies the complete transmission of the seismic force to the object, that could be too fragile to endure;
- an alternative approach is base isolation, i.e. the application of the seismic isolation in the items base, that has proved to be an effective system to mitigate the seismic effects, by reducing the entrant energy.

Some examples of damage of the artistic and cultural heritage are reported below. The earthquake of Umbria-Marche (1997), that caused the collapse and disruption of the frescoes in Basilica of St. Francis of Assisi, and the more recent events in L’Aquila (2009) and Emilia (2012), highlighted the need to reduce the seismic vulnerability of this heritage in Italy. Fig. 2.1 a) shows the destruction of Saturnino Gatti statue in the National Museum of Abruzzo in L’Aquila, because of the seismic event of April 6, 2009, while in Fig. 2.1 b) it is possible to see the overturn of a decorative statue in a private garden in San Felice Sul Panaro after the earthquake of May 21 and May 29, 2012 (Borri & De Maria, 2013 a,b). In Fig. 2.2 is shown the destruction of some showcases and the damage of pottery exhibited at Nias Heritage Museum, after the seismic event of Indonesia in March 28, 2005 (Neurohr, 2005).

A relevant aspect to consider in the seismic protection of artefacts is their high historical and socio-cultural value. Therefore, they require a specific attention in the interventions such that the preservation requirements are fully respected; it is also important to ensure a proper aesthetic result, because the intervention has to appear properly integrated with the context in which it is realized.

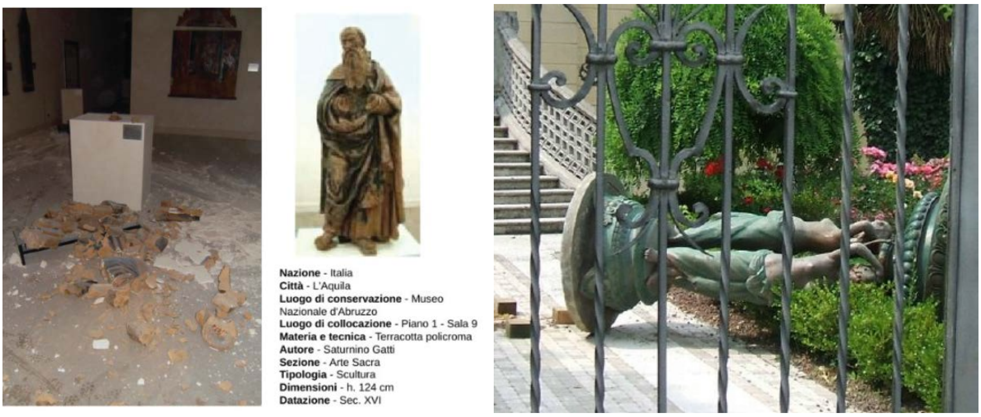

**Nazione** - Italia
**Città** - L'Aquila
**Luogo di conservazione** - Museo Nazionale d'Abruzzo
**Luogo di collocazione** - Piano 1 - Sala 9
**Materia e tecnica** - Terracotta policroma
**Autore** - Saturnino Gatti
**Sezione** - Arte Sacra
**Tipologia** - Scultura
**Dimensioni** - h. 124 cm
**Datazione** - Sec. XVI

*a)* *b)*

*Fig. 2.1 a) Destruction of Saturnino Gatti statue (National Museum of Abruzzo in L'Aquila, April 6, 2009); b) overturning of a decorative statue in a private garden (San Felice Sul Panaro, May 21-29, 2012). Images from Borri & De Maria, 2013 a,b.*

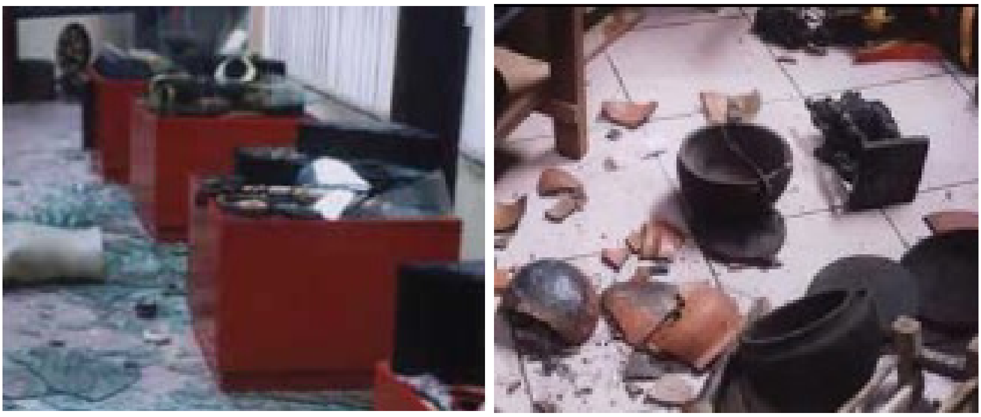

*a)* *b)*

*Fig. 2.2 a) Destruction of some showcases and b) damage of pottery exhibited at Nias Heritage Museum, after the seismic event of Indonesia in March 28, 2005 (Neurohr, 2005).*

- Medical equipment

Medical facilities, as well as Police and Fire stations, are buildings of vital importance during and after seismic events and hence, to ensure their operation even in these situations, a special protection is required against earthquakes. 97% of earthquake-related injuries are recorded within the first 30 minutes following the main shock (Gunn, 1995). Events such as the earthquake in Kashmir (2005) and Sichuan (2008) caused a huge number of injured people, requiring a large reception capacity to hospitals that led to serious operation problems (Achour et al., 2011).

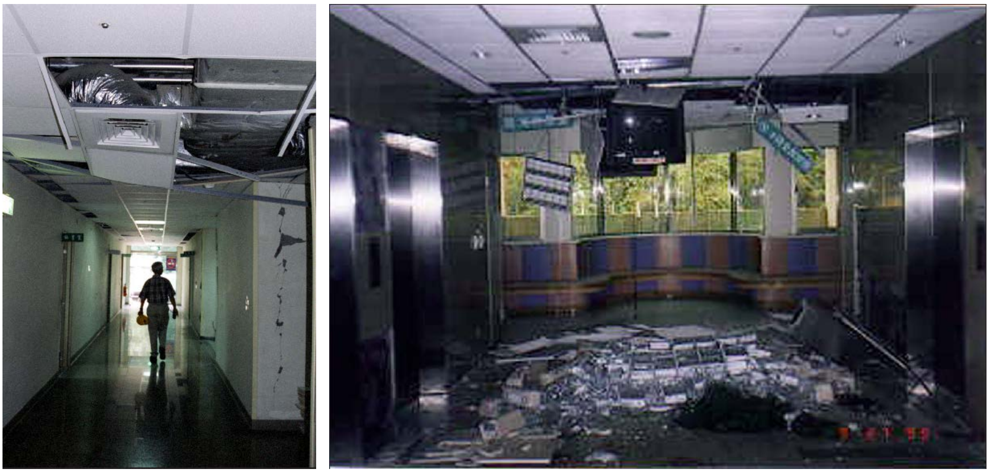

*a) b)*

*Fig. 2.3 Damage to the non-structural components and contents of the Veteran Hospital (a) and Shiu-Tuan Hospital (b) (from Soong & Yao, 2000).*

The structural behaviour influences the response of the non-structural components, because most of them are rigidly connected to the structure, which transmits to them the seismic forces. For example, after the Chi-Chi Earthquake of the 1999 in Taiwan, the Christian Hospital, the Veterans Hospital and Shiu-Tuan Hospital recorded slight structural damage, but catastrophic damage to non-structural contents and machinery (Soong & Yao, 1999 and 2000). The Christian Hospital reduced its capacity by 10% in the moment when it was most needed because of non-structural damage, and required the transfer of many patients; many medical instruments were also damaged, including the hospital's emergency generator. The Veteran Hospital instead reduced its capacity by 50% for non-structural and structural damage, and drastically reduced the services provided because of the massive damage to the hospital equipment (Fig. 2.3 a). Finally, Shiu-Tuan Hospital remained structurally intact, but suffered devastating non-structural damage: it had to be closed, resulting in the deaths of several patients. The floors that suffered the most damage to equipment were the third and the fourth, where operating theatres were located (Fig. 2.3 b).

- Electrical equipment

Electrical equipment such as transformers, HV (High Voltage) Circuit Breakers, switchboards and high-performance computers and servers are generally vulnerable to earthquake damage if not designed, constructed and installed properly. These facilities, which often play a key role during and after the seismic events, include internal parts which are very sensitive to high acceleration (Caldwell et al., 2007). Moreover, usually the electrical units are not properly connected to the floor or to the ground, so they may be driven into rocking or sliding phenomena.

For example in Fig. 2.4 a) the damage can be seen to a public electrical cabinet located at the entrance of Port-au-Prince General Hospital (Haiti), that occurred in the 2010 Haitian earthquake with an estimated PGA (Peak Ground Acceleration) of 0.21g. The cables arriving at the ground level have been torn (Fig. 2.4 b) because of the relative movement of the cabinet on its foundation, due to the lack of anchorage (Goodno et al., 2011).

In Fig. 2.5 a) it is possible to see a MELIS system (Metal-Enclosed Load Interrupter Switchgear) installed on the roof of the U.S. Embassy building in Port-au-Prince (Haiti), and its displacement (Fig. 2.5 b) due to the 2010 Haitian earthquake. The mechanical connection between the system itself and the equipment pad was not sufficient to restrain the motion and in fact one of the base sides had not been connected. After the earthquake, with a PGA estimated of about 0.16 g, the relative displacement measured at the MELIS base was of sufficient magnitude to cause power outages and damage to the devices connected (pumps, transformers, etc.), as well as the destruction of the MELIS system (Goodno et al., 2011).

Thus, the observations carried out in Haiti after the earthquake of 2010, with a magnitude of 7.0 and a distance from 13 to 23 miles from the epicentre, had confirmed that non-structural elements or content objects not properly anchored to their base supports may be subject to dangerous relative movements, which could compromise their functioning.

It is worthwhile to point out the case of the electricity power plants: these are strategic structures and so are required to keep functioning during and after a seismic event. The suspension of power supply can lead to serious damage from economic and social points of view (Oikonomou et al., 2012). Strong earthquakes such as Loma Prieta (1989), Northridge (1994), Kobe (1995), Izmit and Chi-Chi (1999), compromised some of these power plants, creating damage of hundreds millions of dollars per event plus the collateral costs for the repair or replacement of the equipment. Furthermore, blackouts generated severe discomfort at social and economic levels, stopping all human activities which needed electricity.

Generally, the modes of seismic damage for electrical equipment are (Saadeghvaziri & Feng, 2001): overturning (Fig. 2.6 a) , breaking of the anchoring which can cause cables tearing and oil leakage, breakage of the oil seals that results in oil dispersion in the environment, excessive translation such as the case of equipment supported by rail systems of Fig. 2.6 b) (which allow easiness of assembly or disassembly and air circulation), and damage to internal parts due to excessive acceleration or excitation of vibration modes leading to either failure or impact of these internal parts in relative motion. Seismic design of these types of equipment is therefore necessary, considering also the use of the base isolation technique through seismic devices that can be quickly installed and removed, already planning maintenance or retrofitting that do not interrupt the production or supply of electric energy for an excessive period of time.

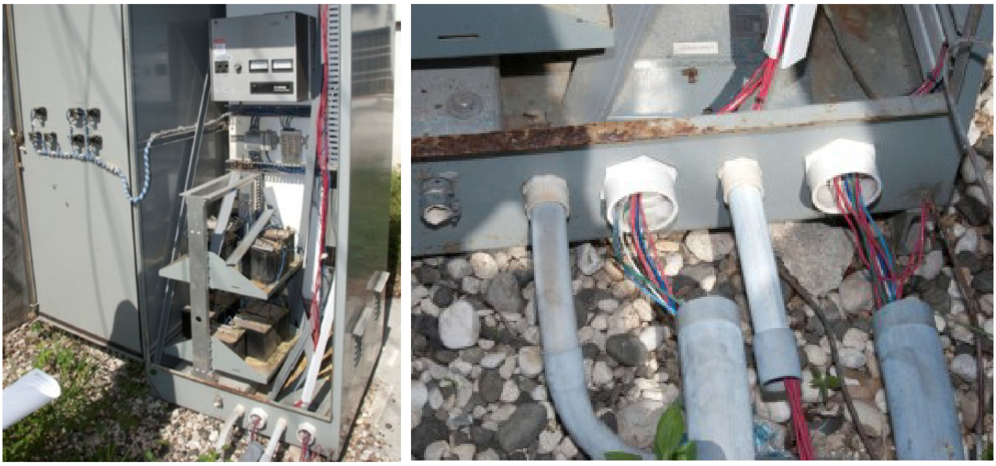

a) b)

*Fig. 2.4 a) General purpose cabinet, unanchored, at General Hospital of Haiti. b) Control wiring conduit damage after 2010 Haitian quake (PGA=0.21g). (From Goodno et al., 2011).*

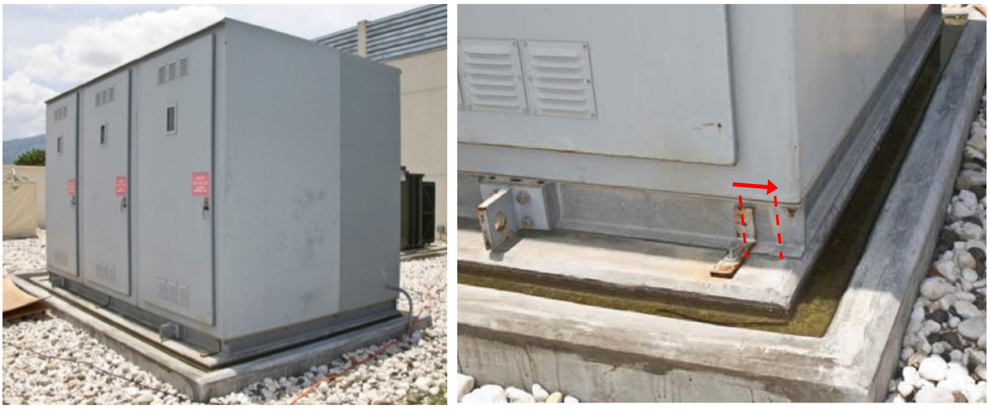

a) b)

*Fig. 2.5 a) Metal-enclosed load interrupter switchgear (MELIS) equipment at the U.S. Embassy. b) and displacement due to the 2010 Haitian quake (PGA=0.16g). (From Goodno et al., 2011).*

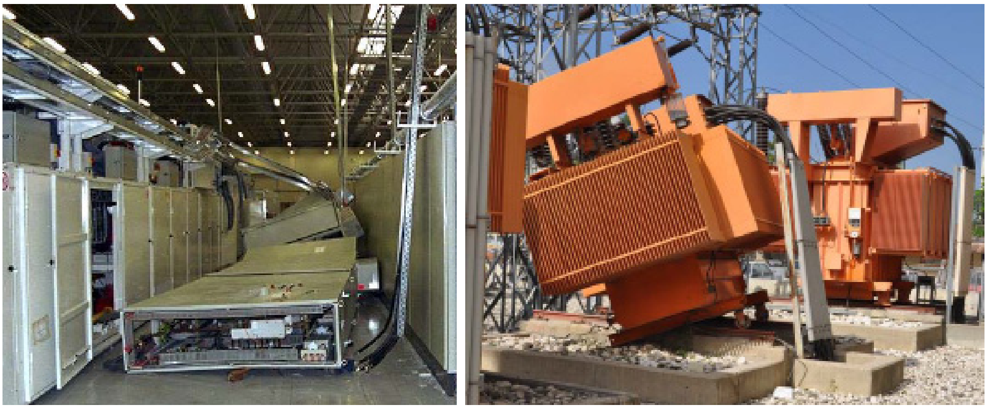

a) b)

*Fig. 2.6 a) Electrical cabinets overturned by 1999 Izmit earthquake –magnitude 7.4- Turkey (photos of NISEE Izmit Collection). b) Rail mounted transformer slipped off rails by 2010 Haiti earthquake –magnitude 7- Port-au-Prince (photos of Eduardo Fierro, BFP Engineers). (From FEMA E-74, Jan. 2011).*

## 2.2 Motions of the rigid bodies and importance of base isolation

A rigid object only rested on a horizontal rigid plane that is moving can have two types of motion relatively to the plane: sliding (or translational movement) and rocking (i.e. oscillatory tilting on the edges of its base). In conditions of perfect adherence, sliding movement can occur when:

$$a_g / g > \mu_f \tag{2.1}$$

where $a_g$ is the absolute acceleration of the horizontal plane, $g$ is the gravitational acceleration and $\mu_f$ is the frictional coefficient between the object and its support plane. When the sliding motion starts, the frictional force transmitted to the object by the movement of the plane is equal to:

$$F_f = Mg\mu_f \tag{2.2}$$

Assuming that sliding is prevented, rocking phenomenon can be initiated if the following inequality, known as West's formula, is verified:

$$a_g / g > B / H \tag{2.3}$$

where $H$ is the height of the centre of gravity $cg$ respect to the support plane and $B$ is the distance projected to the plane of $cg$ from the rotation axis, which coincides with an edge of the object base. If the object is a rectangular parallelepiped, $H$ and $B$ are respectively half height and half base of the object itself. Eqs. (2.1) and (2.3) show that the rigid body will rock if the frictional coefficient $\mu_f$ is bigger than the geometrical ratio B/H, will slide otherwise. Actually, the relative movement of the body might be also a mix between sliding and rocking.

The rocking activation does not mean that the overturn of the body will occur. Several studies were carried out on rocking motion, also with the aim of obtaining some toppling criteria; a summary of these principal studies is reported here below.

The rocking behaviour was first introduced by Housner (1963) who studied the rocking motion of inverted pendulum structures, such as elevated water tanks, survived or collapsed after earthquakes of high intensity. The free vibration of slender rigid blocks is described as an oscillation with two centres of rotation, 0 and $0'$, represented in Fig. 2.7; sliding and bouncing are not considered.

The significant properties of the block in Fig. 2.7 are its weight, W=mg, its moment of inertia $I_0$ about the point 0, the radial distance $R$ between the centre of gravity $cg$ and the centre of rotation 0, the angle $\theta$ that measures the tilting of the block and the angle $\alpha$ between the line $R$ and the long side of the block. The value of $R$ is calculable by the geometric dimensions of the block as $R = \sqrt{h^2 + b^2}$ , where $h$ and $b$ are respectively half base and half height of the block. Considering these properties, the free vibration of the block is described by:

$$I_0 \frac{d^2\theta}{dt^2} = -WR\sin(\alpha - \theta) \tag{2.4}$$

For tall or slender blocks having the angle $\alpha$ less than 20° the sine of the angle $(\alpha - \theta)$ may be approximated by the angle itself; furthermore, if we set $WR / I_0 = p^2$ , the previous equation becomes:

$$\ddot{\theta} - p^2\theta = -p^2\alpha \tag{2.5}$$

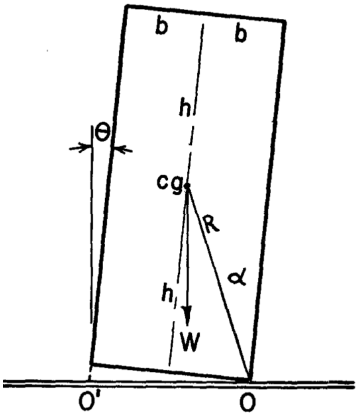

*Fig. 2.7 Representation of the rocking phenomena for a slender rigid block (Housner, 1963).*

The parameter $p$ is the characteristic frequency of the block and expresses its dynamic characteristics. For a uniform rectangular block $p$ can be taken as:

$$p = \sqrt{3g/(4R)} \tag{2.6}$$

For a block left to perform a free vibration from a tilted position, with initial conditions $\theta = \theta_0$ and $\dot{\theta} = 0$ for *t*=0, the differential equation (2.5) has this solution:

$$\theta = \alpha - (\alpha - \theta_0) \cdot \cosh(pt) \tag{2.7}$$

The period of free vibration depends on the amplitude of the initial rotation and it decreases continuously during the successive cycles depending on the restitution factor. The reduction in kinetic energy $r$, that takes place after every impact of the base, is the ratio of the moment of momentum about $0^{/}$ immediately before impact to the one immediately after impact:

$$r \equiv \left( \frac{\dot{\theta}_2}{\dot{\theta}_1} \right)^2 = \left[ 1 - \frac{mR^2}{I_0}(1 - \cos 2\alpha) \right]^2 \tag{2.8}$$

where $\dot{\theta}_1$ and $\dot{\theta}_2$ are the angular velocities before and after impact respectively, and $m$ is the mass of the block.

Housner (1963) investigated also the overturning caused by constant acceleration of infinite duration and by sinusoidal acceleration. An interesting approach to predict the overturning due to earthquake motion was also presented.

For this purpose the ground acceleration is considered as a sequence of discrete step changes in ground velocity ± Δv, randomly distributed over the time of analysis, with the same probability of being positive or negative in sign; the average velocity response spectrum (undamped) considered in this way is a constant. The effect of such ground motion on structures is equal to the one given by discrete and impulsive equivalent inertial forces acting through the centre of mass of the block while the ground is at rest. Consequently, this causes a change in kinetic energy of vibration after every pulse creating a constant power input in the system. The average condition for overturning is mathematically derived considering a probabilistic approach, and corresponds to the reaching of that value of energy associated to a 50% of probability that the ground motion will overturn the block. The damping in the system depends on the amplitude and the frequency of rocking. As the amplitude of the rocking increases, the rate of energy dissipation decreases strongly. Thus, Housner (1963) concluded that the behaviour of the rocking block could be quite variable in the case of an earthquake with relatively small intensity, that may fortuitously build up the amplitude leading to overturning of the block at the beginning of the earthquake.

Finally, Housner (1963) expressed through the Eq. (2.9) the criterion of stability for a rocking structure, with the comparison between the energy input and the energy required to overturn the structure, calculating the energy input from the velocity response spectrum, $S_V$ .

$$\alpha = \frac{S_V}{\sqrt{gR}} \sqrt{\frac{MR^2}{I_0}} \tag{2.9}$$

For slender structures $MR^2 / I_0$ can be sufficiently approximated by the unity; so, the previous equation becomes:

$$\alpha = \frac{S_V}{\sqrt{gR}} \tag{2.10}$$

This equation can be interpreted in the following way: for a given spectrum velocity value $S_V$ , a rigid block with an angle $\alpha$ given by Eq. (2.10) will have approximately a 50% probability of being overturned. Furthermore, this formulation revealed an interesting “scale” effect, for which larger blocks are more stable than smaller ones considering the same geometrical proportion, i.e. same angle $\alpha$ but different values of R (see Fig. 2.7).

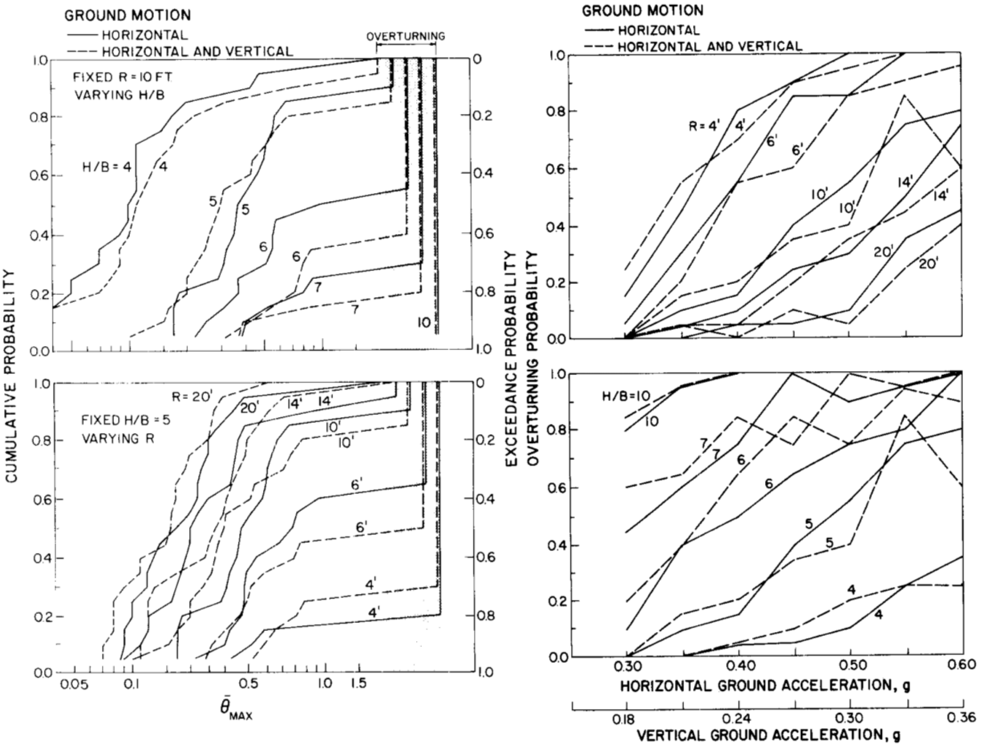

a) b)

*Fig. 2.8 a) Cumulative probability distribution functions for maximum rotation $\theta_{MAX}$ . b) Overturning probability. Different values of R and H/B investigated, for rigid blocks subjected to an ensemble of horizontal and vertical ground motion. (Yim et al., 1980).*

Yim et al. (1980) solved numerically the existing formulations of Housner (1963) in order to study the behaviour of rigid bodies under simple pulses and ground motion. Multiple random seismic scenarios were generated for this scope. A probabilistic approach using cumulative distribution functions of probability was followed, noticing the sensitivity to small changes in the block size and slenderness ratio and to the details of the ground motion (see Fig. 2.8).

The authors found that the ground motion intensity, slenderness ratio and block size have a systematic and intense effect on the seismic stability of the rocking block: while an increase of the seismic intensity and slenderness ratio lead to reduce the structural stability, the increase of the block size keeping the same slenderness ratio would result in a more stable behaviour (Fig. 2.8).

Further studies about rocking and overturning phenomena were carried out by Ishiyama (1984). He managed to validate existing formulations on rocking and proposed new formulations and overturning criteria for rigid bodies, based on numerous shaking table tests and numerical simulations with harmonic and seismic excitations. For the case of a rectangular body, Ishiyama (1984) provided the lower limits of the maximum horizontal acceleration $a_0$, velocity $v_0$ and displacement $d_0$ of the input excitations to overturn the body; for a small value of $\alpha$ these lower limits are:

$$a_0 \simeq \frac{b}{h} g = \frac{B}{H} g \tag{2.11}$$

$$v_0 \simeq 10 \frac{B}{\sqrt{H}} \qquad (unit: \ cm, \ \sec) \tag{2.12}$$

$$d_0 \simeq \frac{B}{10} \tag{2.13}$$

The lower limit $a_0$ agrees with the West's formula (Milne, 1885) and can also be found from the linear kinematic analysis.

These criteria derived from the analyses with sinusoidal excitations but they resulted valid also for seismic excitations. Furthermore, it was found that both the lower limit $a_0$ and $v_0$ must be overcome to overturn the rigid body; limit $d_0$ is instead unnecessary because less precautionary. All these results are summarized in Fig. 2.9 that shows three regions: A, where no rocking nor overturning can occur, B, where only rocking is possible, and C, in which rocking can be followed by overturning.

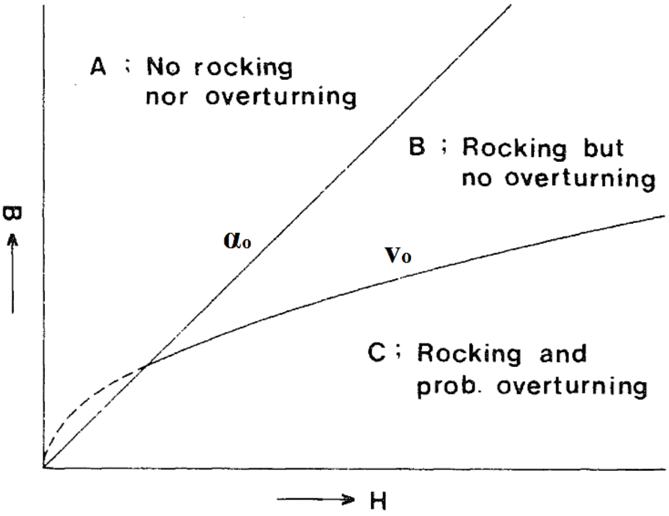
A : No rocking nor overturning
B : Rocking but no overturning
C : Rocking and prob. overturning
$\alpha_0$
$v_0$
B
H

*Fig. 2.9 Overturning criteria for rigid bodies (from Ishiyama, 1984).*

Moreover, a limit period $T_c$ was proposed with the significance that if the period of the input excitation is smaller than $T_c$, the acceleration must be much bigger than $a_0$ in order to overturn the body. This period $T_c$ for slender rectangular bodies is expressed as:

$$T_c \simeq \frac{\sqrt{H}}{16} \qquad (H\ [cm],\ T_c\ [\mathrm{sec}]) \tag{2.14}$$

An alternative approach to study the rocking motion of rigid bodies was introduced by Dimitrkopoulos & DeJong (2012): instead of using dimensional and orientation dependent parameters, the authors proposed the use of dimensionless and orientationless parameters. They discovered in this way a rocking response which is perfectly self-similar for slender bodies and almost self-similar for non-slender bodies. Substantially, self-similarity for structural analysis of bodies subjected to rocking means that the response spectrum does not depend on the intensity and frequency of the harmonic excitation, despite the non-linear and non-smooth behaviour.

It is worth considering also that the freedom to rock can actually help to protect slender objects, isolating them at the acceleration required to induce the rocking motion (Priestley et al., 1978). However, the rocking behaviour is difficult to predict because of its extreme sensitivity to the boundary conditions such as friction and flatness at the base (Aslam et al., 1980).

The problem of sliding, rocking and overturning of rigid bodies is very relevant in the context of the seismic protection of museum artefacts; this is also evidenced by an extensive literature, for example: Agbabian et al. 1988, Augusti et al. 1992 and 1994, Augusti & Sinopoli 1992, Augusti & Ciampoli 1993 and 1996, Liberatore 2000, Caliò & Marletta 2003 and 2004, Neurohr 2005, Lowry et al. 2007, Neurohr & McClure 2008, Borri & De Maria 2011, Berto et al. 2012, De Canio & Modena 2013 and other. The complexity of the topic and the uncertainties on the definition of the design seismic action require the use of simplified and conservative verification criteria (Liberatore, 2000), such as the ones given by the Eqs. (2.1) and (2.3) or (2.11); indeed, according to Ishiyama (1984) the acceleration that induces the rocking motion in Eq. (2.3) is a necessary but not sufficient condition for overturning.

Quite often, the limit values of acceleration that could lead the artworks to slide or rock relatively to the floor, compromising their safety, are relatively small if compared to the seismic excitations. In these cases, some seismic mitigation interventions have to be adopted to prevent the damage of the museum contents. If simple tricks (such as the lowering of the centre of gravity or the interposition of an interface between object base and floor increasing the friction coefficient) applied to the art objects are not satisfactorily practicable to reduce their seismic vulnerability and, if the anchoring technique is too invasive or too dangerous because the objects might not withstand the forces transmitted, the use of seismic isolation becomes necessary (Lowry et al. 2007). Seismic isolation can be achieved by interposing particular devices (seismic isolators) between the base of the items to be protected and the floor, or by suspending the objects.

Until now only the ideal case of rigid body was considered; actually, the objects of content could be not correctly represented by this simplification. This is the case of objects that have internal degrees of freedom, which might be excited by seismic input up to damage the objects themselves, as is very familiar with large structures.

Finally, another consideration has to be done regards the vertical effects of the earthquake: in the case of objects, if not sufficiently anchored, these vertical effects could be much more evident and dangerous compared to the case of civil structures. If the technique of seismic isolation is chosen for the protection of an object, the isolation from vertical motion should be considered besides the traditional decoupling of the horizontal motion, which remains in any case the most important.

## 2.3 Seismic isolation and energy dissipation: effects on the structures

The role of isolation and the additional dissipation of energy in the seismic protection of structures can be easily understood considering the problem in terms of energy balance, according to Uang & Bertero (1990).

The seismic energy entering the structure $E_i$ at generic time $t$ can be subdivided, considering the energy balance, into the following contributions:

$$E_{\mathrm{i}}(t) = E_k(t) + E_e(t) + E_v(t) + E_h(t) \tag{2.15}$$

where $E_k(t)$ is the relative kinetic energy of the structure, $E_e(t)$ is the elastic deformation energy of the structure (elastic potential energy), $E_v(t)$ is the energy dissipated by viscous damping and $E_h(t)$ is the energy dissipated hysterically due to structural damage, friction or plasticization. Terms $E_k(t)$ and $E_e(t)$ represent the returnable part of the energy, while terms $E_v(t)$ and $E_h(t)$ the dissipated part. The Eq. (2.15) does not consider the work of the static forces that are constant during the seismic action, such as the dead loads.

At time $t_R$ , when the seismic event stops and so the original static conditions of the structure are restored, the energy returnable by the system goes to zero and the Eq. (2.15) becomes:

$$E_{\mathrm{i}}(t_r) = E_v(t_r) + E_h(t_r) \tag{2.16}$$

This underlines the fact that the input energy is totally transformed into energy dissipated by viscosity or by structural damage or plasticization (so by hysteretic cycles of the material).

The technique to add benign dissipation capacity to the structure acts on the second members of the Eq. (2.16), increasing their magnitude through the introduction of appropriate additional dissipation technology within the structure. This can be obtained by acting on $E_v(t_r)$ through viscous devices, or on $E_h(t_r)$ through elasto-plastic dissipation devices; in both cases, the purpose is to reduce the relevance of the term $E_h(t_r)$ due to the structure, preserving it from seismic damage, and to guarantee at the same time the balance of the seismic energy.

Alternatively, with the aim to avoid the plasticization of the structure, it is possible to act directly on $E_{\mathrm{i}}(t_r)$ reducing his magnitude by means of a seismic isolation system. In this case, the need to control the displacements of the isolation system, and significantly also the equivalent relative motion between the isolated object and its surroundings, requires a system with a certain dissipation capacity; for this reason, the majority of the technological solutions are a mix between the strategies of isolation and of additional dissipation.

The principal effects of a seismic isolation system on structures with relatively high frequency of vibration are quite simple to understand. This changes the fundamental frequency of the structure, making it much lower than both its fixed-base frequency and the predominant frequency of the ground motion (Naeim & Kelly, 1999). This shift of the natural period causes a reduction in the values of the spectral acceleration for typical earthquake (see Fig. 2.10 a).

This improvement is obtained at the expense of an increase of relative lateral displacements (see Fig. 2.10 b). The damping due to the energy dissipation of the isolation system reduces then the displacement and the acceleration response as shown in Fig. 2.10. However, local conditions of the soil play a decisive role on the reliability of the base isolation: indeed, while for stiff soils a significant reduction in the spectral acceleration is reached, for the soft ones the opposite result could

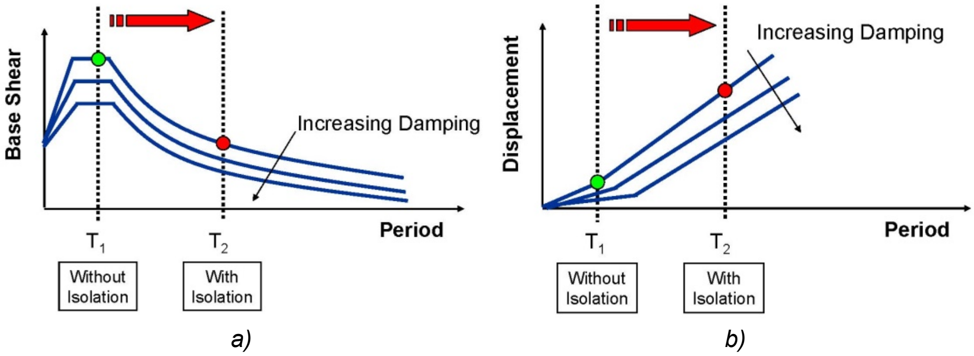

*Fig. 2.10 Effects of the seismic isolation in terms of spectral acceleration (a) and displacement (b) (from Symans, 2004).*

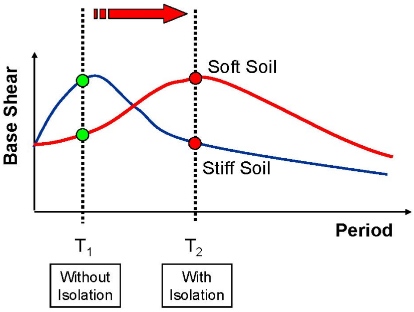

*Fig. 2.11 Effects of the seismic isolation with different response spectra (from Symans, 2004).*

occur (Symans, 2004), as shown in Fig. 2.11. Ideally, we need an isolation system that can easily be designed to achieve any natural frequency, so that it can be tailored appropriately for a specific design spectrum.

## 2.4 Issues of the traditional seismic devices for the content

### *2.4.1 Characteristics of the isolation devices and systems*

The passive control technique of seismic isolation is allowed through some particular devices which present these principal characteristics or functions (Dolce et al., 2010):

- ability to support gravity loads in quiet conditions and during seismic events;

- high deformability in the horizontal direction or low horizontal stiffness to seismic actions;
- appropriate energy dissipation capacity for control of relative displacement;
- adequate resistance for the horizontal non-seismic actions (wind, traffic, etc.).

Re-centering ability is an important feature, although not essential, since it prevents residual displacements at the end of the seismic excitations. Other important characteristics, such as durability, easiness of installation, limited costs and dimensions etc., can influence the appropriate choice of the isolator or isolation system, but do not affect its performance if installed and maintained properly.

A seismic isolation system consists of a set of devices, which combined together result in the desired dynamic behavior of the isolated structure as well as providing a satisfactory connection of the structure to the ground for non-seismic as well as seismic situations. The functions (eg to bear load and to dissipate energy) of the isolation system may be provided through a single set of similar devices, or divided between multiple sets, each with a complementary function. Several devices have been studied and developed in the last 20 years: some of these have found world-wide application.

In more detail, the devices that can be used to realize an isolation system might be subdivided into the following two categories:

- isolators, which support the gravitational loads through a high vertical stiffness and accommodate horizontal displacements by means of a relatively low horizontal stiffness; damping, recentering and lateral restraint for non-seismic actions can be added to the previous functions, thus obtaining a complete isolation device, but they are not characterizing for an isolator;
- auxiliary devices, that could be used to integrate in the isolation system the functions of damping, recentering and lateral restraint for non-seismic horizontal actions (wind, etc.).

To date, focussing on the principle need to support gravity loads while permitting motion relative to the ground, the available isolators can be divided in four groups, which in order of popularity are:

- isolators of rubber laminated with steel, based on the high elastic deformability of the rubber;
- sliding isolators, which take advantage of the low frictional resistance that comes from the relative motion between two surfaces, flat or curved, of materials opportunely treated;
- rolling devices;
- suspension devices.

The first three types of isolator are normally used at the plane between the ground and the base of the superstructure, hence the widely used term “base isolation” coined by Prof. J.M. Kelly.

Fig. 2.12 and Fig. 2.13 show the ideal force-displacement behaviour, or hysteresis loop, for the principal type of isolators and auxiliary devices. Based on this hysteretic behaviour (see Fig. 2.13), the auxiliary devices can be identified as:

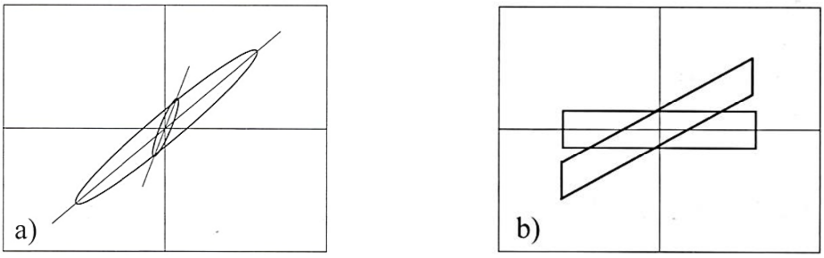

*Fig. 2.12 Ideal force-displacement loops of: a) isolators made of elastomeric material and steel; b) sliding isolators (from Dolce et al., 2010).*

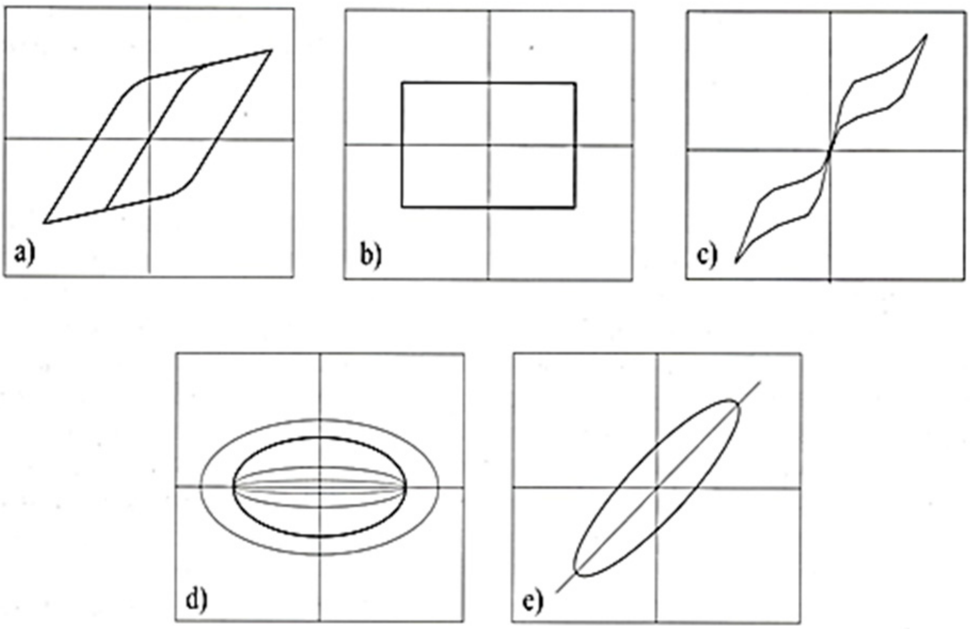

*Fig. 2.13 Ideal force-displacement loops of auxiliary devices based on: a) hysteresis of some metals; b) friction; c) superelastic properties of shape memory materials; d) viscous behaviour; e) quasi-linear or viscoelastic behaviour (from Dolce et al., 2010).*

- non-linear devices, independent on rate deformation, based on the hysteretic behaviour of some metals such as steel and lead (plot a), on the friction between two surfaces opportunely treated (plot b) or on the superelasticity of particular metal alloys such as the shape memory materials which are used obtaining excellent abilities of recentering (plot c);
- viscous devices, dependent on rate deformation, based on the extrusion of highly viscous fluids through orifices of appropriate size in a piston as it is forced to travel through a cylinder (plot d);
- quasi-linear devices (plot e) with viscoelastic behaviour, based on shear deformation of special polymers (ideally show a nested set of scaled loops of constant slope and shape, contrasted with plot a).

An isolation system for civil structures can be consist only of elastomeric isolators (Dolce et al., 2010), either realized with high damping rubber compound or with the insertion of dissipative materials (i.e. lead, viscous fluids, etc.), or only of sliding isolators, which incorporate the damping and recentering functions for intrinsic characteristics, or else by an appropriate combination between generic isolators and auxiliary devices which provide the functions of dissipation, recentering and lateral restraint.

### *2.4.2 Elastomeric isolators*

Elastomeric isolators (Dolce et al., 2010) are devices realized with layers of elastomeric material, from 5 to 20 mm thick, alternated and vulcanized to steel layers of 2 or 3 mm. The function of the steel layers is to constrain the deformation of the elastomeric material, providing in this way a high vertical stiffness to the isolator, such that the vertical displacements in serviceability conditions can be contained in the range 1 to 3 mm; at the same time also the bearing load capacity increases. Furthermore, the steel layers do not significantly affect the horizontal stiffness, which is instead determined by the total thickness of the elastomeric layers and the shear characteristics of the material, resulting in it being appropriately low, because of the exceptionally low shear modulus of rubber.

The intrinsic characteristics of these type of isolators, together with the use of particular high damping compounds (filled rubbers) or special inserts to guarantee the desired damping coefficient with an appropriate horizontal stiffness, make the elastomeric devices able to fulfil all the requirements for an isolation system: thus, this type of isolators can be used alone to realize an isolation system, without any auxiliary device.

To date, there are substantially three categories of elastomeric devices: Natural Rubber Bearings (NRB), High Damping Rubber Bearings (HDRB) and Lead Rubber Bearings (LRB).

The elastomeric with low damping or NRB device (Kelly & Quiroz 1992, Taylor et al. 1992) presents a substantially elastic behaviour (constant stiffness) and provides a damping ratio in the range 2 to 4%, so very small. Between the elastomeric isolators, NRB is the easiest to realize; its behaviour not depend much on the frequency, temperature or strain history. The disadvantage is the needed to use auxiliary devices, in parallel with NRB isolators, to increase the dissipation capacity of the isolation system and to limit its excessive movements due to the service loads (wind, etc.).

The HDRB isolators (see Fig. 2.14 a) or high damping elastomeric devices (Kelly 1991, Derham et al. 1985) are obtained by mixing into the rubber special filler (resin, oil, etc.), which considerably increases the damping level of the isolation system up to values in the range 10% to 20% for shear deformations of about 100%. The nature of the energy dissipation is in part viscous and in part hysteretic; this implies a certain dependence of the isolator behaviour on the oscillation frequency and temperature (for the viscous part). Furthermore, the mechanical characteristics of the elastomeric material depend on the strain amplitude $\gamma$ (see Fig. 2.14 b). For small strain, for example less than 10%, the horizontal stiffness of the isolator is 5 to 10 times bigger than that associated with strains in the range 100% to 150%, which is generally reached with the design seismic conditions. Unlike NRBs, HDRB isolators can alone meet all the requirements of an isolation system, providing all the required functions to isolate and to limit the displacements for service loads.

Finally, the Lead Rubber Bearing (see Fig. 2.15 a) used one or more cylindrical inserts made of lead, placed inside a specific cavity (Robinson 1982, Kelly 1992). This makes possible high values of damping (in the range 15% to 35%) and high stiffness to service loads to be reached. The dynamic behaviour of a LRB device (see Fig. 2.15 b) results in a combination between the linear elastic one of the NRB device and the elasto-plastic one of the lead core subjected to shear deformations; the shear deformation is ensured by the confinement effect of the steel layers. The damping provided by the LRB device depends on the dimension of the lead core and on the imposed lateral displacement (Naeim & Kelly 1999).

The horizontal stiffness $K_H$ of a general elastomeric device, not including the particular case of the Lead Rubber Bearing, can be estimated by Eq. (2.17) and is related to the design load W through Eq. (2.18), where G is the shear modulus of the elastomer, A is the area of an elastomeric layer, $t_r$ is the total thickness of

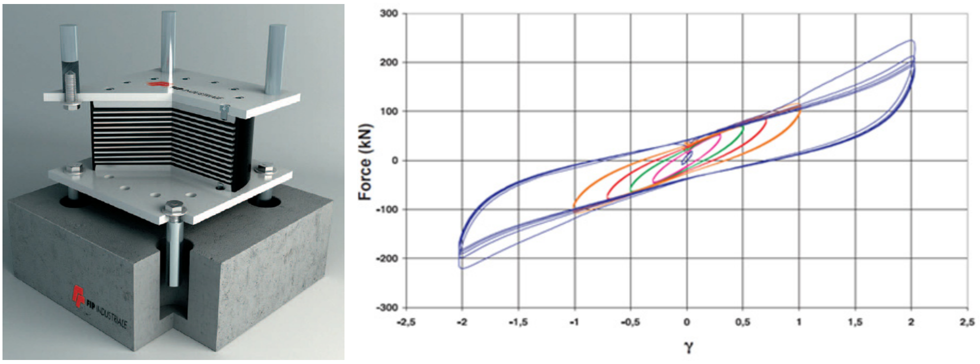

a) b)

*Fig. 2.14 a) Image of a High Damping Rubber Bearing (HDRB). b) Typical hysteresis loops of a HDRB isolator obtained by dynamic tests at increasing shear strain amplitude* $\gamma$ *(from FIP Industriale S.p.A., 2015).*

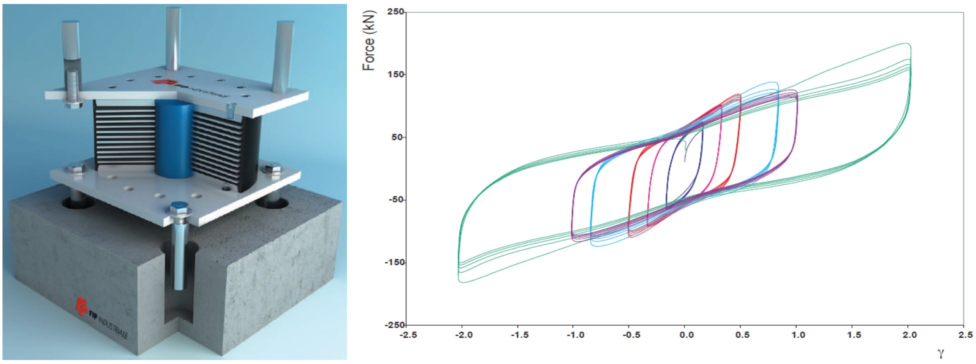

a) b)

*Fig. 2.15 a) Image of the Lead Rubber Bearing (LRB). b) Typical hysteresis loops of a LRB isolator obtained by dynamic tests at increasing shear strain amplitude* $\gamma$ *(from FIP Industriale S.p.A., 2015).*

rubber in the bearing, $f_H$ is the horizontal frequency of oscillation and g is the gravitational acceleration (Kelly, 1993).

$$K_H = GA/t_r \tag{2.17}$$

$$K_H = \frac{W}{g}(2\pi f_H)^2 \tag{2.18}$$

The main issue related to the use of elastomeric bearings to isolate objects of the content is its intrinsic property to couple the two principal functions of an isolation device: support of the gravitational loads and provision of a low horizontal natural frequency (low horizontal stiffness). In the case of the content isolation, in fact, the masses involved (from some hundred kilos to some tons) are one or more orders of magnitude lower than the ones related to general civil structures, for which these isolators have been developed. This means that the design of an isolation system for these lightweight structures, considering the usual periods of isolation, is possible only if the horizontal stiffness of the elastomeric bearing is highly reduced (one or more order of magnitude), as shown by Eq. (2.18). According to Eq. (2.17), the only parameter that can be adjusted to achieve this result is the ratio $A/t_r$ . Unfortunately, the necessary values of this ratio for this purpose would result in too low horizontal deflection capacity and difficulties, according also to UNI EN 15129:2009, of achieving lateral stability under vertical load. Thus, finally, elastomeric bearings of adequate lateral deflection capacity are too stiff for the isolation of the content and although this shortcoming could be met by special designs they would not be economical if compared to other technologies suitable for the isolation of lightweight structures such as the RBRL device (presented later).

### *2.4.3 Sliding isolators*

Current sliding devices are mainly based on friction between stainless steel and Teflon (PTFE), even if new polymeric materials have been recently developed for this purpose. Depending on the geometry of the sliding surface, two kinds of sliding bearings are distinguished: Flat Surface Slider and Curved Surface Slider.

In the case of Flat Surface Slider the sliding takes place along a horizontal plane. This type of isolator cannot realize alone an isolation system, but auxiliary devices are needed to provide an appropriate damping coefficient, horizontal stiffness to service loads and restoring force. In fact, these isolators are generally used in parallel with NRB bearings to isolate buildings in this way: the sliding bearings provide the support function of the gravity loads allowing completely the displacements, while the elastomeric bearings are used as auxiliary devices to guarantee the other requirements. In the case of PTFE surfaces, the dynamic coefficient of friction results in the range 6% to 18% with not lubricated surfaces, 1% to 3% vice versa (Costantinou et al. 1988, Tyler 1977, Dolce et al. 2003); furthermore, it depends on the contact pressure, sliding velocity and temperature. A wide experimentation carried out by Dolce et al. (2003) on the dynamic friction showed that:

- friction increases rapidly with increasing velocity until 150-200 mm/s, after which it remains approximately constant;
- friction linearly decreases with increasing contact pressure;
- friction decreases with increasing temperature;

- friction is strongly dependent on the lubrication conditions; the difference between lubricated and not lubricated surfaces could reach an order of magnitude.

Due to the high variability of the friction coefficient, Flat Surface Sliders are generally used with lubricated surfaces only to support the vertical loads and to accommodate large displacements, while the energy dissipated by the friction is not take into account, because it is difficult to predict.

The Curved Surface Slider (Fig. 2.16 a) is the only sliding isolator that incorporates the functions of recentering and energy dissipation (Fig. 2.16 b), through the use of curved sliding surfaces properly treated; thus it can be used alone to realize an isolation system. The first and more known isolator of this type is the “Friction Pendulum System” (FPS) (Zayas et al. 1987, Al-Hussaini et al. 1994). To date several friction pendulum devices are available, also with more than one concave sliding surface; these last, called Multiple Friction Pendulum Systems, permit to reduce the dimension in plan of the isolator for a given horizontal displacement capacity, ensuring the same high period of vibration, by means of double, triple or multiple concave surfaces and articulated sliders. An important characteristic obtained realizing an isolation system with this type of isolators is the coincidence (in plan) between the centre of mass and the centre of stiffness, due to the proportionality between the mass M and the horizontal stiffness $K_H$ associated with the same slider (see Eq. (2.19)): this ideally avoids the possibility of rotation of the isolated structure around a vertical axis being excited. Another fundamental feature of this type of device is that the vibration period T depends only on the curvature radius R of the surface (Eq. (2.20)) and not on the mass to isolate (Naeim & Kelly 1999): this allows to design an isolated structure with the desired period of vibration whatever the mass, of great significance if the range of live loads is high or if the total load is not known with good accuracy.

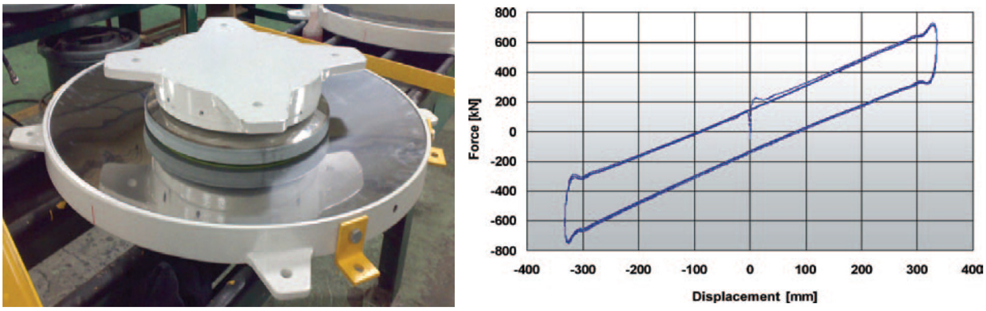

a) b)

*Fig. 2.16 a) Image of a curved surface slider or friction pendulum system (FPS) device. b) Relative hysteresis loop (from FIP Industriale S.p.A., 2015).*

$$K_H = Mg / R = W/R \tag{2.19}$$

$$T = 2\pi\sqrt{R/g} \tag{2.20}$$

With reference to the lightweight items of content, while the Flat Surface Sliders are not suitable because not able to realized alone an isolation system, for the reasons previously seen, the Curved Surface Sliders could be instead considered to isolate such items, even if they must be specially designed. In fact, unlike the case of elastomeric devices, the functions of support of the gravitational loads and provision of a low horizontal natural frequency are not coupled: this allows an isolation system with an appropriate period of vibration to be designed independently of the mass to be isolated (see Eq. (2.20)). However, the forces involved in this case are very different to those in the case of isolation of civil structures. Furthermore, the objects of content such as artefacts or electrical equipment could be much more sensitive, both for intrinsic characteristics and types of support: a redesign process, in particular for the friction coefficient, may thus be needed. The principal problems of the Curved Surface Sliders for the isolation of the content are the big dimension in plan, which could be reduced using Double Friction Pendulum Systems, and the vertical movements associated with the horizontal displacements. Vertical motion, which increases in the case of double concave surfaces, might be dangerous in presence of structures slender or sensitive to rocking, therefore it has to be carefully checked. In the next Section will be show a double-pendulum sliding isolator designed to isolate some statues by Berto et al. (2013).

## 2.5 Seismic isolation devices for lightweight structures

### *2.5.1 Roller or rail-type isolation devices*

#### Linear Rail Isolation Device

The isolation device (Fig. 2.17) presents a decoupling mechanism that allows the relative displacement between the three steel platforms that constitute it (Lowry et al., 2007). The lower frame is connected rigidly to the floor, while the upper one provides an attachment level for the object to be isolated. The upper and middle frames are supported by orthogonal rail systems, consisting of linear bearings, that allow their motion in the plane along the main directions X and Y. The displacements are reduced by a series of springs assembled on rails installed in the central position for every layer; these provide the horizontal stiffness of the system and guarantee its recentering after the seismic event. Two sets of springs in series coexist, with different stiffnesses: the stiffer ones start to work only after the reaching of a certain displacement threshold, in order to contain the horizontal stiffness of the system and, at the same time, to avoid a sudden arrest for the reaching of the maximum allowed displacement. The forces that reach the isolator from a diagonal direction are distributed in the X and Y axes by a lateral "scissoring" action, allowed by the relative displacement between the upper and middle platforms; moreover this configuration prevents the onset of torsional phenomena. The vertical displacement is hindered by a mechanical locks system, which keeps the rails at the same vertical level even during the seismic event.

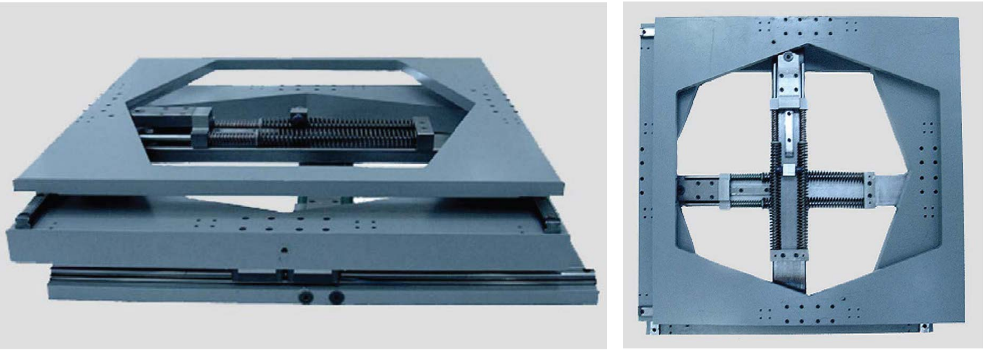

*a)* *b)*

*Fig. 2.17 Seismic isolation device used at the Getty Villa (from Lowry et al., 2007).*

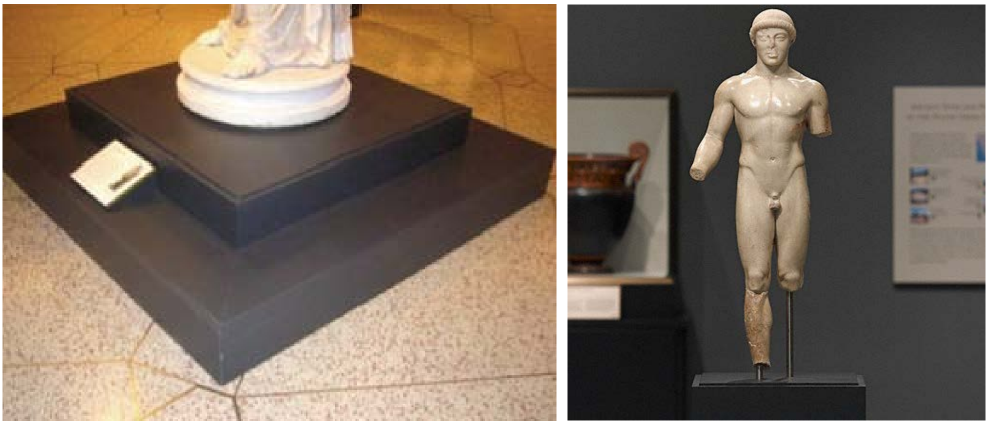

*a)* *b)*

*Fig. 2.18 a) Application of the isolator in situ (Getty Villa); b) application on the Agrigento Youth (http://www.getty.edu).*

Shaking table tests performed in 1990, using a full-scale model of a sculpture, showed the efficacy of the isolator.

This device has been designed specifically for the artworks displayed at Getty Villa Museum in Malibu (Fig. 2.18 a) and has undergone changes and further improvements in the course of time.

The maximum displacement guaranteed by the device is about 45 cm; however this could not always be allowed because of the usually limited space of the museums and for the safety of visitors.

One of the most famous applications of this system is the seismic isolation of a Kouros statue (Agrigento Youth), as can be seen in Fig. 2.18 b).

### Roller-Type Isolation Device

Japan is the country where seismic isolation is most widespread, not only for the protection of the civil structures, but also for the lightweight ones such as special equipment or works of art. Since the Hanshin-Awaji earthquake in 1995, when many artefacts were damaged in several museums, the awareness of the importance to isolate these valuable objects has considerably increased.

For this purpose, a roller-type device has been studied (Ueda et al., 2004) composed by two layers placed over two perpendicular rail systems (Fig. 2.19 a): each of these layers can move in one of the two orthogonal directions of the plane XY, allowing the device displacement in this plane. The rails are rectilinear shape in plan, but circular in vertical section, in order to ensure the requisite restoring force to make the residual displacement negligible at the end of the seismic event. In Fig. 2.19 b) are presented the device components: 1 shows the upper plate, 2 the wheel frame, 3 the bottom plate, 4 a wheel, 5 a bearing, 6 a wheel axle, 7 the rail. The components from 4 to 7 are coated with PTFE (Polytetrafluoroethylene). The isolator in Fig. 2.19 is square plane with 900 mm sides, and 190 mm height. Since the natural period of vibration of the system does not depend on the mass, it is possible to reach high periods (2 to 3 sec) even for relatively light structures, such as showcases.

The efficacy of the device has been proved through 3D shaking table tests, simulating the acceleration history of some historical earthquakes (El Centro 1940, Taft 1952 and Kobe 1955).

This device has been used at the National Western Art Museum at Ueno-Tokyo, where it was installed at the base of “The Thinker” and “Burghers of Calais” (Fig. 2.20 a) by Auguste Rodin. The same has been also integrated below the showcases at Gifu Modern Museum (Fig. 2.20 b) at Gifu prefecture.

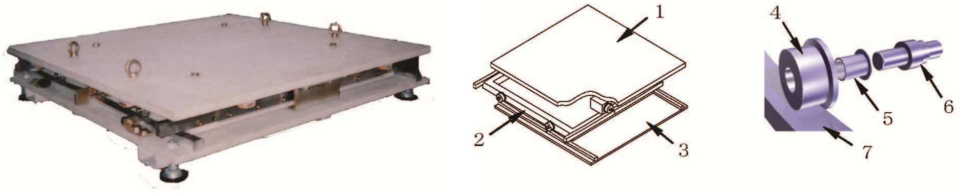

a) b)

*Fig. 2.19Roller-Type Isolation Device: a) image; b) schematic drawing (from Ueda et al., 2004).*

a) b)

*Fig. 2.20 Installation of the Roller-Type Isolation device at the base of: (a) “Burghers of Calais” by Auguste Rodin at National Western Art Museum at Tokyo; (b) showcases at Gifu Modern Museum at Gifu prefecture (from Ueda et al., 2004).*

### *2.5.2 Slider-type isolation devices*

#### Double Concave Curved Surface Sliders (DCCSS)

This double-pendulum isolator (Fig. 2.21 a) has been properly studied and recalibrated for the seismic isolation of “I Prigioni” by Michelangelo, at Galleria dell’Accademia in Firenze (Berto et al. 2013, Baggio et al. 2013, Favaretto 2012). The sliding surfaces are characterized by equal radii of curvature and friction coefficient. Considering the statue features, the device has been designed for a vertical load of 10 kN, and its geometrical characteristics are: 75 mm in height, 270 mm in external diameter, 160 mm in deflection capacity, and the radius of curvature of the single surface is 1500 mm (Baggio et al., 2013).

Some shaking table tests have been performed at the San Diego Laboratory and have showed the good performance of the DCCSS devices.

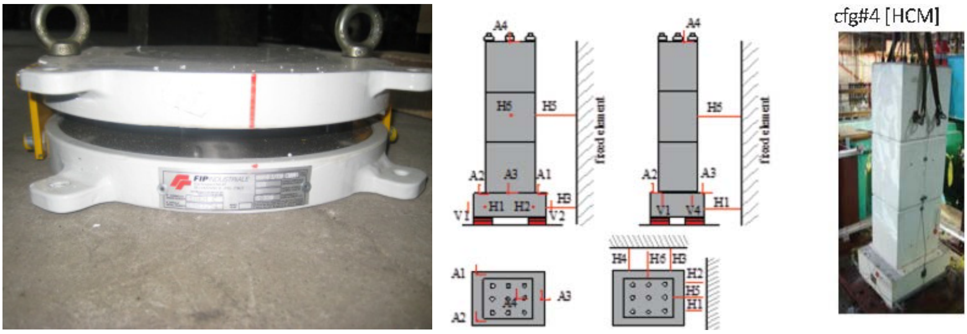
A4
H6
H5
fixed element
A2
A3
A1
H1
H2
H3
V1
V2
V4
H4
cfg#4 [HCM]

a) b)

*Fig. 2.21 a) DCCSS isolator. b) Setup used for shaking table tests (from Berto et al., 2013).*

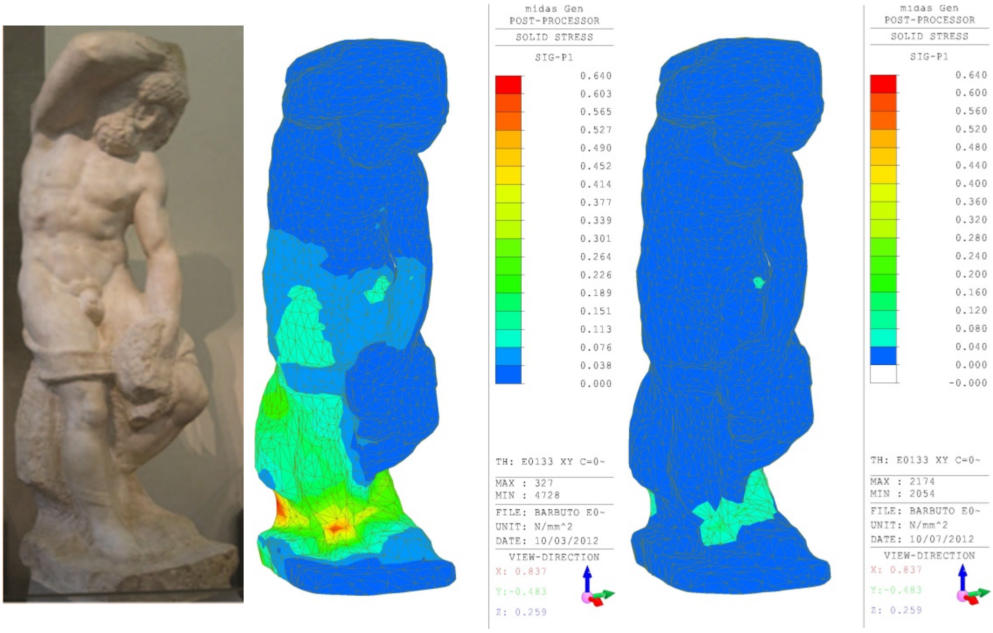
midas Gen
POST-PROCESSOR
SOLID STRESS
SIG-P1
TH: E0133 XY C=0~
MAX : 327
MIN : 4728
FILE: BARBUTO E0~
UNIT: N/mm^2
DATE: 10/03/2012
VIEW-DIRECTION
MAX : 2174
MIN : 2054
DATE: 10/07/2012

a) b) c)

*Fig. 2.22 a) Statue “Prigione Barbuto” by Michelangelo. b),c) Finite Element Model of the statue, with the stress field, for the case without b) and with c) seismic isolation (from Baggio et al., 2013).*

The model of the statue above the isolation system was realized through a set of reinforced concrete (RC) rectangular parallelepipeds, called body blocks, connected together with threaded bars and anchored to a RC base element called the footing block (Fig. 2.21 b). The isolation system comprised four DCCSS devices, one in each corner of the isolation base. The forcings applied were of sinusoidal type and characterized by equal maximum displacement and different frequencies. Some numerical analyses have been performed to predict the dynamic behaviour of the isolated system with the statue of “Prigione Barbuto” by Michelangelo: the parameters used in these simulations, as the friction coefficient, were obtained from the test results. Fig. 2.22 a) represents the statue examined, while results of the numerical analyses are shown in Fig. 2.22 b) and c), in particular the mesh and the stress field due to a certain seismic action (see Baggio et al., 2013) for the fixed base and isolated cases respectively. Reductions up to 80% in stress were found with the isolation system, demonstrating the device effectiveness.

However, some unexpected local phenomena were noticed during the tests, in particular some local fluctuations in the output accelerations; these, as well as the effects of vertical seismic action may be critical for the artworks, and need further study.

### *2.5.3 Rolling-type isolation devices*

#### Ball in Cone device (BNC)

This device comprises two conical steel surfaces that contain a steel sphere (Fig. 2.23). During the seismic event, the ball can move between the two surfaces, causing a displacement of the isolated object which generates lateral recentering forces directly proportional to the weight of the isolated mass. This kind of behaviour makes the centre of mass coincide with the centre of stiffness of the system, minimizing the torsional effects. The damping of the system is negligible, in fact "Ball-in-Cone" (BNC) devices are usually installed in parallel with viscous or friction dampers in order to reduce the maximum horizontal displacement during the earthquake (Kesti et al., 2010).

The working principles of the device have been studied by Kemeny & Szidarovszky (1995). Three types of shape of the BNC surfaces were considered (see Fig. 2.24), which are related to different laws of the restoring force: when the cone apex radius is smaller than the ball radius (path A), the restoring law is discontinuous; when it is larger than the ball radius (path B), bilinear restoring law will be generated; finally, if the surface tends to be spherical (path C), the restoring law tends to be linear. In the study presented by Kesti et al. (2010), the behaviour of path B has been experimental investigated. An important characteristic of the BNC device, due to its conical surfaces, is that it has no characteristic natural frequency of vibration. This could be positive since it avoids resonance effects for the isolated system (ideally without a stiffness), but it has to be carefully checked in relation to the required deflection capacity.

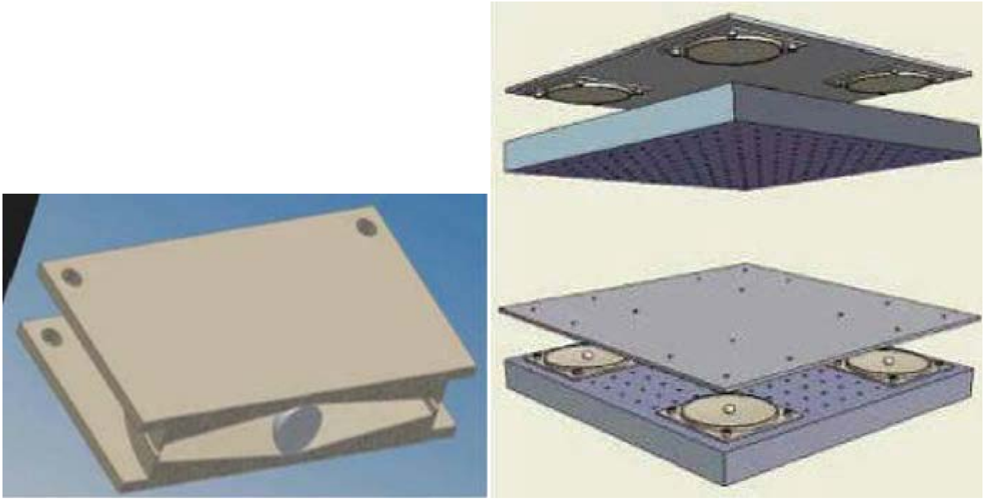

a) b)

*Fig. 2.23 a) Sectioned view of the BNC device. b) Perspective views of the isolation system with BNC devices for the isolation of a showcase (from Erdik et al., 2010).*

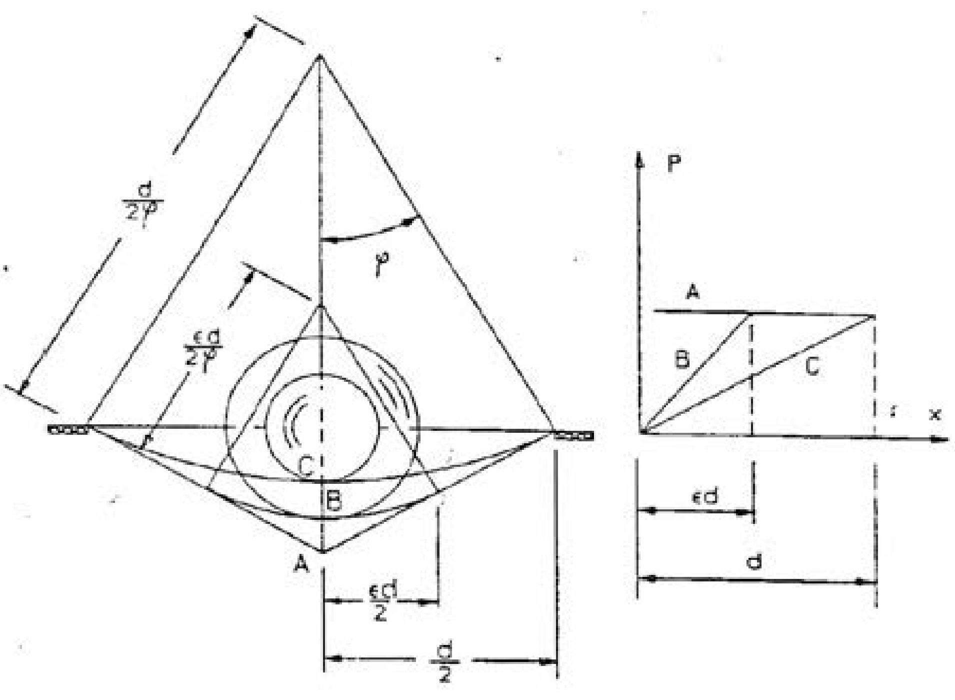
$\frac{d}{2\varphi}$
$\varphi$
$\frac{\epsilon d}{2\varphi}$
C
B
A
$\frac{\epsilon d}{2}$
$\frac{d}{2}$
P
A
B
C
x
$\epsilon d$
d

*Fig. 2.24 BNC geometry and corresponding restoring laws (from Kesti et al., 2010).*

Several research projects have been carried out in Turkey in the field of the seismic risk mitigation for the artefacts in the museums (Erdik et al., 2010), including the one supported by UNESCO (1996-1998), World Bank ProVention (2003 and 2006) and the Turkish Ministry of Culture and Tourism (2004). In particular, in the project of 2006 mentioned above, entitled "Protection of Museum Items Against Earthquake Shaking by Low-Cost Base-Isolation Devices", a BNC device was designed and developed for standard geometries and typical loads of museum objects. In fact, the city of Istanbul in the last 2000 years has suffered earthquakes of medium intensity every 50 years, and earthquakes of high intensity every 300 years, so the city's museums are in a condition of high seismic exposure. Moreover, many of the collections in Istanbul have not been properly protected against earthquake forces and, as a result, many objects are highly susceptible to damage due to rocking, overturning, or collision (see Fig. 2.25). The most recent seismic damage was due to the Kocaeli earthquake of 2009, with the epicentre at 80 km from the city.

The BNC device is particularly suitable in the museum field (Erdik et al., 2010) because it allows a generalized seismic protection of the artefacts at a reasonable cost; in fact using this isolator it is possible to act on different levels of protection, isolating a single object of art as well as a showcase or an entire podium, by placing properly the BNC devices below its base.

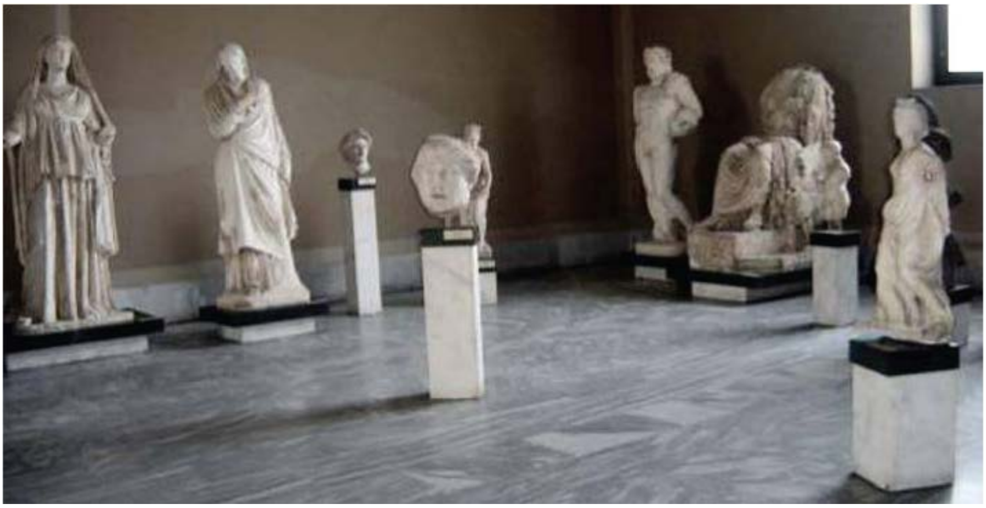

*Fig. 2.25 Museum items at the Istanbul Archaeological Museums (from Erdik et al., 2010).*

Static Dynamic Interchangeable - Ball Pendulum System (SDI-BPS)

The device SDI-BPS (Fig. 2.26 a) consists of two concave steel surfaces (not necessarily with spherical cap shape), one upper and one lower, and some small steel balls placed along the edges, in order to support static or long-term vertical loads and to provide a small frictional damping in the case of small displacements; a bigger steel ball, surrounded by rubbery material, is placed in the middle between the two concave surfaces to provide additional damping in case of large displacements (see Fig. 2.26 b and Fig. 2.27). In the case studied by Tsai et al. (2010), the central rolling sphere had a diameter of 44.55 mm and was coated with natural rubber with a thickness of 6.75 mm and a hardness of 60 degrees IRHD (International Rubber Hardness Degree scale).

In steady state, almost all the vertical load on the device is supported by the small steel balls on the edges, while the fraction of the load transmitted to the coated ball is negligible (Fig. 2.27 (1)). In case of vibrations or small earthquakes, for which the generated horizontal force does not exceed the friction force between the balls and their contact points, the device behaviour is still ruled by the small spheres, which provide a certain frictional damping depending on the contact area and the friction coefficient among the upper concave surface, the supporting steel balls and the housing holes located on the lower concave surface: this contact area and friction coefficient can be properly designed for the specific case (Fig. 2.27 (2)). When the seismic horizontal force exceeds the friction force, the coated ball comes into play beginning to roll between the two concave surfaces (Fig. 2.27 (3)). In this case the side spheres lose the simultaneous contact with the two surfaces and all the vertical load is borne by the central sphere: in this situation the damping of the system is provided only by the deformation of the coating material of the sphere. After the seismic action the ball returns to the original position without showing significant residual displacements (Fig. 2.27 (4)), since the component of the gravity force tangential to the concave surface provides the necessary restoring force. Therefore the coated ball is subject to temporary loads only (for the duration of the earthquake), in this way the creation of semi-permanent or permanent deformations in the rubber coating due to the static loads is prevented.

This device has solved the critical points of a general isolation system with two concave surfaces and a rolling ball in metal, such as the BNC device previously described. These weaknesses are: the negligible damping provided by the rolling ball, resulting in the need of auxiliary damping devices or big sizes of the device to accommodate large deflections, and the highly concentrated stress between sphere

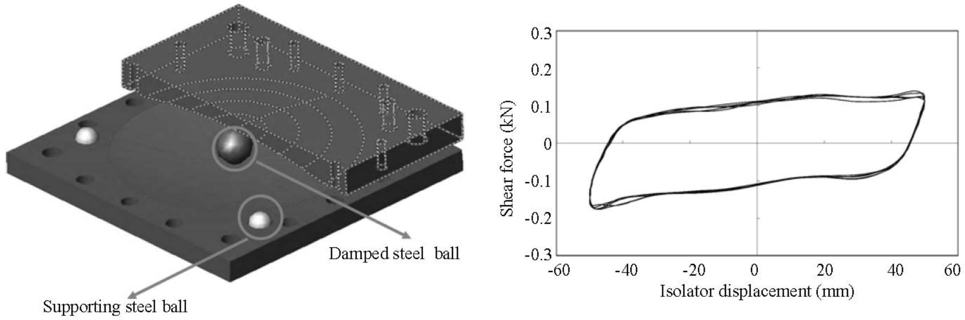

*a)* *b)*

*Fig. 2.26 a) Exploded perspective view of SDI-BPS device; b) related force-displacement hysteresis loop (from Tsai et al., 2010).*

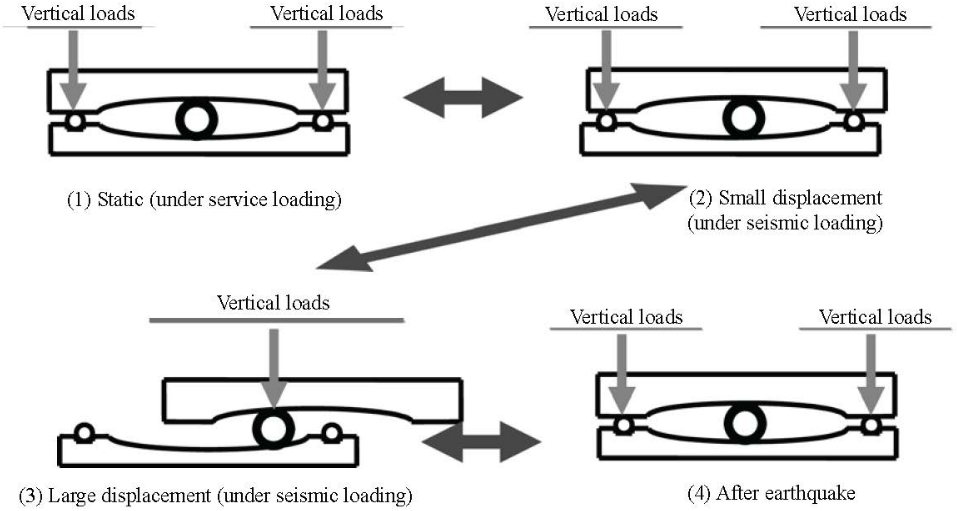
Vertical loads
Vertical loads
Vertical loads
Vertical loads
(1) Static (under service loading)
(2) Small displacement (under seismic loading)
Vertical loads
Vertical loads
Vertical loads
(3) Large displacement (under seismic loading)
(4) After earthquake

*Fig. 2.27 Movements of a SDI-BPS device under service and seismic loadings (from Tsai et al., 2010).*

and concave surfaces, due to a small contact area, that might scratch or damage the two surfaces (Tsai et al. 2006, 2010).

### *2.5.4 Other particular isolators for lightweight structures*

Rolling Double Pendulum device: application to Riace Bronzes

The “Bronzi di Riace”, kept in the “Museo Nazionale della Magna Grecia” in Reggio Calabria, are very important statues belonging to the vast Italian cultural heritage. The need to protect them from possible earthquake damage has led to the study and the subsequent application of a specific isolation device, intended not only to be technically efficient but aesthetically refined: the Rolling Double Pendulum isolator (De Canio 2012, De Canio & Modena 2013). In particular, the base in Carrara marble shown in Fig. 2.28 and Fig. 2.29 was designed to meet the following objectives: to allow an adequate displacement in the horizontal plane, through a low stiffness and a low energy dissipation, and to decouple the horizontal and vertical motions, while using aesthetically compatible materials and form, being easy to maintain, and requiring no irreversible intervention to the Bronzes of Riace.

The surfaces of the marble blocks are internally shaped as ellipsoids of revolution; for this reason, the horizontal stiffness and vibration frequency of the device are not constant, but vary depending on the position along the surface (between 0.015 and 0.025 Hz).

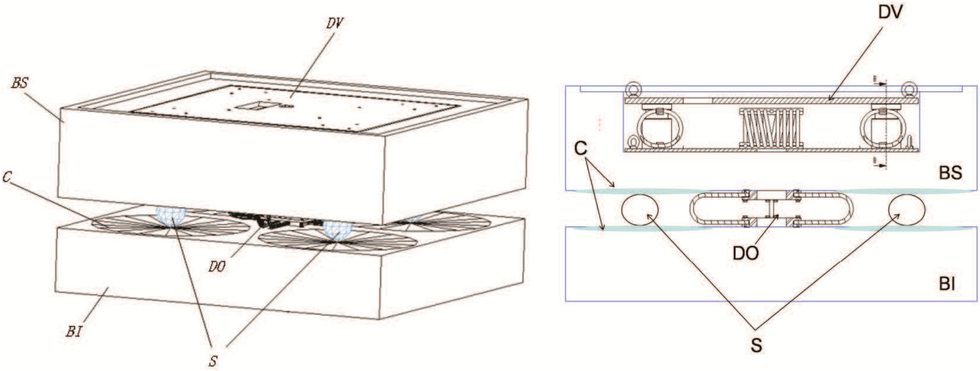

*Fig. 2.28 Scheme of the Rolling Double Pendulum device (from De Canio, 2012).*

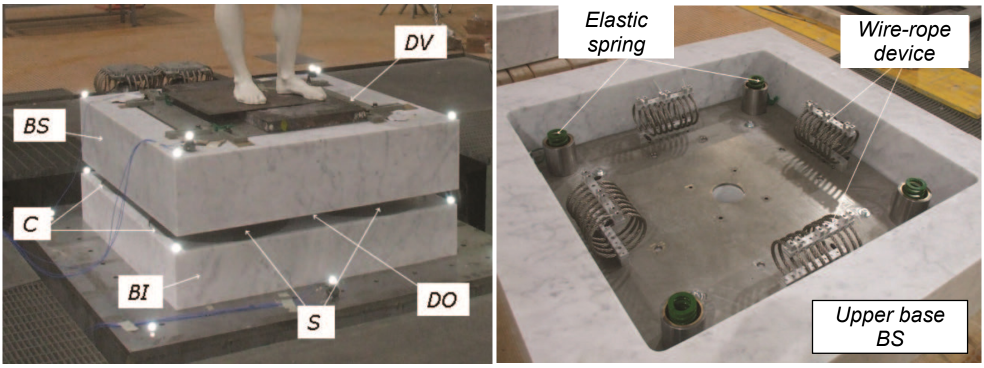

*a)* *b)*

*Fig. 2.29 Principal parts of the isolation system. a) Global view of the device. b) Internal view of the upper base (from De Canio, 2012).*

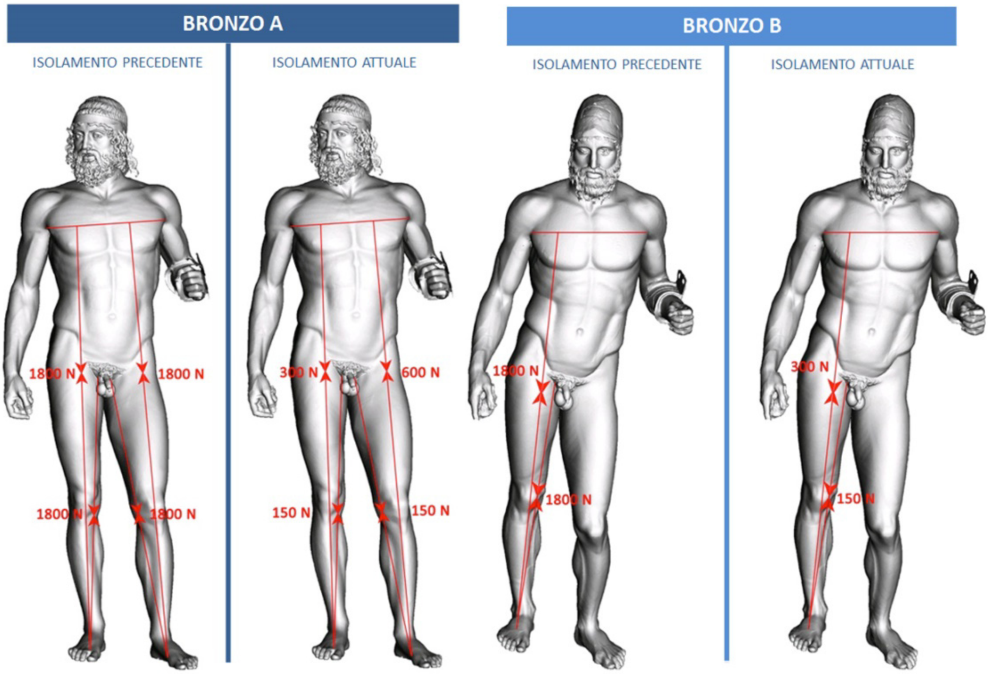

a) b)

*Fig. 2.30 a) Forces acting in the internal anchoring cables, before and after the installation of the new isolation system: a) “Bronzo A”, the “Young”; b) “Bronzo B”, the “Old” (from De Canio & Modena, 2013).*

Between the surfaces are inserted four spheres of the same material, which ensure the support of the vertical load and the low horizontal stiffness, while a dissipative system consisting of stainless steel cables restricts the horizontal movements and provides the restoring force. In summary, the system is composed by the following elements (Fig. 2.28 and Fig. 2.29): BI = lower marble block, BS = upper marble block, S = marble balls, DO = recentering device that reduces the horizontal displacements and provides damping, DV = vertical isolation device placed in the upper marble block. The vertical isolation is provided by two stainless steel plates connected by four shock absorbers or wire-rope devices (see section below) composed by dissipative cables, and four springs inserted in piston guides that decouple the vertical motion to the horizontal one.

The Riace Bronzes were previously placed on the ground floor of the museum and provided with elastomeric isolators; the replacement of the statues on the upper floor has required the adjustment of the devices, especially in light of the new seismic classification of the Italian territory. The previous devices provided anchors with cables passing through the legs of the statues and put in tension with forces of 1800 N per leg, to avoid the statue overturning. The new device has allowed to reduce such force to 600 N and 300 N, as it can be seen in Fig. 2.30. These values are not random but are equivalent to the forces that were transmitted to the statues by the parts that have been lost (for example a shield on left arm and a spear on right arm), bringing the stress field of the statue to the original condition.

Steel Cable Dampers or Wire-Rope device

The device consists of a single twisted stainless steel cable, wrapped around drilled bars made of aluminium alloy (Fig. 2.31). It can be used for the seismic protection of the slender structures, that may present problems of rocking when subjected to an earthquake. Rather than suppressing such rocking, the system is engineered to harness it as a mode of vibration with a suitably low natural frequency to achieve horizontal isolation, excited in a benign way during an earthquake. The rocking phenomenon creates actions of tension and compression on the Wire-Rope devices, whose mechanical flexibility provides excellent isolation properties in all the three main directions.

This is another effective way to seismically isolate a structure, alternative to the more traditional isolation method that considers only the horizontal relative displacement to decouple the motion of the structure from the one of the ground.

The Wire-Rope device has been studied, experimentally and analytically, by Demetriades et al. in 1993, and it was often used to control the vibrations of military hardware and industrial equipment (Schwanen, 2004). However, its application at the base of HV ceramic circuit breakers (Alessandri et al., 2014) represents the first installation as an integral seismic isolation system (see Fig. 2.32).

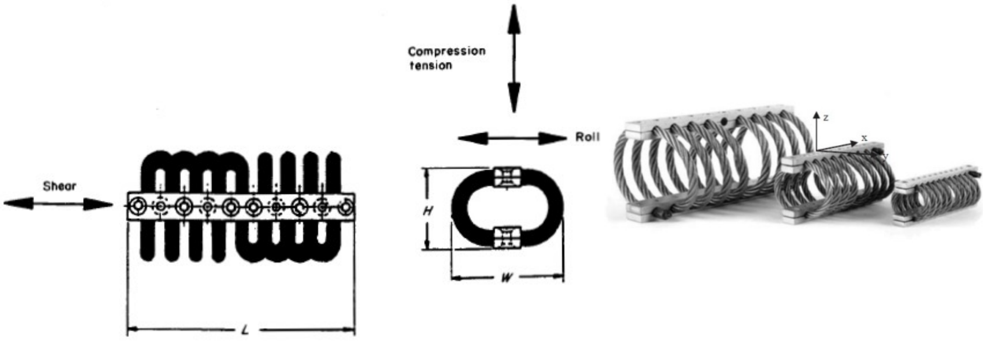

a) b)

*Fig. 2.31 "Wire-Rope" or "Steel Cable Dampers" device. Images from: a) Demetriades et al., 1993 and b) Alessandri et al., 2014.*

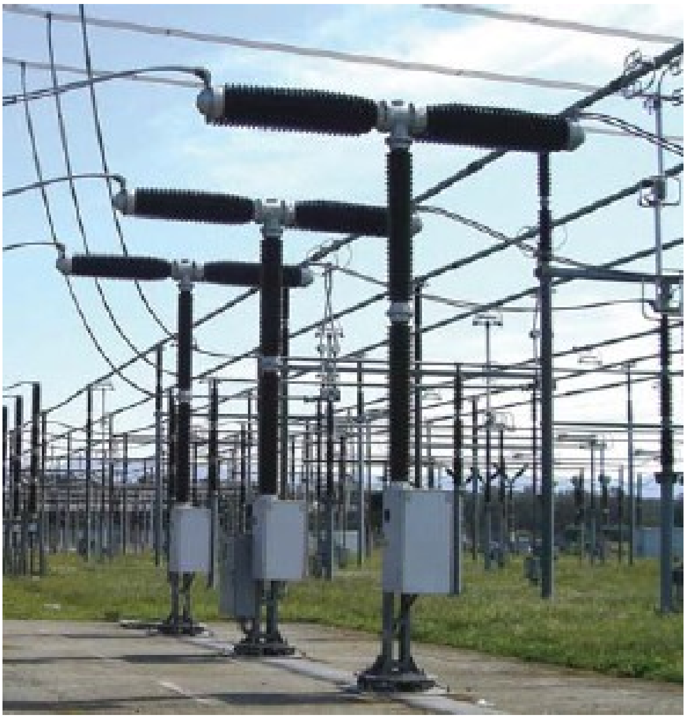

*Fig. 2.32 Installation of the seismic isolation system with Wire-Rope devices at the base of a HV circuit breakers in a power plant (from Alessandri et al., 2014).*

Substations are one of the most important parts in the electric power networks, thus they play a vital role in the stability of the electric transmission system (Alessandri et al., 2014). Furthermore, the consequences of recent earthquakes in Italy (Emilia-Romagna 2012) have shown that some components of the electrical substations, such as HV circuit breakers, are very vulnerable to seismic action, and their damage and malfunctioning can affect the overall reliability of the system. Their seismic vulnerability lies in their slender shape, with a large mass concentrated on the top, and in their ceramic composition (see Fig. 2.32). The Italian Transmission System Operator (TERNA) has collaborated with the University of Roma Tre (Alessandri et al., 2014) to reduce the seismic vulnerability of HV circuit breakers and consequently of the entire national electric system through the study and installation of Wire-Rope isolation devices. Traditional isolation devices cannot be used in this case, and these structures are usually designed only for horizontal shear forces and axial compression forces, allowing only a limited variation in the vertical stress, and always in compression. Therefore, these slender structures are very vulnerable in the event of an earthquake, especially because of the high bending moment acting at the base. The analyses conducted to verify the effectiveness of the isolation system with Wire-Rope devices have used linear elastic theory (ceramic and steel being the materials involved), and the individual elements were modelled as linear elastic beam. The results from numerical modelling have been validated through a series of shaking table tests. Different configurations of the isolation system were analysed, varying the type and the arrangement of the Wire-Rope devices; the final choice was a compromise between the need to reduce the maximum stress in the structure and the need to control its displacement due to the wind, which might cause an excessive movement of the connected electrical cables.

Another example of seismic isolation of electrical equipment is given by the application of the Rolling-Ball Rubber-Layer system (RBRL), extensively described in the next Chapter, at the base of a Gas-Insulated-Substation (GIS) of about 5000 kg. This application was part of the REEDS project, a partially EU funded project aimed at the development of new anti-seismic devices for installation in electrical components like GIS (Bettinali et al., 2001). The Finite Element model of the GIS structure and the RBRL device used in this application are shown in Fig. 2.33. Some results proving the efficacy of the RBRL isolation system are presented in Fig. 2.34.

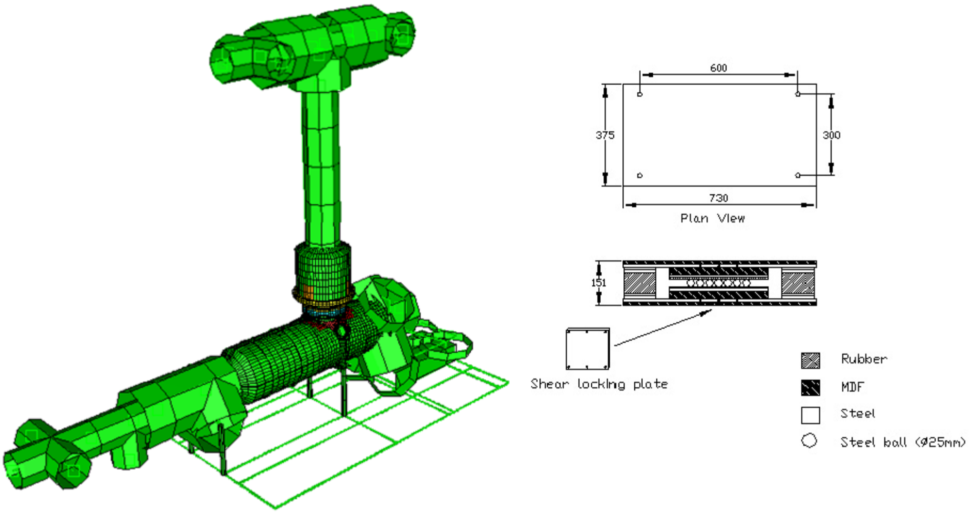

a) b)

*Fig. 2.33 a) GIS 3-Dimensional Finite Element model. b) RBRL isolation device (see next Chapter for more details about this device, in particular Tab. 3.1).*

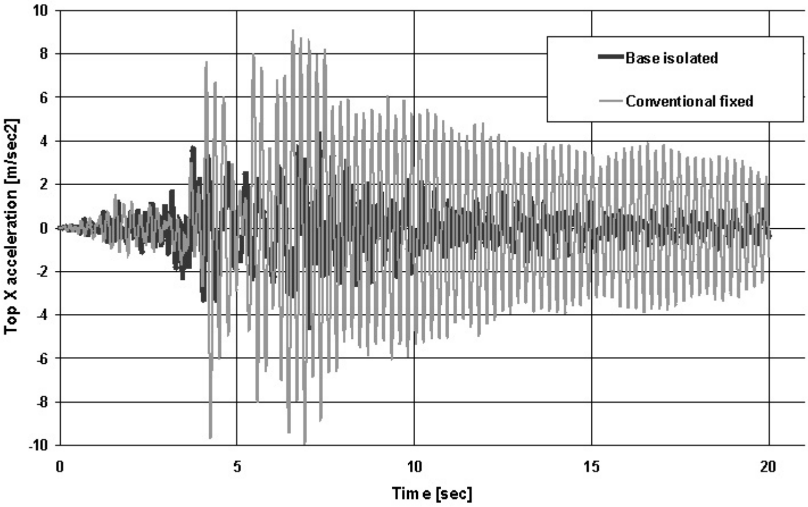

a)

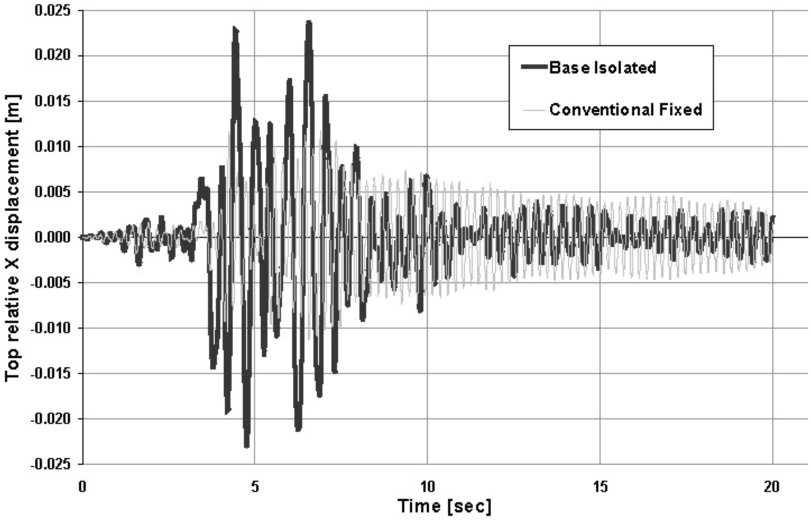

b)

*Fig. 2.34 a) GIS top acceleration and b) GIS top displacement (Tolmezzo earthquake, 1976, PGA 0.35g). Comparison between fixed base and isolated base solution.*

Other types of isolation device useful for the seismic protection of laboratory or electrical equipment are the Robinson devices, in particular “RoGlider” (Robinson et al., 2006) and “LoGlider” (see http://www.robinsonseismic.com/our-products-base-isolators.html). Fig. 2.35 shows RoGlider seismic isolator.

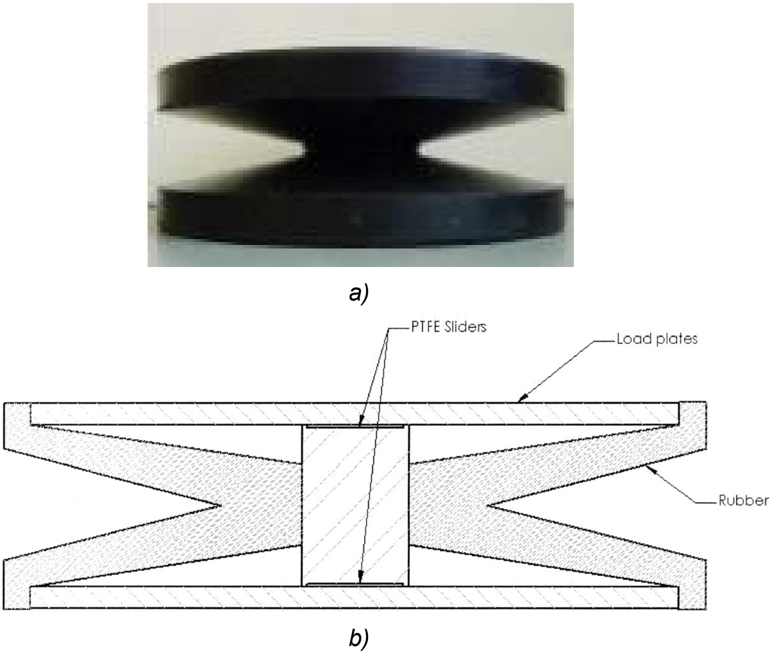
a)
PTFE Sliders
Load plates
Rubber
b)

*Fig. 2.35 RoGlider seismic isolator: a) image (from http://www.robinsonseismic.com) and b) section (from Robinson et al., 2006).*

# 3 BACKGROUND OF RBRL SYSTEM AND RUBBER DYNAMIC BEHAVIOUR

## 3.1 RBRL isolation system

The rolling-ball rubber-layer isolation (RBRL) system, originally proposed by Prof. A.G. Thomas, was developed at TARRC to enable isolation of low-mass (< 10 t) structures. The system comprises RBRL bearings and rubber recentering springs; these may be combined in single packages as shown in Fig. 3.1 (Donà et al. 2014).

The principal device components are better visible in the simplified representation of Fig. 3.2 (from Guerreiro et al., 2007); their principal functions are:

- steel rolling balls system – this enables support of gravity loads and accommodation of large horizontal displacements;
- rubber-layer tracks – these provide an appropriate energy dissipation capacity and an adequate resistance for horizontal non-seismic actions;
- rubber springs – these provide the recentering function and the system stiffness in the steady-state rolling phase.

The device assembly is relatively economical and is easy to tailor for the specific case, in terms of geometry and performance.

Depending on the choice of parameters, the RBRL system provides a rich variety of possibilities, including primary seismic mitigation strategies of isolation, damping or fuse functions.

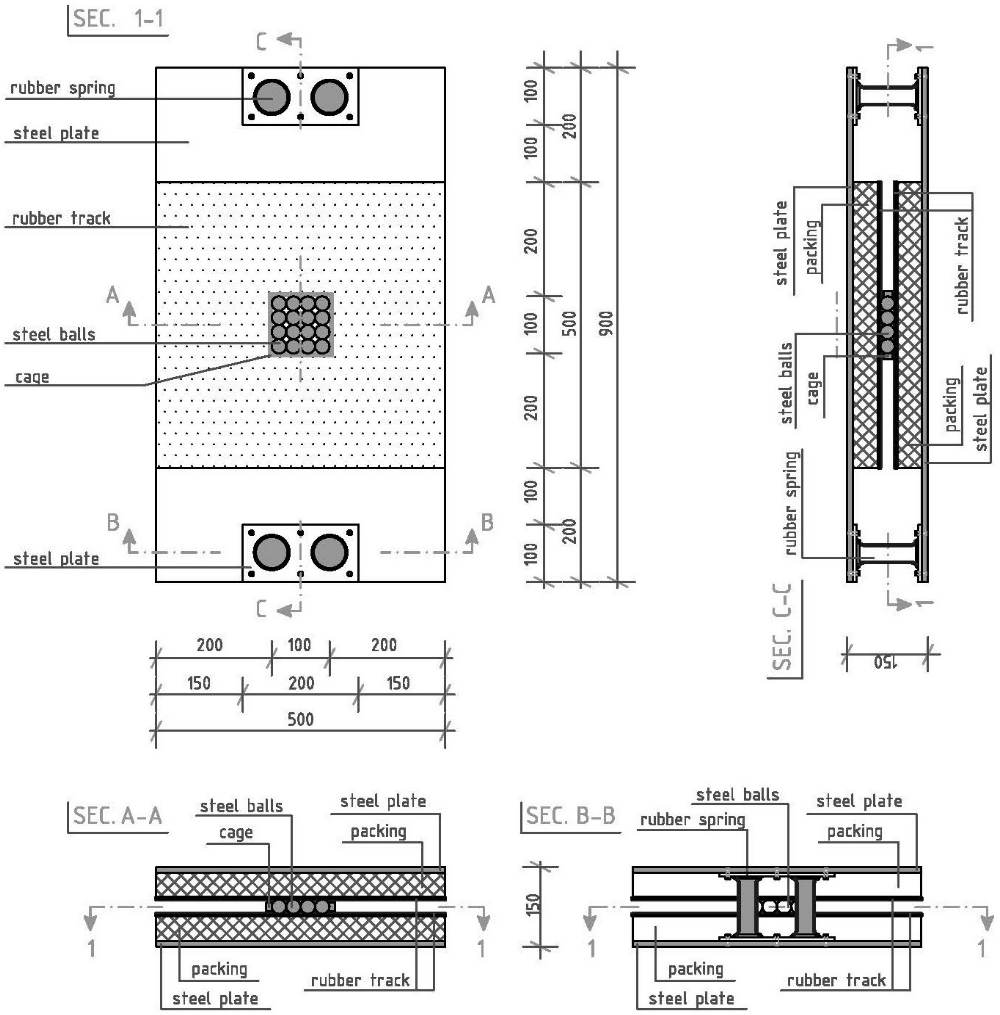
SEC. 1-1
C
rubber spring
steel plate
rubber track
A
A
steel balls
cage
B
B
steel plate
C
100
100
200
100
200
100
100
200
500
900
200
200
100
200
150
200
150
500
steel plate
packing
rubber track
steel balls
cage
packing
steel plate
rubber spring
1
1
SEC. C-C
150
SEC. A-A
steel balls
cage
steel plate
packing
1
1
packing
steel plate
rubber track
SEC. B-B
steel balls
rubber spring
steel plate
packing
150
1
1
packing
steel plate
rubber track

*Fig. 3.1 Combined package of RBRL bearing and recentering springs as used for REEDS and ECOEST projects, by Donà et al. (2014).*

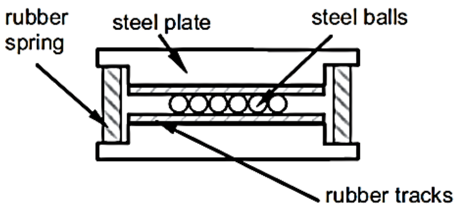
rubber spring
steel plate
steel balls
rubber tracks

*Fig. 3.2 Simplified representation of the RBRL system (from Guerreiro et al. 2007).*

### *3.1.1 Previous research studies*

Extensive experimental studies of this system were undertaken by TARRC and collaborating research centres (Tab. 3.1) in the period 1995 - 2002, resulting in four publications on shaking table tests and two more publications restricted to laboratory characterisation of the system itself. The systems studied were diverse, involving different design natural frequencies and levels of damping.

Large amounts of data were gathered, most notably on the 1999 project *"Parametric Seismic Tests of Rolling_Ball Isolation System"* - following indicated as "ECOEST" project - funded under the ECOEST 2 (European Commission Earthquake and Shaking Tables 2) Programme, and only a summary of the findings with a few highlights has so far appeared in the literature.

In this thesis further analyses of the results of the ECOEST project are presented in order to more clearly establish the behaviour of the system.

| **Project / Publication** | **Type of tests** | **Tracks** | **Springs** | **Superstructure** |
|---|---|---|---|---|
| *INCLUDING SHAKING TABLE TESTS* | | | | |
| EERC<br>(Foti and Kelly, 1996) | monoaxial | high damping, Jakarta compound (Lab Rep 96. Compound 009-06) | steel coil, soft | flexible – model building |
| ENEL/ISMES/TARRC collaboration<br>(Muhr and Bergamo, 2010) | monoaxial | high damping, probably the same as EERC | steel coil, soft | rigid – concrete slab |
| REEDS<br>(Bettinali et al., 2001) | triaxial | low damping A,<br>inside $\phi$ of 190 mm,<br>high damping B outside<br>(ball array $\phi \sim$ 190mm) | rubber B, stiff (1.3Hz) | flexible - electrical substation structure |
| ECOEST<br>(Guerreiro et al., 2007) | monoaxial<br>biaxial<br>triaxial | low damping A,<br>both or upper,<br>high damping B, lower | rubber A, soft and none | rigid or flexible model building |
| *LABORATORY BASED STUDIES* | | | | |
| DEGREE PROJECT<br>(Cook et al., 1997) | monoaxial | unfilled NBR | none | none |
| PhD PROJECT<br>(Muhr et al., 1997) | monoaxial | unfilled NR (two levels of curatives) and NBR | none | none |

*Tab. 3.1 Summary of earlier studies done by TARRC and collaborating research centres on RBRL device, from Donà et al. (2014).*

### *3.1.2 Highlights of the RBRL system behaviour*

Previous experimental studies have shown that the RBRL isolation system has three key types of behaviour, differentiated according to the magnitude of the displacements relative to the ground.

1. For small displacements the system has nonlinear force-displacement characteristics, with high damping and high stiffness, albeit the stiffness declining rapidly as the displacement amplitude is increased. In this regime the behaviour is dominated by the continued location of the balls within a viscoelastic depression, or pit, formed during the long period under static load in the absence of seismic excitation. This behaviour contrasts with that of a sliding system, which presents a very high elastic stiffness, bordering on rigidity, for small excitations.

2. If a characteristic threshold horizontal force is applied, for example by a sufficiently large ground acceleration, the balls will escape from the locality of the viscoelastic depressions, and roll with an approximately constant opposing resistance, significantly lower than the characteristic threshold force. In this regime, the system behaves like a mechanical fuse, the force applied to the superstructure being truncated at the value of the characteristic peak, or threshold, force. This behaviour is akin to that of a sliding system subjected moderate excitations, but with the additional feature that there is a memory effect of the viscoelastic depressions that tends quite strongly to recapture the rolling balls in their initial reference configuration. The displacement time history of the isolated structure therefore exhibits periods of small displacement, with occasional larger excursions; the force-time history is clipped at the characteristic threshold force.

3. For strong excitations with many fluctuations (as opposed to a discrete pulse), continuous free rolling will be induced. In this regime, the recentering springs provide a well-defined stiffness so that a natural frequency of isolation may be defined: it is not strongly amplitude-dependent, and can be designed to have any desired value. The equivalent linear damping level can be calculated for the design displacement from the rolling resistance of the balls and the spring stiffness, and there is a very good scope for meeting any desired level of damping. The system thus behaves like a classical linear isolation system, but enables great scope for choice of natural frequency and damping ratio.

### 3.1.3 Available numerical modelling

An objective of this thesis is to derive a generalised numerical description of the characteristics of the system. The state of the art about modelling of RBRL is limited to only three papers, by Cook et al. (1997), Guerreiro et al. (2007) and Muhr & Bergamo (2010). The first one presents the simplest hysteresis loop that could be used to design the device, according to the secant method. The third paper presents instead the equivalent linear viscoelastic parameters for very small horizontal deflections of the device, while in the second of these papers a possible specific mathematical model is given.

- Cook et al. (1997)

An idealised hysteresis loop for an isolation system consisting of rolling-ball dissipative-layer isolators and auxiliary springs is shown in Fig. 3.3 (Kelly 1993, Ahmadi & Muhr 1995). The effective stiffness corresponding to rolling the ball from its position of rest is assumed to be infinite.

The design parameters of a seismic isolation system are generally the period ($T$) and the damping coefficient ($\zeta$) for a typical design deflection ($d$). Considering a damping ratio that does not grossly exceed 20%, we can use this relation between $T$, $K$ (elastic stiffness of the isolation system) and $M$ (mass of the isolated structure):

$$\frac{2\pi}{T}=\sqrt{\frac{K}{M}} \tag{3.1}$$

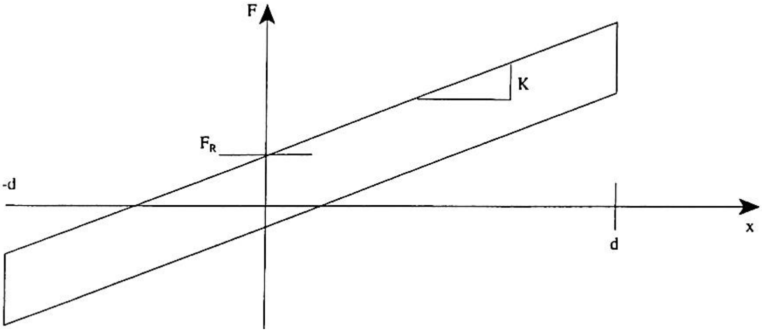

*Fig. 3.3 Schematic hysteresis loop for isolation system comprising rolling-ball dissipative-layer isolators and springs (from Cook et al., 1997).*

To calculate the value of $\zeta$ we have to consider the area $A$ of the hysteretic loop in Fig. 3.3:

$$A \simeq 2F_R \cdot 2d \tag{3.2}$$

where $F_R$ represents the rolling friction force; using the Secant Method (Ahmadi & Muhr, 1997), the effective loss angle $\delta$ may be calculated by:

$$sin\delta = \frac{A}{\pi\left(Kd + F_R\right)d} = \frac{4F_R}{\pi\left(Kd + F_R\right)} \tag{3.3}$$

Since the damping coefficient is related to loss angle by (Ferry 1980, Ahmadi & Muhr 1997):

$$\zeta \simeq \frac{1}{2} tan\delta \tag{3.4}$$

which, using Eq. (3.1) and Eq. (3.3), gives:

$$F_R = \frac{4\pi^3 Md\zeta}{T^2\left(2-\zeta\pi\right)} \tag{3.5}$$

we arrive at the following equation for the rolling friction coefficient $\mu$, in terms of the design parameters of the seismic isolation system of a damping ratio $\zeta$ and a period $T$.

$$\mu \equiv \frac{F_R}{Mg} = \frac{1}{g} \frac{2\pi^3 d\zeta}{T^2\left(1-\pi\zeta/2\right)} \tag{3.6}$$

- Thus, for chosen values of $T$ and $\zeta$, we can get the value of $d$ by using an appropriate design spectrum, and the value of $K$ and $\mu$ can be obtained respectively from Eq. (3.1) and (3.6);
- then, a suitable number and size of balls could be decided considering the requirement that $Mg/R^2$ is not so high that the rubber is ruptured;
- finally, the type of rubber compound and the thickness of rubber layer could be chosen to get the wanted value for $\mu$.

It is relevant to note that for earthquakes much smaller than the design one the idealized loop of Fig. 3.3 is not appropriate: if the seismic excitations is not sufficient for the peak roll-out force to be generated, the behaviour of the device will be governed by the effective dynamic stiffness of the balls in their static depressions, since the balls will rock in their pits.

Some experiments reported in the paper of Cook et al. (1997) show that, for the NBR compound used, the steady-state friction levels achieved are of the correct magnitude to be useful for typical isolation systems, being $0.03 \le \mu \le 0.06$, and thus by calculations: $0.1 \le \zeta \le 0.3$, $1 \le T \le 3\ s$, $0.02 \le d \le 0.1\ m$.

- Guerreiro et al. (2007)

The results from the ECOEST project were summarised by Guerreiro et al. (2007), and a time-domain model was presented to describe the 1D force-deflection behaviour, which for convenience we shall refer to as the Guerreiro model. The basis of the model is presented in Fig. 3.4.

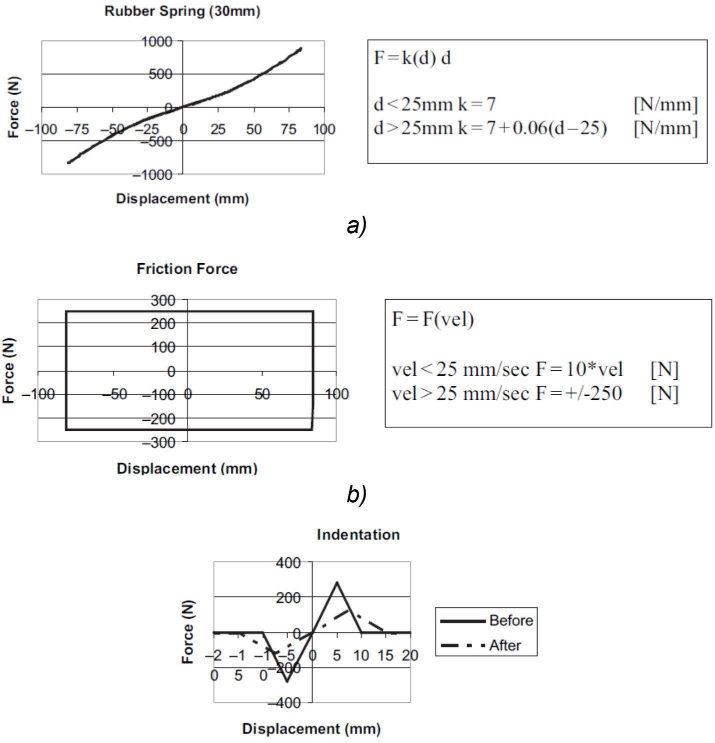

F = k(d) d

d < 25mm k = 7 [N/mm]
d > 25mm k = 7 + 0.06(d − 25) [N/mm]

a)

F = F(vel)

vel < 25 mm/sec F = 10*vel [N]
vel > 25 mm/sec F = +/-250 [N]

b)

c)

*Fig. 3.4 a) Rubber spring analytical model, b) track surface friction model, c) analytical model of the indentation effects, by Guerreiro et al. (2007).*

It consists of a rubber spring, having a small degree of nonlinearity (Fig. 3.4 a), in parallel with a friction force (Fig. 3.4 b), characteristic of steady-state rolling and associated with all deflections, and a special behaviour for displacements from the initial state of reference less than 15 mm to capture the effect associated with indentations developed by the balls in the rubber track under static load (Fig. 3.4 c). In particular, the assumed values in Fig. 3.4 a) simulate the behaviour of the 4 rubber springs with a diameter of 30 mm present in the test. The stiffness definition for the analytical model was obtained by fitting the results obtained in the shaking-table tests, but it agrees quite well with the characterization tests previously performed and reported in Guerreiro et al. (2007). For the rolling friction force a PP (Perfectly Plastic) hysteresis loop was proposed associated with a velocity dependent transition law, to avoid a sudden change in the force when the movement changes direction; the friction force assumed in the model is related to all 4 RBRL devices assembled in the isolation base (mass of isolated structure = 1528 kg, n° of balls =16 each device, rubber layers 2 mm thick and of type A-low damping, diameter of steel balls = 25 mm). For the modelling of the indentation effects, as shown in Fig. 3.4 c), two different states were considered, before and after the first roll-out of the balls from their pits, according to the sinusoidal mono-axial tests results.

As shown by Guerreiro et al. (2007), the Guerreiro model gives reasonably good predictions of response in moderately large seismic events, for which the RBRL system experiences excursions large enough to involve steady-state rolling.

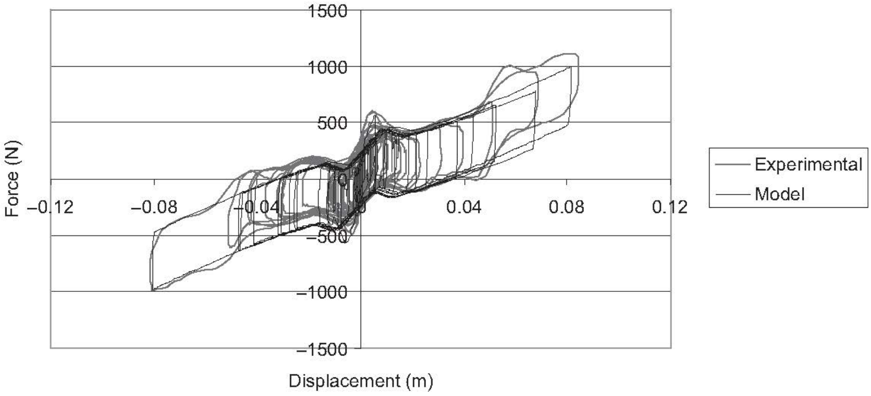

*Fig. 3.5 Force-displacement response results comparison using the Guerreiro Model and for the seismic input of Northridge Kagel Canyon - monoaxial (+3dB), by Guerreiro et al. (2007).*

In Fig. 3.5 a comparison is reported, between the model prediction an the experimental results obtained for the mono-axial Northridge-Kagel Canyon excitation at +3 dB, corresponding to a peak table acceleration of 0.5 g (test configuration: “mass-down”, thus 1 DOF).

Some considerations about this model, positive aspects and weaknesses, will be presented in the section 4.4.

- Muhr & Bergamo (2010)

A different modelling approach based on viscoelastic framework, at least for the small horizontal deflections of the device, is shown in Muhr & Bergamo (2010) in which some experimentations carried out at ISMES (Bergamo, Italy) in 2000 are summarised, comprising double shear tests and shaking table tests both with sinusoidal input and real accelerograms recorded.

For the sinusoidal tests on the shaking table, an isolated structure of mass 581 kg, 4 RBRL devices with 8 balls each and coil springs with three different horizontal stiffnesses were used. The rubber involved is probably the same used in the EERC Project, i.e. Jakarta compound (Foti & Kelly, 1996). Each test consisted of exciting the table at 5 Hz for 15 cycles, using acceleration amplitudes covering the range from approximately 0.23 to 7.6 ms$^{-2}$. The experimental hysteresis loops, obtained measuring the accelerations $a(t)$ and the relative displacements $S(t)$ of the mass, were used to calculate the force-displacement ( $F(t)-S(t)$ ) loops, by:

$$F(t) = M \cdot a(t) \tag{3.7}$$

These loops were thus analyzed to find the Equivalent Linear Viscoelastic Frequency-Domain (ELVFD) parameters, i.e. the complex stiffness ( $K^*$ ) and the loss angle ( $\delta$ ); to do this, the Secant Method (Ahmadi & Muhr, 1997) was used:

$$K^* \equiv \hat{F} \big/ \hat{S} \tag{3.8}$$

$$\sin\delta \equiv A \big/ \pi \hat{F} \hat{S} \tag{3.9}$$

where $\hat{F}$ and $\hat{S}$ are peak force and relative displacement respectively, and $A$ is the area of the hysteresis loop. In the Fig. 3.6 these results for the ELVFD representation are reported.

It is clear that the springs have little effect on the dynamic properties of the system at small deflections, so the principal contribution to $K^*$ and $\delta$ is given by

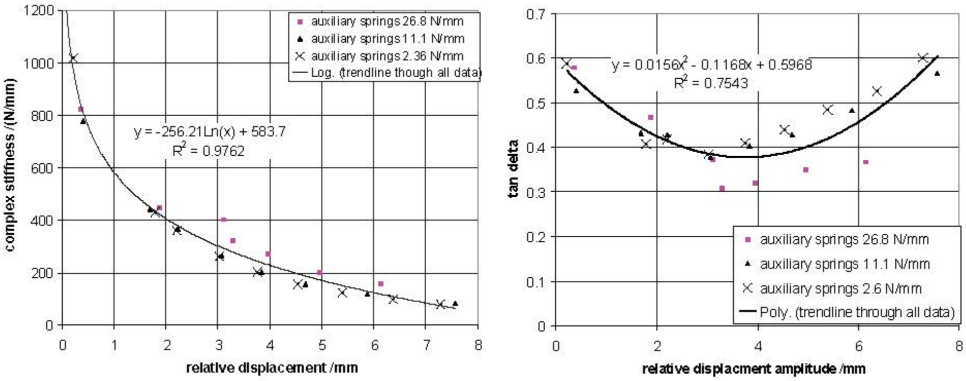

*Fig. 3.6 Complex stiffness and loss tangent results, both versus relative displacement amplitude, for the systems used in the sinusoidal shaking table tests carried out at ISMES, Bergamo, 2000 (from Muhr & Bergamo, 2010).*

the RBRL isolator (without coil springs). The dynamic properties presented in Fig. 3.6 are useful for the response prediction of the system in the case of small seismic excitations, not sufficient for the peak roll-out force to be generated.

The equivalent representation of the behaviour of a device based on rubber through the ELVFD parameters, and the principal available methods, will be better discussed later in this Chapter.

### *3.1.4 Theory of Muhr et al. (1997) for rolling resistence on thin rubber layers: formulation and errors of assessment*

In 1997, Muhr et al. developed a very interesting theory about friction coefficient for the rolling of a steel ball over thin rubber layers. The working of this theory would mean the possibility to calculate the friction force value for the relative movements of the two steel plates of the device, given the principal parameters that influence its behaviour: type of rubber compound, thickness of rubber layer, steel sphere diameter, stress parameter or load for each ball. Following, the principal concepts and formulations of this theory are reported (Muhr et al., 1997).

- Relationship of Rolling Friction to Indentation Work and Hysteresis

We start defining frictional force $Q$ as the work done when the ball rolls a unit distance on a single viscoelastic track and, indentation work $U$ as the work done by the load $W$ as it is applied to the ball to indent the rubber surface and create a pit. If we consider, according to Gent & Henry (1969), that $U$ is applied and relaxed $1/2a$ times in unit rolling distance, where $a$ is the contact radius, and that a fraction $\alpha$ of the indentation work is lost on each cycle, it's possible to write:

$$Q \simeq \alpha U / 2a \tag{3.10}$$

Fig. 3.7 shows possible schemes for the measure of $Q$.

The parameter $\alpha$ may be calculated as:

$$\alpha = \pi \sin \delta \tag{3.11}$$

where $\delta$ is the loss angle in a dynamic shear experiment at appropriate amplitude and frequency (Thomas, 1973). The appropriate value of $\alpha$, according to Greenwood et al. (1961), is two or three times higher than the one observed in a simple uniaxial stress cycle, because the complicated stress cycles suffered by rubber elements during rolling will result in greater energy dissipation. Thus, as it will be also highlighted later presenting the parametric tests results performed to verify the goodness of this theory, the $\alpha$ parameter is the one more critical and needs of experimentations to be defined.

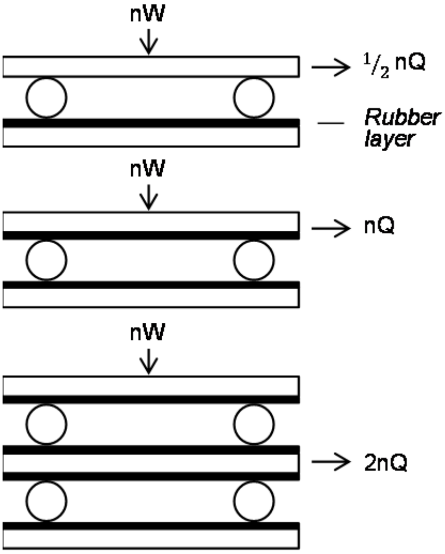

*Fig. 3.7 Possible schemes, with the position of balls and rubber layers, for experimental determination of rolling resistance; n indicates the number of balls in one layer.*

Being the friction coefficient $\mu$ the ratio between the friction force $Q$ and the weight $W$, we have:

$$\mu \equiv Q/W \simeq \alpha U/2aW \tag{3.12}$$

- Theoretical Equation for Rolling Friction for an Infinitely Thick Layer

The indentation depth $d$ and the contact radius $a$, according to Hertz's equations, for an elastic half space of Young's modulus $E$ are given by (Timoshenko, 1934):

$$a = \left[\frac{3}{4}WR\left(\frac{1-\nu^2}{E}\right)\right]^{\frac{1}{3}} = \left[\frac{9}{16}\frac{WR}{E}\right]^{\frac{1}{3}} \tag{3.13}$$

$$d = \frac{a^2}{R} = \left(\frac{9}{16}\right)^{\frac{2}{3}}\left(\frac{W^2}{E^2R}\right)^{\frac{1}{3}} \tag{3.14}$$

in which $W$ is the vertical load, $R$ the sphere radius, and the Poisson's ratio, $\nu$, has been set to 0.5, the material being rubber.

Eq. (3.15) give the work of indentation $U$ in terms of the previous parameters:

$$U = \int_0^d W\,dx = \frac{16}{9}ER^{\frac{1}{2}}\int_0^d x^{\frac{3}{2}}\,dx = \frac{2}{5}\frac{16}{9}ER^{\frac{1}{2}}d^{\frac{5}{2}} = \frac{2}{5}\left(\frac{9}{16}\right)^{\frac{2}{3}}\left(\frac{W^5}{E^2}R\right)^{\frac{1}{3}} \tag{3.15}$$

Combining equations (3.12), (3.13) and (3.15), we can obtain the formulation for the rolling friction of Gent & Henry, for an infinitely thick layer (for this reason indicated with subscript $\infty$):

$$\mu_\infty \simeq \frac{1}{5}\left(\frac{9}{16}\right)^{\frac{1}{3}}\left(\frac{W}{ER^2}\right)^{\frac{1}{3}}\alpha \simeq 0.165\left(\frac{W}{ER^2}\right)^{\frac{1}{3}}\alpha \tag{3.16}$$

- Theoretical Equation for a Layer of Finite Thickness

An interesting experimental investigation, performed by Waters (1965), on the influence of the thickness of rubber layer on the indentation, has shown the possibility to relate the parameters $a$ and $d$ in the same way as in the Hertz theory (see Eq. (3.14)):

$$a = \sqrt{dR} \tag{3.17}$$

provided that $d$ is not the Hertzian value $d_\infty$ (related to a rubber layer of infinite thickness) but the one modified through the equation:

$$d = d_\infty f(t/a) = \left(\frac{9}{16}\right)^{\frac{2}{3}} \left(\frac{W^2}{E^2 R}\right)^{\frac{1}{3}} f(t/a) \tag{3.18}$$

where $t$ is the thickness of rubber layer and $f(t/a)$ is the following function empirically determined by Waters, true within the regime of small loads and indentations:

$$f(t/a) \simeq 1 - \exp(-At/a) \tag{3.19}$$

$A$ is a parameter for the boundary conditions at the back of the rubber sheet, and is set 0.417 for the bonded condition and 0.67 for the lubricated one.

To introduce the Waters' function in the calculation of the indentation work $U$, we need to express $W$ in terms of $d$. If we use Eq. (3.17) to substitute a function of $d$ for $a$ in Eq. (3.18), we can solve this last equation for $W$ as a function of $d$:

$$W = \left(\frac{d}{f\left(t/\sqrt{dR}\right)}\right)^{\frac{3}{2}} E R^{\frac{1}{2}} \frac{16}{9} = \left(\frac{E t^3}{R}\right)\left(\frac{16}{9}\right) g(s) \tag{3.20}$$

where:

$$g(s) = \left[s^2 / f\left(s^{-1}\right)\right]^{\frac{3}{2}} \tag{3.21}$$

$$s = a/t = \sqrt{(dR)}/t \tag{3.22}$$

$$f\left(s^{-1}\right)=1-\exp\left(-A/s\right) \tag{3.23}$$

Indeed, if in the Gent & Henry (1969) theory the calculation of indentation work $U$ is obtained with an integration of $W$ until the value of $d$ , that depends only by Hertz theory, now we need to use a variable substitution with $s$ because the problem variables are two: $d$ , function also of $t$ , and $t$ . Hence:

$$\begin{aligned} U &= \int_0^d W\,dx = \left(Et^3/R\right)(16/9)\left(2t^2/R\right)\int_0^s g(s)\,s\,ds \\ &\equiv \left(Et^5/R^2\right)(32/9)\,I(s) \end{aligned} \tag{3.24}$$

where:

$$I(s)=\int_0^s g(s)\,s\,ds \tag{3.25}$$

If $s$ is equal to 0, the term $1/f(s^{-1})$ is unity and, as $s$ increases, it rises monotonically with $s$ (see Eq. (3.19)). So, we can deduced that:

$$s^5/5<I(s)<\left(s^5/5\right)\left[f\left(s^{-1}\right)\right]^{-3/2} \tag{3.26}$$

Substituting Eq. (3.24) for $U$ into Eq. (3.12) for $\mu$ , and expressing $a$ in terms of $d$ using Eq. (3.17), we find an expression to calculate $\mu$ as a function of $d$ :

$$\begin{aligned} \mu &= \frac{\alpha}{2W}d^{-1/2}R^{-1/2}\left(Et^5/R^2\right)(32/9)\,I(s)=\alpha\,(16/9)\left(Et^4/WR^2\right)s^{-1}I(s) \\ &= (16/9)\,\alpha\left(W/ER^2\right)^{1/3}\left(Et^3/WR\right)^{4/3}s^{-1}I(s) \end{aligned} \tag{3.27}$$

From the Eq. (3.16) we can rewrite the term $\alpha(W/ER^2)^{1/3}$ as $\mu_\infty/0.165$ , where $\mu_\infty$ is the rolling friction ratio for a semi-infinite layer, and from Eqs. (3.20) and (3.21) the term $(Et^3/WR)^{4/3}$ as $(9/16)^{4/3}[f(s^{-1})]^2 s^{-4}$ ; thus:

$$\mu=\mu_\infty 5\left[f\left(s^{-1}\right)\right]^2 s^{-5}I(s)\equiv\mu_\infty\Phi(s) \tag{3.28}$$

The non-dimensional quantity $\Phi(s)$, that is a function of $WR / Et^3$, should tend to 1 if $W$ tends to 0 or tends to ∞, and to 0 if tends to 0. From inequality (3.26) it is possible to deduce that:

$$\left[f\left(s^{-1}\right)\right]^2 < \Phi(s) < \left[f\left(s^{-1}\right)\right]^{1/2} \qquad (3.29)$$

The qualitative prediction of this theory by Muhr et al. (1997), given in a dimensionless sketch in the paper, is reproduced here in Fig. 3.8. In this graph the values of the “reduced friction ratio” $\mu / \mu_\infty$ or $\Phi(s)$ (see Eq. (3.28)) are reported versus the values of the “reduced rubber thickness” $(t / R)/(W / ER^2)$ or $[(16/9)g(s)]^{-1/3}$ (see Eq. (3.20)). The ordinate is obtained using Eqs. (3.19), (3.24) and (3.28) by numerical integration of $I(s)$ (see Appendix A), while the abscissa is calculated by Eqs. (3.19) and (3.21). To construct the plot, a sufficiently wide range of the parameter $s$ is considered. Fig. 3.8 also shows that the Hertzian theory is applicable when this inequality is satisfied:

$$\left(t / R\right) > \sim 10\left(W / ER^2\right)^{1/3} \qquad (3.30)$$

Some mistakes were found in the paper of Muhr et al. (1997), regarding the equations numbered there 5 and 13; the corresponding equations, herein correctly reported, are the Eqs. (3.14) and (3.30).

- Scaling Rules and Dimensional Analysis

Scaling rules represent an interesting possibility, since they permit to carry out tests on one scale to predict the rolling friction ratio $\mu$ at other scales.

If a scale factor $\lambda$ for linear dimensions ($R$ = radius, $t$ = thickness) is adopted:

$$R \to \lambda R, \qquad t \to \lambda t \qquad (3.31)$$

the load $W$ must be multiplied by $\lambda^2$ to keep the stresses the same (and thus all dimensionless quantities, such as strains and angles):

$$W \to \lambda^2 W \qquad (3.32)$$

Being dimensionless, the value of $\mu$ should be unaltered scaling $W$ by $\lambda^2$. Because the hysteretic factor $\alpha$ may depend on rate, the rolling velocity $v$ should also be scaled by $\lambda$ , to keep the frequency $v/2a$ constant:

$$v \to \lambda v \tag{3.33}$$

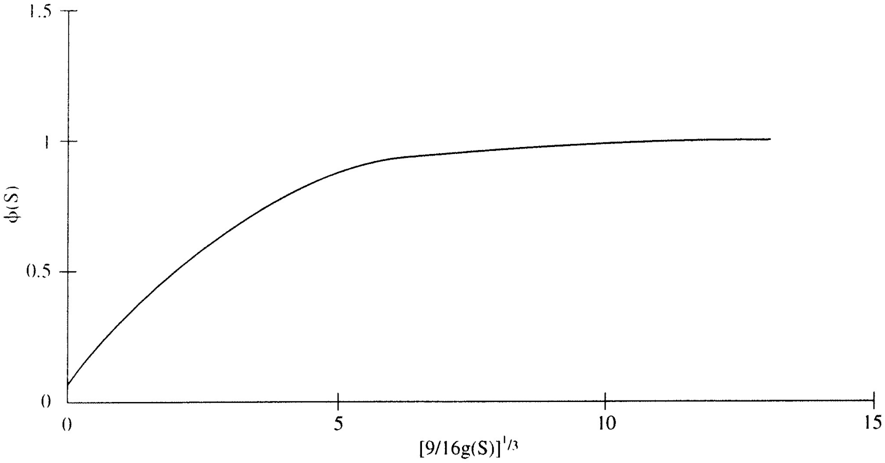

*Fig. 3.8 Schematic plot of reduced friction ratio versus reduced rubber thickness (Eq.(3.28), Muhr et al., 1997).*

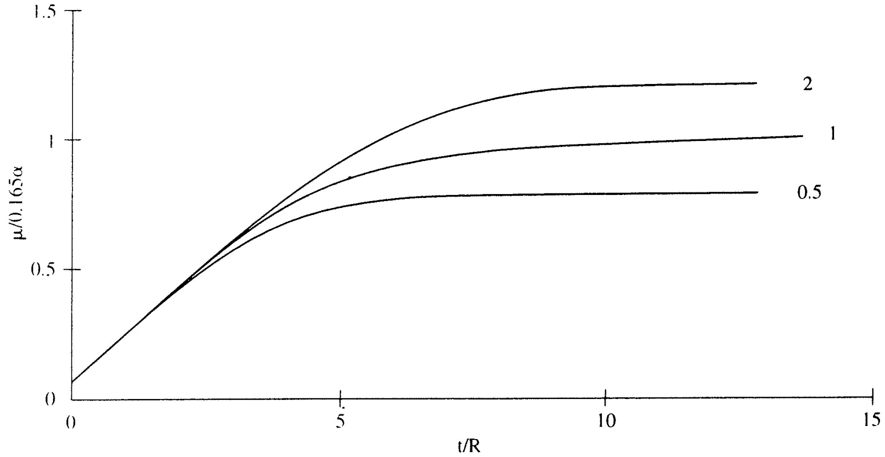

*Fig. 3.9 Parametric schematic plots of rolling friction ratio μ, scaled using α, versus dimensionless ratio of rubber layer thickness to ball radius (Eqs.(3.28),(3.16)). $W/ER^2$ is the stress parameter (Muhr et al., 1997).*

So, for one type of rubber at one rate, $\mu$ must depend only on $W / R^2$ and $t / R$. Moreover, if the rubber properties enter only through the parameters $E$ and $\alpha$, it is possible to derive parametric plots of $\mu / \alpha$ versus $t / R$, related to a specific value of the parameter $W / ER^2$. Examples of such plots, based on the theory reported above of Muhr et al. (1997) for layers of finite thickness and low load, are given in Fig. 3.9. This Figure is derived from the previous one by multiplying both the ordinate and the abscissa values by the factor $(W / ER^2)^{1/3}$. According to Gent & Henry (1969), we would expect the theory to be satisfying provided $W / ER^2$ (stress parameter) is sufficiently low.

- Experimentation by Muhr et al. (1997) to verify the theory

A parametric experimentation was carried out by Muhr et al. (1997) to check the effectiveness of the above theory. In these tests a lightly crosslinked unfilled natural rubber (NR) compound was used, with a value of $G$ = 0.26 MPa (shear modulus) and $\delta$ = 3.8° (loss angle), from dynamic test results at 0.1 Hz and 50% strain. The standard physical properties and the other dynamic shear properties of this rubber are reported in Table 1 of Muhr et al. paper, under the name “No. 3”. Layers of this rubber were bonded directly to steel rolling plates (74x145x12 mm) during vulcanisation, using Chemlok 220. The rubber surfaces were moulded against Mylar (polyester film) to keep them clean and to produce a smooth surface profile. The surface of the rubber layers, on which the balls were rolled, were dusted with talc to avoid possible effects of sticking.

The experimental setup is reported in Fig. 3.10. A set of four balls was inserted between the two steel plates with rubber tracks. The bottom plate was fixed to the base of an Instron uniaxial test machine, while the top rolling plate was connected to the load cell and cross-head of the Instron by nylon-coated multistrand wire passing round a pulley. When the cross-head of the Instron machine travels upwards, the cable is pulled and the top rolling plate starts to move forward. The cross-head speed was 1 mms$^{-1}$ and the temperature was 23±2 °C.

The parameters considered in this experimentation were:

| | |
|---|---|
| - rubber layers thickness ($t$): | 9 values, ranging from 0.254 mm to 3.70 mm; |
| - balls radius ($R$): | 11 values, ranging from 1.58 mm to 6.25 mm; |
| - stress parameter ($W / R^2$): | 3 values, 1.0, 2.0 and 5.2 MPa. |

Hence, the load per ball ($W$) was changed every test to hold the stress parameter constant over the range of $t / R$ values investigated.

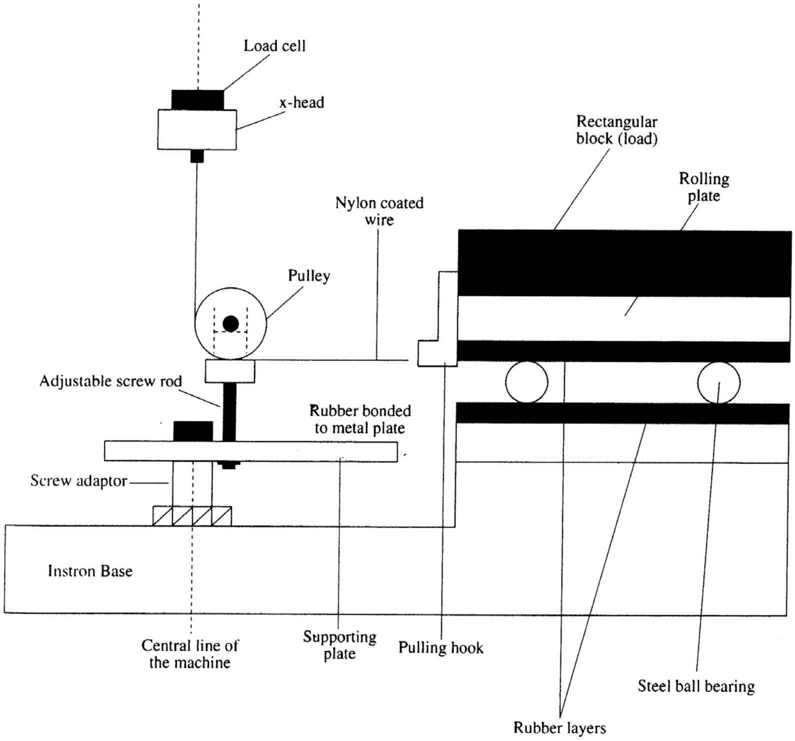
Load cell
x-head
Rectangular block (load)
Rolling plate
Nylon coated wire
Pulley
Adjustable screw rod
Rubber bonded to metal plate
Screw adaptor
Instron Base
Central line of the machine
Supporting plate
Pulling hook
Steel ball bearing
Rubber layers

*Fig. 3.10 Tests setup for measuring rolling forces (Muhr et al., 1997).*

The results obtained consist of the force-displacement curve for each test, from which the steady-state rolling friction ratio $\mu$ was calculated: these values for all the tests are reported here in Fig. 3.11. Firstly, the results shows that the scaling rule works, despite the cross-head speed being kept constant at 1 mms$^{-1}$; probably the influence of rate is very weak. A comparison, made between the plateau value of $\mu$ from tests and the relative theoretical values from Gent & Henry (1969) (see Eq. (3.16)), is reported in Fig. 3.12. The value of the hysteresis parameter $\alpha$=0.208, calculated through the Eq. (3.11) and from the value of $\delta$ reported before, was used to obtain the theoretical line representative of $\mu_\infty$ for a semi-infinite layer. The conclusions reported in Muhr et al. (1997), about this experimentation, are:

1) the results are in conflict with the extension of the theory, about rolling friction ratio, to rubber layers of finite thickness, since (Fig. 3.11):

- a) the results are strongly dependent on the stress value even before the plateau are reached;
- b) the plateau region seems to be reached at quite low values of $t / R$;

2) at the lower loads, the plateau value of $\mu$ seems in agreement with the theory of $\mu_\infty$ for a semi-infinite layer (Fig. 3.12); however the real dependence on

load seems to be stronger than predicted, so that at the highest load the plateau value of $\mu$ is 35% higher than the value of $\mu_\infty$ by Gent & Henry (1969).

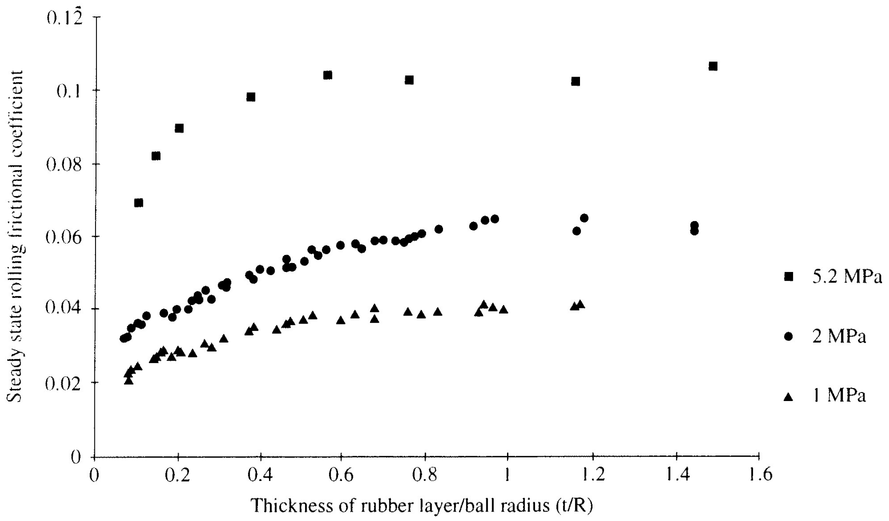

*Fig. 3.11 Experimental results for steady-state rolling friction coefficient, versus ratio of rubber layer thickness to ball radius, for three different values of W/$R^2$ (Muhr et al., 1997).*

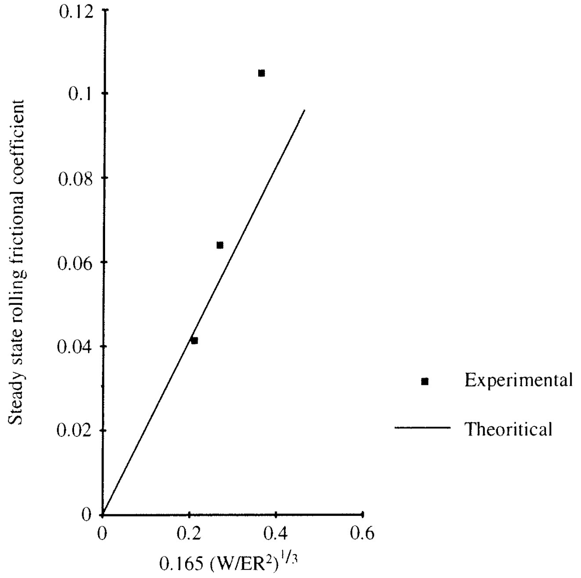

*Fig. 3.12 Comparison of theory for the plateau value of μ (Eq. (3.16)) with experimental results, for steady-state rolling resistance as a function of load (Muhr et al., 1997).*

Studying the paper of Muhr et al. (1997), no evidence can be seen about how the plots reproduced in Fig. 3.8 and Fig. 3.9 were generated, and it seems that possibly they are simply sketches of the qualitative behaviour, intended to indicate the evolution from the low $t / R$ limit to the high $t / R$ limit rather than plots of the quantitative numerical integrations required to evaluate the equations. So it has been decided to recalculate the non-dimensional quantity $\Phi(s)$ (see Eq. (3.28)) through numerical integration carried out with Matlab software. The new dimensionless curves reported below in Fig. 3.13 and Fig. 3.14, as we expected, show that the ones presented in Muhr et al. (1997) are distorted or stretched in horizontal direction.

The correct shape of the new theoretical plots modifies the conclusion 1a) of Muhr et al. (1997), because also the theoretical values of $\mu$, before the plateaux are reached, are strongly dependent on the stress parameter value; however, this correction seems not sensible to contrast the other conclusion 1b), because the $t / R$ values for which the plateau are reached were not significantly reduced if compared to the previous plots of Muhr et al. (1997). This point might to be surpassed considering that the $\mu$ experimental values obtained for the highest values of $t / R$ don't correspond to the plateau values; this is not true for the case of $W / R^2$ = 5.2 MPa, for which the theory is not valid because of the high stresses that cause permanent rolling tracks, but could be the case for the other stress parameters. To verify it, we decide to plot again the non-dimensional quantity $\Phi(s)$ using a smaller range for the abscissa values, compatible with the range investigated by the parametrical tests (see Fig. 3.15): thus, we observed that the shape of the theoretical plot is very similar to the trend of the experimental results (see Fig. 3.11) and what in the paper of Muhr et al. (1997) was considered like plateau is, instead, only a large reduction of the initial gradient with which the theoretical curve starts. In view of the above, the extension of the theory to rubber layers of finite thickness would seems effective. Therefore it was decided to make a direct comparison between the theoretical plots and the experimental results; to do that, the theoretical values of $\mu$ have been calculated from the values of $\mu / 0.165\alpha$ of Fig. 3.14. A critical issue is the value of the hysteresis parameter $\alpha$ that, according to Greenwood et al. (1961), should be taken two or three times higher than the one observed in a simple uniaxial stress cycle ($\pi \sin\delta$): so, without knowing the correct value of $\alpha$ or if it is dependent on the stress parameter, we decided to use for each level of stress that value that leads to the best fitting between experimental and prediction values of $\mu$. This comparison and the values used for $\alpha$ are reported in Fig. 3.16, in which the experimental values derive from the digitalization of Fig. 3.11. From this we may conclude that, excluding the case in

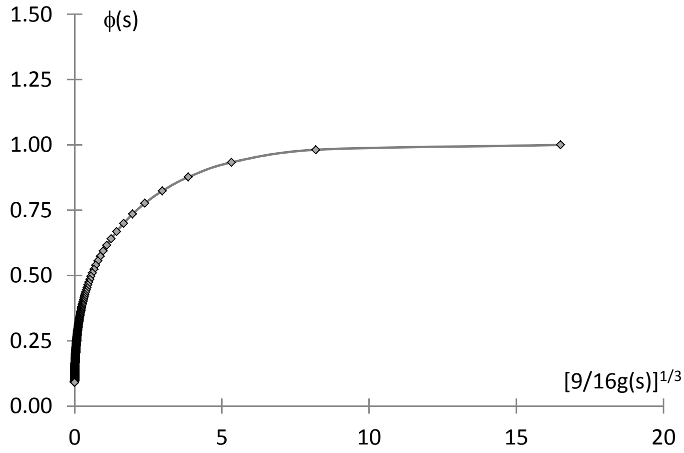

*Fig. 3.13 New calculation of the theoretical plot of reduced friction ratio versus reduced rubber thickness (Eq. (3.28)).*

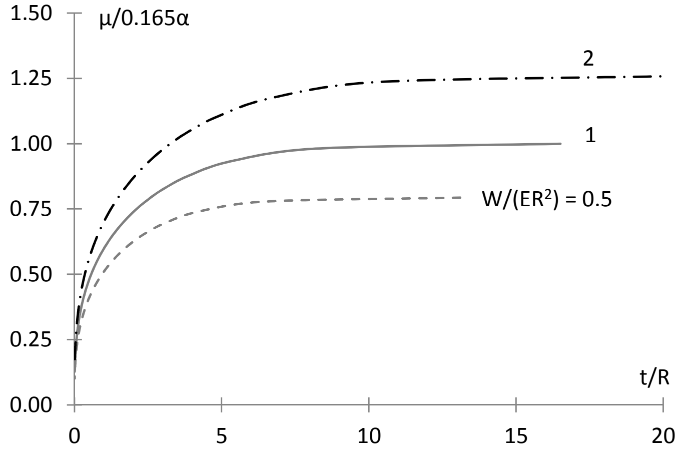

*Fig. 3.14 New calculation of the theoretical plots of rolling friction ratio μ, scaled using α, versus dimensionless ratio of rubber layer thickness to ball radius (Eqs. (3.28),(3.16)). W/ER$^2$ is the stress parameter.*

which the stress level is too high and so beyond the range of the assumptions made in the theory, the theory of Muhr et al. (1997) seems to work subject to the following considerations:

- $\alpha$ is $g$ times (2 ÷ 3) higher than the one observed in a simple uniaxial stress cycle (Greenwood et al., 1961);
- $g$ , in general, is a function of the stress parameter, $g = g(W / ER^2)$ .

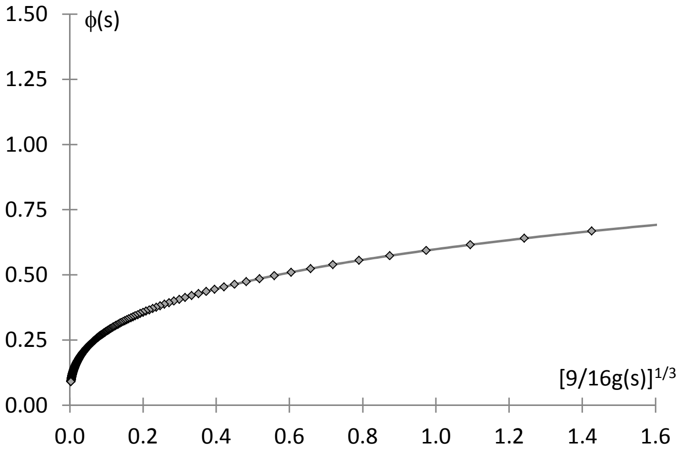

*Fig. 3.15 New calculation of the theoretical plot of reduced friction ratio versus reduced rubber thickness (Fig. 3.13), represented for a smaller range of abscissa values, compatible with the experimentation.*

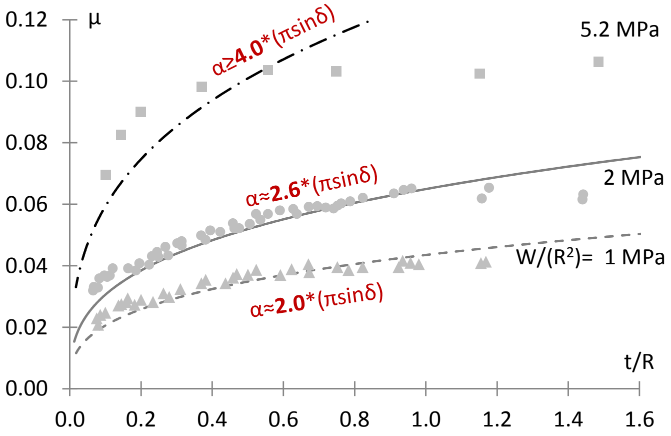

*Fig. 3.16 Comparison between the predicted values of μ (lines), by theory of Muhr et al. (1997), and the experimental data (dots), reported here through the digitalization of Fig. 3.11. α value to get the best fitting is reported for each stress level ($W/R^2$) considered.*

Regarding the conclusion 2) of Muhr et al. (1997), relating to the comparison shown in Fig. 3.12, the apparently good agreement (excluding the case of highest stress level) between the theoretical line of the plateau value $\mu_\infty$ (see Eq.(3.16)) and the tests results is due to the following two reasons: the theoretical values were not multiplied by the $g$ factor, as might be expected to be appropriate from Greenwood et al. (1961), and the experimental values did not correspond to the plateau values of $\mu$, as indicated in the paper and seen before. Instead the

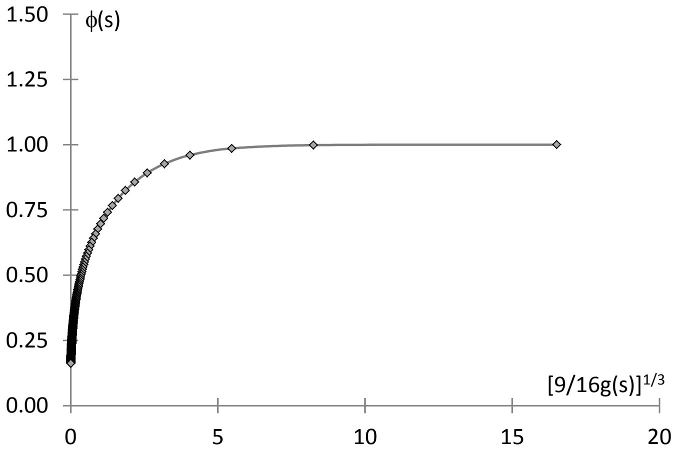

*Fig. 3.17 Theoretical plot of reduced friction ratio versus reduced rubber thickness (Eq. (3.28)), for lubricated condition.*

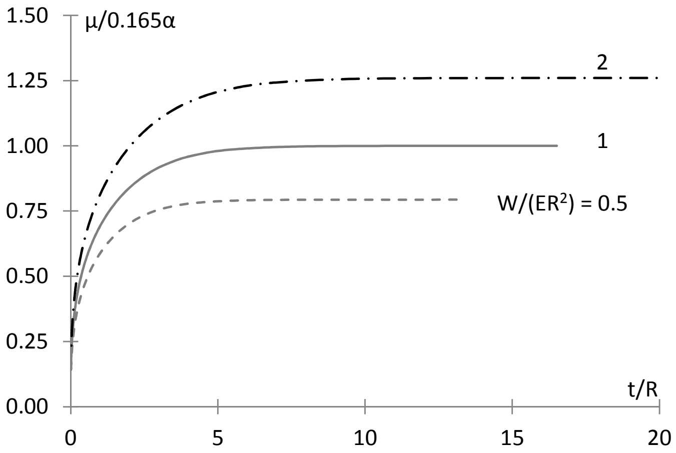

*Fig. 3.18 Theoretical plots of rolling friction ratio μ, scaled using α, versus dimensionless ratio of rubber layer thickness to ball radius (Eqs. (3.28), (3.16)), for lubricated condition. W/ER$^2$ is the stress parameter.*

comparison should be made at the appropriate value of $t/R$, not using the plateau value $\mu_\infty$ reached by $\mu$ for high $t/R$.

The validation of Muhr et al. (1997) theory, that permits to calculate the rolling friction ratio for the rolling of a steel ball on rubber tracks of finite thickness, knowing $W$ (load per ball), $R$ (ball radius), (rubber layers thickness), $E$ (Young's modulus of the rubber) and $\alpha$ (rubber hysteresis) parameters, would be really important at two different levels:

- one more general, related to the technological and scientific research in the rubber field;

- one more specific, related to the modelling of the steady-state rolling friction force of the RBRL device.

Since the only results available in the literature to verify this theory are the ones presented in Muhr et al. (1997), that are related to a unique type of rubber compound and, furthermore, present nowadays only in hard copy, it would be interesting to perform a new parametric experimentation to validate it.

The empirical function of Eq. (3.19) given by Waters (1965), on which this theory is based, was calibrated for both the boundary conditions at the back of the rubber sheet, bonded and lubricated, through the parameter $A$ ; if until now the results for the bonded condition ( $A$ =0.417) was considered, in the Fig. 3.17 and Fig. 3.18 are presented the same theoretical plots, as above, for the case of lubricated condition ( $A$ =0.67).

## 3.2 Dynamic properties of rubber and viscoelastic linearization methods

The Kelvin model (Fig. 3.19) is the simplest system among the ones obtained as combinations of springs and dashpots used to achieve vibration or shock isolation (Ahmadi & Muhr, 1997). Whether the use of this simple model associated with a mass is widely used by engineers to describe the behaviour of a damped harmonic oscillator, the real properties of rubber springs are not as widely known: the challenge to encompass all the effects of strain rate, history and amplitude in a single model able to predict the non-linear behaviour of rubber (mainly caused by the use of reinforcing fillers to increase damping and stiffness), could also contribute to give a perception that the design of rubber isolators remains rather uncertain. An alternative and commonly used approach is to use the equivalent Kelvin model for a rubber spring, taking into account the frequency and amplitude representative of the application in setting the parameters.

Traditionally rubber has been regarded as a viscoelastic material: this means that its behaviour could be represented by a number (possibly infinite) of interconnected springs and dashpot with appropriate values of stiffness and damping constant. In accord to the linear viscoelasticity theory, the knowledge of only one of the following parameters, over the full range of time or frequency, is sufficient to describe the stress-strain properties or characteristics (in shear, for example):

$G(t)$ : relaxation shear modulus

$G^{/}(\omega)$ : dynamic storage shear modulus

$G^{//}(\omega)$ : dynamic loss shear modulus

$G^{/}(\omega)$ and $G^{//}(\omega)$ are defined by the sinusoidal stress response $\tau(t)$ to an imposed sinusoidal shear strain $\gamma(t)$, in this way:

$$\begin{aligned} \gamma(t) &= \tilde{\gamma} \cdot \sin(\omega t) \\ \tau(t) &= \tilde{\gamma} \cdot \left[ G^{/}(\omega)\sin(\omega t) + G^{//}(\omega)\cos(\omega t) \right] \\ &\equiv \tilde{\gamma} \left| G^{*}(\omega) \right| \sin(\omega t + \delta) \end{aligned} \tag{3.34}$$

where $\tilde{\gamma}(t)$ is the strain amplitude, $\tan\delta \equiv G^{//} / G^{/}$ , $\left|G^{*}\right| \equiv \sqrt{G^{/2} + G^{//2}} \equiv \tilde{\tau} / \tilde{\gamma}$ and $\tilde{\tau}(t)$ is the stress amplitude (see Fig. 3.20). Instead, $G(t)$ is defined by the stress response to an initial and constant strain $\gamma_0$ , that relaxes as a function of time (see Fig. 3.21):

$$\begin{aligned} \gamma_0 &= \gamma(t=0) \\ \tau(t) &= \gamma_0 \cdot G(t) \end{aligned} \tag{3.35}$$

The relations between the parameters above is possible through the Boltzmann superposition principle, according to which the stress $\tau(t)$ at time t arising from a strain history $\gamma(s)$, with s ≤ t, is obtained by adding up the contributions from all the strain increments, subject to relaxation for the appropriate time elapsed since each increment was made:

$$\tau(t) = \int_0^t G(t-s) \frac{d\gamma(s)}{ds} ds \tag{3.36}$$

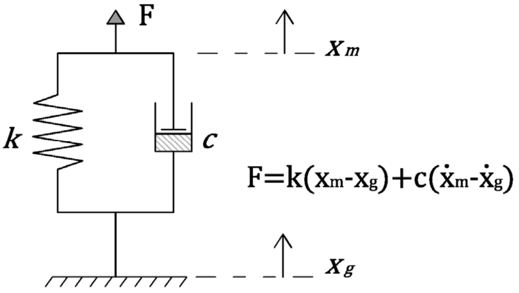

Fig. 3.19 Kelvin model

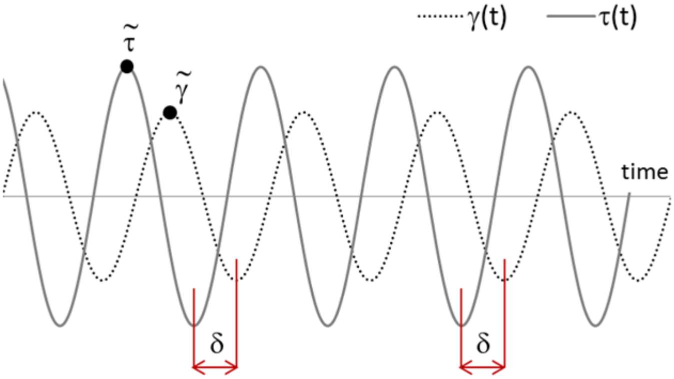

Fig. 3.20 Sinusoidal stress response $\tau(t)$ to an imposed sinusoidal shear strain $\gamma(t)$ for a viscoelastic material.

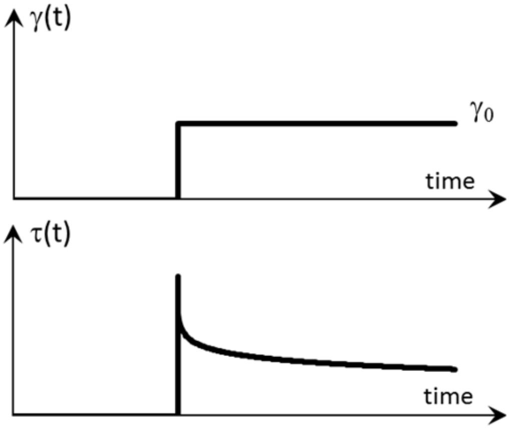

Fig. 3.21 Stress response $\tau(t)$ to an initial constant strain $\gamma_0$ for a viscoelastic material.

Indeed from Boltzmann integral, with the lower limit replaced by $-\infty$ to give steady state at time t, and Eq. (3.34) for $\tau(t)$ in terms of $G^{/}$ and $G^{//}$ is possible to write:

$$\begin{aligned} G^{/}(\omega) &= G(\infty) + \omega\int_0^{\infty}\left(G(s) - G(\infty)\right)\sin(\omega s)ds \\ G^{//}(\omega) &= \omega\int_0^{\infty}\left(G(s) - G(\infty)\right)\cos(\omega s)ds \end{aligned} \tag{3.37}$$

and with a useful first order approximation:

$$G^{//}(\omega) \approx (\pi/2)\frac{dG^{/}(\omega)}{d\ln(\omega)} \approx -(\pi/2)\left.\frac{dG(t)}{d\ln(t)}\right|_{t=1/\omega} \tag{3.38}$$

It is found that the theory of linear viscoelasticity describes the properties of most unfilled elastomers quite well and its application also extends to finite strain in simple shear.

Eq. (3.34) corresponds to an elliptical stress-strain hysteresis loop (for a forced sinusoidal strain) with the major axis independent of the strain amplitude, as for the Kelvin model. The area of this loop, $W_L$, is the energy dissipated in that cycle and is calculated by:

$$W_L = \pi\left|G^*\right|\tilde{\gamma}^2\sin\delta \tag{3.39}$$

As mentioned, the reinforcing filler generally presents in the rubber, leads to have a non-linear behaviour, so hysteresis loops are not perfect ellipses and their slope shows a relatively high dependence on amplitude. This phenomenon is called Payne effect (Payne, 1962; Ahmadi & Muhr, 2011) and consist in a rapidly decreasing of the storage modulus with increasing in strain amplitude, approximately until a value of 25% of strain; in this range the loss modulus reaches it maximum value. The Payne effect depends on the filler content of the material and vanishes for unfilled elastomers. This effect can be seen in Fig. 3.22 , which shows the results of the characterization tests for the rubber A (low damping – unfilled) and B (high damping – filled) used in the ECOEST experimentation, obviously for the only rubber B. Another amplitude-dependent effect is the Mullins effect (Mullins & Tobin, 1965; Ahmadi et al., 2008; Kingston & Muhr, 2011), that can be idealized for many purposes as an instantaneous and irreversible softening of the stress–strain curve that occurs whenever the strain increases beyond its prior maximum value. Mullins softening is a viscoelastic effect, although in filled rubber

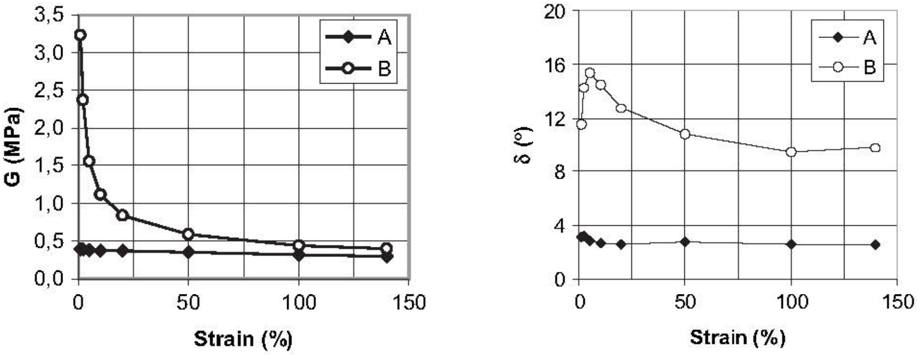

*a)* *b)*

*Fig. 3.22 Dynamic shear properties of rubbers A (unfilled) and B (filled) used for the RBRL devices in the ECOEST project. Rubber B shows Payne effect (from Guerreiro et al., 2007).*

this might be more evident, and could be managed with the pre-conditioning or “scragging” of the rubber to the maximum deformation not expected ever to be exceeded.

Despite these effects depending by strain amplitude, it is believed that the use of the linear viscoelastic theory to predict the response of an elastomeric isolator with non-linear behaviour, under steady-state conditions, is still adequate provided the parameters are chosen appropriately. Thus, for a given value of amplitude and frequency, the non-linear elastomeric isolator could be characterised by a Kelvin model calibrated through the equivalent linearized viscoelastic frequency-domain (ELVFD) parameters $K'$ and $K''$ (analogous to $G'$ and $G''$):

$$\begin{aligned} c &\equiv K''/\omega \\ k &\equiv K' \end{aligned} \tag{3.40}$$

In this case, the values of the parameters $c$ and $k$ must be changed if the amplitude or frequency is changed, since $K'$ and $K''$ are functions of these variables. It doesn’t exist a unique way of defining the equivalent linearized parameters, e.g. $|G^*|$ and $\delta$, being the loops not elliptical. Here below three alternative methods are presented and discussed (Ahmadi & Muhr, 1997).

- Secant method

This method defines $\left|G^*\right|$ as:

$$\left|G^*\right| = \tau_{peak} / \tilde{\gamma} \tag{3.41}$$

where $\tau_{peak}$ is the peak stress (see Fig. 3.23 a); Eq. (3.39) is then used to calculate $\sin\delta$.

- Harmonic method

This method consists in calculating the Fourier components of the periodic stress response at the fundamental frequency $\omega$:

$$\tau(t) = \tilde{\tau}_1 \sin(\omega t + \delta_1) + \tilde{\tau}_2 \sin(2\omega t + \delta_2) + \ldots \tag{3.42}$$

Only the first harmonic components are retained in the linearised model, so:

$$\left|G^*\right| = \tilde{\tau}_1 / \tilde{\gamma} \tag{3.43}$$

To calculate $\tilde{\tau}_1$ and so $\left|G^*\right|$ the following Fourier equations are used:

$$\begin{aligned} \tilde{\tau}_1 \cos\delta_1 &= \frac{\omega}{\pi} \oint \tau(t) \sin(\omega t) dt \\ \tilde{\tau}_1 \sin\delta_1 &= \frac{\omega}{\pi} \oint \tau(t) \cos(\omega t) dt \end{aligned} \tag{3.44}$$

which have to be resolve by numerical integration.

Similarly, the energy dissipated in one cycle is given by:

$$W_L = \oint \tau \, d\gamma = \oint \tau \, \tilde{\gamma} \, \omega \, \cos(\omega t) = \pi \tilde{\tau}_1 \tilde{\gamma} \sin\delta_1 \tag{3.45}$$

It is possible to observe that Eq. (3.45) is equivalent to Eq. (3.39), through Eq. (3.43), with $\sin\delta_1$ in place of $\sin\delta$. Therefore, to calculate $\left|G^*\right|$ and $\sin\delta_1$, two ways are possible: by calculating numerically both the Eqs. (3.44) or, one of these integrals together with the determination of $W_L$ by some other means.

- Skeleton curve method (or equivalent energy method)

At first the "skeleton curve" is constructed by taking the mean values of $\tau$ corresponding to increasing and decreasing $\gamma$ (see Fig. 3.23 b). Then, a straight line is derived such that the area under it, in the range $0 \le \gamma \le \tilde{\gamma}$, is equal to the one under the skeleton curve $W_S$. The value of $\left|G^*\right|$ is thus obtained as slope of this line, and so:

$$\left|G^*\right| = \frac{2W_S}{\tilde{\gamma}^2} \tag{3.46}$$

Eq. (3.39) has to be used to define $\sin\delta$.

It has been shown by Ahmadi & Muhr (1997) that the three linearisation methods described lead to differencies in the values of the equivalent linear viscoelastic frequency domain (ELVFD) parameters for filled rubber: the loss factor increases in the order "Skeleton > Harmonic > Secant", while the dynamic shear modulus increases in the reverse order.

Furthermore, Ahmadi & Muhr (1997) carried out some comparisons between the responses predicted from numerical integration of the equation of motion of an isolated mass using a proposed non-linear model and from equivalent linearisations of the non-linear model. It was observed that, for steady-state responses to sinusoidal excitations, all the three linearisation methods are satisfactory, in particular the Harmonic method. Differences are greater for transient responses, but, provided linearised parameters are chosen at appropriate strain levels, the differences are usually less than 20%.

In this thesis project only unfilled rubbers have been considered for the rolling tracks of the RBRL device. However, the basic concepts about viscoelastic linearization and ELVFD parameters have been presented because these will be used to described the global non-linear behaviour of the RBRL system for small displacements, where the stiffness and damping of the device highly depend on the deflection amplitude despite the unfilled rubber.

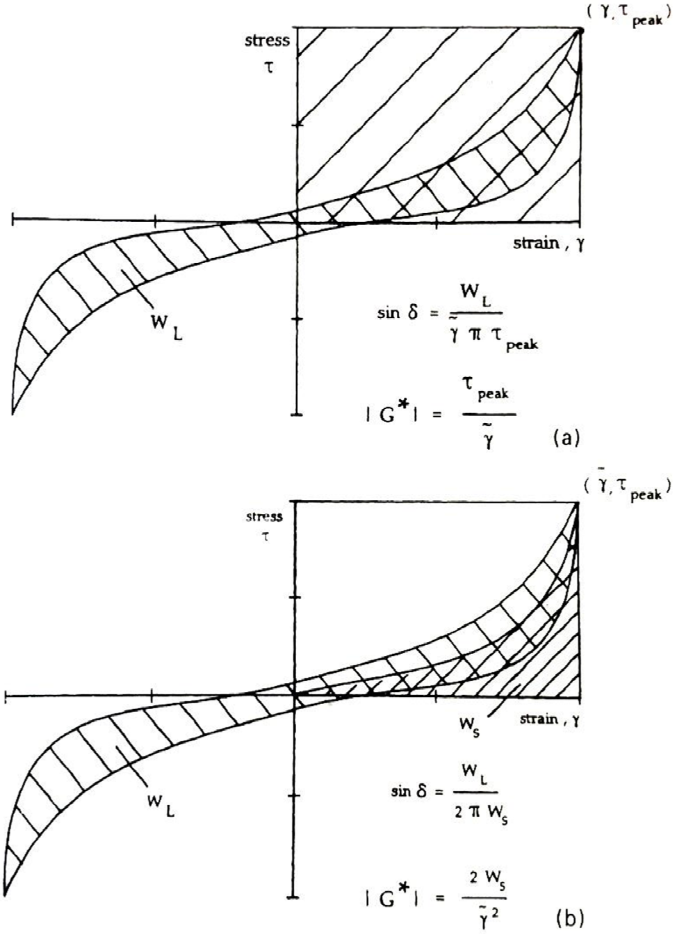

*Fig. 3.23 Hysteresis loops showing non-linear behaviour typical of filled rubber at high strain and illustrating: a) Secant method; b) Skeleton curve method (from Ahmadi & Muhr, 1997).*

## 3.3 Shortcomings and need of further researches

1- The project “Parametric Seismic Tests of Rolling_Ball Isolation System” funded under the ECOEST 2 Programme in 1999, or “ECOEST” project, involved 34 shaking table tests of an isolation system comprising 4 RBRL devices; 2 different mass configurations were tested, corresponding to either a rigid superstructure or one of the same mass and a single translational degree of freedom. Both sinusoidal imposed motions and natural or artificial earthquakes were applied on the table. The RBRL systems were realized with different types of rubber track (low (A) and high (B) damping types), and different geometries of the recentering rubber springs. The tests addressed the dependence of the system performance on its principal parameters. Large amounts of data were gathered from this project, but only a summary of the findings with a few highlights has so far appeared in the literature (Guerreiro et al., 2007). Thus, performing further numerical analyses on these experimental results seems appropriate. In particular, attention should be given to small-deflections behaviour of the system, influenced by the creation of pits in the rubber layer due to the viscoelastic properties of the rubber.

2- Further analyses using the Guerreiro model (Guerreiro et al., 2007) should be undertaken for verifying its goodness in prediction of the RBRL system behaviour. Albeit this model was proved to work sufficiently well for relatively big deflections of the device, for small displacements it is still to verify. Moreover, the approach used to describe the effects of initial indentation is not based on a viscoelastic framework, as would be expected to be appropriate from a device made of rubber, and as presented by Muhr & Bergamo (2010).

3- The rolling friction theory of Muhr et al. (1997) could be very useful for predicting the adimensional rolling resistance of steel balls, under a vertical load, on steel tracks covered with a thin rubber layer. However, a parametric experimentation is needed to prove its usefulness. This theory could be important at two different levels: one more general, related to technological research in the rubber field, and one more specific, associated with modelling of the rolling force in steady-state conditions for the RBRL system with a view to the design of RBRL isolators.

4- For design purposes, the main parameters of the RBRL system are the steady-state rolling force and, obviously, the stiffness of the recentering rubber springs. Because of their non-linear behaviour, these rubber springs require characterization tests to verify and complete the information already available in the related literature (Guerreiro et al., 2007). This knowledge is needed for the correct design of the isolation system as well as for calibration of a possible time-domain model.

5- Another issue to be deepened is associated with the definition of a general design procedure for the RBRL isolation system. In particular, a method leading to the determination of all the system parameters, starting from chosen values of isolation period and damping ratio and for a specific design spectrum and vertical load, should be investigated. This procedure could be based on the one proposed by Cook et al. (1997), but refined and made more comprehensive.

6- Finally, further studies are required for a better characterization of the system behaviour for small deflections, focusing on the rocking of the balls inside their pits and on the rolling of the balls in the transition phase between their roll-out from the pits and their steady-state rolling behaviour. Parametric tests are thus necessary to get sufficiently comprehensive data on the small-deflections behaviour of the system, and to enable the proposal of an appropriate time-domain model for quantifying the system efficacy through time-history analyses. In this characterization phase, simple monoaxial sinusoidal tests may be preferable to biaxial ones or shaking table tests, which may be too complicated for the aim.

# 4 NUMERICAL ANALYSES OF ECOEST PROJECT RESULTS AND APPLICATIONS OF ELVFD REPRESENTATION

## 4.1 Introduction

Some numerical analyses, including also Time-History simulations in OpenSees, are presented starting from the results of the ECOEST Project, an extensive experimental study on the RBRL system involving diverse shaking-table tests (Guerreiro et al., 2007). The purpose is to investigate the performance of the RBRL device, particularly for the small-deflections behaviour.

The characteristics of the RBRL seismic isolation system are shown through results for force versus displacement, covering a range of amplitudes and varying sinusoidally with time, and through results for the acceleration and drift of the upper slab of an isolated model SDOF superstructure subjected to seismic excitations (see the “Mass Up configuration” presented in section 4.2).

It is shown how these characteristics may be described approximately by equivalent linear viscoelastic parameters $K^{/}$ and $K^{//}$, or alternatively $K^*$ and $\delta$, these being functions of frequency and amplitude. This may be thought of as a frequency-domain approach.

Alternatively, the same characteristics may be described approximately using a non-linear time domain model, and two alternative ones are assessed here. The first has been presented previously (Guerreiro et al., 2007), and a new one is presented for the first time. An objective way of comparing the accuracy of such time domain models is to compare the equivalent linear viscoelastic parameters extracted from their predictions for sinusoidal excitations, and this reveals that the new model agrees considerably better with the directly measured behaviour of the actual system.

The system is very versatile, a great range of equivalent natural frequencies and coefficients of damping being achievable through the independent choice of rubber spring and rubber rolling track layer. It is suitable for isolating light structures, and much more effective at low excitations than an equivalent sliding system would be.

## 4.2 Advantageous small-deflections behaviour of RBRL system

The model superstructure in the ECOEST project (Guerreiro et al., 2007) consisted of two concrete slabs which could either be clamped together as in Fig. 4.1 a) (Mass Down configuration) or separated by four M16 studs 500 mm long, as in Fig. 4.1 b), to give a first mode fixed base response at ~2.5 Hz (Mass Up configuration). Both the configurations, isolated on the RBRL system, were subjected to a range of acceleration time histories. The results recorded (see Fig. 4.2 a) consist of relative displacements, between the bottom slab and the shaking table and between the two slabs, and of absolute accelerations of table, bottom slab and top slab.

ECOEST data for the Mass Up configuration (Fig. 4.2 a), for peak accelerations of the shaking table, lower and upper slab, and for the drift between the slabs, were compared to results from OpenSees simulations of the relative “fixed-base” case (Fig. 4.2 b).

The time histories were truncated in this exercise such that steady-state rolling of the balls did not occur, but they merely rocked in the “pits” formed in the rubber tracks due to creep in the rubber for the period under static load. The maximum displacement of the lower mass relative to the table for this to be so, was taken in this exercise to be 5 mm. The measured table accelerations were used in the OpenSees simulations, rather than the command time histories, to make the comparison as close as possible. The fixed-base case represents also the behaviour of a sliding isolation system, for excitations insufficient to overcome the static friction.

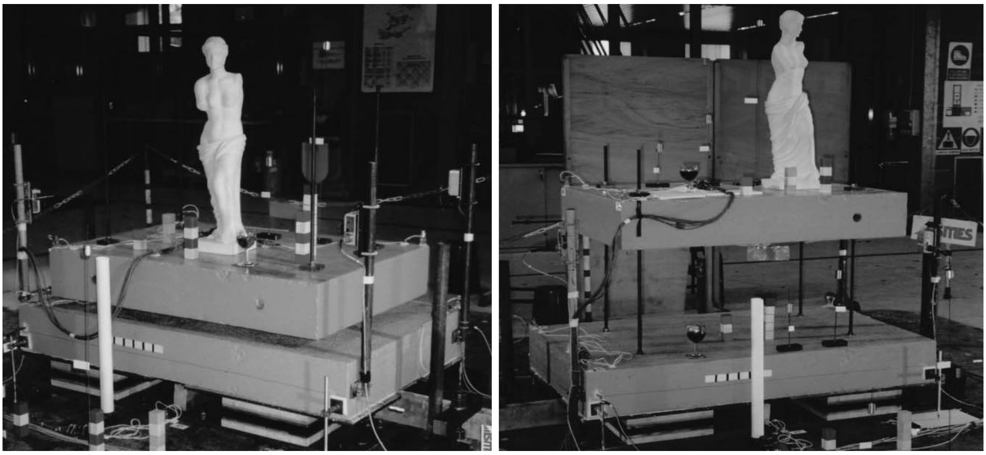

a) b)

*Fig. 4.1 a) View of the two test set-ups used in the ECOEST experimentation: a) Mass Down and b) Mass Up configuration (from Guerreiro et al., 2007).*

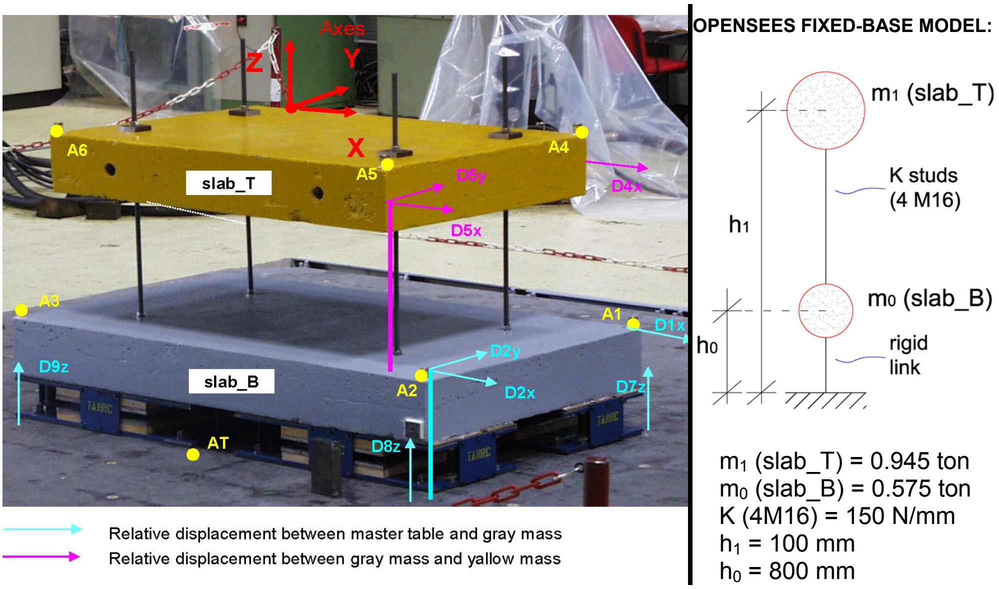
Axes
Z
Y
X
A6
A5
A4
slab_T
D5y
D4x
D5x
A3
A1
D1x
D2y
D9z
slab_B
A2
D2x
D7z
AT
D8z
Relative displacement between master table and gray mass
Relative displacement between gray mass and yallow mass
OPENSEES FIXED-BASE MODEL:
m1 (slab_T)
K studs (4 M16)
h1
m0 (slab_B)
rigid link
h0

$m_1$ (slab_T) = 0.945 ton
$m_0$ (slab_B) = 0.575 ton
K (4M16) = 150 N/mm
$h_1$ = 100 mm
$h_0$ = 800 mm

a) b)

*Fig. 4.2 a) Mass Up configuration with indication of the transducers (A = accelerations; D = displacements). b) Relative fixed-base model analyzed in OpenSees for comparisons.*

The earthquakes considered were: Northridge_PCKC, Tolmezzo, Faial, EC8(05) and EC8(02) (see Fig. 4.3). Artificial records were used for EC(02) and EC(05) earthquakes, according to Eurocode 8 (Soil type B, $\zeta$ =5%): (02) and (05) signify that the original records were applied with low frequency cut-offs of 0.2 and 0.5 Hz respectively because of the maximum displacement limitation of the table (±100mm). For each case, the original record with a given peak ground accelerations ($PGA_0$) was scaled to different PGA levels through the parameter K[dB] = 20·log· ($PGA/PGA_0$) to get a certain range of seismic intensities. The results obtained considering these acceleration time series are presented in Fig. 4.4 to Fig. 4.8, whose captions report the values of K considered for each earthquake. The low damping rubber, type A, was used for both the rolling tracks of the devices in all the tests here considered, except for the earthquake EC8(02) where the device presented one layer of rubber A and one of high damping rubber B (for more details see Guerreiro et al., 2007). For all the earthquakes analysed, the conclusions are the same: the compliance and damping at small excitations has the great advantage of both changing the mode shape and suppressing excitation of the vibration modes of the isolated structure even for small seismic intensities, in contrast to the case of sliding bearings below their threshold force.

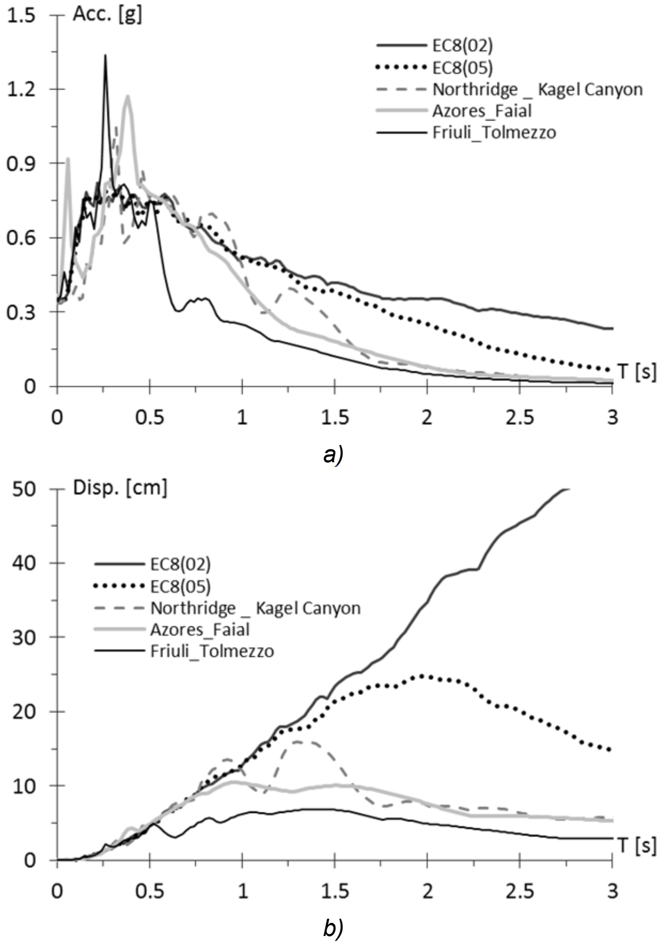

*a)*

*b)*

*Fig. 4.3 a) Acceleration and b) displacement response spectra of the ground motion selected for the tests with Mass Up configuration, as recorded at the table ( $\zeta$ = 5%).*

The parameters compared in the graphs from Fig. 4.4 to Fig. 4.8 are:

- for the real isolated system, by ECOEST results:
  - a [g] table = accel. of the shaking table;
  - a [g] slab_B = accel. of the bottom slab;
  - a [g] slab_T = accel. of the top slab;
  - Θ[%] Isolated = drift between the slabs as % of their separation
- for the fixed-base system, by OpenSees simulations:
  - a [g] table = accel. of the shaking table;
  - a [g] slab_T_Fixed = accel. of the top slab;
  - Θ[%] Fixed = drift between the slabs as % of their separation

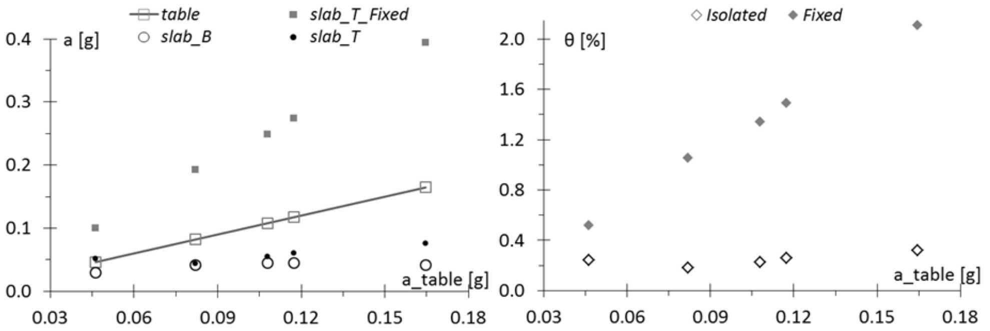

*a)* *b)*

*Fig. 4.4 a) Top("T")-bottom("B") slab accelerations a[g] and b) drifts θ [%] between the two slabs versus peak table acceleration from ECOEST results, for the isolated-base case, compared with the simulated fixed-base case ("Fixed") (≈ sliding isolator for small seismic intensity), for Northridge_PCKC different-scaled earthquakes (K= -12, -6, -4, -3, 0 dB).*

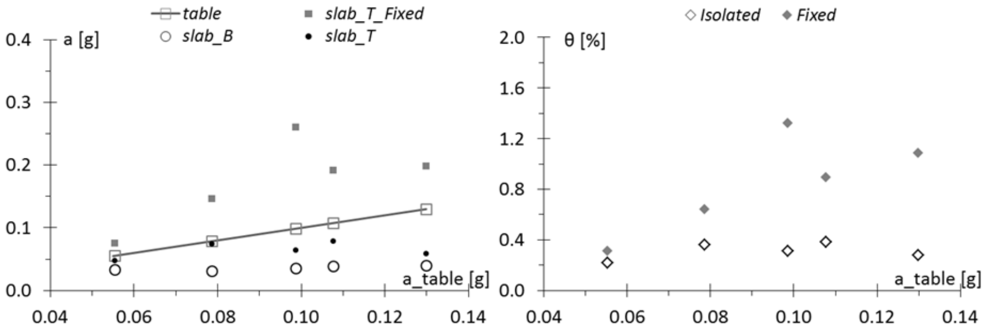

*a)* *b)*

*Fig. 4.5 As Fig. 4.4, for Tolmezzo different-scaled earthquakes (K= -12, -6, 0, +3, +5 dB).*

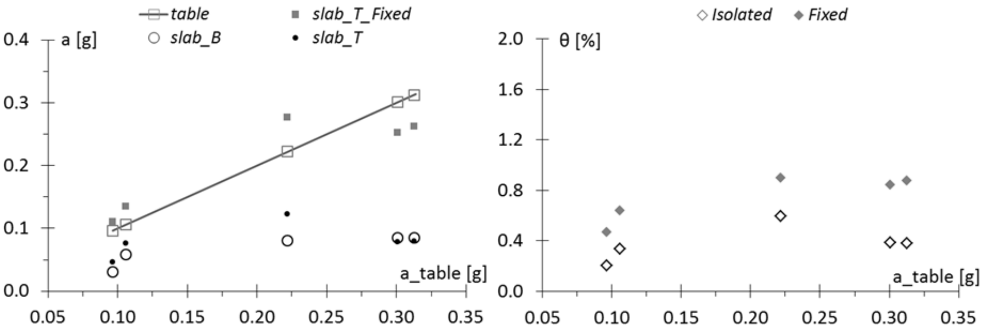

*a)* *b)*

*Fig. 4.6 As Fig. 4.4, for Faial different-scaled earthquakes (K= -12, -6, 0, +3, +3 dB).*

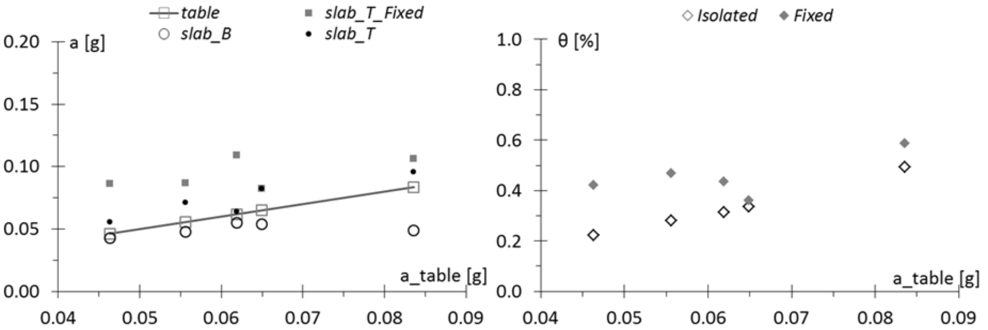

*a)* *b)*

*Fig. 4.7 As Fig. 4.4, for EC8(05) different-scaled earthquakes (K= -15, -12, -9, -6, -3 dB).*

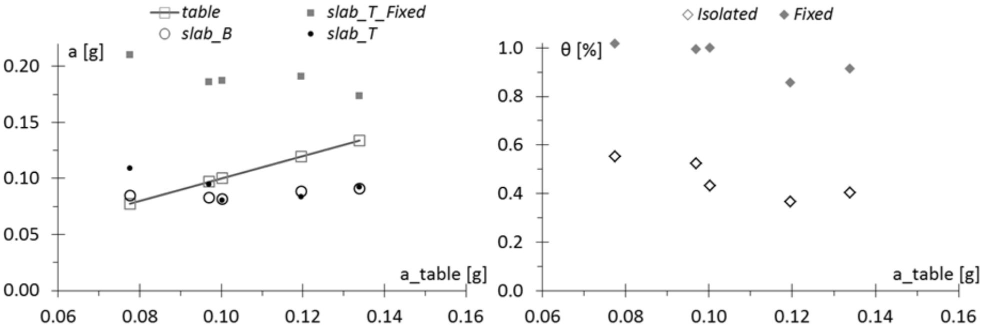

*a)* *b)*

*Fig. 4.8 As Fig. 4.4, for EC8(02) different-scaled earthquakes (K= -12, -9, -9, -7, -6 dB). For these tests a combination of rolling tracks A (low damping) – B (high damping) was used.*

## 4.3 ELVFD representation of system behaviour from ECOEST tests

The force-deflection behaviour of the RBRL system is controlled by rubber properties, either through the rubber springs, which predominantly provide the restoring force, or through the rubber layers on the tracks, which provide energy dissipation but also, for small oscillations, contribute to the restoring force. The resulting overall behaviour is thus non-linear and originates from viscoelasticity, so it is natural to consider a description in terms of equivalent linearized viscoelastic parameters. The viscoelastic parameters we shall use are the storage and loss stiffnesses, $K^{/}$ and $K^{//}$, respectively, defined as the in- and out-of-phase amplitudes of steady-state harmonic force required to impose a harmonic displacement of unit amplitude:

$$\begin{aligned} x(t) &= \tilde{x} \cdot \sin(\omega t) \\ f(t) &= \tilde{x} \cdot (K^{/} \sin(\omega t) + K^{//} \cos(\omega t)) \end{aligned} \tag{4.1}$$

Sometimes the complex stiffness $K^{*} = \sqrt{K^{/2} + K^{//2}}$ and loss factor $\tan\delta = K^{//} / K^{/}$ are used instead.

If we consider a Kelvin model (spring $k$ and dashpot $c$ in parallel) then we have:

$$\begin{aligned} x(t) &= \tilde{x} \cdot \sin(\omega t) \\ f(t) &= \tilde{x} \cdot (k \sin(\omega t) + c\omega \cos(\omega t)) \end{aligned} \tag{4.2}$$

so it is apparent that $k \equiv K^{/}$ and $c \equiv K^{//} / \omega$. This implies that if $K^{/}$ and $K^{//}$ are independent of frequency then the equivalent Kelvin parameter $c$ is inversely proportional to frequency. For a typical rubber a better approximation of the behaviour is found to be that $K^{/}$ and $K^{//}$ are both linearly dependent on $\ln(\omega)$, so that they do have a weak frequency dependence which may be neglected for limited ranges. We shall refer to the frequency $\omega_{ch}$ at which $K^{/}$ and $K^{//}$ are measured as the characterisation frequency, and the frequency $\omega$ at which (say) the Kelvin model is used to be the application frequency. The coefficient of critical damping of a mass $m$ mounted on a Kelvin model is:

$$\zeta = \frac{c}{2m\nu} \equiv \frac{1}{2} \tan\delta \frac{\nu}{\omega} \tag{4.3}$$

where $\nu = \sqrt{k/m}$ is the undamped natural frequency.

Seismic isolation systems are generally excited at their natural frequency, so we have $\zeta \approx 1/2 \cdot tan\delta$ and, for an equivalent Kelvin model for an isolation system, $c = tan\delta \cdot K^{/} / \nu$ .

Calculation methods for the equivalent viscoelastic parameters have been presented by Ahmadi and Muhr (1997) and reported in the section 3.2 of this thesis. Here, the Harmonic Method is used, which corresponds to calculation of the Fourier components of the periodic force at the fundamental frequency $\omega$. The parameters may be converted to the equivalent Kelvin model, if a time domain model is needed, provided the frequencies of the responses to be predicted are within a factor of 10 or so of that at which $K^{/}$ and $K^{//}$ were characterised. A more sophisticated viscoelastic model consisting of a spectrum of Maxwell elements is required to capture the linear dependence of $K^{/}$ and $K^{//}$ on $\ln(\omega)$, as discussed for example by Ahmadi et al. (2008) and Ahmadi & Muhr (2011).

Results for $K^{/}$ and $K^{//}$ for tests on the rolling tracks AA obtained performing shaking table tests at 5 Hz on a rigid mass placed on the RBRL isolators with the recentering springs, in the ECOEST project, are given in Fig. 4.9. It is evident that the parameters depend on the amplitude of motion, showing the properties are non-linear, despite the equivalent linearization. This, however, does not prevent the parameters being useful, as discussed by Ahmadi & Muhr (2011). Firstly, they can be used to provide a time-domain Kelvin model for seismic response; iterations are required in which the peak amplitude is predicted by the model, from which fresh values of $K^{/}$ and $K^{//}$ can be calculated and hence the Kelvin model updated and rerun to update the prediction of amplitude. Convergence is usually found to be very rapid, e.g. only 2 or 3 iterations are required to reach a peak amplitude consistent with that used to determine $K^{/}$ and $K^{//}$. Secondly, the equivalent viscoelastic parameters enable different non-linear time-domain models for the system to be compared quantitatively and objectively with the real behaviour, by comparing directly measured parameters with those extracted – using the same Harmonic Method – from hysteresis loops simulated using the models. The parameters themselves correspond to representations of the hysteresis loops as ellipses, as illustrated in Fig. 4.10. This figure compares results for force directly obtained from the mass acceleration using Newton’s second law, plotted against the relative displacement measured across the isolation system, with loops plotted for a Kelvin representation of the equivalent viscoelastic parameters over a range of amplitudes.

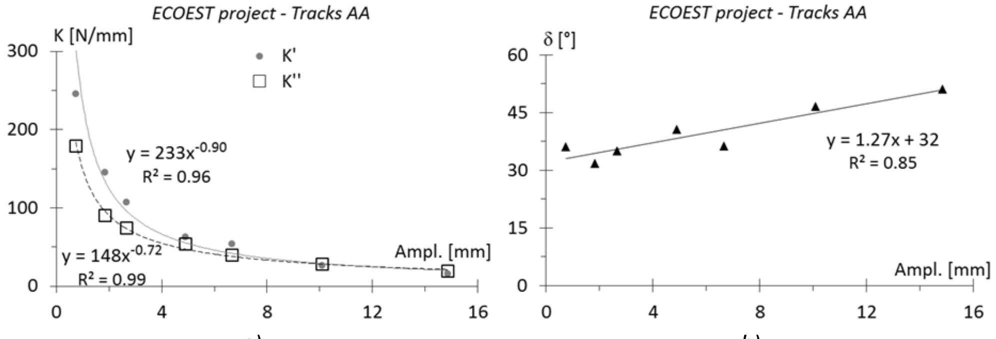

a) b)

*Fig. 4.9 Equivalent linear viscoelastic parameters obtained from ECOEST sinusoidal tests at 5Hz: a) $K^{/}$ $K^{//}$, b) δ.*

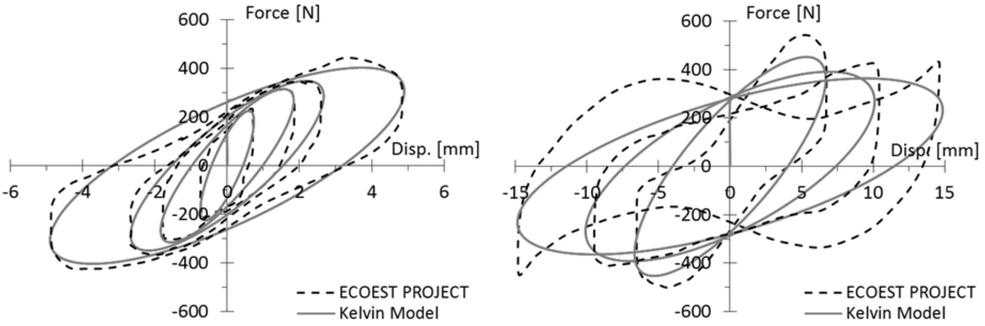

a) b)

*Fig. 4.10 Force-displacement loops obtained for AA tracks during the ECOEST project and compared with equivalent linear viscoelastic representations a) amplitudes up to 5 mm b) amplitudes up to 15 mm.*

## 4.4 Guerreiro Model performance through ELVFD representation

As shown by Guerreiro et al. (2007), the Guerreiro model (see Section 3.1.3) gives reasonably good predictions of response in moderately large seismic events, for which the steady-state rolling of the isolation system is involved.

Here we report a new comparison for the NorthridgePCKC earthquake. Fig. 4.11 compares predictions of the model with results from the ECOEST project for the acceleration obtained for the case of isolated base: “mass-up” configuration (2 DOF) for the time histories NorthridgePCKC not scaled (0 dB) and scaled with (-12 dB). For Fig. 4.11 a) the amplitude is generally relatively high and the model works well, but for Fig. 4.11 b) amplitude is smaller and the model is less good.

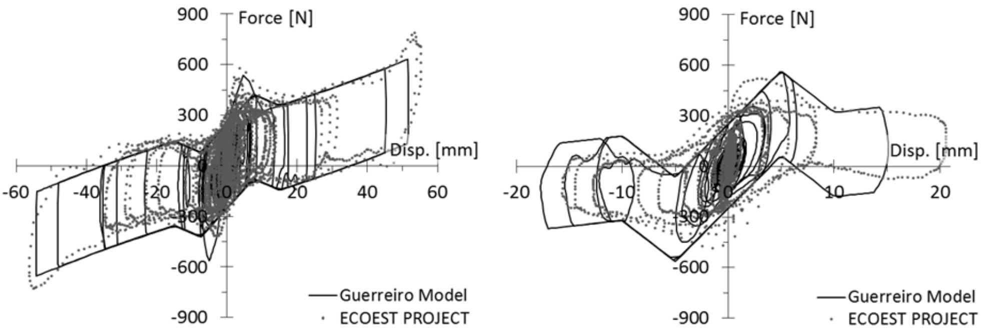

*a)* *b)*

*Fig. 4.11 Comparison of directly measured and modelled force-displacement plots for NorthridgePCKC: a) 0 dB; b) –12 dB.*

To illustrate the performance of that model, a parametric sinusoidal analysis was performed, from which the values of the equivalent viscoelastic parameters were calculated. The analyses covered amplitudes from 1 mm to 20 mm, in steps of 1mm, and then up to 50 mm in steps of 5 mm, and the frequencies 0.1, 0.5, 1.0, 2.5 and 5.0 Hz. Fig. 4.12 gives selected sinusoidal force-displacement loops obtained from the analyses and Fig. 4.13 gives $K'$ and $K''$ values as functions of amplitude for all the amplitudes and frequencies analysed.

It is evident that there is a very high frequency dependence of the behaviour of the Guerreiro model for small amplitudes, substantially with regard to the dissipation of energy (see Fig. 4.13 b), which would not be expected to be the case for a system based on rubber. In addition, the shape of the loops at moderate amplitudes does not bear even much qualitative resemblance to the experimental loops, shown in Fig. 4.10. We would like to emphasize that the most frequent earthquakes are characterized by a “small displacement response”: so the design (ULS) spectra is not the only for which good performance of the anti-seismic device is required (at least for the protection of sensible lightweight structures, such as artefacts, statues and sensitive industrial or medical equipment).

Although the Guerreiro model works quite well for high amplitudes (see Fig. 4.11 a), it was decided to evolve a more realistic uniaxial model, to better capture the low and moderate amplitude behaviour, before attempting generalisation to the biaxial case. A new simpler and no-updating model could be also useful in the design process to speedily get the best isolation solution.

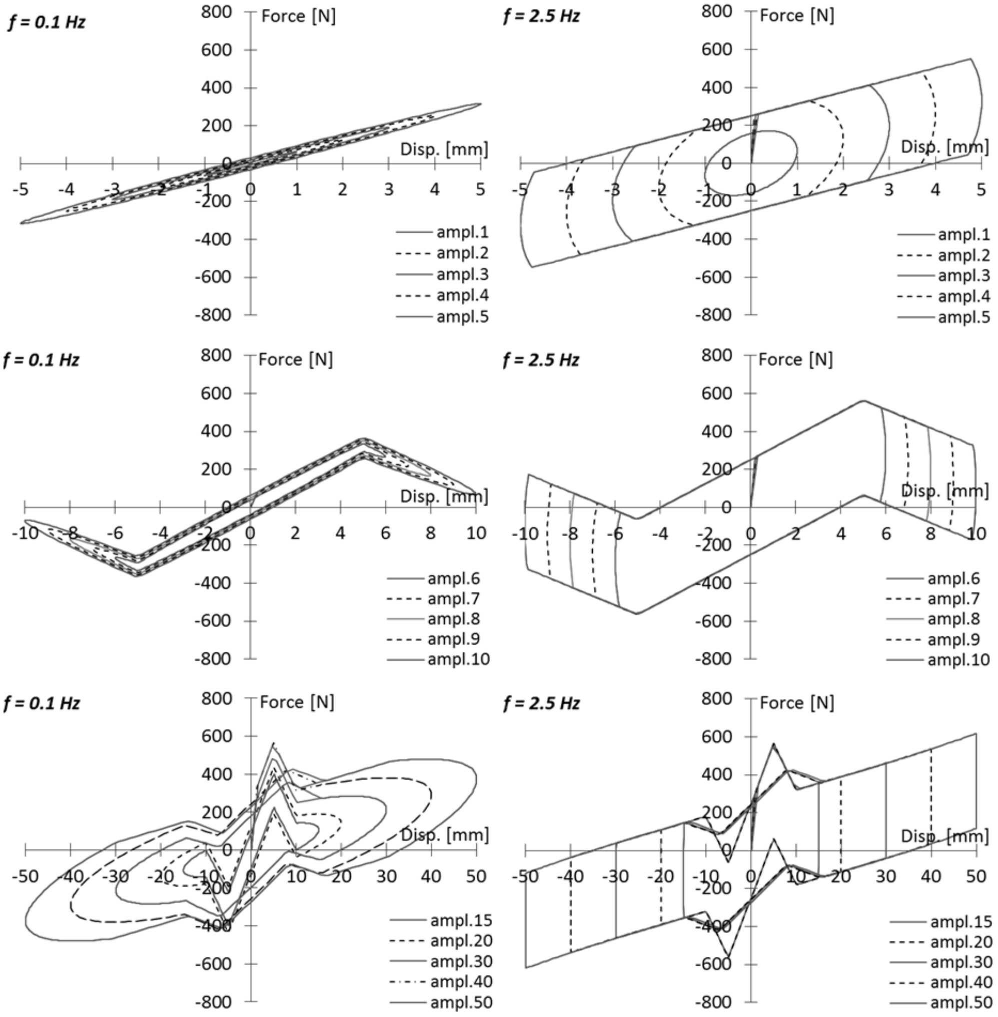

*Fig. 4.12 Force-disp. loops from Guerreiro model for selected amplitudes and frequencies.*

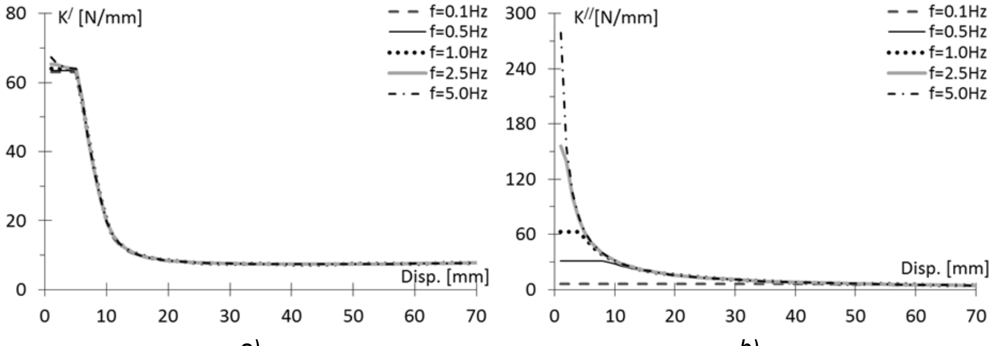

*a)* *b)*

*Fig. 4.13 a) $K^{/}$, b) $K^{//}$ from the Guerreiro model for all the amplitudes and frequencies analysed.*

## 4.5 Proposal of a simplified model based on ELVFD representation

The intention was to devise a model that would be efficient to program and to run in simulation software, hence ideally not involving any internal parameters that call for updating during analyses. The model uses a viscoelastic framework for describing the restoring force and energy dissipation in accord with their origins in rubber, and should ideally be straightforward to generalise in a natural way to the biaxial case.

Fig. 4.14 gives a schematic diagram of the model. A simple characteristic is provided for the rubber spring. The resistance to steady rolling over the rubber tracks is, as for the Guerreiro model, considered to be a constant force, and is introduced in series with the Kelvin model that represents the amplitude-dependent behaviour for small deflections, caused by the indentations formed by the balls in the rubber track due to the time under static load. Although this model is simple and does not call for updating of parameters, it has to be used iteratively for a time-history analysis to capture the real behaviour for small amplitudes. The value of the Kelvin model parameters ($k_1$, $c_1$) are changed in accord with the new values of $K^{/}$ and $K^{//}$ obtained by interpolating equations given in Fig. 4.9 a) for the new amplitude value resulting from the previous run of the model.

The model is simple to calibrate, because the three behaviours - recentering spring, pit and steady-state rolling - are independently represented. The values of the equivalent viscoelastic parameters for the recentering rubber springs, $K^{/}_2$ = 8 Nmm$^{-1}$ and $K^{//}_2$ = 0.4 Nmm$^{-1}$, and the fuse force, $f$ = 250 N, are directly obtained by experimental results performed in the ECOEST project. The $f$ (fuse) parameter could be obtained also from the theory about rolling friction coefficient for the rolling on a finite thickness layer of rubber (Muhr et al., 1997). $K^{/}_1$ and $K^{//}_1$, equivalent viscoelastic parameters for the behaviour in the pit, are obtained in accord with the Eqs. (4.4) considering that $K^{/}$ and $K^{//}$, from the ECOEST results reported before, are related to the global behaviour of the RBRL device together with the recentering rubber springs.

$$\begin{aligned} K^{/}{}_1 &= K^{/} - K^{/}{}_2 \\ K^{//}{}_1 &= K^{//} - K^{//}{}_2 \end{aligned} \qquad (4.4)$$

Once the equivalent viscoelastic parameters are known ($K^{/}_1$, $K^{//}_1$, $K^{/}_2$, $K^{//}_2$), the relative Kelvin parameters ($k_1$, $c_1$, $k_2$, $c_2$) are calculated through the relations (4.5).

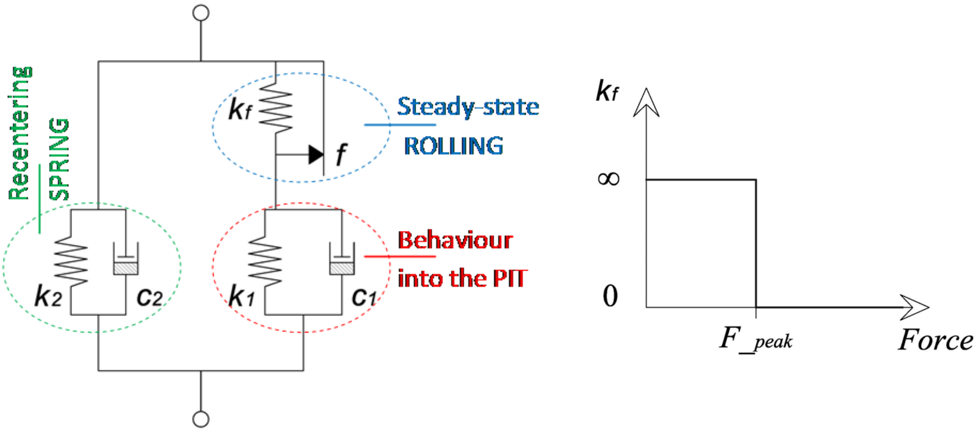

*Fig. 4.14 Author' proposal for a new simple "no-updating" model.*

$$\begin{aligned} k &\equiv K^{/} \\ c &\equiv K^{//}/\omega \end{aligned} \tag{4.5}$$

The $F_{\_peak}$ value is the maximum force that can be absorbed by the Kelvin model representing the in-pit behaviour after which the fuse modelling the steady-state rolling is activated. The value of $F_{\_peak}$ = 400 N was opportunely assumed, from experimental results, to capture the change in the global model behaviour (from two Kelvin models in parallel to one Kelvin model in parallel with a fuse) during the transition phase of the RBRL device. To also simplify the model and ensure the model switches to the fuse behaviour for the relatively big amplitudes, the values of $K^{/}$ and $K^{//}$ calculated for an amplitude of 15 mm are assumed to also hold for amplitudes greater than 15 mm.

The same parametric sinusoidal analysis as performed for the Guerreiro model was performed for the new model, and is reported in Fig. 4.15. The only assumption made is that the values of $K^{/}$ and $K^{//}$ are not significantly dependent on the frequency (or velocity), thus we used the equivalent viscoelastic parameters obtained by ECOEST results for 5 Hz (Fig. 4.9 a) for all the different frequencies analysed. This was confirmed by the new monoaxial-sinusoidal tests performed and presented in the following chapters.

The hysteresis loops, with this new model, seem more similar to the real ones for the small amplitudes (Fig. 4.10). Being a simple model, although it is able to represent the real behaviour for the small amplitudes and for the steady rolling with a sufficient approximation, it is not able to capture the return of the balls into the original indentations (as in Guerreiro model), or the complicated behaviour in the transition between the small strain behaviour and free rolling.

Following, in Fig. 4.16, the comparison of the equivalent linearized viscoelastic parameters, calculated by the parametric sinusoidal analysis performed using the Guerreiro and the author model, and by the sinusoidal tests of the ECOEST project, is reported for different sinusoidal amplitudes.

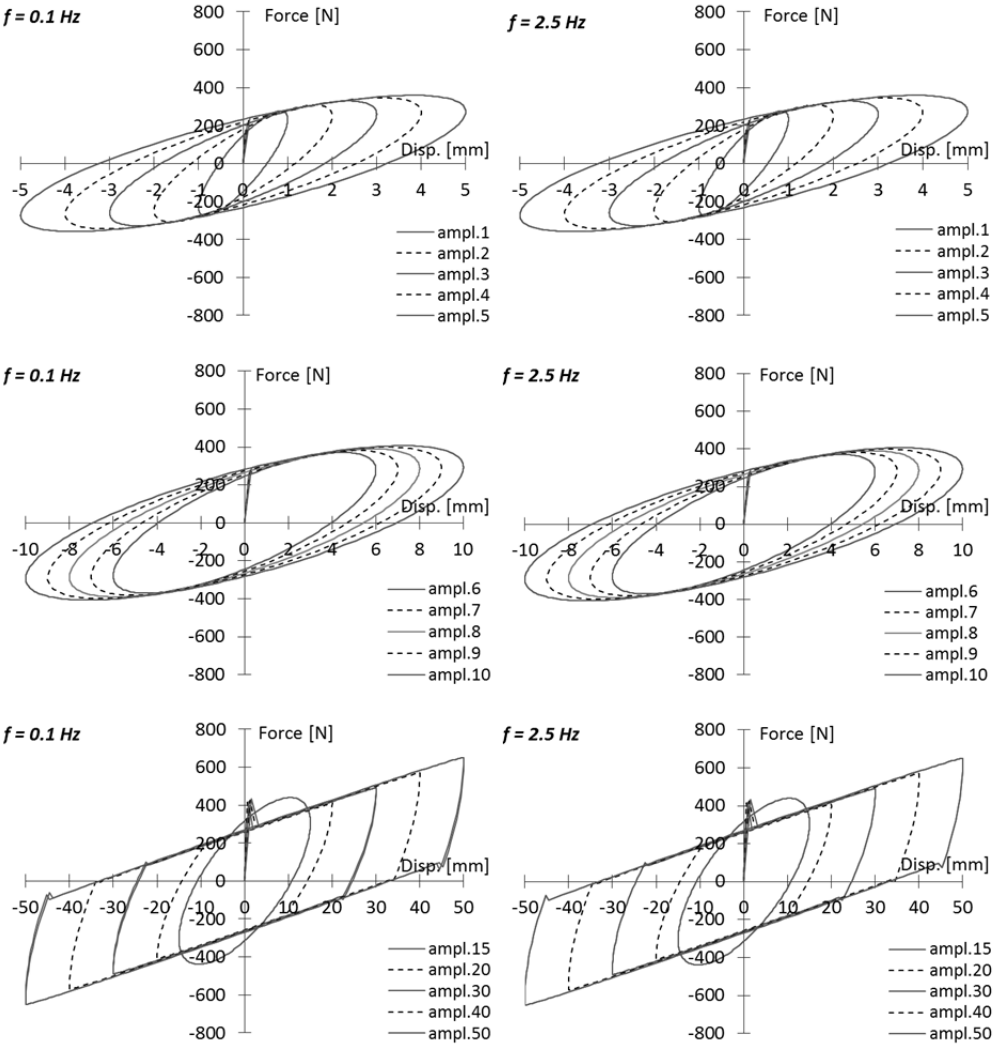

*Fig. 4.15 Force-disp. loops from author model for selected amplitudes and frequencies.*

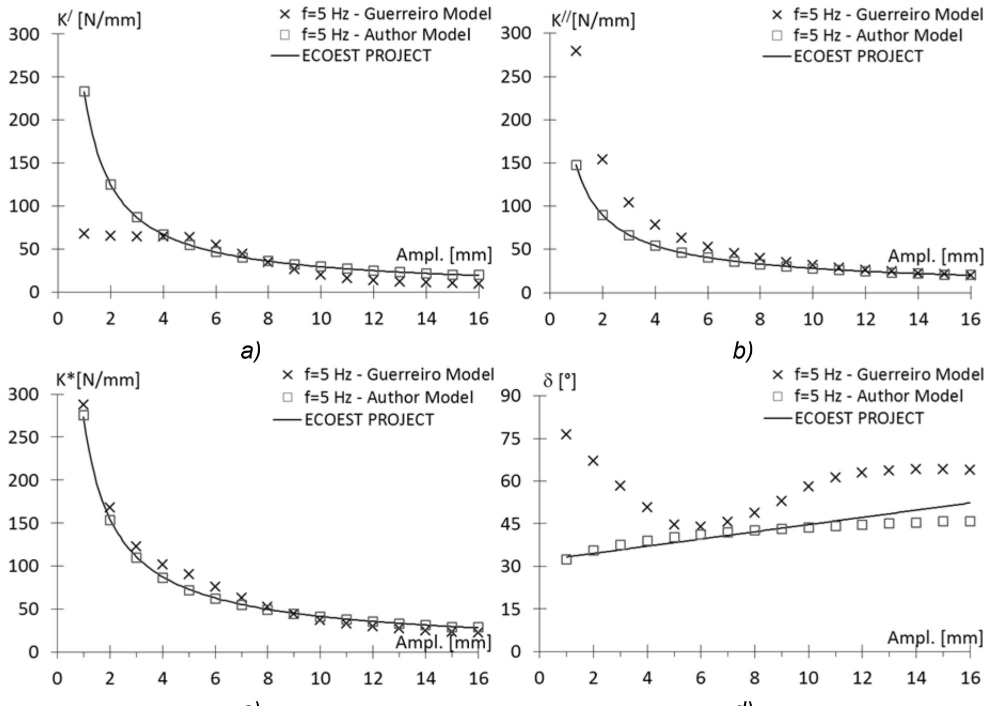

*a)* *b)*

*c)* *d)*

*Fig. 4.16 Comparison of the ELVFD parameters, which describe the non-linear dynamic behaviour of the RBRL device, calculated by Guerreiro Model, Author Model and sinusoidal tests of the ECOEST project for different sinusoidal amplitudes: a) storage stiffness $K^{/}$; b) loss stiffness $K^{//}$; c) complex stiffness K*; d) loss angle δ.*

## 4.6 Conclusions

1- The ECOEST (1999) results confirm that the RBRL isolation system provides very effective reduction of excitation of the first mode of the isolated structure for small seismic events, for a wide range of frequency content, despite its being very much stiffer when the deflections across the isolators are small (< 5mm). The primary factor responsible is probably the very high damping, together with the changed mode shape resulting from the compliance of the isolators, although the non-linear behaviour may also be significant.

2- For larger seismic excitations the system was shown earlier to perform very well (Guerreiro et al., 2007), as expected from an isolation system that offers good scope in choice of period and damping.

3- Equivalent linearized viscoelastic frequency-domain (ELVFD) parameters and force-displacement loops have been used to compare the properties of the actual RBRL system with two different time-domain models. An error in Fig. 9 of Guerreiro et al. (2007) has been identified; the experimental data actually gives 10 times the stiffness values reported there.

4- A new simplified time-domain model is presented, which gives a better representation of the behaviour of the RBRL system than the Guerreiro model. Being a simple model, it is able to represent with a sufficient approximation the real behaviour for the very small amplitudes (when balls rock inside their pits) and the steady-state rolling (when balls rolled-out from their initial indentations), but it is not able to capture other effects such as the return of the balls into their original pits (which is captured by the Guerreiro model), or the complicated behaviour in the transition phase between small-strain and free-rolling behaviours, although less important. It is based on the ELVFD parameters and requires 2 or 3 iterations for the prediction of the small deflection behaviour, through the value updating of these parameters, because of the non-linear viscoelastic behaviour inside the pit. The choice to use a Kelvin model and not a Solid Linear Standard (SLS) model or more complicated viscoelastic models is due to simplicity in calibration and use of this RBRL model, which represents also a conceptual model. Furthermore, if the seismic excitation is able to make the balls roll out from their pits for most of the earthquake, the dynamic behaviour of the RBRL isolation system can be sufficiently predicted considering only the rolling friction and the stiffness of the recentering springs, without any iterations, since the return of the balls into their original pits should be unlikely considering the real effects of an earthquake, which would be biaxial rather than uniaxial.

5- To better describe the global dynamic behaviour of the RBRL system, through a more comprehensive and generalizable time-domain model (not calibrated only on a specific test), further experimentations are required. In particular, investigation should regard the calculation of the rolling force based on the parameters of the device, and the small displacements of the system, both inside their pits and in the transition phase to the free rolling. Performing of parametric experimentations changing the principal parameters of the device, as well as the rubber type, seems the correct approach for investigating these aspects. These new experimental studies will be presented in the following chapters.

# 5 PARAMETRIC CHARACTERIZATION TESTS ON RBRL SYSTEM: PROPOSAL OF A GENERAL DESIGN PROCEDURE

## 5.1 Introduction

The objective is to get an effective and simplified design procedure for the non-linear RBRL system. The rolling friction theory of Muhr et al. (1997) could be very useful for predicting the steady-state rolling force, but a parametric experimentation on the RBRL device is desirable to verify its efficacy. In this characterization phase, simple monoaxial sinusoidal tests could be preferred to biaxial ones or shaking table tests, that may be too complicated for the aim.

For design purposes, the main performance parameters are the steady-state rolling force and, obviously, the stiffness of the recentering rubber springs. So, in addition to the experimentation regarding the device behaviour for the steady-state rolling, with the aim to check the usefulness of the theory of Muhr et al. (1997), another parametric test programme on the recentering rubber springs is herein presented.

Tests for the steady-state rolling have been carried out changing the principal device parameters that control behaviour, i.e. the rubber compound, the thickness of the rubber layers, the ball diameter and the stress parameter per ball. Before starting, some characterization tests have been executed to get the dynamic properties of the rubber compounds used in the tests; this was essential for the correct design of the following experimentations. In particular, tests involved three different rubber compounds, mainly to have the possibility to verify the Muhr et al. theory (1997) even for different materials (also because of the uncertainty about the rubber hysteresis parameter $\alpha$ ). From the ECOEST project tests (Guerreiro et al., 2007) it was concluded that it is unnecessary to use a thick layer of a high-damping rubber compound (type B) for the tracks to get the appropriate energy dissipation ratio for the RBRL system, but it is advantageous to use a correct low value of the stiffness of the rubber recentering springs and a rubber compound with appropriate damping and a high stress capability (type A). Moreover the compound A exhibits $G$ (shear modulus), $\delta$ (loss angle) and $\alpha$ (hysteresis parameter) values which are independent of the input strain level, so they are easy to define to design the tests, differently from the compound B for which $G$ , $\delta$ and $\alpha$ depend on strain amplitude (typical of filled rubber). Compound A, finally, allows to use a higher value of the stress parameter per ball without the generation of deep semi-permanent rolling tracks. For all these reasons the rubber compounds designed and produced at TARRC, for the new parametric experimentation, are:

- compound “A”, the same of ECOEST project experimentation;
- compound “A+”, a bit stiffer than the compound A;
- compound “A-” , a bit softer than the compound A.

The characterization tests on the rubber compounds are reported below.

As well as the rubber compounds, the RBRL devices were realized at TARRC’s engineering laboratory. The principal realization phases of the devices are listed below (see Fig. 5.1).

1. Production of the raw rubber sheets. (a)
2. Preparation of the steel plate surfaces by sandblasting and cleaning with degreasing agent. (b)
3. Painting of the steel plate surfaces with Chemlok_220 as bonding agent. (c)
4. Preparation of small rubber sheets (10 x 10 inches) of wanted thickness (1.5, 2, 3 mm) in a sufficient number to cover all the steel plate (38 x 38 cm) by using a manual press, for a time of ~ 1 minute at a temperature of ~ 80°C. The rubber surfaces were moulded against Mylar (polyester film) to produce a smooth surface profile and to keep it clean. (c)
5. Covering of the steel plates with the previous small rubber sheets, using sufficient rubber with respect to the mould cavity volume to compensate for any possible spillage of the rubber during the next phase. (c)
6. Curing of the rubber tracks by using an automatic press at ~ 140°C for ~ 45 minutes. The bonding was achieved during vulcanisation because of the presence of Chemlok_220. (d)

7. Preparation of the rubber tracks surface through indicating marks for the steel balls positioning (f), and a light dusting with talc to avoid any undesired and unpredictable sticking effects. (e)

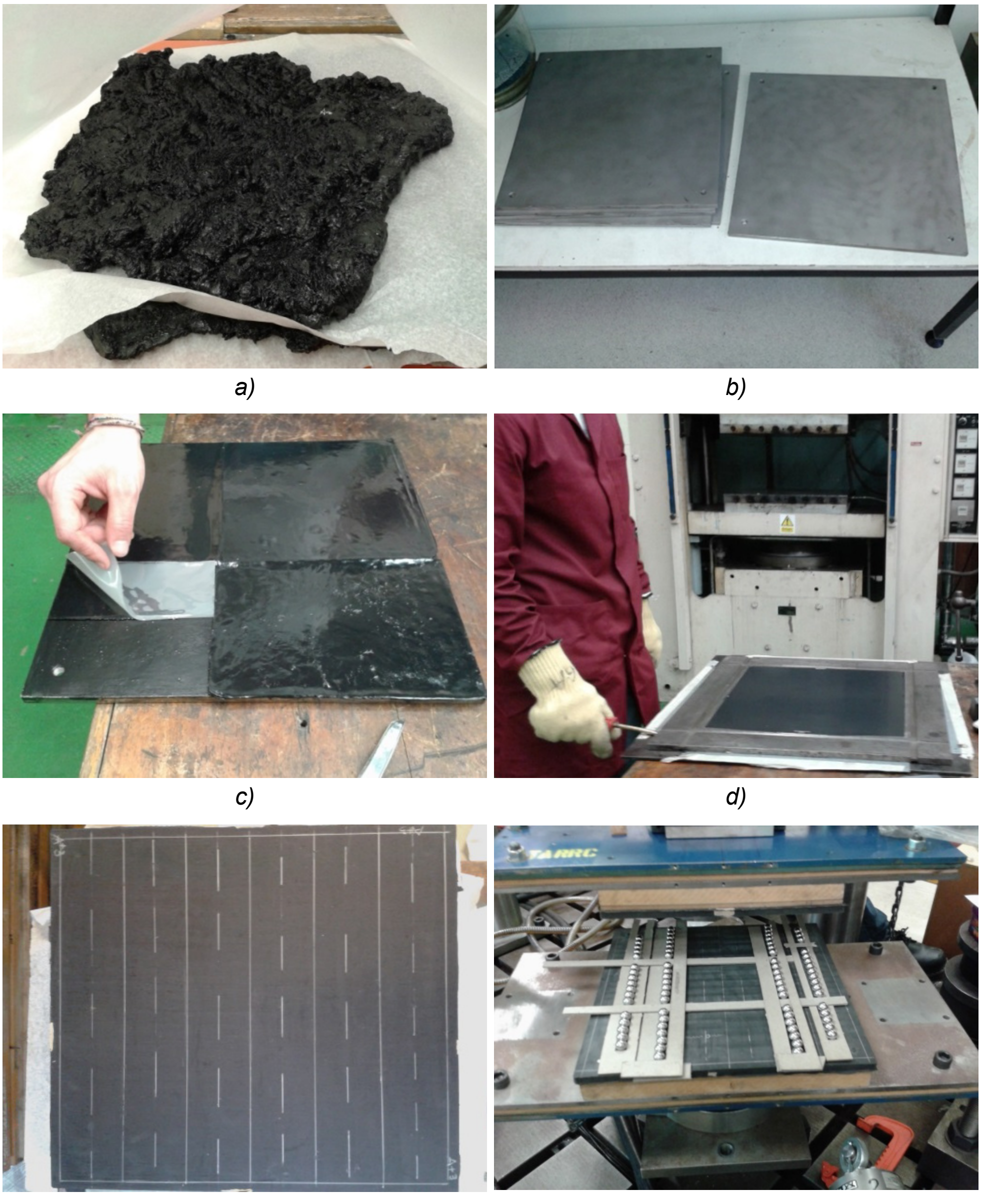

*a)* *b)*

*c)* *d)*

*e)* *f)*

*Fig. 5.1 Some images of the principal realization phases of the RBRL devices at TARRC.*

## 5.2 Characterization tests of the rubber compounds

Double shear test pieces as in Fig. 5.2 were used for the rubber characterization tests, moulded directly on to steel pieces, according to ISO 8013:2006, two from each of the rubber compounds A, A+ and A-. Bonding was achieved during vulcanisation, in an automatic press at ~ 140°C for ~ 45 minutes, because of the presence of Chemlok_220.

The specific characteristics of these samples are reported in Tab. 5.1. Every test piece has a circular cross-section with a diameter of ~25 mm (area ~500mm$^2$).

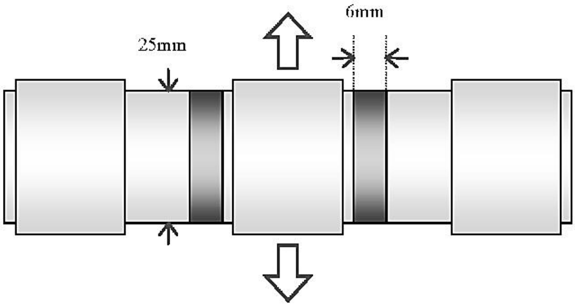

*Fig. 5.2 Cylindrical double shear test piece that shows the nominal thickness of the rubber disc (darker colour) sandwiched between three metal pieces (from Ahmadi et al., 2008).*

| Compound | N° of sample | Total height without rubber (mm) | Total height with rubber (mm) | Height of one rubber part (mm) |
|---|---|---|---|---|
| A+ | 1 | 87.32 | 98.72 | 5.7 |
| A+ | 2 | 87.25 | 98.74 | 5.745 |
| A | 1 | 87.14 | 98.78 | 5.805 |
| A | 2 | 87.24 | 98.84 | 5.8 |
| A- | 1 | 87.45 | 98.77 | 5.66 |
| A- | 2 | 87.33 | 98.67 | 5.67 |

*Tab. 5.1 Geometric characteristics of the test pieces.*

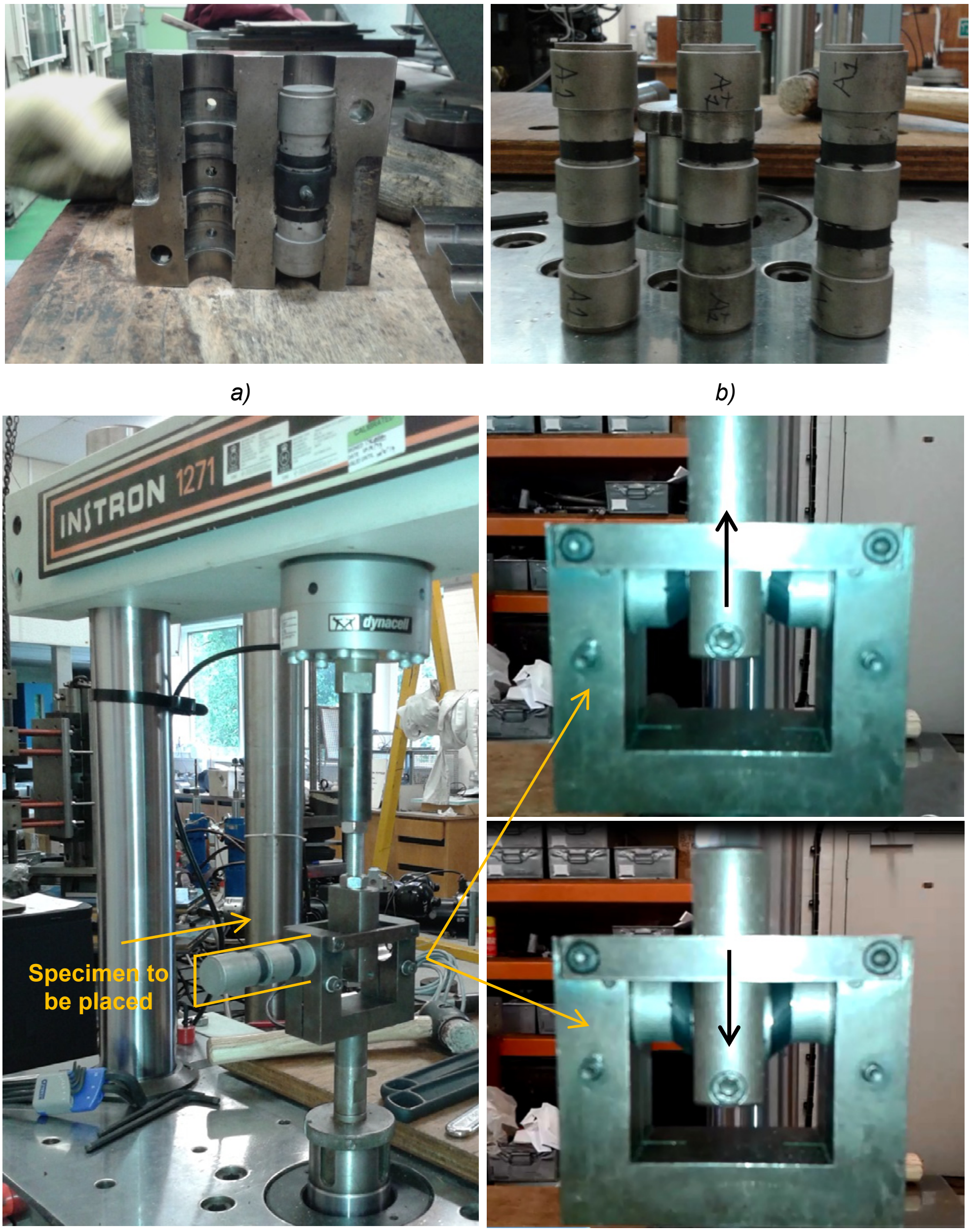
INSTRON 1271
dynacell
Specimen to be placed

*a)* *b)*

*c)* *d)*

*Fig. 5.3 a) Production of the test pieces for the rubber characterization. b) View of the three test pieces used in the double shear tests. c) Test setup using Instron 1271 servo hydraulic test machine (the specimen is not yet placed in the loading rig). d) Images from test execution.*

### *5.2.1 Dynamic tests and rubber dynamic properties*

Firstly dynamic properties of the test pieces A+1, A1 and A-1 were measured using an Instron 1271 servo hydraulic test machine under computer control. The two metal end pieces of the samples (see Fig. 5.2) were fixed in the stationary clamp of the testing jig, attached to the load cell. The actuator of the servo hydraulic testing machine displaced the central steel piece along the direction shown by the arrows of Fig. 5.2. Fig. 5.3 shows the test pieces production and the tests setup.

Two different type of test were performed:

- at a fixed frequency of 1Hz, with different values of strain: amplitudes 5%, 10%, 25%, 50%, and 100%;
- at a fixed strain of 5% and 10%, with different values of frequency: 0.1, 0.5, 1, 5, 10 and 20 Hz.

Six sinusoidal cycles were carried out for each test, then at least 60 seconds was allowed to pass with the test piece held at zero strain before starting the next one.

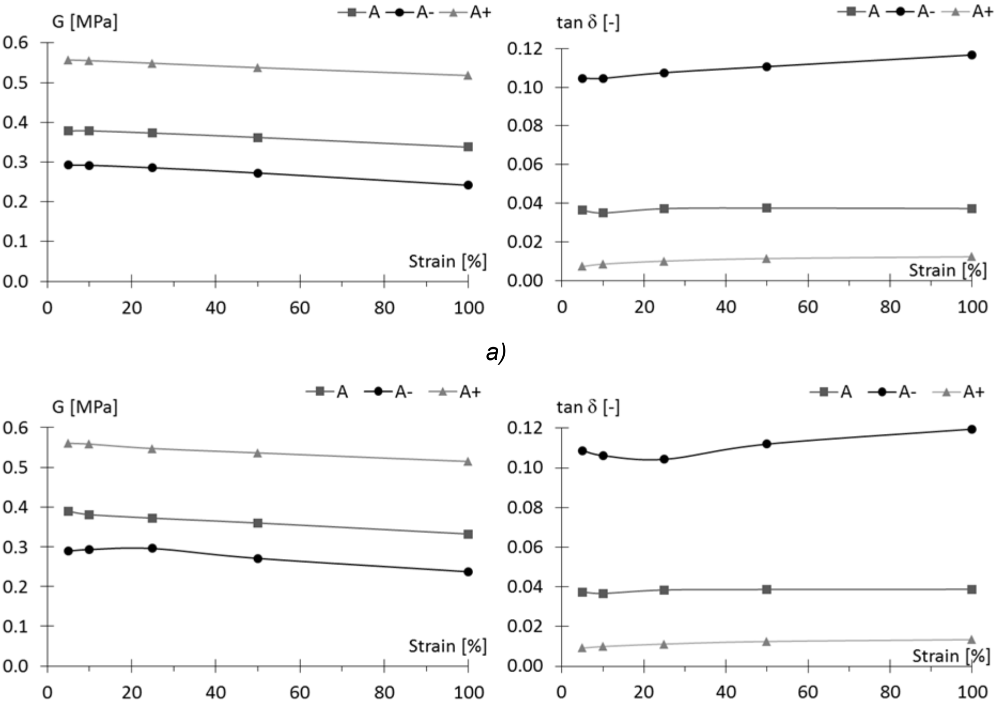

*a)*

*b)*

*Fig. 5.4 Dynamic shear properties of rubber compounds (A, A+,A-) by Harmonic (a) and Secant (b) linearization method – influence of strain level at 1 Hz frequency.*

The tests were performed for all the test pieces of different compounds in this order: fixed frequency tests, then the ones at 5% of strain and finally those at 10%, in following days.

The results obtained using both the Harmonic and Secant linearization method (see section 3.2) are reported in Fig. 5.4, Fig. 5.5 and Fig. 5.6.

The results obtained for compound A are very similar to the ones reported in Guerreiro et al. (2007) for the same compound. This type of compound, like A+ and A-, is characterized by moderate damping and exhibits shear modulus (G) and loss factor (δ) values which are quite independent of the input strain level, unlike the filled rubber compound B shown in Guerreiro et al. (2007). Furthermore, all the compounds herein studied are not very sensitive to the frequency content of the motion, although a slight increase in both values can be observed with the increase of frequency, in particular for the compound A and A-.

Compound A+ is the one with the highest G and the lowest δ, while for the compound A- it is the opposite; compound A presents G and δ values between the ones of A+ and A-.

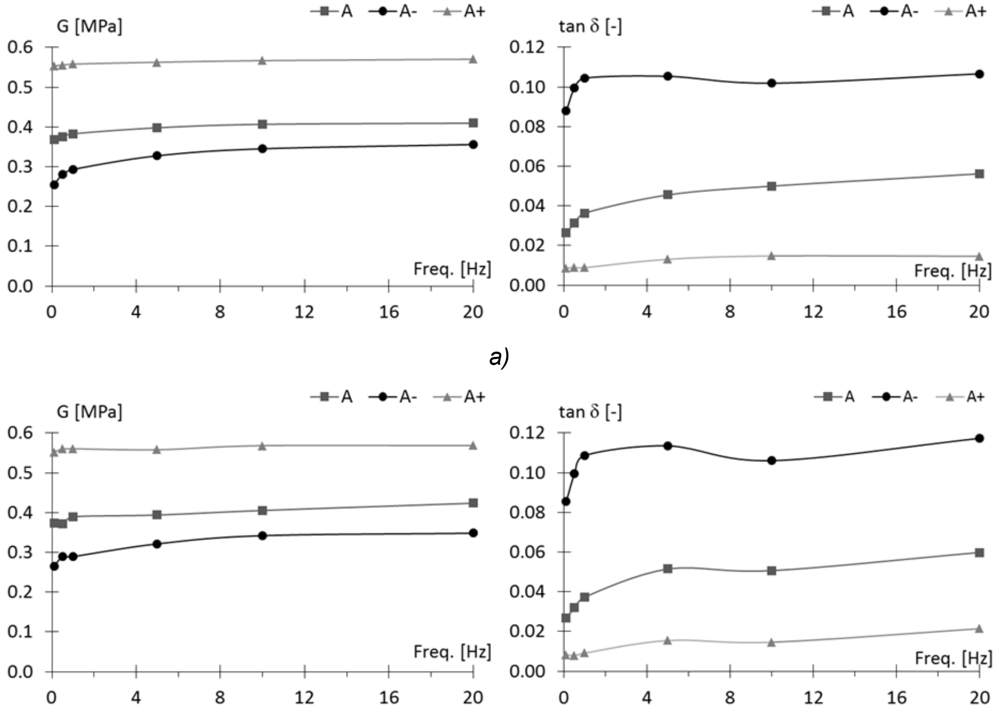

a)

b)

*Fig. 5.5 Dynamic shear properties of rubber compounds (A, A+,A-) by Harmonic (a) and Secant (b) linearization method – influence of frequency for a 5% strain.*

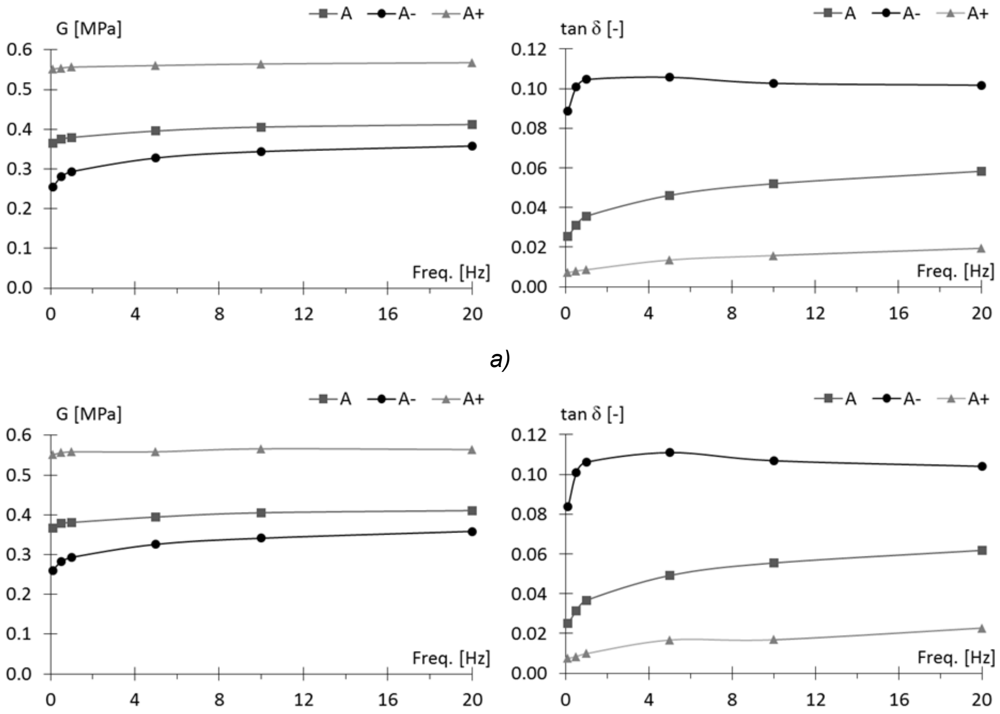

a)

b)

*Fig. 5.6 Dynamic shear properties of rubber compounds (A, A+,A-) by Harmonic (a) and Secant (b) linearization method – influence of frequency for a 10% strain.*

Harmonic and Secant linearization methods gave substantially the same results, as is to be expected, since the departures from linearity are very small.

### *5.2.2 Creep tests and rubber relaxation moduli*

It is known that the results are affected by the strain history of the sample and that reproducibility of the results is improved by mechanical conditioning so, according to ISO 8013:2006, the creep tests on test pieces A+2, A2 and A-2 were anticipated by some tests for the mechanical conditioning; in particular, the specimen has been deformed by about 25% ± 2% in the same direction at a rate of 25 mm/min, and then returned to approximately zero deflection; this was repeated to give a total of five deformations. Moreover, the suggested (ISO 8013:2006) minimum and maximum waiting time between mechanical conditioning and testing, respectively of 16 and 48 hours, was respected.

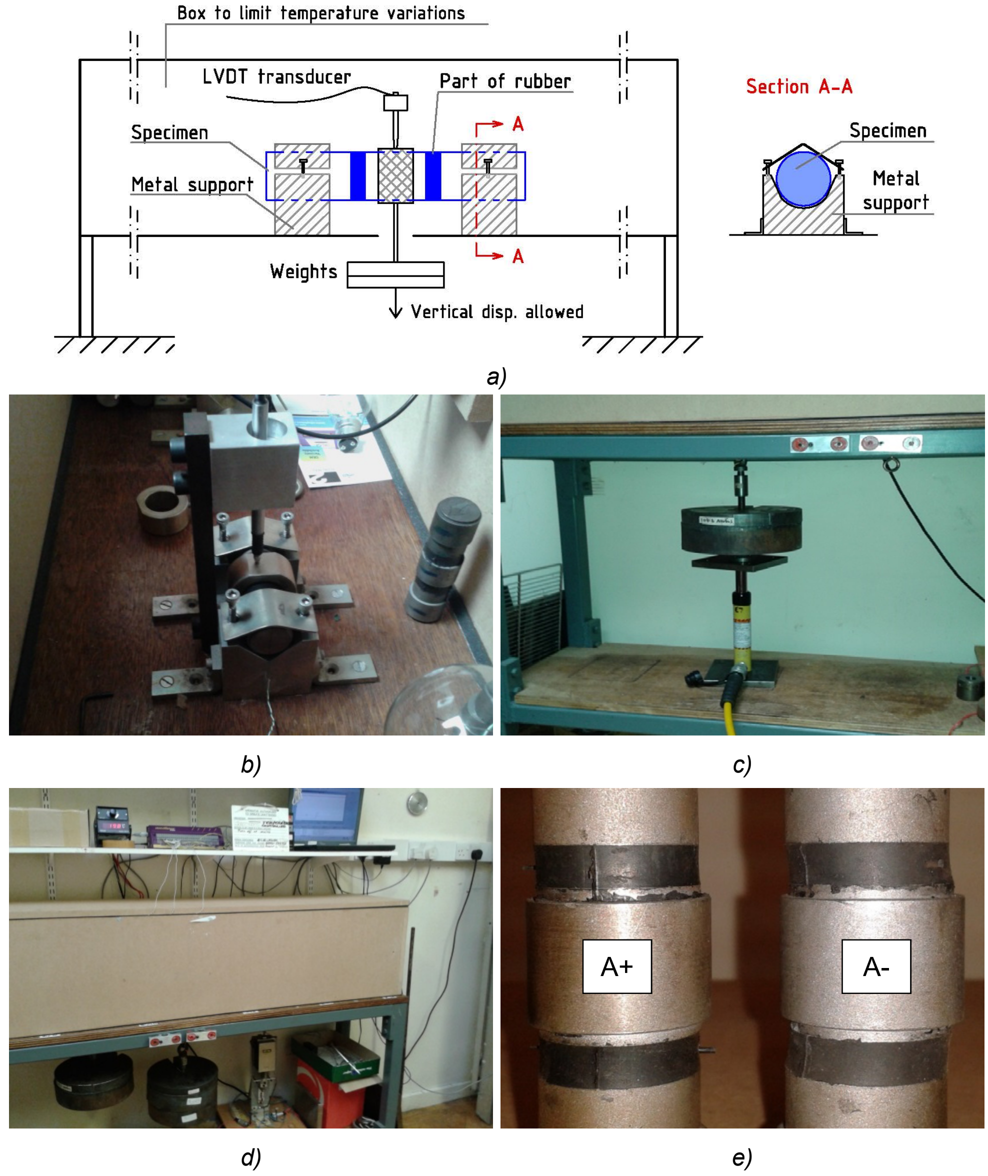
Box to limit temperature variations
LVDT transducer
Part of rubber
Specimen
Metal support
A
A
Weights
Vertical disp. allowed
Section A-A
Specimen
Metal support
a)
b)
c)
A+
A-
d)
e)

*Fig. 5.7 a) Schematic drawing of the creep test setup; b) installation of the test piece (view of the LVDT transducer); c) application of the load through an hydraulic jack minimizing the load oscillations; d) general view of the setup during the creep tests; e) comparison of the residual strain, between specimens A+ and A-, just finished the test.*

| Test pieces: | A+(2) | A(2) | A-2 (interrupted) | A-1 (repeated) |
|---|---|---|---|---|
| Force (N): | 528 | 370 | 212 | 106 |

*Tab. 5.2 Forces used in the creep tests.*

Concerning the force that should be used in the creep tests, ISO 8013:2006 recommends a value such that the initial strain in the test piece is 20% ± 2%. We decided to use a higher value of force (Tab. 5.2), to reach approximately a strain of 100% to better observe the creep phenomena.

In Fig. 5.7 is presented the test setup, with the installation of the test piece and the application of the load; for the latter, the use of an hydraulic jack is necessary to avoid load oscillations as much as possible, since the creep phenomena have a linear dependence with the logarithm of the time, so the loss of the data for the first seconds of the test might be significant for the subsequent processing of the results. In the same figure (d), a comparison of the residual strain just finished the test, between specimens A+ and A-, is shown: the second one is visibly more deformed than the first one, as expected.

The load for each specimen remained applied for approximately one week, so 10000 minutes; the shear deformation of each test piece was logged every second, from time 0 to 50 minutes at least, then every minute, until the test time 100 minutes, finally every five minutes until the end of the test.

During the creep test for the specimen A-2, unfortunately, the strain reached by the sample leaded to it touching the bottom part of the test yoke; thus we had to repeat the same test but with the specimen A-1 to a smaller shear strain.

The results obtained from the creep tests are shown in Fig. 5.8 and Fig. 5.9. The principal parameters to fit a discrete Prony series (Ahmadi et al., 2008), G ($t_c$=1 min) and $H_0$, were calculated from these results using Eqs. (5.1), (5.2) and (5.3) (Gent, 1962): the values are reported in Tab. 5.3 for each compound. These parameters are normally required by FEA packages to approximate the relaxation modulus G(t) of the rubber (time domain representation).

$$\begin{aligned} H_0 &\equiv -\frac{dG(t)}{d\ln(t)} \\ &\simeq \left(\frac{S}{100}\right)\cdot G(t_c)\cdot 0.4343 = \left(\frac{S}{100}\right)\cdot G(t_c)\cdot 0.6822\cdot\frac{\pi}{2} \end{aligned} \tag{5.1}$$

where:

$$G(t_c) \simeq \frac{F}{2\cdot A_{sample}\cdot\gamma(t_c)} \tag{5.2}$$

$$\begin{aligned} S &\equiv -100\frac{dG(t)}{d\log_{10}(t)}\frac{1}{G(t_c)} = -100\frac{dG(t)}{0.4343\ d\ln(t)}\frac{1}{G(t_c)} \\ &\equiv +100\frac{d\gamma(t)}{d\log_{10}(t)}\frac{1}{\gamma(t_c)} = +100\frac{d\gamma(t)}{0.4343\ d\ln(t)}\frac{1}{\gamma(t_c)} \end{aligned} \tag{5.3}$$

where S is known as the stress relaxation rate (or creep rate), $t_c$ is a characteristic time usually taken as 1 minute and F is the force applied in the test.

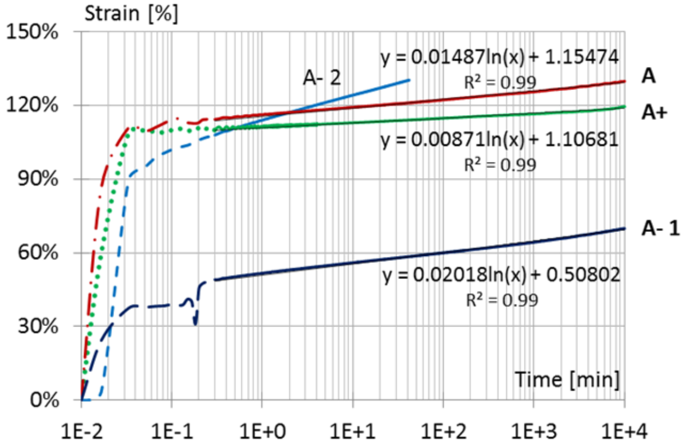

*Fig. 5.8 Creep plots for all the specimens tested.*

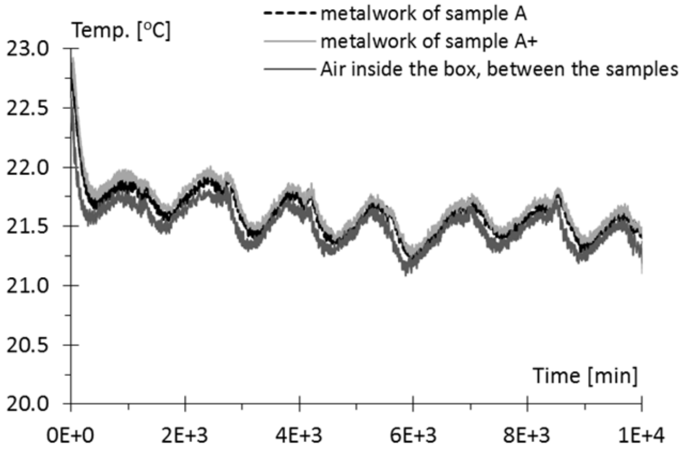

*Fig. 5.9 Temperatures measured during the creep tests for the specimens A and A+.*

| Compound | G ($t_c$=1min) (MPa) | $H_0$ (MPa) | S (%) |
|---|---|---|---|
| A+ | 0.48 | 0.00375 | 1.81 |
| A | 0.32 | 0.00412 | 2.97 |
| A- | 0.21 | 0.00827 | 9.15 |

*Tab. 5.3 Parameters to calibrate a discrete Prony series (Ahmadi et al., 2008).*

Eq. (5.4) was derived from Eqs. (5.2) and (5.3); it enables the relaxation moduli to be plotted versus log(t) from the results in Fig. 5.8.

$$\frac{dG(t)}{dt} = -\frac{F(t_c)}{2 \cdot A_{sample} \cdot \gamma(t_c)^2} \frac{d\gamma(t)}{dt} \tag{5.4}$$

The results clearly show that the creep value for compound A- is actually higher than the one for compound A or A+, which present a similar and very low value of $H_0$. By the comparison of the results in Fig. 5.10, for the specimen A-(1) and A-(2), it is possible to note that creep phenomena (or $H_0$ parameter) is not dependent by the strain values, differently from the shear modulus that become a bit smaller with higher strain levels. The influence of the strain amplitude on the shear modulus, albeit modest, is visible in Fig. 5.4 for all the compounds analyzed.

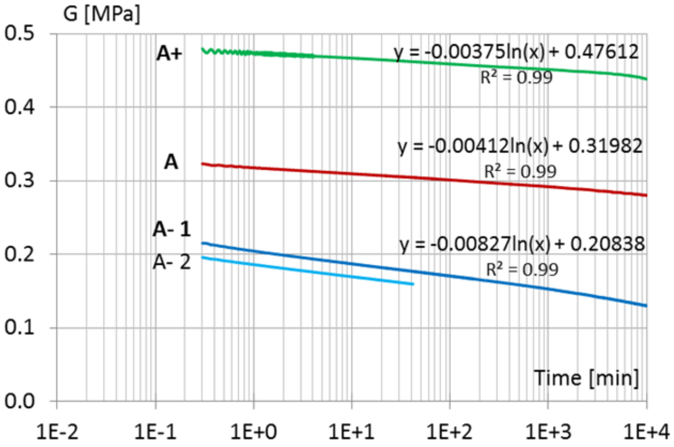

*Fig. 5.10 Relaxation moduli for all the compounds tested, calculated by the creep test results of Fig. 5.8.*

## 5.3 Sinusoidal uniaxial tests on new RBRL devices: validation of the rolling friction theory of Muhr et al. (1997)

### *5.3.1 Description of the tests*

The experimentation has involved the following device conditions:

| | |
|---|---|
| - 3 rubber compounds: | A; A+; A- |
| - 3 rubber layer thicknesses (t): | 1,5 – 2 – 3 mm |
| - 4 steel ball diameters (D): | 15 – 20 – 25 – 30 mm |
| - 5 stress parameters ($W^* = W/ER^2$): | 0,4 – 0,8 – 1,2 – 1,6 – 2 |

where W is the load per ball, E is the Young's modulus of the rubber and R is the radius of the steel ball. Three different RBRL devices were produced for each rubber compound, moulding rubber tracks for each thickness indicated: overall, 9 devices were realized.

The tests consisted of 3 sinusoidal cycles, with a displacement amplitude of 65 mm and a frequency of 0.5 Hz.

Combining three different ball diameters (among the ones indicated) with the five values of the stress parameter, 15 tests for each RBRL device were performed: this means 45 tests for each compound (15 tests for 3 different thicknesses) and 135 tests globally (45 tests for 3 different compounds).

Finally, another 18 "special tests" with rubber compound A and higher values of the stress parameter, 3 and 4, were executed to individuate possible stress limits for the applicability of the theory of Muhr et al. (1997).

Young's modulus (E) of the rubber compounds is a necessary parameter for the correct design of the parametric tests, since it defines the stress parameter. The values of E and δ, needed for the comparison with the theory, are summarized in

Tab. 5.4: they came from dynamic test results on the rubbers at a frequency of 1 Hz and a strain amplitude of 25%.

Tab. 5.5 (for compound A), Tab. 5.6 (A-) and Tab. 5.7 (A+) show the tests planning for the specific rubber compound. Once the ball diameter and the stress parameter were decided, the number of the steel balls to use in the test was chosen to get a total vertical load as close as possible to the structural weight of the test setup (150 kg), already supported by the RBRL device (see Fig. 5.11): in this way the adding vertical load was minimized. A minimum value of 4 balls was considered.

All the tests were performed in single shear configuration for one RBRL device with no recentering springs: the test setup is shown in Fig. 5.11. The steel roller bearings shown in figure a) permit translation of the tope plate in the x and z directions, but prevent rotation of it about any axis. The sinusoidal motion was controlled by the actuator and transmitted to the top steel plate of the device, which supports the weight, through a rose joint connection that permits small rotations. This connection was necessary to avoid bending stresses related to a non-perfect vertical alignment between actuator and top plate of the device, and to accommodate the small z-displacement as the balls out of and into their pits.

The horizontal forces (x-axis) were measured by the multiaxial load cell placed under the bottom plate of the device, which was fixed on it. This was preferred to the direct measurement of the forces by the actuator load cell, to avoid inclusion of the friction inside the linear rolling bearings which constrain the top

| Compound | G (MPa) | E (MPa) | tg δ (-) |
|---|---|---|---|
| A+ | 0.56 | 1.68 | 0.010 |
| A | 0.38 | 1.14 | 0.037 |
| A- | 0.29 | 0.87 | 0.108 |

*Tab. 5.4 Summary of the parameters for the rubber compounds (from dynamic test).*

| thickness of rubber tracks = **1.5 mm** | | | | | thickness of rubber tracks = **2 mm** | | | | | thickness of rubber tracks = **3 mm** | | | | |
|---|---|---|---|---|---|---|---|---|---|---|---|---|---|---|
| D ball (mm) | W/(ER$^2$) (-) | **N° balls** (-) | W tot (kg) | **ΔW test** (kg) | D ball (mm) | W/(ER$^2$) (-) | **N° balls** (-) | W tot (kg) | **ΔW test** (kg) | D ball (mm) | W/(ER$^2$) (-) | **N° balls** (-) | W tot (kg) | **ΔW test** (kg) |
| 20 | 0.4 | 36 | 167.4 | 17.4 | 20 | 0.4 | 36 | 167.4 | 17.4 | 20 | 0.4 | 36 | 167.4 | 17.4 |
| 20 | 0.8 | 18 | 167.4 | 17.4 | 20 | 0.8 | 18 | 167.4 | 17.4 | 20 | 0.8 | 18 | 167.4 | 17.4 |
| 20 | 1.2 | 12 | 167.4 | 17.4 | 20 | 1.2 | 12 | 167.4 | 17.4 | 20 | 1.2 | 12 | 167.4 | 17.4 |
| 20 | 1.6 | 10 | 186.0 | 36.0 | 20 | 1.6 | 10 | 186.0 | 36.0 | 20 | 1.6 | 10 | 186.0 | 36.0 |
| 20 | 2.0 | 8 | 186.0 | 36.0 | 20 | 2.0 | 8 | 186.0 | 36.0 | 20 | 2.0 | 8 | 186.0 | 36.0 |
| 25 | 0.4 | 24 | 174.4 | 24.4 | 25 | 0.4 | 24 | 174.4 | 24.4 | 25 | 0.4 | 24 | 174.4 | 24.4 |
| 25 | 0.8 | 12 | 174.4 | 24.4 | 25 | 0.8 | 12 | 174.4 | 24.4 | 25 | 0.8 | 12 | 174.4 | 24.4 |
| 25 | 1.2 | 8 | 174.4 | 24.4 | 25 | 1.2 | 8 | 174.4 | 24.4 | 25 | 1.2 | 8 | 174.4 | 24.4 |
| 25 | 1.6 | 6 | 174.4 | 24.4 | 25 | 1.6 | 6 | 174.4 | 24.4 | 25 | 1.6 | 6 | 174.4 | 24.4 |
| 25 | 2.0 | 6 | 218.0 | 68.0 | 25 | 2.0 | 6 | 218.0 | 68.0 | 25 | 2.0 | 6 | 218.0 | 68.0 |
| 30 | 0.4 | 16 | 167.4 | 17.4 | 30 | 0.4 | 16 | 167.4 | 17.4 | 15 | 0.4 | 58 | 151.7 | 1.7 |
| 30 | 0.8 | 8 | 167.4 | 17.4 | 30 | 0.8 | 8 | 167.4 | 17.4 | 15 | 0.8 | 30 | 156.9 | 6.9 |
| 30 | 1.2 | 6 | 188.3 | 38.3 | 30 | 1.2 | 6 | 188.3 | 38.3 | 15 | 1.2 | 20 | 156.9 | 6.9 |
| 30 | 1.6 | 4 | 167.4 | 17.4 | 30 | 1.6 | 4 | 167.4 | 17.4 | 15 | 1.6 | 16 | 167.4 | 17.4 |
| 30 | 2.0 | 4 | 209.3 | 59.3 | 30 | 2.0 | 4 | 209.3 | 59.3 | 15 | 2.0 | 12 | 156.9 | 6.9 |
| "special test" - only for rubber A | | | | | "special test" - only for rubber A | | | | | "special test" - only for rubber A | | | | |
| 15 | 3 | 8 | 156.9 | 6.9 | 15 | 3 | 8 | 156.9 | 6.9 | 15 | 3 | 8 | 156.9 | 6.9 |
| 15 | 4 | 6 | 156.9 | 6.9 | 15 | 4 | 6 | 156.9 | 6.9 | 15 | 4 | 6 | 156.9 | 6.9 |
| 20 | 3 | 6 | 209.3 | 59.3 | 20 | 3 | 6 | 209.3 | 59.3 | 20 | 3 | 6 | 209.3 | 59.3 |
| 20 | 4 | 4 | 186.0 | 36.0 | 20 | 4 | 4 | 186.0 | 36.0 | 20 | 4 | 4 | 186.0 | 36.0 |
| 25 | 3 | 4 | 218.0 | 68.0 | 25 | 3 | 4 | 218.0 | 68.0 | 25 | 3 | 4 | 218.0 | 68.0 |
| 25 | 4 | 4 | 290.6 | 140.6 | 25 | 4 | 4 | 290.6 | 140.6 | 25 | 4 | 4 | 290.6 | 140.6 |

**ΔW test** = additional load to be applied on the test. Initial vertical load of the test steup is **150 kg**

*Tab. 5.5 Tests planning for rubber compound A.*

| thickness of rubber tracks = **1.5 mm** | | | | | thickness of rubber tracks = **2 mm** | | | | | thickness of rubber tracks = **3 mm** | | | | |
|---|---|---|---|---|---|---|---|---|---|---|---|---|---|---|
| D ball | W/(ER$^2$) | **N° balls** | W tot | **ΔW test** | D ball | W/(ER$^2$) | **N° balls** | W tot | **ΔW test** | D ball | W/(ER$^2$) | **N° balls** | W tot | **ΔW test** |
| (mm) | (-) | (-) | (kg) | (kg) | (mm) | (-) | (-) | (kg) | (kg) | (mm) | (-) | (-) | (kg) | (kg) |
| 20 | 0.4 | **44** | 156.1 | **6.1** | 20 | 0.4 | **44** | 156.1 | **6.1** | 20 | 0.4 | **44** | 156.1 | **6.1** |
| 20 | 0.8 | **22** | 156.1 | **6.1** | 20 | 0.8 | **22** | 156.1 | **6.1** | 20 | 0.8 | **22** | 156.1 | **6.1** |
| 20 | 1.2 | **16** | 170.3 | **20.3** | 20 | 1.2 | **16** | 170.3 | **20.3** | 20 | 1.2 | **16** | 170.3 | **20.3** |
| 20 | 1.6 | **12** | 170.3 | **20.3** | 20 | 1.6 | **12** | 170.3 | **20.3** | 20 | 1.6 | **12** | 170.3 | **20.3** |
| 20 | 2.0 | **10** | 177.4 | **27.4** | 20 | 2.0 | **10** | 177.4 | **27.4** | 20 | 2.0 | **10** | 177.4 | **27.4** |
| 25 | 0.4 | **28** | 155.3 | **5.3** | 25 | 0.4 | **28** | 155.3 | **5.3** | 25 | 0.4 | **28** | 155.3 | **5.3** |
| 25 | 0.8 | **14** | 155.3 | **5.3** | 25 | 0.8 | **14** | 155.3 | **5.3** | 25 | 0.8 | **14** | 155.3 | **5.3** |
| 25 | 1.2 | **10** | 166.4 | **16.4** | 25 | 1.2 | **10** | 166.4 | **16.4** | 25 | 1.2 | **10** | 166.4 | **16.4** |
| 25 | 1.6 | **8** | 177.4 | **27.4** | 25 | 1.6 | **8** | 177.4 | **27.4** | 25 | 1.6 | **8** | 177.4 | **27.4** |
| 25 | 2.0 | **6** | 166.4 | **16.4** | 25 | 2.0 | **6** | 166.4 | **16.4** | 25 | 2.0 | **6** | 166.4 | **16.4** |
| 30 | 0.4 | **20** | 159.7 | **9.7** | 30 | 0.4 | **20** | 159.7 | **9.7** | 15 | 0.4 | **76** | 151.7 | **1.7** |
| 30 | 0.8 | **10** | 159.7 | **9.7** | 30 | 0.8 | **10** | 159.7 | **9.7** | 15 | 0.8 | **38** | 151.7 | **1.7** |
| 30 | 1.2 | **8** | 191.6 | **41.6** | 30 | 1.2 | **8** | 191.6 | **41.6** | 15 | 1.2 | **26** | 155.7 | **5.7** |
| 30 | 1.6 | **6** | 191.6 | **41.6** | 30 | 1.6 | **6** | 191.6 | **41.6** | 15 | 1.6 | **20** | 159.7 | **9.7** |
| 30 | 2.0 | **4** | 159.7 | **9.7** | 30 | 2.0 | **4** | 159.7 | **9.7** | 15 | 2.0 | **16** | 159.7 | **9.7** |

**ΔW test** = additional load to be applied on the test. Initial vertical load of the test steup is **150 kg**

*Tab. 5.6 Tests planning for rubber compound A-.*

| thickness of rubber tracks = **1.5 mm** | | | | | thickness of rubber tracks = **2 mm** | | | | | thickness of rubber tracks = **3 mm** | | | | |
|---|---|---|---|---|---|---|---|---|---|---|---|---|---|---|
| D ball | W/(ER$^2$) | **N° balls** | W tot | **ΔW test** | D ball | W/(ER$^2$) | **N° balls** | W tot | **ΔW test** | D ball | W/(ER$^2$) | **N° balls** | W tot | **ΔW test** |
| (mm) | (-) | (-) | (kg) | (kg) | (mm) | (-) | (-) | (kg) | (kg) | (mm) | (-) | (-) | (kg) | (kg) |
| 20 | 0.4 | **24** | 164.5 | **14.5** | 20 | 0.4 | **24** | 164.5 | **14.5** | 20 | 0.4 | **24** | 164.5 | **14.5** |
| 20 | 0.8 | **12** | 164.5 | **14.5** | 20 | 0.8 | **12** | 164.5 | **14.5** | 20 | 0.8 | **12** | 164.5 | **14.5** |
| 20 | 1.2 | **8** | 164.5 | **14.5** | 20 | 1.2 | **8** | 164.5 | **14.5** | 20 | 1.2 | **8** | 164.5 | **14.5** |
| 20 | 1.6 | **6** | 164.5 | **14.5** | 20 | 1.6 | **6** | 164.5 | **14.5** | 20 | 1.6 | **6** | 164.5 | **14.5** |
| 20 | 2.0 | **6** | 205.6 | **55.6** | 20 | 2.0 | **6** | 205.6 | **55.6** | 20 | 2.0 | **6** | 205.6 | **55.6** |
| 25 | 0.4 | **16** | 171.3 | **21.3** | 25 | 0.4 | **16** | 171.3 | **21.3** | 25 | 0.4 | **16** | 171.3 | **21.3** |
| 25 | 0.8 | **8** | 171.3 | **21.3** | 25 | 0.8 | **8** | 171.3 | **21.3** | 25 | 0.8 | **8** | 171.3 | **21.3** |
| 25 | 1.2 | **6** | 192.7 | **42.7** | 25 | 1.2 | **6** | 192.7 | **42.7** | 25 | 1.2 | **6** | 192.7 | **42.7** |
| 25 | 1.6 | **4** | 171.3 | **21.3** | 25 | 1.6 | **4** | 171.3 | **21.3** | 25 | 1.6 | **4** | 171.3 | **21.3** |
| 25 | 2.0 | **4** | 214.2 | **64.2** | 25 | 2.0 | **4** | 214.2 | **64.2** | 25 | 2.0 | **4** | 214.2 | **64.2** |
| 30 | 0.4 | **12** | 185.0 | **35.0** | 30 | 0.4 | **12** | 185.0 | **35.0** | 15 | 0.4 | **40** | 154.2 | **4.2** |
| 30 | 0.8 | **6** | 185.0 | **35.0** | 30 | 0.8 | **6** | 185.0 | **35.0** | 15 | 0.8 | **20** | 154.2 | **4.2** |
| 30 | 1.2 | **4** | 185.0 | **35.0** | 30 | 1.2 | **4** | 185.0 | **35.0** | 15 | 1.2 | **14** | 161.9 | **11.9** |
| 30 | 1.6 | **4** | 246.7 | **96.7** | 30 | 1.6 | **4** | 246.7 | **96.7** | 15 | 1.6 | **10** | 154.2 | **4.2** |
| 30 | 2.0 | **4** | 308.4 | **158.4** | 30 | 2.0 | **4** | 308.4 | **158.4** | 15 | 2.0 | **8** | 154.2 | **4.2** |

**ΔW test** = additional load to be applied on the test. Initial vertical load of the test steup is **150 kg**

*Tab. 5.7 Tests planning for rubber compound A+.*

plate motion. The alternative test setup would have consisted of a double shear configuration with two identical RBRL devices, measuring the horizontal forces directly by the actuator load cell, that would have moved the linked plates of the two devices; this option, even if scientifically correct, is too demanding in terms of RBRL devices production.

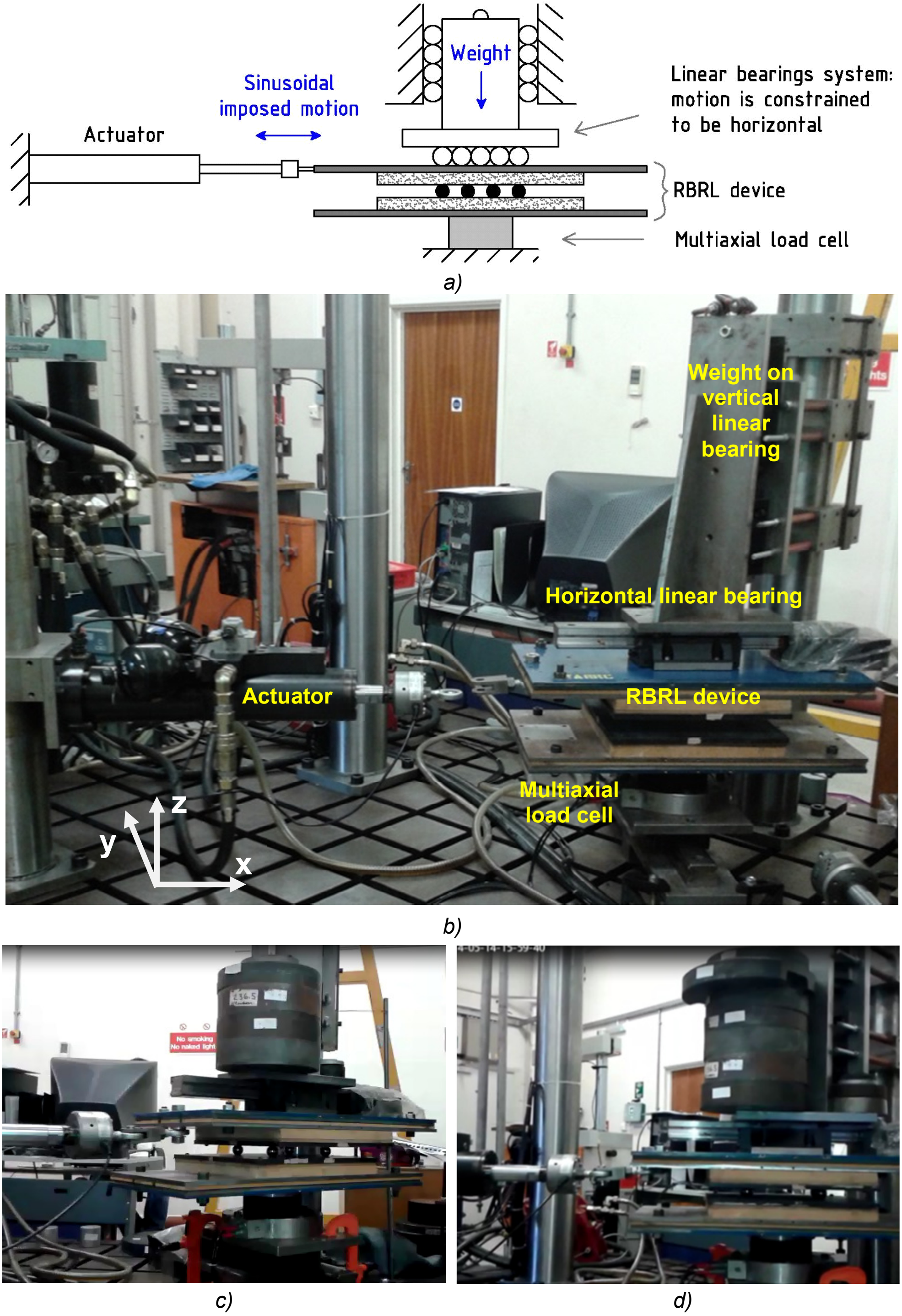
Weight
Sinusoidal imposed motion
Actuator
Linear bearings system: motion is constrained to be horizontal
RBRL device
Multiaxial load cell
a)
Weight on vertical linear bearing
Horizontal linear bearing
Actuator
RBRL device
Multiaxial load cell
z
y
x
b)
c)
d)

*Fig. 5.11 Setup of the sinusoidal uniaxial tests to verify the theory of Muhr et al. (1997): a) schematic drawing, b) photo. c), d) Images from running tests (with additional weight).*

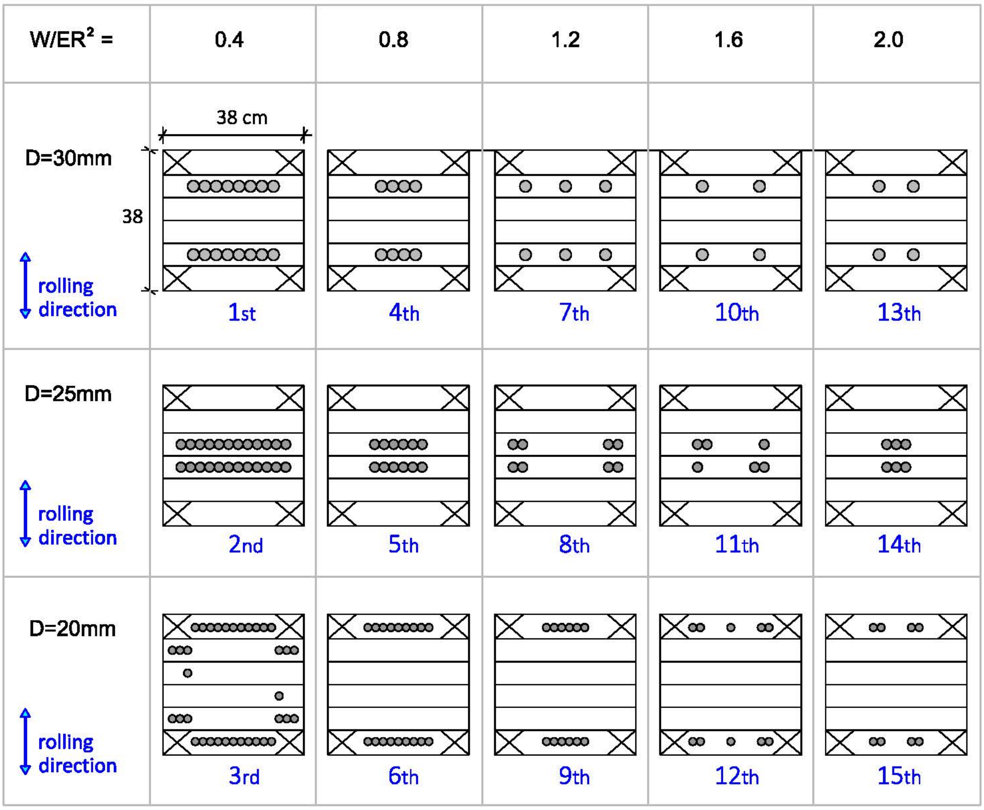
W/ER² =
0.4
0.8
1.2
1.6
2.0
D=30mm
38 cm
38
rolling direction
1st
4th
7th
10th
13th
D=25mm
rolling direction
2nd
5th
8th
11th
14th
D=20mm
rolling direction
3rd
6th
9th
12th
15th

*Fig. 5.12 Planning of the tests execution order and balls position: rubber A, layer thickness 1.5 mm*

Tests execution order and balls position were planned too, in order to have for each test the most part of fresh rubber (see Fig. 5.12 and Fig. 5.13). In particular, the rubber layer was subdivided in 6 rows with the same width: every ball diameter was associated with two of these rows, symmetrically positioned. Tests execution order followed the stress parameter increasing order and, for the same stress parameter, the ball diameter decreasing order. Within their own rows the balls were positioned to avoid that the rolling tracks of the previous test could influence the ones of the following test, especially for high stress parameters. Fig. 5.13 shows the rubber layers after some tests and the correct planning of the balls position. It is worth noting, with regards to Fig. 5.13, although the rubbers analyzed are low-damping compounds, and thus the rolling tracks should recover very quickly, these tracks are still visible after the tests (in the images): this is only due to the fact that the rubber surfaces were dusted with talc.

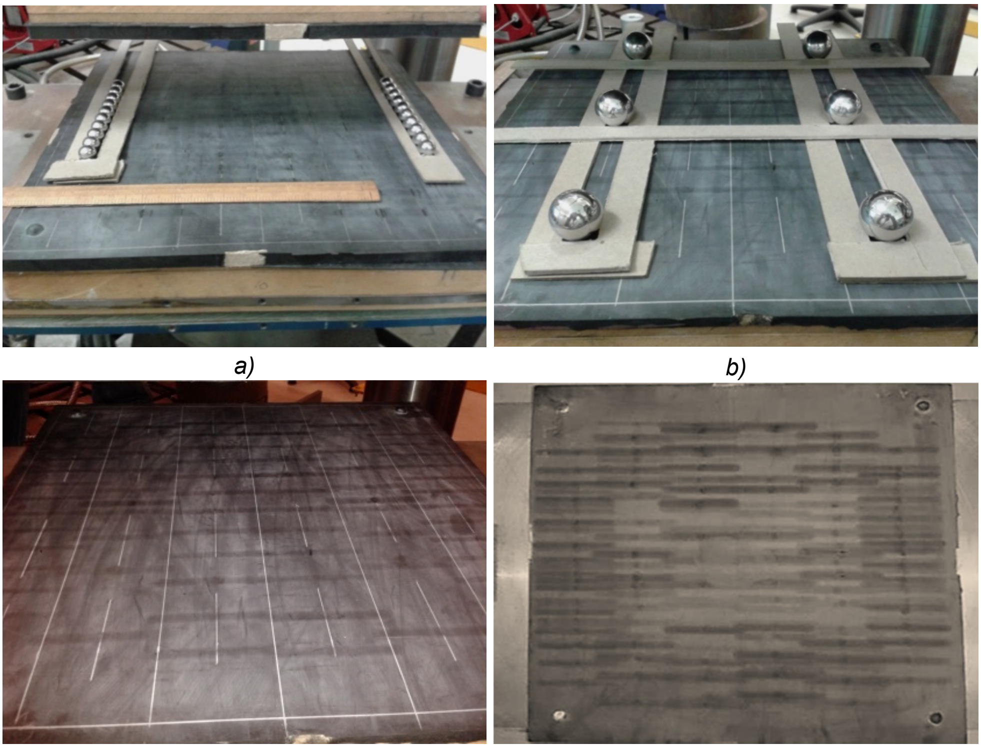

*a)* *b)*

*c)* *d)*

*Fig. 5.13 a), b) Images of balls positioning. Images of rubber tracks, lower (c) and upper (d), after running some (c) / all (d) tests associated with that RBRL device.*

### *5.3.1 Results*

The rolling friction force in steady state condition was obtained, for each test, from the second of the three sinusoidal cycles performed (Fig. 5.14 a). These force values were divided by the vertical load used in the relative test, obtaining the rolling friction coefficients μ (Fig. 5.14 b), to allow a consistent comparison of all the results, and between the results and the theory of Muhr et al.

As it is possible to note from the example reported in Fig. 5.14, the rolling friction coefficients do not have the same value for the various quadrants: this is believed to be due to the viscoelastic behaviour of the rubber. The μ value for the first passage of the balls on the rubber track (1st and 3rd quadrant) should theoretically be a bit bigger than when the balls return using the same rolling tracks (2nd and 4th quadrant), due to a reduced thickness of the rolling tracks for the return path. Moreover, rubber is rate dependent, thus the rolling friction would also depend on the velocity of the test, albeit slightly. The approximate theory of Muhr et al.

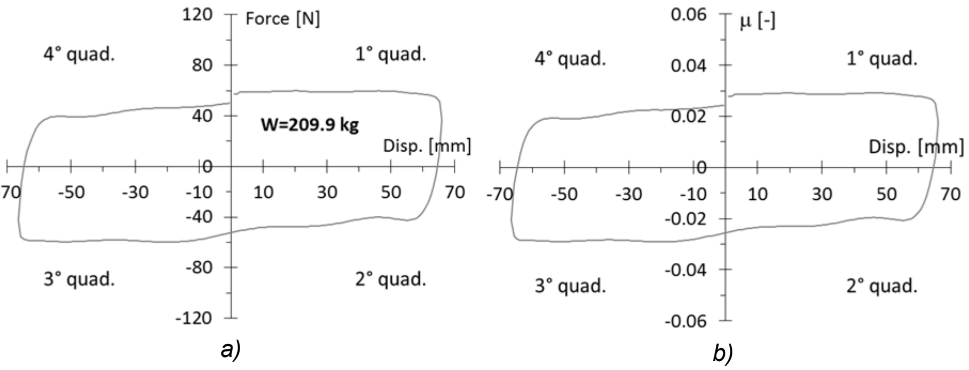

*Fig. 5.14 a) Example of force (F)-displacement (D) loop, for the second sinusoidal cycle, for the case: A, t=2mm, D=20mm, $W/ER^2=3$. b) The same, in terms of friction coefficient μ (=F/Wg). The quadrants are numbered following the rolling of the balls.*

(1997) does not conceive these aspects and uses the unique parameter α, only related to the rubber type (see Eq. (3.11)), to describe the energy dissipation during the rolling. Considering the various sources of uncertainty in the test setup, test execution and devices production (such as the realization of the correct thickness of rubber over the entire device surface), and furthermore not considering the velocity dependence for the rolling friction, the value of μ averaged over the quadrants was assumed for all the tests, and gives the most stable value.

Currently, the principal uncertainty factor of the theory of Muhr et al. is the hysteretic parameter α, that authors like Greenwood et al. (1961) suggest to be two or three times higher than the one observed in a simple uniaxial stress cycle, because the complicated stress cycles suffered by rubber elements during rolling would result in greater energy dissipation. Thus, this parameter needs to be calibrated with the experimentation. The basic assumption herein made is to consider this α parameter to depend not only on the type of the rubber compound (through the loss factor δ), but also on the stress level inside the rubber (through the stress parameter $W/ER^2$):

$$\alpha = \pi \cdot \sin\delta \cdot g\left(\frac{W}{ER^2}, rubber\ \ compound\right) \tag{5.5}$$

Considering all the experimental values of μ, separately for rubber type, the $g$ parameter was calculated for each stress level in order to minimized the sum of the squared deviations between the test results and the relative theoretical values. The comparison of the rolling friction values obtained by the tests and the theory, considering the calibration of the theoretical curves through the $g$ parameter, is shown for the different compounds in Fig. 5.15, Fig. 5.16 and Fig. 5.17.

It is possible to observe a really good fitting between the experimental results and the theory of Muhr et al. (1997), calibrated as explained before, for all the rubber compounds analyzed. Only the tests with very high stress parameters, 3.0 and 4.0, gave results a bit different from the theoretical line (see Fig. 5.15 b), showing that there are some limits, in terms of stress level, for the applicability of the theory; indeed, for these high stress levels, sometimes it was also possible to note some semi-permanent rolling tracks at the end of the test, as it is shown in Fig. 5.18.

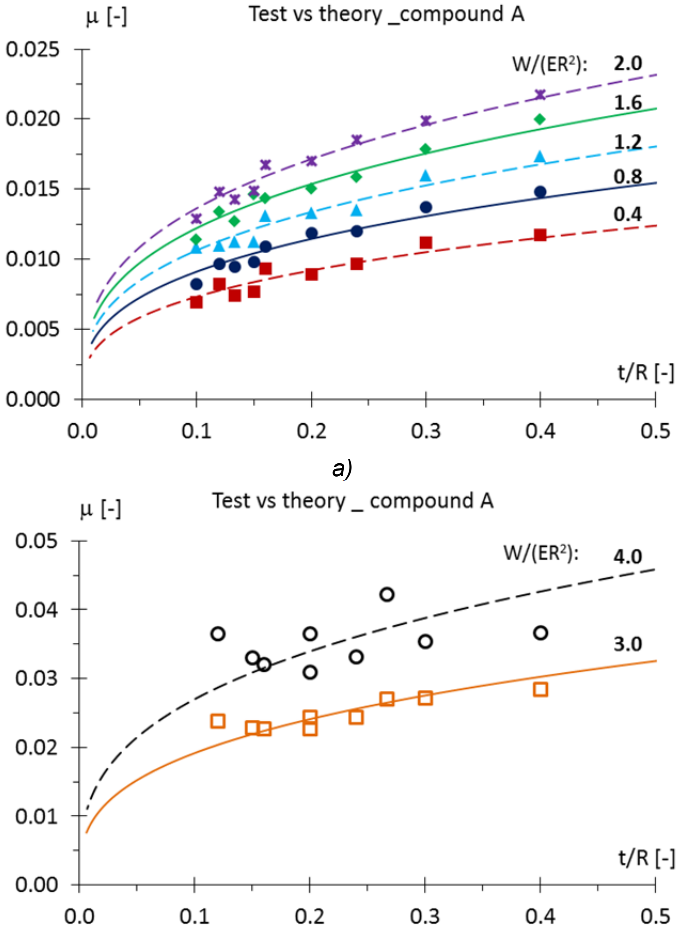

*a)*

*b)*

*Fig. 5.15 Comparison, for the compound A, of the rolling friction values (μ) obtained by the tests and the theory, for different values of the thickness/radius ratio (t/R). (a) Stress parameters ($W/ER^2$) from 0.4 to 2.0 (b) Tests with higher stress parameters: 3.0 and 4.0.*

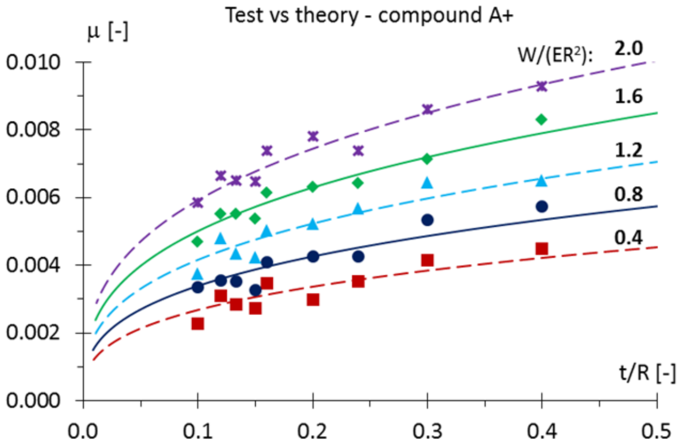

*Fig. 5.16 Comparison, for the compound A+, of the rolling friction values (μ) obtained by the tests and the theory, for different thickness/radius ratios (t/R) and stress parameters ($W/ER^2$).*

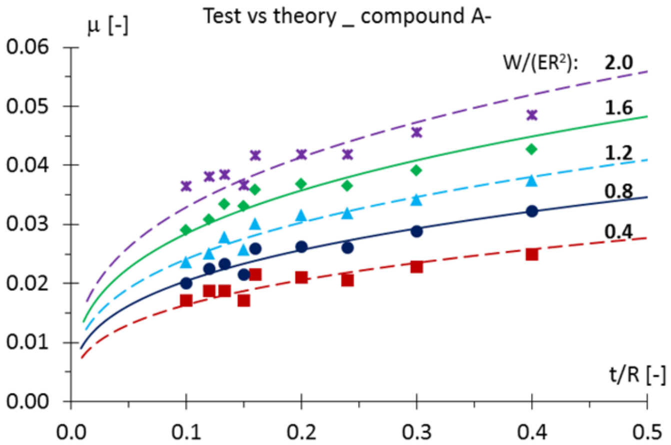

*Fig. 5.17 Comparison, for the compound A-, of the rolling friction values (μ) obtained by the tests and the theory, for different thickness/radius ratios (t/R) and stress parameters ($W/ER^2$).*

Fig. 5.19 presents for the compound A the rolling friction theory, calibrated with the experimentation and for a big range of t/R ratios, sufficient to obtain the maximum friction value due to an infinite thickness of the rubber layer. The t/R range considered in the experimentation is also indicated: this is actually smaller than the minimum value of t/R needed to reach the plateau value of μ (that changes with the stress level), but this is also the most realistic for the RBRL device. The fact that the test results fit the theory well in this small range of t/R, where there is the

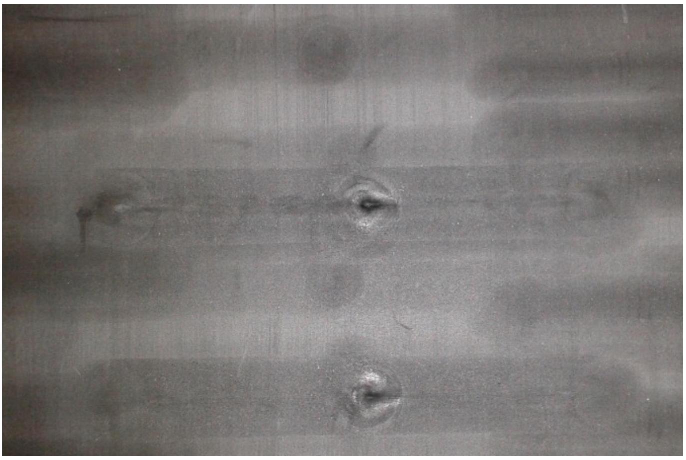

*Fig. 5.18 Semi-permanent rolling tracks after a test with rubber A and stress parameter 4.*

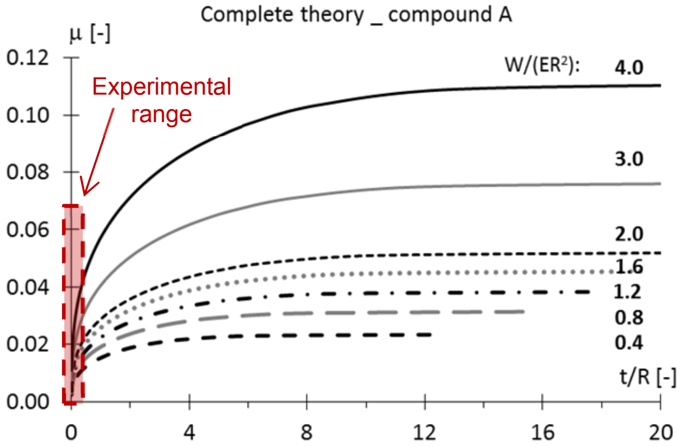

*Fig. 5.19 Complete theory in terms of (t/R), for rubber A, calibrated from experimentation.*

greatest variability in the μ values, gives hope for the utility of the theory also for bigger range of t/R.

Fig. 5.20 a) shows the values of the parameter $g$ calculated, according to Eq. (5.5), to get the best fitting between the theory and the test results. These values show that $g$, hence the parameter α, is a function of the stress level and depends on the type of the rubber compound (consistently with the initial assumptions for α). Moreover, the values of this parameter $g$ agree with the indications of Greenwood et al. (1961) previously reported.

Fig. 5.20 b) shows instead the possibility to calculate $g$ for any rubber, starting from the knowledge of the function $g$ (W/ER$^2$) for a reference compound

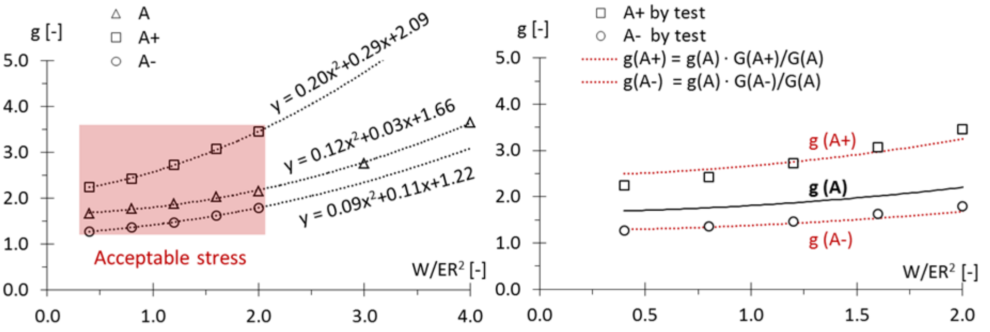

*a)* *b)*

*Fig. 5.20 a) $g$ parameter (see Eq. (5.5)) needed to scale the hysteretic parameter value, calculated as α=π·sinδ, to have the best fitting between theory and test results. b) Comparison, for rubber A+ and A-, between the values of the parameter $g$ obtained by tests and the ones calculated by Eq. (5.6), in which compound A is the reference one.*

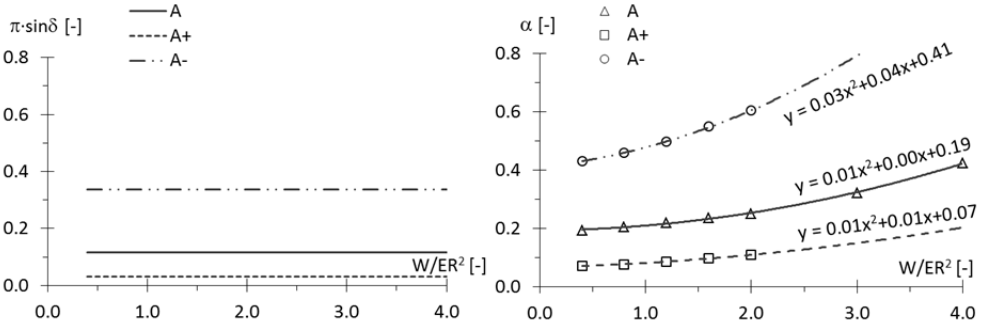

*a)* *b)*

*Fig. 5.21 a) Values of the hysteretic parameter α considering the classic definition: α=π·sinδ. b) α values calibrated from tests to have the best fitting with the theory (Eq. (5.5)).*

and using the following relation:

$$g\left(\frac{W}{ER^2}, rubber_i\right) = g\left(\frac{W}{ER^2}, rubber_{REF}\right) \cdot \frac{G_i}{G_{REF}} \tag{5.6}$$

The values of the α parameter are reported in Fig. 5.21 for all the rubbers analyzed: while in figure a) the classic definition of α was used ($\alpha = \pi \sin\delta$), in figure b) the values plotted are the experimental ones (i.e. the classic α values scaled by $g$). The values obtained for the parameter $g$, and hence α, suggest that the dissipated energy ratio, between a complex stress cycle and a simple uniaxial stress cycle, increases with the load applied (or stress level); furthermore, this ratio increases with the increasing of the shear modulus of the rubber, probably because this leads to a reduction of the dissipated energy in a simple uniaxial stress cycle and thus, in relative terms, to an increase of this ratio.

Finally, for an adequate range of t/R ratios, Fig. 5.22 provides the theoretical value of the rolling friction, calibrated through the performed experimentation, for each rubber compound and stress parameter analyzed.

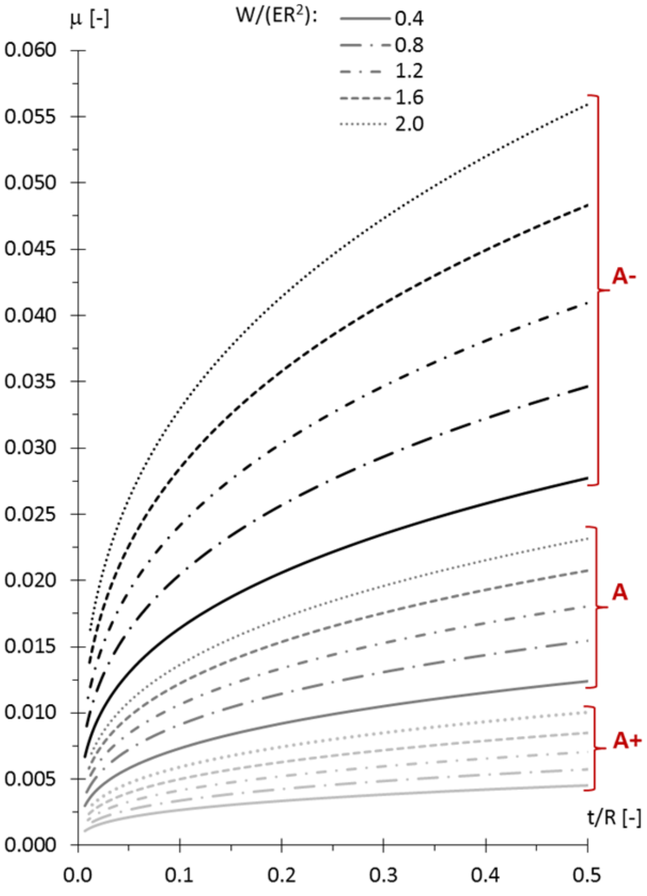

*Fig. 5.22 Theoretical μ values, calibrated through the experimentation, for each compound (A+, A, A-) and stress parameter ($W/ER^2$) analyzed, on an adequate range of t/R ratios.*

## 5.4 Sinusoidal double-shear tests on recentering rubber springs

### 5.4.1 Description of the tests

Fig. 5.23 shows the setup for the double shear tests carried out for the behaviour characterization of the recentering rubber springs. These springs are cylinders of rubber 80 mm long, bonded to steel endplates; they were moulded for the ECOEST Project from rubber compound A (Guerreiro et al., 2007), in three different diameters: 30, 40 or 50 mm (see Fig. 5.24).

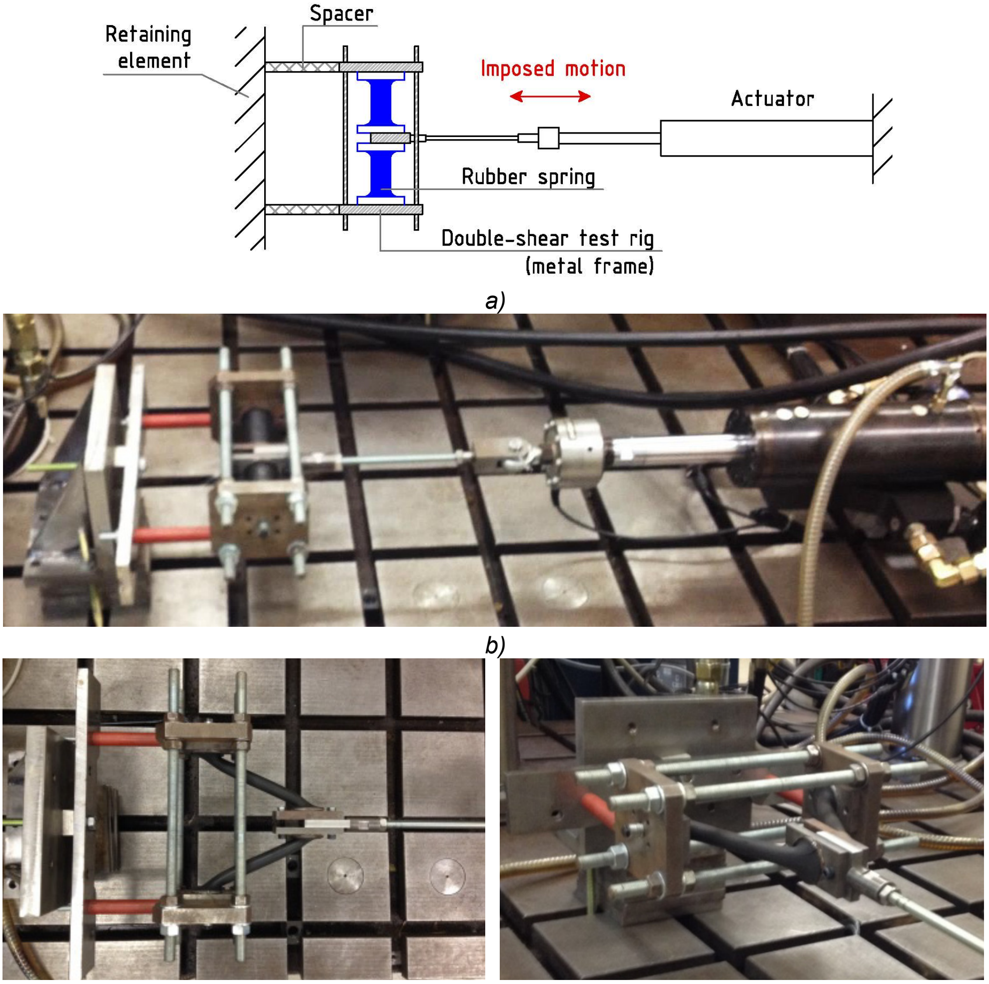
Spacer
Retaining element
Imposed motion
Actuator
Rubber spring
Double-shear test rig (metal frame)

a)

b)

c)

d)

*Fig. 5.23 a) Schematic drawing and b) image of the double shear test setup for the behaviour characterization of the recentering rubber springs. c),d) Images from quasi-static test for spring ϕ30 at 150 mm of deflection.*

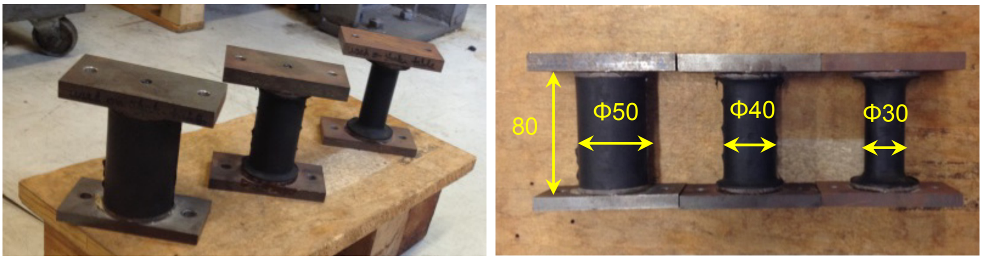

*Fig. 5.24 Tested recentering rubber springs; diameter (ϕ), from left to right: 50, 40, 30 mm.*

| | | |
|---|---|---|
| **Sinusoidal tests**<br>*different amplitudes* | *Frequency*<br>*Amplitudes* | **1 Hz**<br>2.5; 5; 7.5; 10; 20; 30; 40; 50; 60; 75 mm |
| **Sinusoidal tests**<br>*different frequencies* | *Amplitude*<br>*Frequencies* | **75 mm**<br>0.1; 0.5; 1; 2 Hz |
| **Quasi-static tests** | *Velocity*<br>*Displacements* | **1 mm/s**<br>from 0 to 150 mm |

*Tab. 5.8 Double shear tests carried out on the recentering rubber springs.*

Every test was conducted using two springs with the same diameter, constrained into a steel frame appositely designed for this purpose. The steel plate connecting the two spring endplates was linked to the arm of the actuator.

Both sinusoidal and quasi-static tests were considered, according to Tab. 5.8. In particular, concerning the imposed sinusoidal motion, tests were carried out with different amplitudes (from 1 to 75 mm) for the same frequency (1 Hz) and with different frequencies (from 0.1 to 2 Hz) for the same amplitude (75 mm).

### *5.4.2 Results*

Results from the sinusoidal tests are reported as force-displacement loops, Fig. 5.25 and Fig. 5.26, and in terms of equivalent linear viscoelastic frequency-domain (ELVFD) parameters, Fig. 5.27 and Fig. 5.28. In particular, Fig. 5.27 and Fig. 5.28 show the comparison for the ELVFD parameters calculated using the Harmonic and Secant linearization methods (Ahmadi & Muhr, 1997, see Section 3.2). Fig. 5.25 and Fig. 5.26 show force-displacement loops overlapped, indicating a not significant dependence on the velocity for the hysteretic behaviour of the recentering springs. From Fig. 5.27 and Fig. 5.28 it can be seen that the different linearization methods give approximately the same results for the ELVFD parameters. From these results, furthermore, it is easy to understand that if $K^{/}$ and $K^{//}$ increase with the increasing in the diameter value of the spring, the loss factor $\delta$ remains quite constant. Thus, the damping ratio $\zeta$ of these springs results

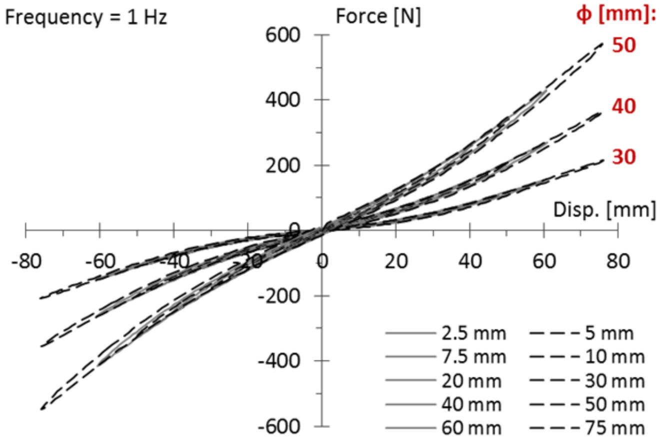

*Fig. 5.25 Hysteretic loops from the sinusoidal tests with same frequency,1 Hz, and different amplitudes; diameters of the springs tested: 30, 40, 50 mm. Values for one spring.*

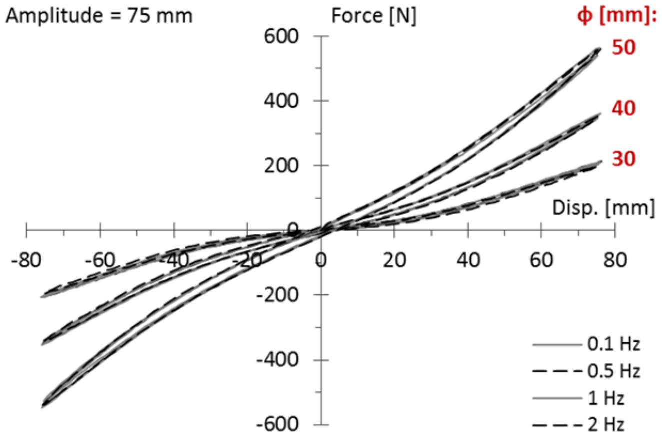

*Fig. 5.26 Hysteretic loops from the sinusoidal tests with same amplitude,75 mm, and different frequencies; diameters of the springs tested: 30, 40, 50 mm. Values for one spring.*

included in the range 1% to 2.5%, depending on the amplitude of the test, this ratio being roughly equal to $1/2 \cdot \tan\delta$ (by a Kelvin model representation). Fig. 5.27 gives also the equations (for the 30 mm spring) of the ELVFD parameters in function of the deflection amplitude; these could be used to calibrate a simple Kelvin model that, iteratively used, could be able to predict the spring behaviour. Moreover, it is possible to notice that the dependence of these parameters on the displacement amplitude shows the same shape for all the diameters analyzed. Fig. 5.28, furthermore, indicates what has already been seen in Fig. 5.26: the dynamic behaviour of the rubber springs has a negligible frequency dependence, although a

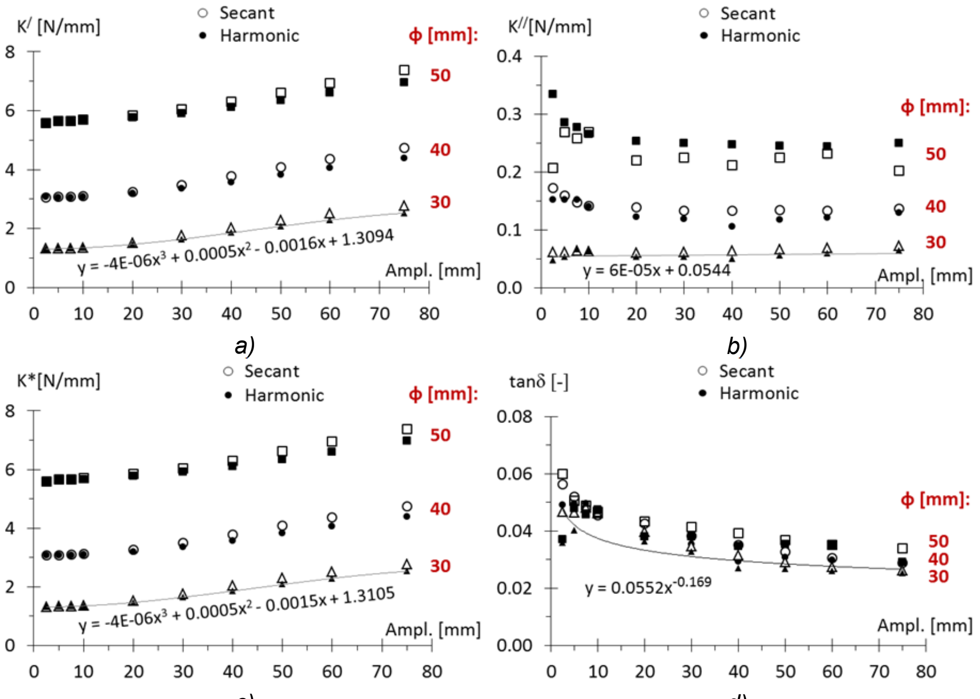

*a)* *b)* *c)* *d)*

*Fig. 5.27 ELVFD parameters from sinusoidal tests at the same frequency, 1 Hz. Comparison between the Harmonic and Secant linearization methods. Values for one spring.*

very slight increase in the values of the ELVFD parameters is visible with increasing frequency.

A limit of this sinusoidal experimentation is represented by the maximum displacement allowed by the actuator: 75 mm in each direction. To bypass this, quasi-static tests were also carried out on the same springs by the same actuator, but using its full stroke of 150 mm to reach a maximum spring deflection of 150 mm in one direction from the stress-free reference state.

These tests, whose results are reported in Fig. 5.29, were thus essential to understand the behaviour of the recentering springs for displacements bigger than 75 mm, this being actually not linear. The values plotted in Fig. 5.30, secant (a) and tangent (b) stiffnesses, were calculated from the results of the quasi-static tests using the equations below, in which “ $i$ ” indicates the generic recording step:

$$K^{i}_{\sec} = F^{i}/\Delta^{i} \tag{5.7}$$

$$K^{j}_{\tan} = (F^{i+1} - F^{i})/(\Delta^{i+1} - \Delta^{i})$$
$$associated \quad with: \quad \Delta^{j} = (\Delta^{i+1} + \Delta^{i})/2 \tag{5.8}$$

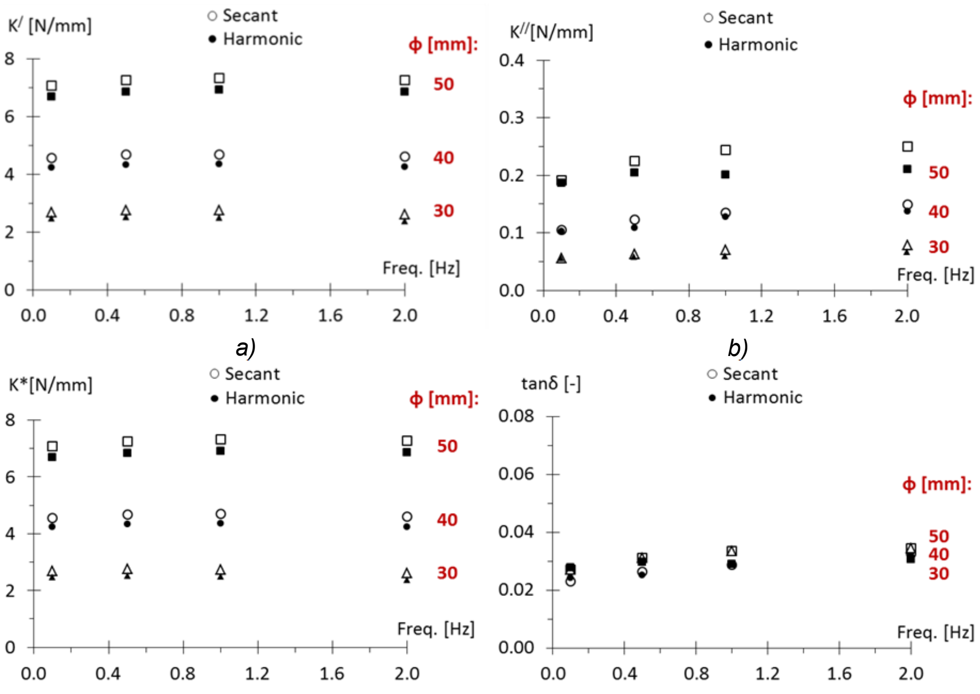

*a)* *b)*

*c)* *d)*

*Fig. 5.28 ELVFD parameters from sinusoidal tests at the same amplitude, 75 mm. Comparison between the Harmonic and Secant linearization methods. Values for one spring.*

While the secant stiffness is useful for design purpose (based on the concept of the equivalent stiffness at maximum displacement), the tangent one is needed in a time-history analysis (THA) for the prediction of the spring behaviour. As in the case of the ELVFD parameters by dynamic tests (Fig. 5.27), the dependence of the secant and tangent stiffnesses on the displacement amplitude (Fig. 5.30) exhibits the same shape for all the diameters analyzed.

The secant stiffness $K_{sec}$ (from quasi-static tests) and the storage stiffness $K^{/}$ (from dynamic tests) have substantially the same meaning, despite the fact that they are measured using different test methods. The comparison between these stiffnesses, reported in Fig. 5.31, shows an overall good overlap in the stiffness values for all the diameters. The principal and higher difference is limited to the first values of deflection. For displacements that tend to 0, indeed, the stiffness $K_{sec}$ tends to the value of the static stiffness $K_{st}$, calculated with Eq. (5.9) valid for small deformations and elastic material, while the storage stiffness $K^{/}$ tends to a bigger initial value (only experimentally calculable). Two equations for $K_{st}$ are reported below for a comparison, according respectively to Timoshenko's beam theory Corradi, 1993) and to Rivlin & Saunders (1949): the related values of $K_{st}$ for the diameters investigated are shown in Tab. 5.9.

$$K_{st} = \frac{12EJ}{(1+\beta)L^3}, \quad where \quad \beta = \frac{12EJ}{L^3}\frac{\chi L}{GA} \tag{5.9}$$

$$K_{st} = \frac{G}{1+\left(L^2/36k_r^2\right)}\frac{A}{t} \tag{5.10}$$

where E and G are respectively the Young's and shear moduli of the rubber, J is the second moment of area, L the length and A the cross area of the spring. $\beta$ is the shear deformability factor and $\chi$ is the Timoshenko's shear coefficient, equal to 10/9 for circular cross sections. $k_r$ is the radius of gyration of the cross section about the neutral axis: for a circular section $k_r^2 = \phi^2/16$.

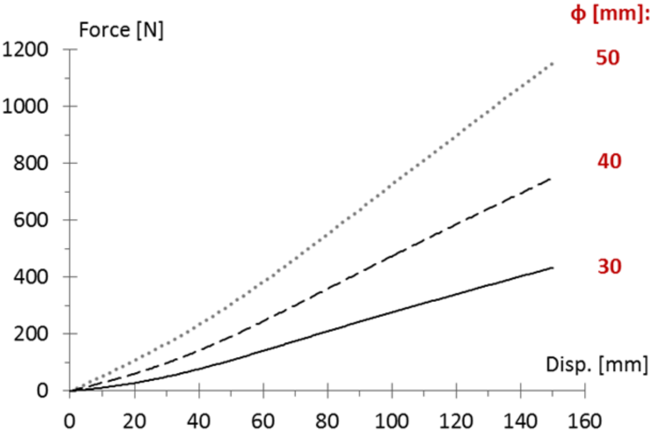

*Fig. 5.29 Force-deflection plots from quasi-static tests; diameters of the springs tested: 30, 40, 50 mm. Values for one spring.*

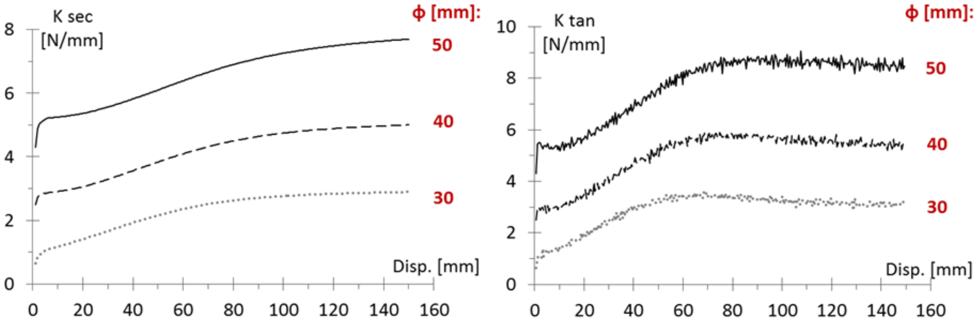

*a)* *b)*

*Fig. 5.30 a) Secant stiffness and b) tangent stiffness plots calculated from the results of the quasi-static tests (Fig. 5.29). Values for one spring.*

From Fig. 5.31 it is also observable that the dependence of the spring behaviour on the velocity of the test execution is more visible when the deflections are smaller and the diameters bigger. The dynamic behaviour of the springs is of primary interest for the characterization of the RBRL system, but it is possible to use the quasi-static tests results for the displacements bigger than 75 mm (the limit for the dynamic tests), so the stiffness finally considered derives from the dynamic stiffness values $K^{/}$ until 75 mm, and from the static stiffness values $K_{sec}$ for higher deflections (as indicated by the dashed interpolation lines in Fig. 5.31).

In Fig. 5.32 are reported the stiffness values obtained subtracting from the experimental results shown in Fig. 5.31 the initial values of $K^{/}$ associated with each diameter. The result obtained by this elaboration is that the nonlinear dependence of the $K^{/}$ stiffness of the springs on the displacement amplitude is similar for all the diameters analyzed; thus, it was approximated by the following equation, interpolating the mean values between the different diameters:

$$\Delta K^{/}\left(D\right)=1.41\cdot 10^{-8}\cdot D^{4}-5.11\cdot 10^{-6}\cdot D^{3}+5.37\cdot 10^{-4}\cdot D^{2}-7\cdot 10^{-4}\cdot D \qquad (5.11)$$

where $D$ indicate the deflection of the spring (in mm) and $\Delta K^{/}\left(D\right)$ the storage stiffness contribution related to the displacement (in N/mm).

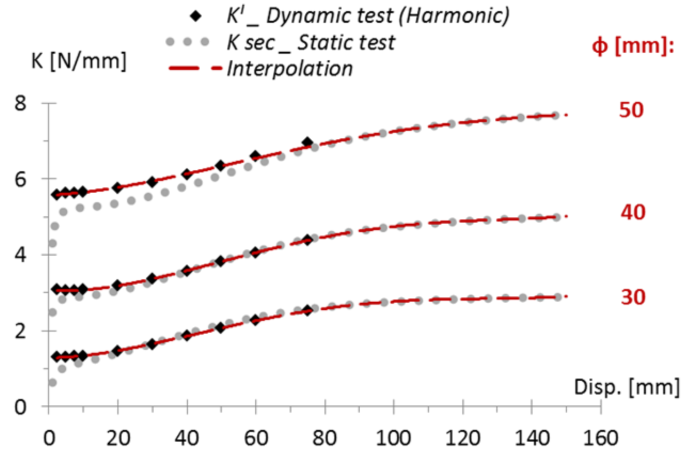

*Fig. 5.31 Comparison between the storage stiffness $K^{/}$, from dynamic tests, and the secant one $K_{sec}$, from quasi-static tests. The stiffness finally considered derives from $K^{/}$ values until 75 mm, and from $K_{sec}$ values for higher deflections (as indicated by the dashed lines).*

| $K_{st}$ : | $\phi=30mm$ | $\phi=40mm$ | $\phi=50mm$ |
|---|---|---|---|
| *from Eq. (5.9)* | 0.8 N/mm | 2.2 N/mm | 4.4 N/mm |
| *from Eq. (5.10)* | 0.8 N/mm | 2.3 N/mm | 4.6 N/mm |

*Tab. 5.9 Static stiffness $K_{st}$ values, according to Eqs. (5.9)-(5.10), for the various diameters.*

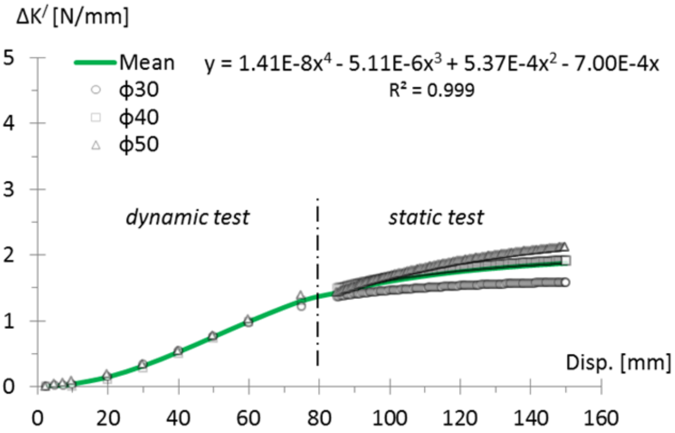

*Fig. 5.32 Nonlinear dependence of the stiffness $K^{/}$ on deflection. Values obtained by the ones of Fig. 5.31 subtracting the initial values of stiffness $K^{/}$ associated with each diameter.*

It was also understood that the difference between the initial values of the dynamic stiffness $K^{/}$, for two different diameters analyzed, is related to the difference between the relative values of the static stiffness $K_{st}$ (see Eq. (5.9)) through a factor of about 1.25. Thus it is possible to write:

$$\begin{aligned} K^{/}_{init}\left(\phi_i\right) &= K^{/}_{init}\left(\phi_{ref}\right) + \Delta K^{/}\left(\phi_i,\phi_{ref}\right) = \\ &= K^{/}_{init}\left(\phi_{ref}\right) + \left[K_{st}\left(\phi_i\right) - K_{st}\left(\phi_{ref}\right)\right]\cdot 1.25 \end{aligned} \tag{5.12}$$

where $\phi_{ref}$ and $\phi_i$ are respectively the diameter of reference and the one for which the initial value of the storage stiffness $K^{/}_{init}$ has to be calculated. From the two previous equations it is thus possible to get the following equation:

$$K^{/}\left(\phi_{i,}D\right) = K^{/}_{init}\left(\phi_i\right) + \Delta K^{/}\left(D\right) \tag{5.13}$$

where $K^{/}_{init}\left(\phi_i\right)$ and $\Delta K^{/}\left(D\right)$ are respectively calculated by Eqs. (5.12) and (5.11).

This equation is very useful for the design purpose, predicting the stiffness values $K^{/}$ for different values of spring diameter and deflection. These values are shown in Fig. 5.33 for different diameters in the range 20 to 60 mm and up to 150 mm of deflection; in particular, these values were calculated through Eq. (5.13) considering a reference diameter of 30 mm, so a value of $K^{/}_{init}\left(\phi_{ref}\right)$ equal to 1.31 N/mm.

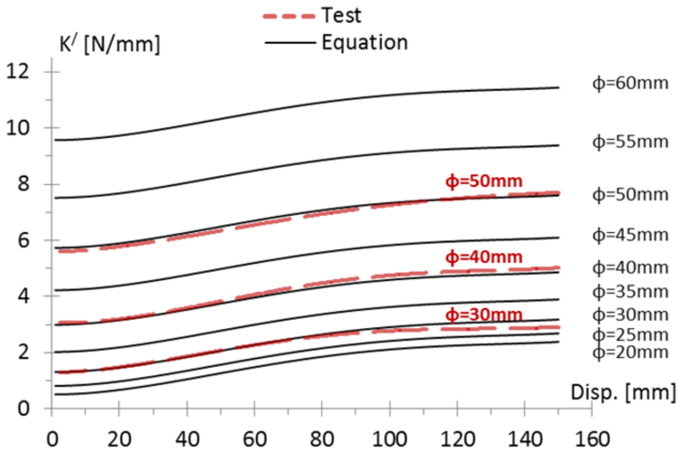

*Fig. 5.33 Prediction of the storage stiffness values K/, using Eq. (5.13), and comparison with the experimental values for the diameters 30, 40 and 50 mm.*

The same elaboration procedure concerning the K/ stiffness values, needed for the design purpose, was replicated considering the tangent stiffness values $K_{tan}$, that are necessary for the prediction of the spring behaviour through a time-history analysis. The tangent stiffness values were calculated using the Eq. (5.8). Consistently with what has been done previously, these values were obtained from dynamic tests or K/ values until 75 mm, using F=K/·D in the Eq. (5.8), while for bigger deflections the values from static tests were considered (see Fig. 5.30 b). The nonlinear dependence of the tangent stiffness of the springs on the deflection, $\Delta K_{\tan}(D)$, is reported in Fig. 5.34: with some approximations, it could be represented with a unique equation interpolating the mean values between the various diameters tested:

$$\begin{aligned}\Delta K_{\tan}(D) = &-6.02\cdot 10^{-10}\cdot D^5 + 2.736\cdot 10^{-7}\cdot D^4 - 4.38\cdot 10^{-5}\cdot D^3 + \\ &+ 2.65\cdot 10^{-3}\cdot D^2 - 1.47\cdot 10^{-2}\cdot D\end{aligned} \quad (5.14)$$

Similarly to Eq. (5.13) for K/, it is possible to write the following equation for the tangent stiffness prediction, depending on the spring diameter and deflection:

$$K_{\tan}(\phi_{i,}D) = K^{/}_{init}(\phi_i) + \Delta K_{\tan}(D) \quad (5.15)$$

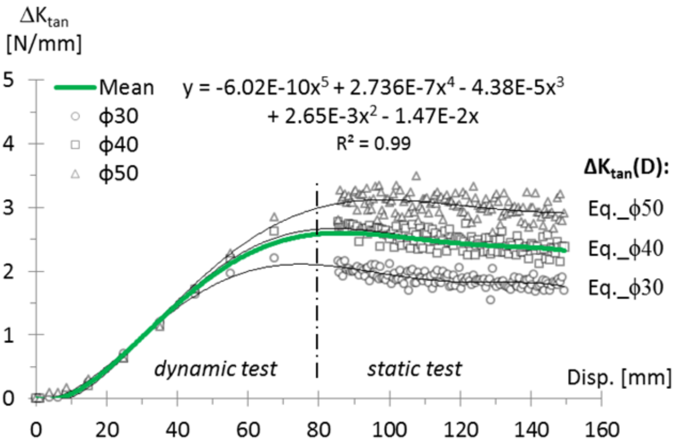

*Fig. 5.34 Nonlinear dependence of the tangent stiffness $K_{tan}$ of the springs on deflection.*

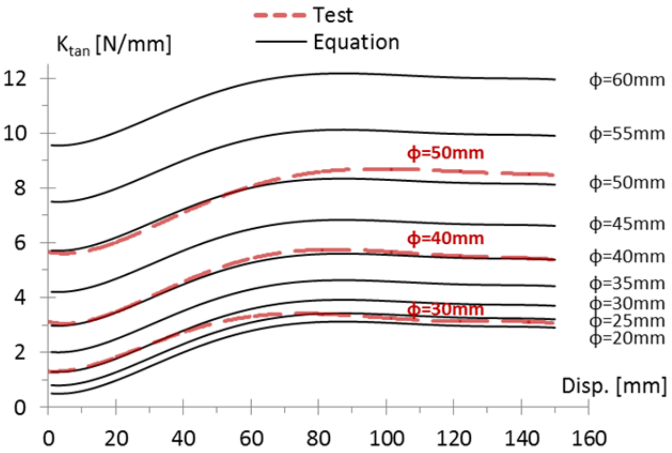

*Fig. 5.35 Prediction of the tangent stiffness values $K_{tan}$, using Eq. (5.15), and comparison with the experimental values for the diameters 30, 40 and 50 mm.*

where $K^{/}_{init}(\phi_i)$ and $\Delta K_{\tan}(D)$ are respectively calculated by Eqs. (5.12) and (5.14). The stiffness values, calculated using this equation, are shown in Fig. 5.35 for different diameters in the range 20 to 60 mm and up to 150 mm of deflection. Also in this case, the 30 mm diameter was taken as reference in the Eq. (5.12).

If more accuracy is required in the calculation of the tangent stiffness, $\Delta K_{\tan}(D)$ and $K^{/}_{init}(\phi_i)$ are reported in Tab. 5.10 for each diameter tested. Thus, for those diameters and by Eq. (5.15), the $K_{\tan}$ values can be predicted more precisely.

| $\phi_i$ [mm] | $K^{/}_{init}$ [N/mm] | $\Delta K_{\tan}(D)$ [N/mm] |
|---|---|---|
| 30 | 1.31 | $\Delta K_{\tan}(D) = -7.30\cdot10^{-10}\cdot D^5 + 3.096\cdot10^{-7}\cdot D^4 - 4.56\cdot10^{-5}\cdot D^3 +$<br>$+ 2.47\cdot10^{-3}\cdot D^2 - 8.19\cdot10^{-3}\cdot D$ |
| 40 | 3.08 | $\Delta K_{\tan}(D) = -6.91\cdot10^{-10}\cdot D^5 + 3.144\cdot10^{-7}\cdot D^4 - 5.05\cdot10^{-5}\cdot D^3 +$<br>$+ 3.10\cdot10^{-3}\cdot D^2 - 2.41\cdot10^{-2}\cdot D$ |
| 50 | 5.57 | $\Delta K_{\tan}(D) = -3.86\cdot10^{-10}\cdot D^5 + 1.967\cdot10^{-7}\cdot D^4 - 3.53\cdot10^{-5}\cdot D^3 +$<br>$+ 2.37\cdot10^{-3}\cdot D^2 - 1.18\cdot10^{-2}\cdot D$ |

*Tab. 5.10 Initial value of the storage stiffness, $K^{/}_{init}$, and nonlinear dependence of the tangent stiffness on the deflection, $\Delta K_{\tan}(D)$, for the various diameters $\phi_i$ tested.*

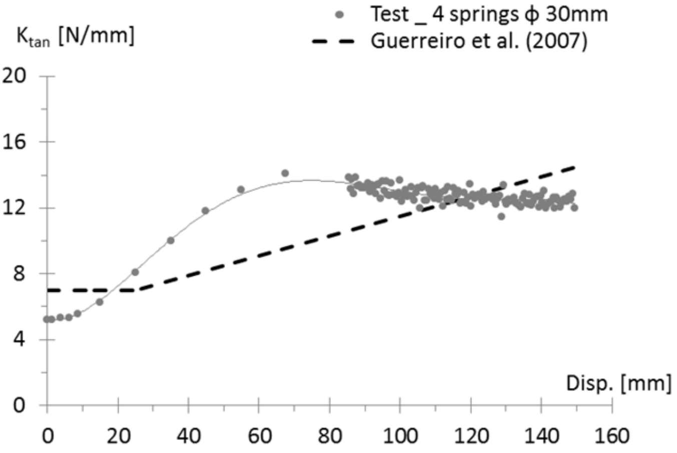

*Fig. 5.36 Tangent stiffness calculated by the experimental results, compared with the one proposed in the Guerreiro et al. (2007) Model for the RBRL device, relatively to the recentering springs system used in the ECOEST Project (4 spring, diameter 30 mm).*

Finally, Fig. 5.36 presents the tangent stiffness calculated by the experimental results here presented, compared with the one proposed in the Guerreiro et al. (2007) Model for the RBRL device, relatively to the recentering springs system used in the ECOEST Project (4 spring, diameter 30 mm).

## 5.5 Design procedure of the RBRL system: parametric investigation

All the tests described have been aimed at obtaining an effective and simplified design procedure for the non-linear RBRL system, hereinafter presented. Following what is reported in section 3.1.3, according to Cook et al. (1997), the values of the stiffness $K$ and rolling friction coefficient $\mu$ of the RBRL system can be determined through the equations reported below, if the values of period $T$ and damping ratio $\zeta$ have been decided and if the displacement D from the damped spectrum and the mass $M$ to be isolated are known.

$$K = \frac{4\pi^2 M}{T^2} \tag{5.16}$$

$$\mu \equiv \frac{F_R}{Mg} = \frac{1}{g} \frac{2\pi^3 D\zeta}{T^2\left(1-\pi\zeta/2\right)} \tag{5.17}$$

These equations were obtained considering an elasto-plastic hysteresis loop (Fig. 3.3) as dynamic response of the RBRL system, and using the Secant linearization method (Ahmadi & Muhr, 1997). These can be used if parameter $\zeta$ does not grossly exceed 20% and if the seismic excitation is sufficient for the peak roll-out force to be generated for much of the time history. For lower seismic excitations, the behaviour of the device will be governed by the effective dynamic stiffness of the balls rocking in their static depressions or “pits”: for this reason the method here presented is proposed for use only for design purposes, considering the maximum response spectrum as the design spectrum.

When the values of $K$ and $\mu$ have been calculated, together with the ultimate displacement by the damped DRS, the geometric characteristics of the RBRL system can be determined through the previous experimental results. Using the parametric plots of Fig. 5.33, represented here below in Fig. 5.37, the correct diameter of the recentering springs to achieve the target stiffness of the system can be easily found by entering the figure with the values of displacement and $K$. Once the stress parameter has been decided, then, the value of the ratio $t/R$ needed to get the correct $\mu$ can be obtained using the theory of Muhr et al. (1997) experimentally calibrated in the $\alpha$ value or, more directly, using the parametric plots of Fig. 5.22 if the rubber type is one of those tested. Tab. 5.11 reports some results from the calibrated theory in terms of $\mu$ and related $t/R$ for some chosen values of stress parameter: these results cover the most realistic range of possibilities for the RBRL device with rubber A. This table has to be used entering with the values of $\mu$ and $W / ER^2$, so finding the relative value of $t / R$. Finally, the radius $R$ of the steel ball needs to be decided to get the value of the rubber layer thickness $t$ and, according to Eq. (5.18), the number of the balls $N_b$.

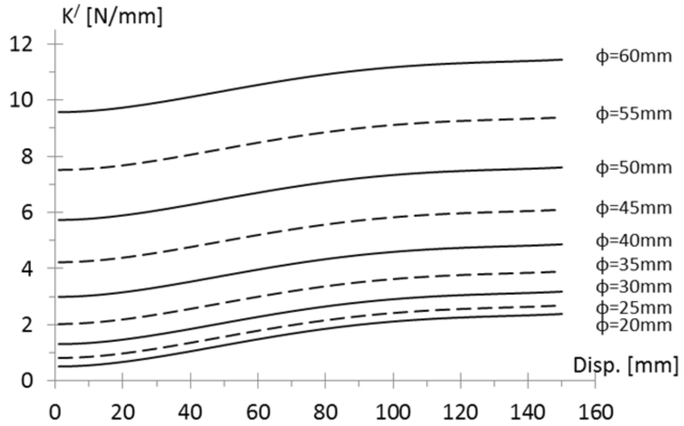

*Fig. 5.37 Prediction of the storage stiffness values K/, using Eq. (5.13).*

| | W/ER²=0.6 | W/ER²=0.8 | W/ER²=1 | W/ER²=1.2 | W/ER²=1.4 | W/ER²=1.6 |
|---|---|---|---|---|---|---|
| ***μ [-]*** | ***t/R [-]*** | | | | | |
| *0.008* | 0.09 | | | | | |
| *0.009* | 0.13 | 0.10 | | | | |
| *0.01* | 0.18 | 0.14 | 0.11 | | | |
| *0.011* | 0.23 | 0.18 | 0.14 | 0.11 | | |
| *0.012* | 0.31 | 0.24 | 0.19 | 0.15 | 0.12 | |
| *0.013* | 0.39 | 0.30 | 0.24 | 0.19 | 0.15 | 0.13 |
| *0.014* | 0.49 | 0.38 | 0.30 | 0.24 | 0.19 | 0.16 |
| *0.015* | 0.61 | 0.47 | 0.37 | 0.30 | 0.24 | 0.19 |
| *0.016* | 0.75 | 0.57 | 0.45 | 0.36 | 0.29 | 0.24 |
| *0.017* | 0.91 | 0.69 | 0.54 | 0.43 | 0.35 | 0.28 |
| *0.018* | | 0.83 | 0.65 | 0.52 | 0.42 | 0.34 |
| *0.019* | | 0.98 | 0.77 | 0.61 | 0.49 | 0.40 |
| *0.02* | | | 0.90 | 0.72 | 0.58 | 0.47 |
| *0.021* | | | 1.05 | 0.84 | 0.67 | 0.54 |
| *0.022* | | | | 0.97 | 0.78 | 0.63 |
| *0.023* | | | | 1.12 | 0.89 | 0.72 |
| *0.024* | | | | | 1.02 | 0.82 |
| *0.025* | | | | | | 0.93 |
| *0.026* | | | | | | 1.06 |

*Tab. 5.11 Rolling friction for rubber A calculated from stipulated values of thickness ratio t/R and selected stress parameter values W/ER$^2$ using the theory of Muhr et al. (1997), experimentally calibrated.*

$$N_b = \frac{M \cdot g}{\left(W/ER^2\right) \cdot E \cdot R^2} \tag{5.18}$$

Design procedure calls for two free choices to be made, the values of $W/ER^2$ and $R$. A different combination of the stress parameter $W/ER^2$ with the parameter $t/R$, that leads to the same $\mu$, does not change the steady-state behaviour of the device and, as will be seen in the next Chapter, this is not expected to influence the roll-out behaviour too. The appropriate value of this stress parameter is thus a compromise between cost and the necessity to avoid the creation of semi-permanent rolling tracks. Indeed, using higher stress levels, thus fewer balls and a thinner layer of rubber, the system becomes cheaper but the stress in the rubber layers increases. Considering the lack of knowledge about the stress limit to avoid permanent deformation or rupture of the rubber sheets, we believe that convenient and safe values of the stress parameter could stay in the range 1 to 1.4. At the end of the design procedure also the parameter $R$ has to be decided: this does not influence the steady-state response of the device, but seems to affect the distance of roll-out of the balls from their initial depressions (see next Chapter). Once again, this choice is important from an economic point of view, the steel balls being one of the principal cost components. All these remarks are not so important thinking of the single application of the RBRL system, but become strategic considering that the device is relatively economical and easy to tailor for the specific case in terms of geometry and performance, thus conveniently applicable on a large scale (like inside a museum to isolate single artefacts, showcases or podia).

Here below are reported some design examples of the RBRL system. For this purpose the following input data were assumed:

- isolation period, $T$ : 1, 2, 3, 4 seconds;
- damping coefficient, $\zeta$ : 10%, 20%, 30%;
- mass to isolate, $M$: 0.3, 0.6, 1.2 ton.
- The seismic action considered is obtained from the elastic displacement response spectrum proposed by EC8 (2004), assuming a spectrum of “type 1”, a ground of “type B” and a bedrock acceleration of 0.15 [g]. Fig. 5.38 shows the damped design spectra ($\zeta$ >5%) in addition to the elastic reference spectrum ($\zeta$ =5%); the ordinates of the damped spectra $D(T,\zeta)$ were derived from the ones of the elastic spectrum $D_{el}(T)$ with the following equations (from EC8, 2004):

$$D(T,\zeta) = D_{el}(T) \cdot R_{\zeta} \tag{5.19}$$

where $$R_{\zeta} = \left( \frac{10}{5+\zeta(\%)} \right)^{0.5} \tag{5.20}$$

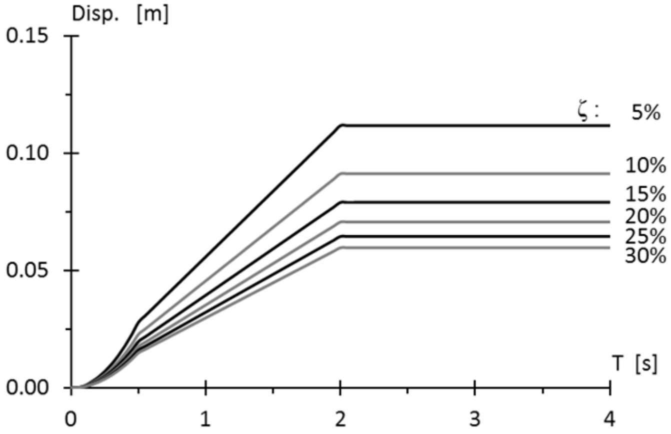

*Fig. 5.38 Design displacement response spectra from EC8 (2004), assuming a spectrum of "type 1", a ground of "type B" and a bedrock acceleration of 0.15 [g].*

| | | | | **M** = 0.3 t | M = 0.6 t | M = 1.2 t |
|---|---|---|---|---|---|---|
| *ζ* [%] | ***T*** [s] | *Disp.* [mm] | ***μ*** [-] | ***K*** [N/mm] | | |
| 10 | 1 | 46 | 0.034 | 11.8 | 23.7 | 47.4 |
| | 2 | 91 | 0.017 | 3.0 | 5.9 | 11.8 |
| | 3 | 91 | 0.008 | 1.3 | 2.6 | 5.3 |
| | 4 | 91 | 0.004 | 0.7 | 1.5 | 3.0 |
| 20 | 1 | 35 | 0.065 | 11.8 | 23.7 | 47.4 |
| | 2 | 71 | 0.033 | 3.0 | 5.9 | 11.8 |
| | 3 | 71 | 0.015 | 1.3 | 2.6 | 5.3 |
| | 4 | 71 | 0.008 | 0.7 | 1.5 | 3.0 |
| 30 | 1 | 30 | 0.107 | 11.8 | 23.7 | 47.4 |
| | 2 | 60 | 0.054 | 3.0 | 5.9 | 11.8 |
| | 3 | 60 | 0.024 | 1.3 | 2.6 | 5.3 |
| | 4 | 60 | 0.013 | 0.7 | 1.5 | 3.0 |

*Tab. 5.12 Values of μ and K needed to obtain a RBRL isolation system able to provide the relative isolation periods and damping ratios, considering the design spectrum above. The highlighted values of μ are the ones more compatible with a rubber of type A.*

Tab. 5.12 provides the rolling friction coefficient $\mu$ and the stiffness $K$ of the isolation system at the ultimate displacement for all the combinations of the assumed design parameters ($\zeta$ ,$T$ and $M$); these values were obtained using Eqs. (5.16) and (5.17).

If we would isolate, for example, an object with a mass of 1.2 t providing an isolation period of 3 seconds and a damping coefficient of 20%, from the Tab. 5.12 the requisite values of $K$ and $\mu$ are respectively 5.3 N/mm and 0.015. The recentering system can next be designed through the parametric plots of Fig. 5.37; to achieve a stiffness of 5.3 N/mm for a displacement of 71 mm (see Tab. 5.12) more options are possible: use only one spring of 45 mm diameter, two springs of 30 mm, etc… Using the results from the theory of Muhr et al. (1997) reported in Tab. 5.11 and assuming a stress parameter of 1.4, the ratio $t / R$ needed to get the requisite value of $\mu$ results to be 0.24. Finally, considering a radius of the ball of 12.5 mm, the necessary thickness of the rubber layers $t$ is 3 mm, and the number of balls $N_b$ to be used is 48, according to Eq. (5.18)).

## 5.6 Conclusions

This chapter has given results for tests on the RBRL system, and pointed to a general design procedure. It should be noted that all the rubber surfaces were dusted with talc to avoid adhesion effects between the rolling tracks and the steel balls, albeit slight, in order to have also the same test conditions for all the devices. The conclusions emerged are listed below.

1- The theory of Muhr et al. (1997) for rolling friction on thin rubber layers was implemented numerically and compared to experimental results. The theory proved useful with calibration of the hysteresis parameter α, which was experimentally obtained for three different rubbers (A, A+, A-) through sinusoidal monoaxial parametric tests on diverse RBRL devices. In particular, 153 tests in total were performed considering diverse combinations of the parameters of the device.

2- This theory permits calculation of the rolling friction ratio for the rolling of a steel ball between two rubber-layered tracks, if the following parameters are known: load per ball W, radius R of the ball, thickness t of the rubber layers, Young's modulus E and hysteresis parameter $\alpha$ of the rubber. This result could be important at two different levels:

- one more general, related to technological and scientific research in the rubber field, for which this theory could be a useful tool;
- one more specific, related to modelling of the rolling friction force for the RBRL device in steady-state conditions, for design purposes and for the device behaviour assessment.

3- For the prediction of the rolling friction coefficient using a different rubber compound than the ones tested and for which the theory of Muhr et al. was calibrated, it is still possible to use this theory with Eq. (5.5) and (5.6) for the calculation of the parameter α, within an acceptable range of stress level (stress parameter less than 2). Thus, knowing the function $g$ (W/ER$^2$) for a reference compound and the shear moduli of the rubbers, the one chosen for the application and the reference one, it is possible to generalize the use of this theory for any unfilled natural rubber.

It is noteworthy that the choice made to calculate the mean value of friction between the first and second pass of the ball on the same rolling track does not affect the verification of the utility of the theory. This choice only influences the calibration of the parameter α, leading to μ values that are approximate and not able to capture second-order effects such as those of velocity or repeated passes on the same rolling track. In particular, considering a difference of friction force between the first and second pass of the ball in the range of 10% to 30% (depending on test conditions and rubber compound), the calibration of the theory through this experimentation could lead to underestimate μ values within a range of about 5% to 15%.

4- An experimentation on the recentering rubber springs of the RBRL system is also presented, consisting of different monoaxial sinusoidal tests and quasi-static tests. Three types of spring were analyzed, characterized by a different diameter; these springs were made with the same low-damping compound (A) as for the ECOEST project. The characterization of the dynamic behaviour of the recentering springs is a fundamental phase in the comprehension of the global behaviour of the RBRL system, since they provide its stiffness in the steady-state rolling phase, determining the fundamental oscillation period of the isolated structure. The results from these tests are presented in terms of force-displacement loops and ELVFD parameters. A non-linear amplitude-dependent response with a negligible energy dissipation, in particular for the smaller diameters, was observed. The numerical elaborations of the results led to obtain parametric empirical formulations for the prediction of the secant and tangent stiffness of the spring, as a function of diameter and deflection of the spring itself. For simple handling, the results obtained by these formulations are also presented in parametric plots. If the knowledge of the secant stiffness of the spring at the maximum deflection of the RBRL system is fundamental for the design purposes, the knowledge of the tangent stiffness becomes essential for the assessment of the behaviour of the isolation system using a time-domain model.

5- All the tests described in this chapter have been aimed at obtaining an effective and simplified design procedure for the non-linear RBRL system. According to the procedure presented in Cook et al. (1997) and to the theory of Muhr et al. (1997), and considering the results gathered by the experimentations presented, a design procedure is proposed which is able to provide all the parameters of the RBRL system, for a specific design spectrum and vertical load, when the values of isolation period and damping ratio are chosen.

# 6 INVESTIGATIONS ON SMALL-DEFLECTIONS BEHAVIOUR OF RBRL SYSTEM: PROPOSAL OF A TIME-DOMAIN MODEL

## 6.1 Introduction

The absence of available experimental results for the characterization of the device behaviour for small deflections, namely with balls rocking in their pits or rolling in the transition phase between the initial static configuration and the free rolling, suggest the necessity to carry out further parametric experimentation.

Three different sets of experiments are herein presented and discussed.

- The first one consists of some parametric sinusoidal monoaxial tests on the new RBRL devices, produced at TARRC specifically for this purpose (see Section 5.1): the force-displacement behaviour for small deflections was investigated, with different imposed sinusoidal motions, considering a dwell time of the load of 25 hours.

- The second set concerns the direct measurement, immediately after unloading, of the pit geometric profiles and maximum indentation values, to find some relations between these and the associated non-linear force-displacement responses at small deflections. For this experimentation, using the same realization procedure followed for the RBRL devices (see Section 5.1), new smaller samples were produced; the same rubber compound, A+, A, A- were used.

- The last set of experiments herein described consists of sinusoidal monoaxial tests, but the tested devices are the same ones used in the ECOEST Project, thus with rubber tracks of type A, low damping, and B, high damping, moulded 15 years ago. These tests were carried out considering different dwell times of the load in its static configuration. Thus, useful information was gathered, not only for the device behaviour with a rubber aged of 15 years or with a high-damping compound (B), but also about the influence of the dwell time on the initial indentation and, hence, on the peak force for roll-out of the balls.

All the experimental results, and the associated numerical elaborations presented below, address the behaviour of the devices at small-deflections and all those phenomena that influence it. This enables provision of a time-domain model for the RBRL system: such a model is necessary for the prediction of the system behaviour, and hence a prerequisite for the quantification of the seismic mitigation efficacy of the system and for the achievement of the design objectives.

## 6.2 Sinusoidal uniaxial tests on new RBRL devices: small-deflections behaviour

### *6.2.1 Description of the tests*

The RBRL devices used in these tests are the ones produced at TARRC (see section 5.1) and already used for the parametric experimentation on steady-state rolling friction, presented in the previous chapter. The test setup is the same as illustrated in section 5.3.1. The devices were tested without the recentering rubber spring.

The input of these sinusoidal test sequences is presented in Tab. 6.1. It is composed of 25 tests, each consisting of a sinusoidal motion of three cycles, with imposed displacements of increasing amplitude from 1 to 20 mm. Every amplitude was associated with two sinusoidal tests: one with the same maximum velocity value, equal to 31,4 mm/s, and the other with the same frequency value, equal to 1 Hz. Each sinusoidal test was spaced from the previous and following ones by 8 seconds, in order to recreate approximately the undisturbed conditions. For the case of 5 mm amplitude, the frequency of 1 Hz corresponds to a velocity amplitude of 31 mm/s, so only one sinusoidal test was run for this amplitude; the tests with constant frequency below 5 mm amplitude are characterized by a maximum velocity lower than 31 mm/s, vice-versa for the tests with amplitudes greater than 5 mm.

| *STEP:* | Amplitude | Frequency | Max. velocity | N° cycles | Time test | N° points | Sample freq. |
|---|---|---|---|---|---|---|---|
| | [mm] | [Hz] | [mm/s] | [-] | [s] | [-] | [Hz] |
| *1* | 1 | 5 | **31.4** | 3 | 0.6 | 200 | 1000 |
| *2* | 1 | **1** | 6.3 | 3 | 3 | 200 | 200 |
| *3* | 2 | 2.5 | **31.4** | 3 | 1.2 | 400 | 1000 |
| *4* | 2 | **1** | 12.6 | 3 | 3 | 400 | 400 |
| *5* | 3 | 1.67 | **31.4** | 3 | 1.8 | 600 | 1000 |
| *6* | 3 | **1** | 18.8 | 3 | 3 | 600 | 600 |
| *7* | 4 | 1.25 | **31.4** | 3 | 2.4 | 800 | 1000 |
| *8* | 4 | **1** | 25.1 | 3 | 3 | 800 | 800 |
| *9* | **5** | **1** | **31.4** | 3 | 3 | 1000 | 1000 |
| *10* | 6 | 0.83 | **31.4** | 3 | 3.6 | 1200 | 1000 |
| *11* | 6 | **1** | 37.7 | 3 | 3 | 1200 | 1200 |
| *12* | 7 | 0.71 | **31.4** | 3 | 4.2 | 1400 | 1000 |
| *13* | 7 | **1** | 44.0 | 3 | 3 | 1400 | 1400 |
| *14* | 8 | 0.63 | **31.4** | 3 | 4.8 | 1600 | 1000 |
| *15* | 8 | **1** | 50.3 | 3 | 3 | 1600 | 1600 |
| *16* | 9 | 0.56 | **31.4** | 3 | 5.4 | 1800 | 1000 |
| *17* | 9 | **1** | 56.5 | 3 | 3 | 1800 | 1800 |
| *18* | 10 | 0.5 | **31.4** | 3 | 6 | 2000 | 1000 |
| *19* | 10 | **1** | 62.8 | 3 | 3 | 2000 | 2000 |
| *20* | 12.5 | 0.4 | **31.4** | 3 | 7.5 | 2500 | 1000 |
| *21* | 12.5 | **1** | 78.5 | 3 | 3 | 2500 | 2500 |
| *22* | 15 | 0.33 | **31.4** | 3 | 9 | 3000 | 1000 |
| *23* | 15 | **1** | 94.2 | 3 | 3 | 3000 | 3000 |
| *24* | 20 | 0.25 | **31.4** | 3 | 12 | 4000 | 1000 |
| *25* | 20 | **1** | 125.7 | 3 | 3 | 4000 | 4000 |

*Tab. 6.1 Sinusoidal input of the tests and characteristics of the output data. Every step was spaced from the previous one by 8 seconds to recreate the undisturbed conditions.*

| *N° test* | t | D ball | W/(ER$^2$) | N° balls | W tot | ΔW test |
|---|---|---|---|---|---|---|
| | [mm] | [mm] | [-] | [-] | [kg] | [kg] |
| | | | Rubber **A** | | | |
| *1* | 1.5 | 25 | 1.2 | 8 | 174.4 | 24.4 |
| *2* | 2 | 20 | 1.2 | 12 | 167.4 | 17.4 |
| *3* | 2 | 25 | 0.4 | 24 | 174.4 | 24.4 |
| *4* | 2 | 25 | 0.8 | 12 | 174.4 | 24.4 |
| *5* | 2 | 25 | 1.2 | 8 | 174.4 | 24.4 |
| *6* | 2 | 25 | 1.6 | 6 | 174.4 | 24.4 |
| *7* | 2 | 25 | 2.0 | 6 | 218.0 | 68.0 |
| *8* | 2 | 30 | 1.2 | 6 | 188.3 | 38.3 |
| *9* | 3 | 25 | 1.2 | 8 | 174.4 | 24.4 |
| | | | Rubber **A-** | | | |
| *10* | 2 | 25 | 1.2 | 10 | 166.4 | 16.4 |
| | | | Rubber **A+** | | | |
| *11* | 2 | 25 | 1.2 | 6 | 192.7 | 42.7 |

**ΔW test** = additional load to be applied on the test. Initial vertical load of the test steup is 150 kg

▨ = *Reference case*

*Tab. 6.2 Load conditions for test sequences using the sinusoidal input given in Tab. 6.1.*

Each sequence of sinusoidal tests, as defined by Tab. 6.1, was repeated for a range of vertical load conditions. For each such condition, a dwell time of the vertical load of 25 hours was allowed before running the sequence of sinusoidal tests, to allow viscoelastic relaxation of the rubber and thus the creation of a representative indentation under the loaded ball. The peak force for the roll-out of the ball from the indentation is expected to depend on this dwell time.

The load conditions are reported in Tab. 6.2. In particular, the case of rubber A, thickness *t* of the rubber layer of 2 mm, diameter *D* of the steel ball of 25 mm and stress parameter $W/ER^2$ (or $W^*$) of 1.2 was treated as a reference case, while the other tests enable useful comparisons to be made in terms of the parameters D, t, W* and for the types of rubber.

### *6.2.2 Results*

The principal results of these sinusoidal tests are reported below in terms of dimensionless horizontal forces or rolling friction μ (horizontal force / weight) versus displacement.

The principal observations regarding the plots from Fig. 6.1 to Fig. 6.6, for the reference case of rubber A, t = 2mm, D = 25 mm and $W/ER^2 = 1.2$, are briefly summarized below.

- The difference between the μ-disp loops belonging to the first cycle with respect to the ones of the successive cycles (second and third) is related to the values of the maximum force for the roll-out of the balls from their pits (see Fig. 6.1 and Fig. 6.2). This difference is due to the recovery of the rubber and depends on its viscoelastic properties. In fact within the amplitude of 5 mm, which could be approximately taken as the displacement of the top plate corresponding to roll-out of the balls and below which the balls remain inside their pits, the difference between successive μ-disp loops is negligible (compare Fig. 6.4 a, Fig. 6.5 a and Fig. 6.6 a). A difference in the maximum values of μ is clearly visible only for the positive and negative displacements of the first cycle and also between the first cycle and the subsequent cycles. Between cycles subsequent to the first one this difference becomes insignificant, proved by the similar shape of the μ-disp loops (compare Fig. 6.5 to Fig. 6.6).

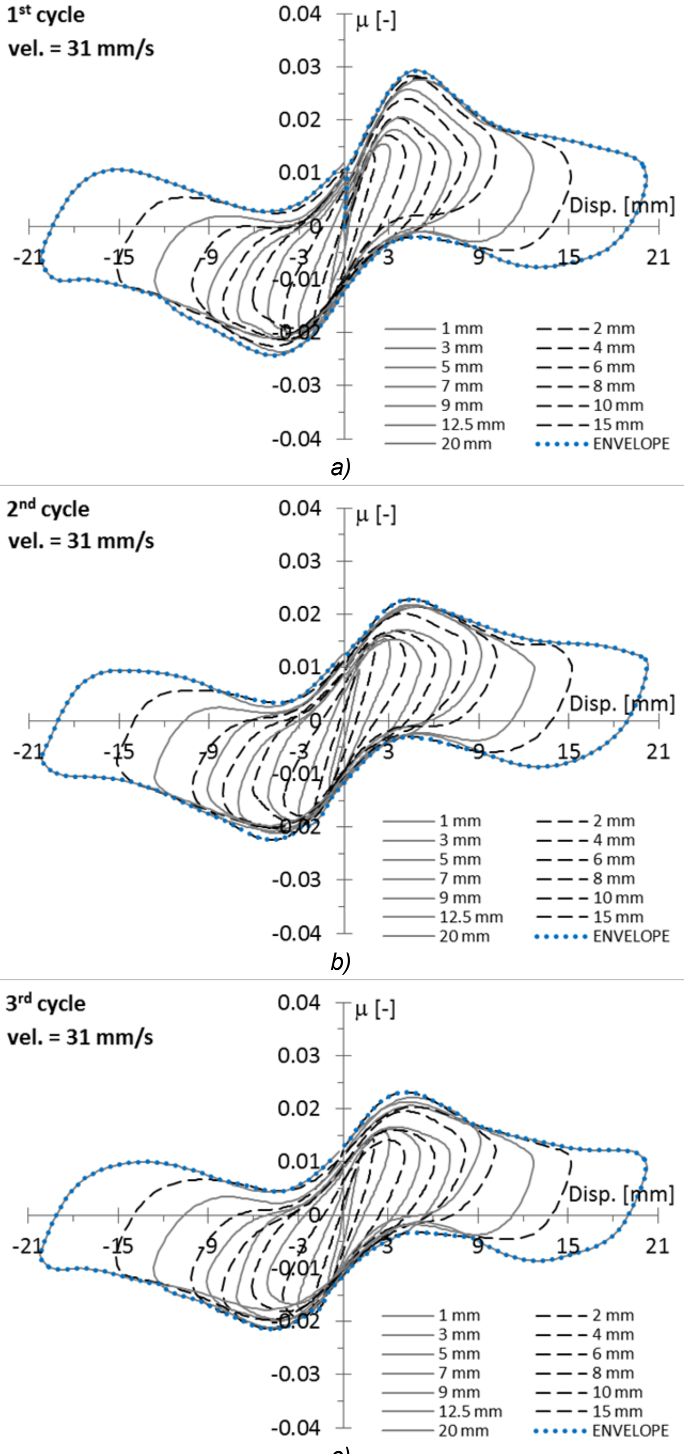

a)

b)

c)

*Fig. 6.1 μ-disp loops. Rubber A, t=2mm, D=25mm, W/ER$^2$=1.2, constant max. velocity.*

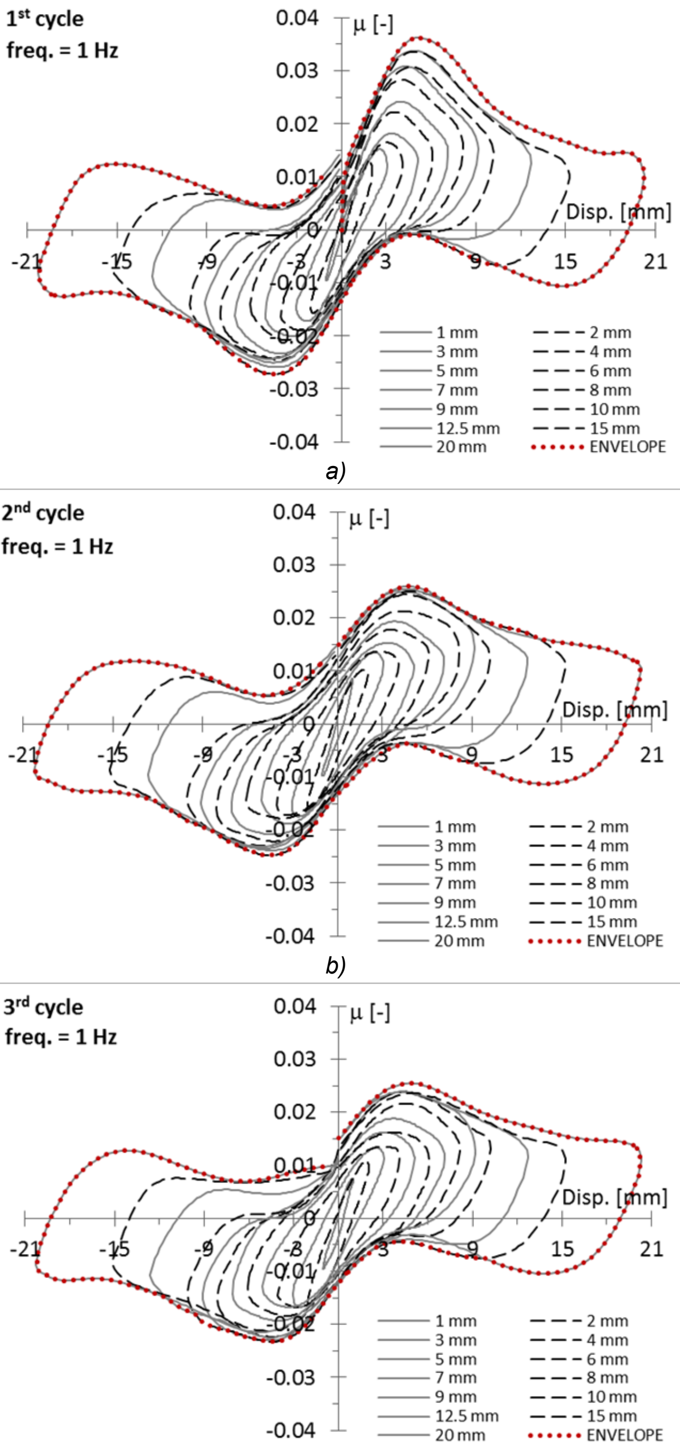

a)

b)

c)

*Fig. 6.2 μ-disp loops. Rubber A, t=2mm, D=25mm, W/ER$^2$=1.2, constant frequency.*

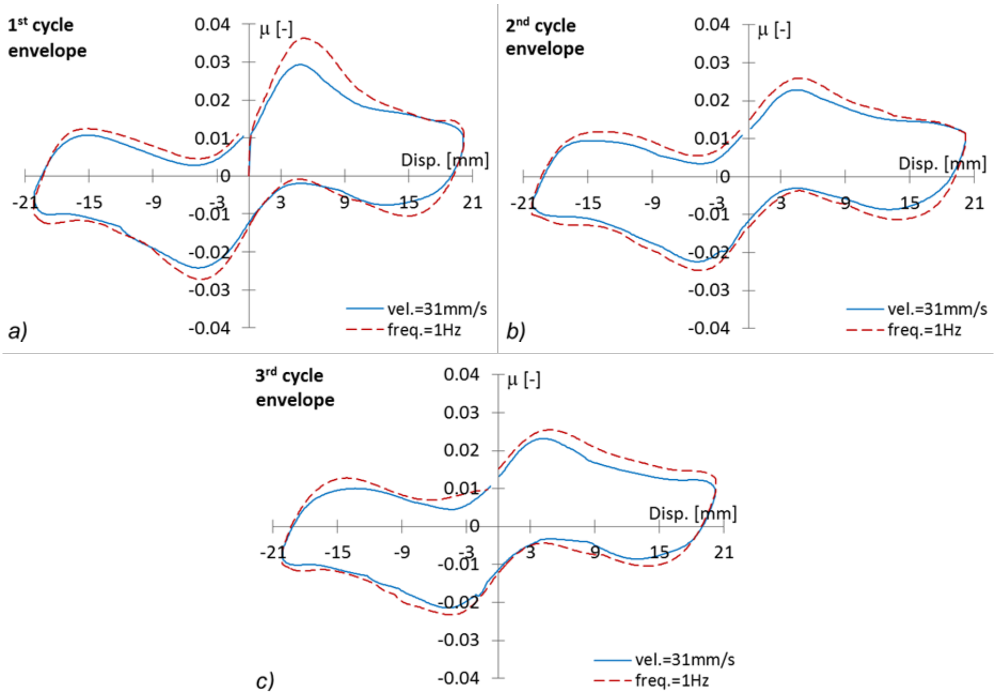

Fig. 6.3 Envelopes of μ-disp loops. Rubber A, t=2mm, D=25mm, $W/ER^2$=1.2.

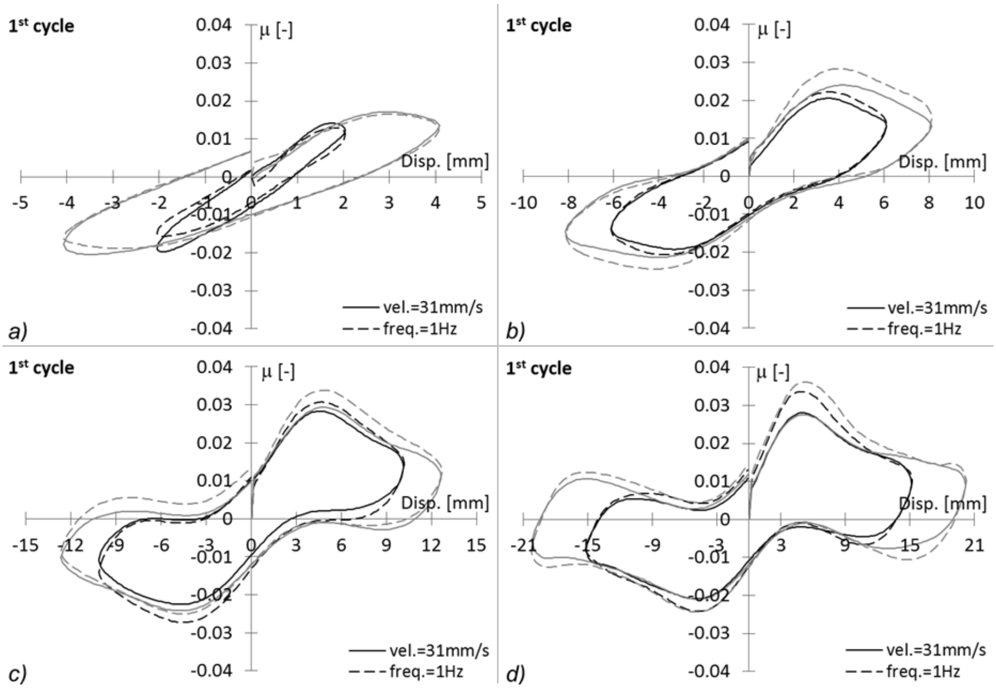

Fig. 6.4 Comparisons of μ-disp loops - 1st cycle. Rubber A, t=2mm, D=25mm, $W/ER^2$=1.2.

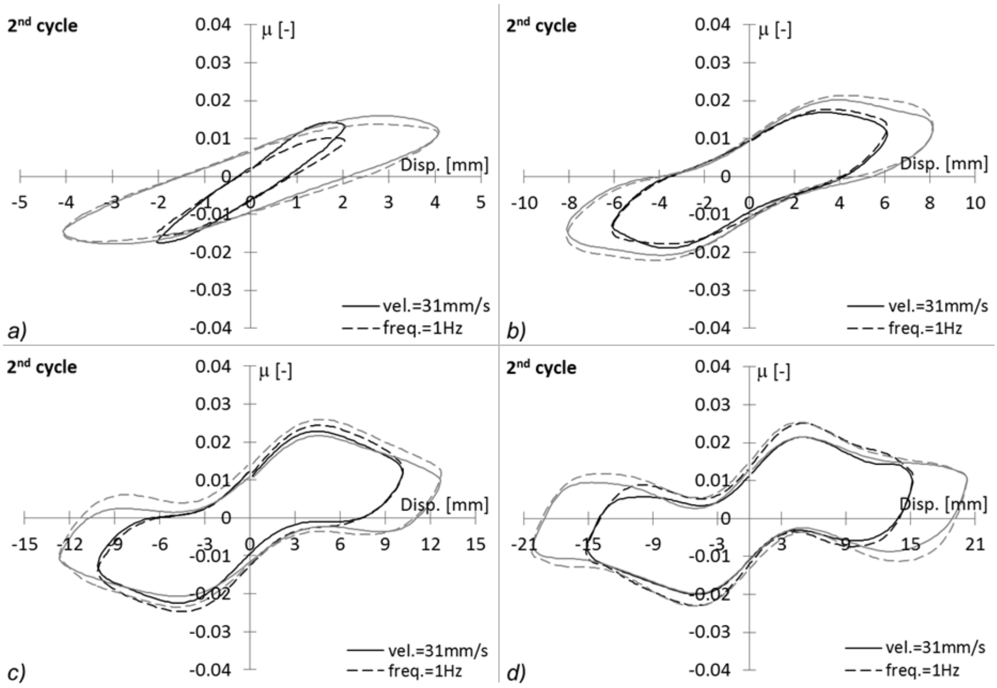

*Fig. 6.5 Comparisons of μ-disp loops - 2$^{nd}$ cycle. Rubber A, t=2mm, D=25mm, W/ER$^2$=1.2.*

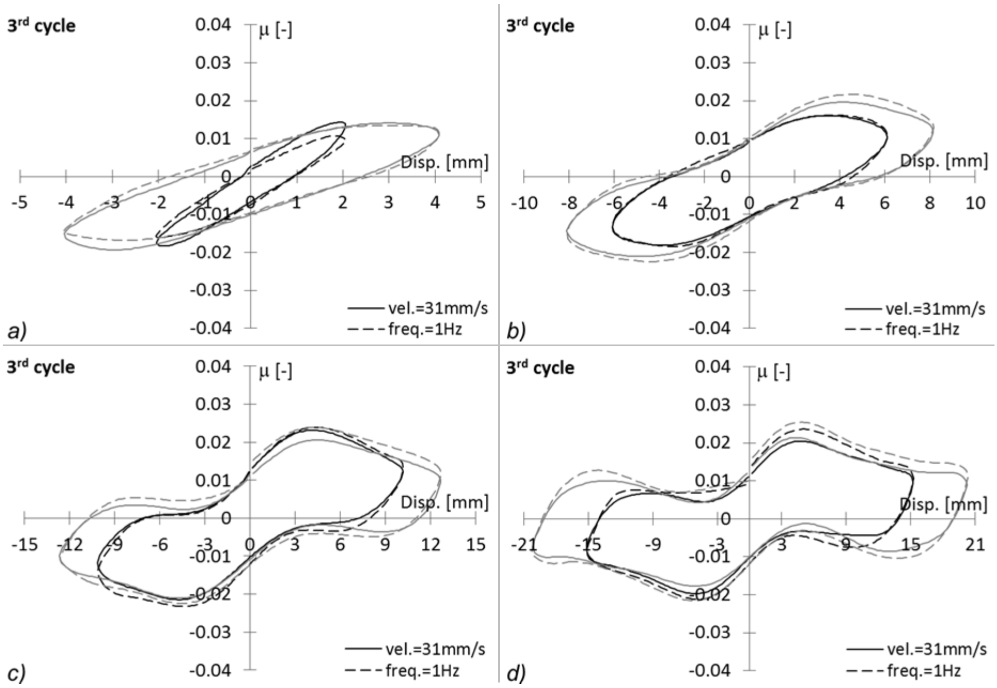

*Fig. 6.6 Comparisons of μ-disp loops - 3$^{rd}$ cycle. Rubber A, t=2mm, D=25mm, W/ER$^2$=1.2.*

- The behaviour of the RBRL device depends also on the velocity, as could be expected for a device based on rubber. This influence, shown in Fig. 6.3, is considerably amplified by the presence of the initial indentation and results in greater forces, for the balls roll-out, in the cases of sinusoidal input with constant frequency (f = 1 Hz), for which, for amplitudes greater than 5 mm, the maximum velocities are bigger than the reference value of 32 mm/s. This influence, being amplified by the presence of the initial pit, is more visible when the effects of this pit are more visible, e.g. for the μ-disp loops from the first cycle and with the biggest amplitudes (see Fig. 6.4 d). Furthermore, Fig. 6.4, Fig. 6.5 and Fig. 6.6 show that this influence is very small when the balls rock in their pits (with sinusoidal amplitudes less than about 5 mm) and decreases with increasing distance from the point of roll-out of the balls. In fact, the dependence of the steady-state rolling friction on the velocity is quite negligible considering the typical range of frequencies of an earthquake, as will be shown later in the section 6.4; this is consistent with the dynamic behaviour of a typical rubber, which presents the parameters $K^{/}$ (storage stiffness) and $K^{//}$ (loss stiffness) both linearly dependent on the logarithm of the frequency.

- Lastly, information can be gathered looking at the shape of these μ-disp loops; in particular, these will be very useful for devising a model for the RBRL device in the time domain. Three different situations are clearly visible, each of them with a different shape of the associated loop; these are listed here below.

_ The μ-disp loops appear elliptical for amplitudes up to 5 mm or so (see Fig. 6.4 a, Fig. 6.5 a, Fig. 6.6 a): within this deflection the balls only rock in their pits.

_ The values of μ tend to the steady-state value for displacements bigger than 15 mm (see Fig. 6.4 d, Fig. 6.5 d and Fig. 6.6 d): in this case the μ-disp loops consist of a first zone where the maximum force for the roll-out of the balls is developed, and a second zone characterized only by the steady-state rolling friction (as also seen in the previous Chapter).

_ The μ-disp loops of intermediate amplitude belong to a transition phase of the behaviour of the RBRL device (see Fig. 6.4 b-c, Fig. 6.5 b-c, Fig. 6.6 b-c). This is the most critical phase for the modelling, being highly non-linear, dependent on the viscoelastic properties of the rubber (thus on the dwell time of the load and on the recovery time of the rubber), and more influenced by the velocity than that could happen in the steady-state rolling, and with a strong frictional nature.

This discussion will be resumed in section 6.6, leading to a proposal for a time-domain model for the RBRL device.

The same considerations made about the results for the reference case (rubber A, t=2mm, D=25mm, W*=1.2) can also be extended to the other cases analyzed. A summary of the results for the same case of rubber A but with stress parameter equal to 2 (from Fig. 6.7 to Fig. 6.9), and for the cases of rubber A+ (from Fig. 6.10 to Fig. 6.12) and rubber A- (from Fig. 6.13 to Fig. 6.15), is reported below, the stress level and the type of rubber being the more influential parameters. These results are again presented in terms of μ-disp loops.

The results for rubber A+ (see Fig. 6.10) show values of the rolling friction μ about one third of those for the reference case with rubber A; this is obviously due to the higher value of the shear modulus of the compound A+, besides its lower loss angle and its limited relaxation phenomena (or low value of $H_0$). These very low values of friction explain the increase in the relative noise level of the output forces.

The case of rubber A-, instead, is opposite: here the rolling friction presents the greatest values among all the tests performed, also 2 or 3 times greater than the ones associated with the reference case with rubber A.

A small difference between the case of rubber A- and the other cases, is related to the peak force for the roll-out of the balls. In this case, indeed, the maximum friction reached by the rocking of the balls inside their pits (amplitudes smaller than 5 mm) is very close to the maximum values of μ of the following loops that involve the balls roll-out.

To have the possibility to objectively describe and compare the behaviour of the RBRL device, shown until now through the μ-disp loops, the equivalent linearized viscoelastic frequency-domain (ELVFD) representation was used (see sections 3.2 and 4.3). In particular, the Harmonic linearization method (Ahmadi & Muhr, 1997) was chosen to calculate the ELVFD parameters directly from the μ-disp loops; these parameters are: storage stiffness $K^{/}$, loss stiffness $K^{//}$, complex stiffness K* and loss angle δ. $K^{/}$ and $K^{//}$ are respectively defined as the in- and out-of-phase stiffness factors for calculating the “best-fit” steady-state harmonic force amplitudes required to impose a harmonic displacement of a given amplitude, i.e. the best fit elliptical approximation to the force-displacment loop. While the parameter $K^{/}$ is directly related to the slope (or to the stiffness) of the μ-disp loops, the stiffness $K^{//}$ represents instead the energy dissipation. The magnitude of the complex stiffness K* and the loss angle δ are related to $K^{/}$ and $K^{//}$ by:

$$\begin{aligned} K^{*} &= \sqrt{K^{/2} + K^{//2}} \\ \tan\delta &= K^{//} / K^{/} \end{aligned} \qquad (6.1)$$

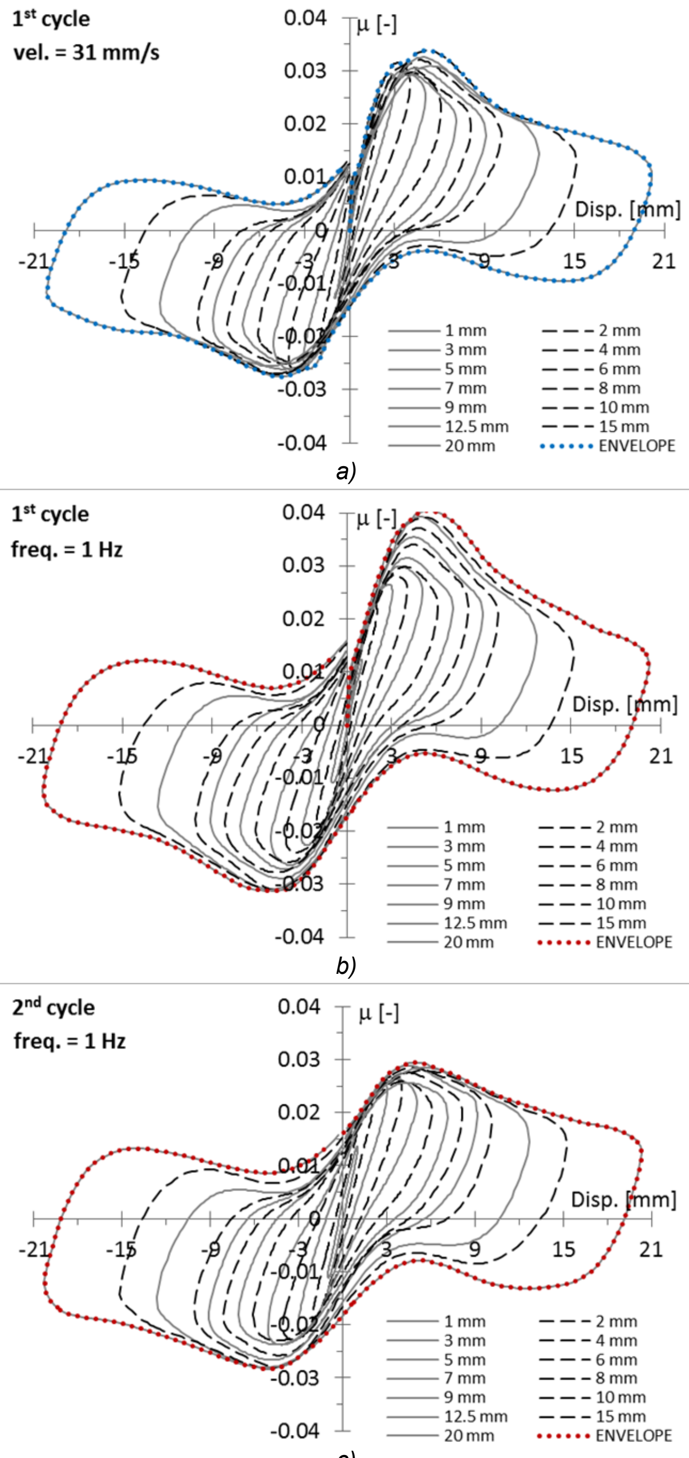

a)

b)

c)

*Fig. 6.7 μ-disp loops. Rubber A, t=2mm, D=25mm, W/ER$^2$=2.*

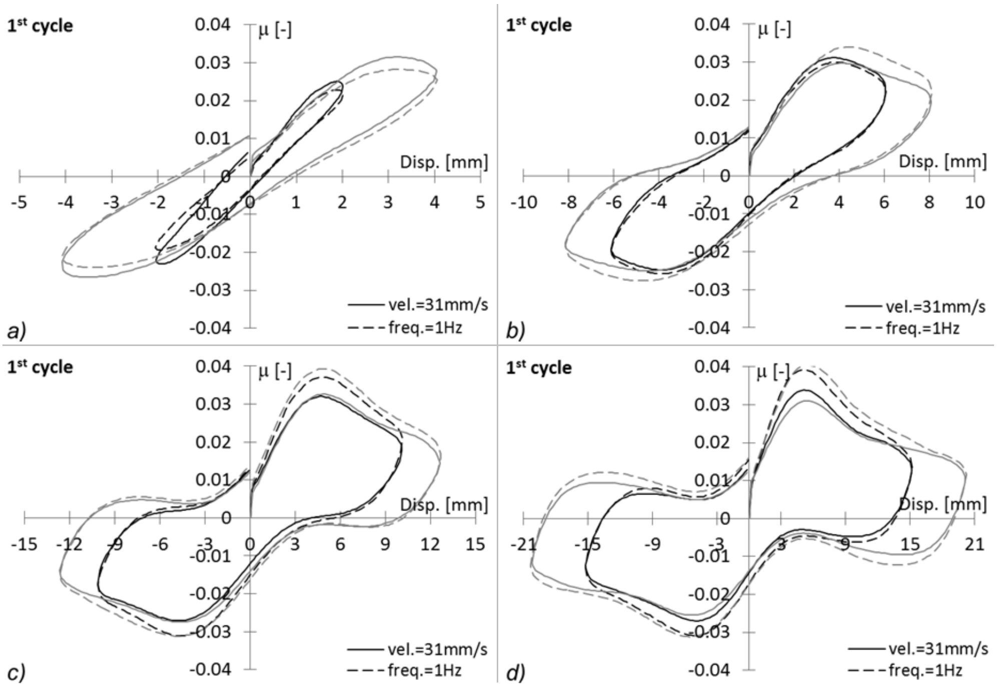

*Fig. 6.8 Comparisons of μ-disp loops – $1^{st}$ cycle. Rubber A, t=2mm, D=25mm, W/ER$^2$=2.*

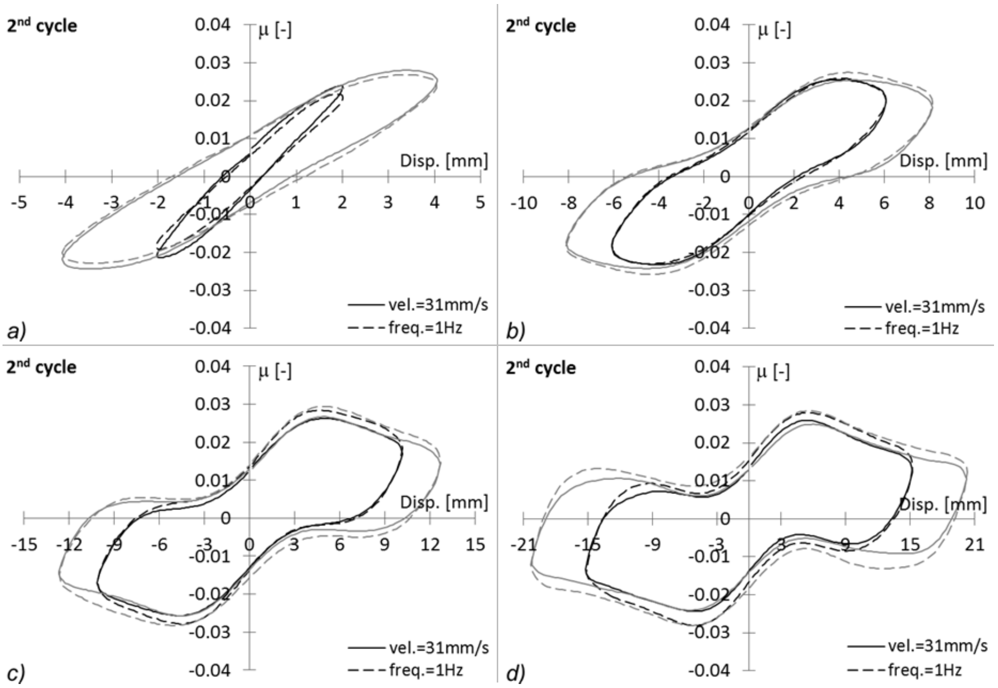

*Fig. 6.9 Comparisons of μ-disp loops – $2^{nd}$ cycle. Rubber A, t=2mm, D=25mm, W/ER$^2$=2.*

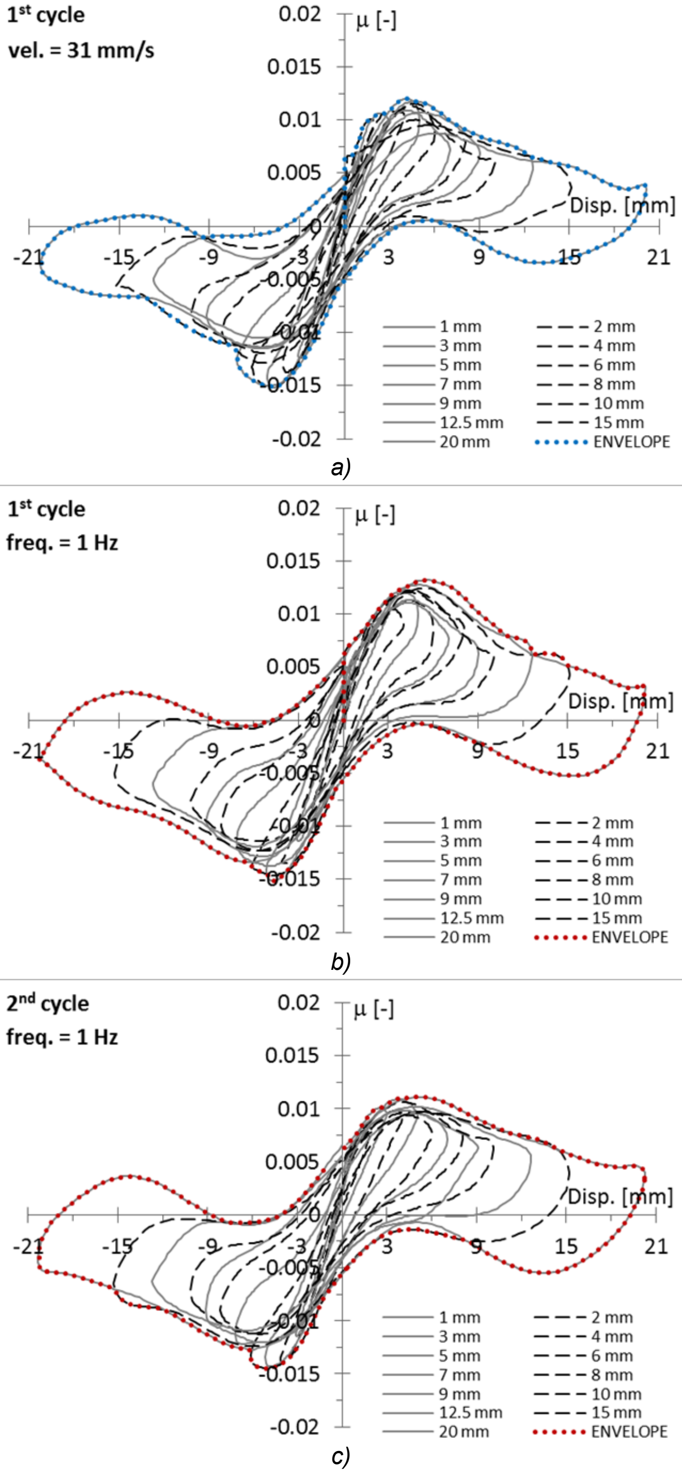

*Fig. 6.10 μ-disp loops. Rubber A+, t=2mm, D=25mm, W/ER$^2$=1.2.*

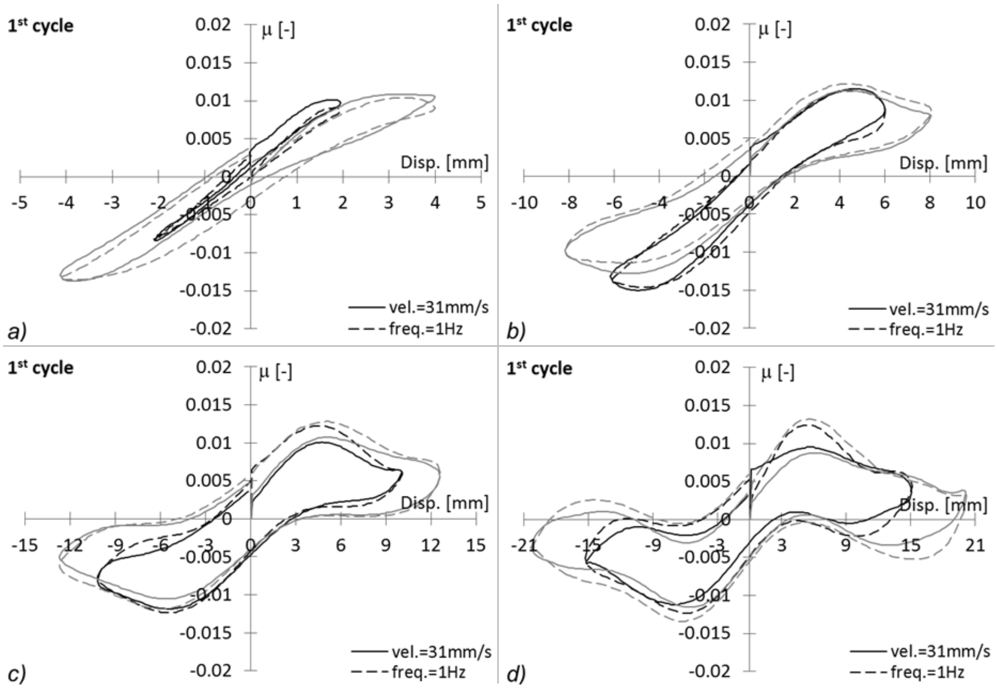

*Fig. 6.11 Comparisons of μ-disp loops–$1^{st}$ cycle. Rubber A+, t=2mm, D=25mm, W/ER$^2$=1.2.*

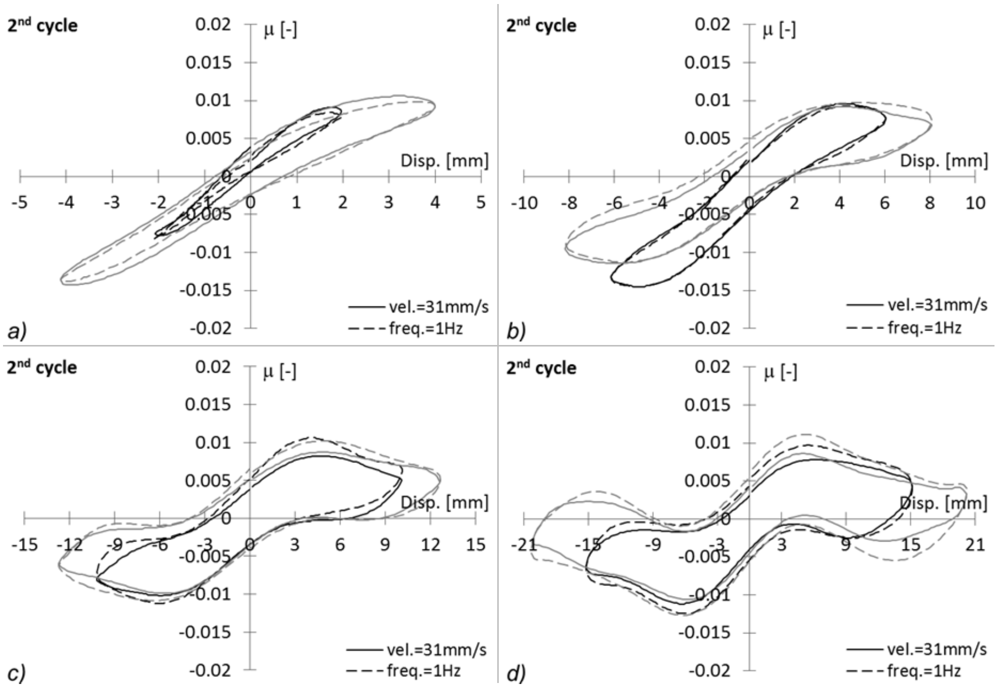

*Fig. 6.12 Comparisons of μ-disp loops–$2^{nd}$ cycle. Rubber A+, t=2mm, D=25mm, W/ER$^2$=1.2.*

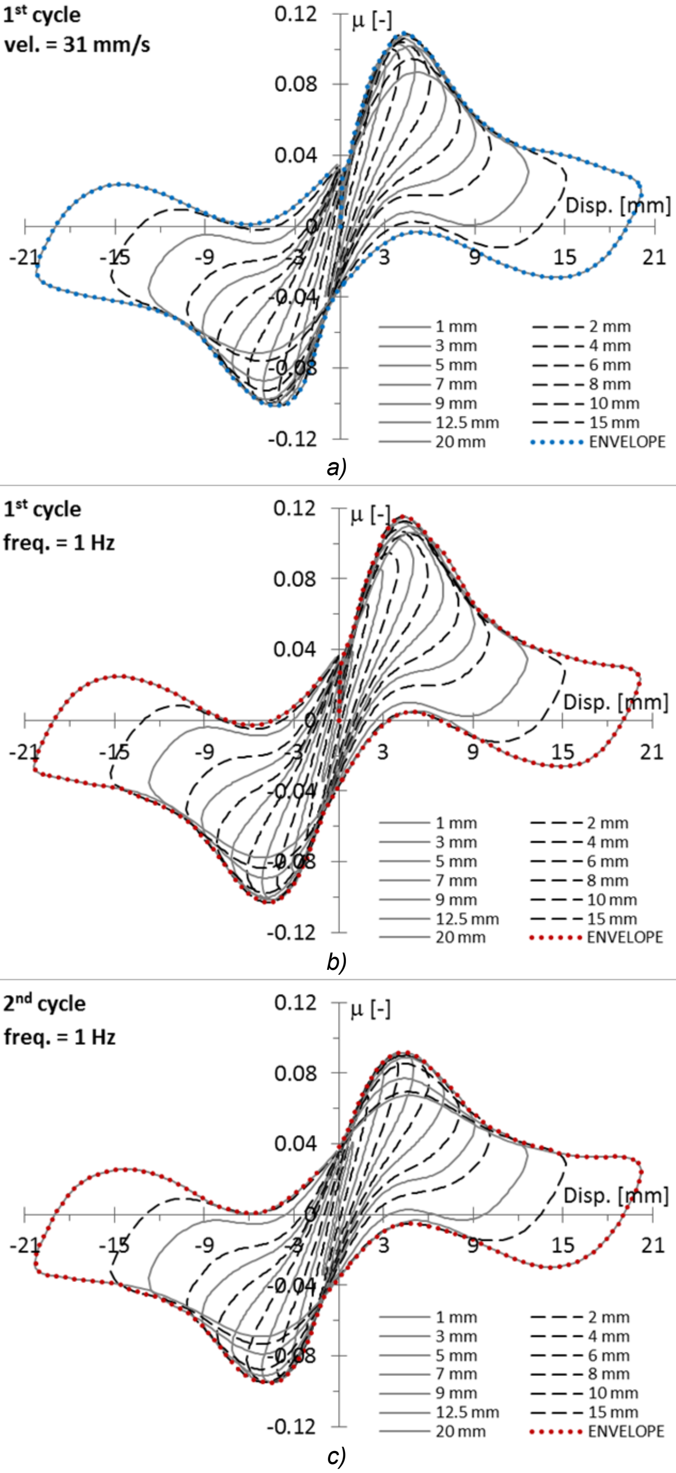

a)

b)

c)

*Fig. 6.13 μ-disp loops. Rubber A-, t=2mm, D=25mm, W/ER$^2$=1.2.*

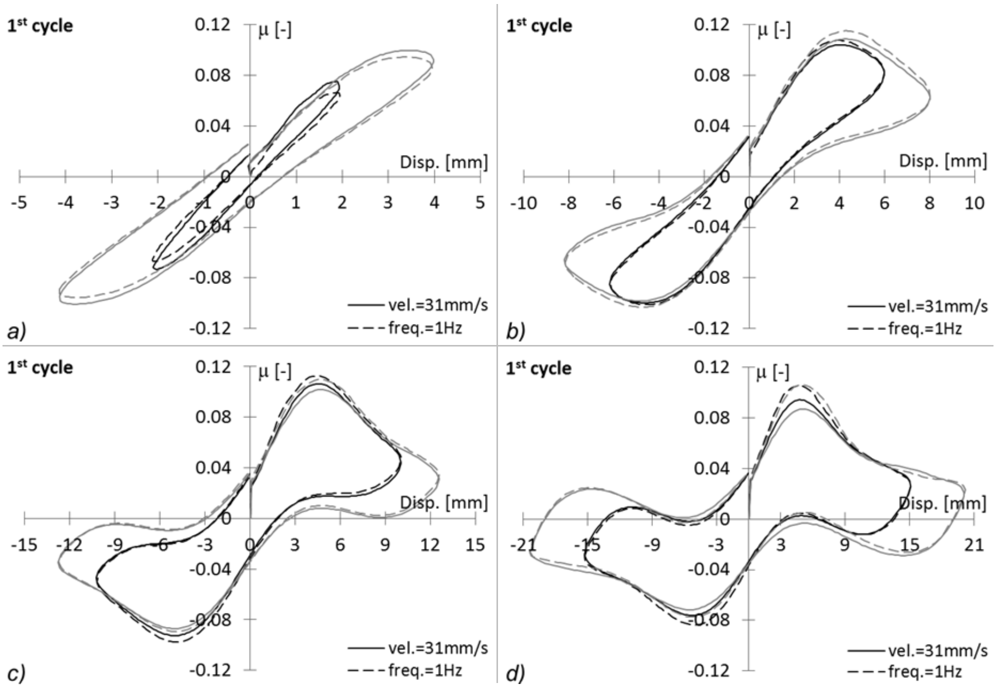

*Fig. 6.14 Comparisons of μ-disp loops–1st cycle. Rubber A-, t=2mm, D=25mm, W/ER$^2$=1.2.*

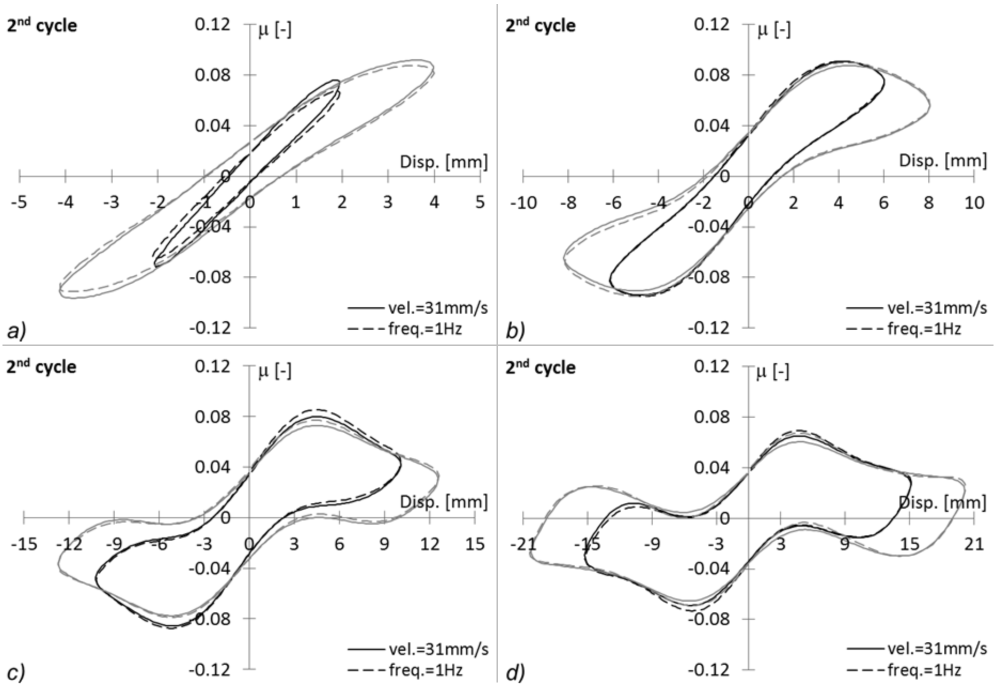

*Fig. 6.15 Comparisons of μ-disp loops–2nd cycle. Rubber A-, t=2mm, D=25mm, W/ER$^2$=1.2.*

In the case of a linear viscoelastic system, $K^{/}$ and $K^{//}$ give a perfect fit to the steady-state harmonic force, and are in general functions of test frequency. For a non-linear system, the fit is imperfect, but is often good for a fixed displacement amplitude, though $K^{/}$ and $K^{//}$ now depend on amplitude as well as on frequency.

If we consider a Kelvin model (spring and dashpot in parallel) the coefficient of critical damping $\zeta$ is approximately related to the loss angle δ by Eq. (6.2) (see for more details section 4.3).

$$\zeta \simeq \frac{1}{2}\tan\delta \tag{6.2}$$

The values of the ELVFD parameters, plotted versus the amplitude of the sinusoidal displacement, are reported for the reference case (rubber A, t=2mm, D=25mm, W*=1.2) from Fig. 6.16 to Fig. 6.19. These results are shown at first comparing the three sinusoidal cycles of each test, separately for the case of tests with same velocity (Fig. 6.16) and tests with same frequency (Fig. 6.17), and subsequently are presented comparing the cases of constant velocity and frequency for the 1st cycle (Fig. 6.18) and for the 2nd cycle (Fig. 6.19). The principal considerations about these results are listed below.

- The ELVFD parameters depend strongly on the amplitude of the sinusoidal displacement, as already seen in the section 4.3 elaborating the results of the ECOEST project; this is due to the overall non-linear behaviour of the RBRL device.

- The comparisons between the three sinusoidal cycles of Fig. 6.16 and Fig. 6.17 show a variability of the ELVFD parameters that is negligible. Only some oscillations can be observed in the values of $K^{//}$ for the first amplitudes, especially for the tests with constant velocity that correspond to the ones with the biggest values of frequency (see Tab. 6.1): this might be due to the real limits of the test setup. The related $K^{/}$ are instead very stable and present the greatest values, the associated μ-disp loops being the ones with the highest slope (see Fig. 6.4 a).

- The comparison among the tests with constant frequency and constant velocity of Fig. 6.18 and Fig. 6.19 show how the velocity influences significantly the value of $K^{/}$ for the first amplitudes, but not the loss stiffness $K^{//}$. Before 5 mm amplitude the tests with constant velocity present higher velocities and thus show greater values of $K^{/}$, while the opposite happens after 5 mm. However this variability is really visible only before 5 mm, since $K^{/}$ rapidly decreases with the amplitude.

- Fig. 6.18 and Fig. 6.19 show substantially the same comparison, the variability of the ELVFD parameters by the number of the sinusoidal cycle being negligible (as seen before).

- Looking at the shape of the function $K'$ *(amplitude)*, three different phases could be recognized. The first one, within 5 mm or so, is related to the rocking of the balls inside their pits and is characterized by high values of the storage stiffness that rapidly decreases with increasing in amplitude. From 5 to about 15 mm, the function of $K'$ shows a gradient greatly reduced from that before: this part represents the transition phase of the RBRL device, after the roll-out of the balls from their pits. Finally, the gradient decreases again after about 15 mm, leading $K'$ to tend to 0 for amplitudes tending to infinity: this phase corresponds to the steady-state rolling of the balls. This consideration is consistent with a previous observation about the three different types of shape of the μ-disp loops, which can be observed starting from very small amplitudes up to the free rolling of the balls (see for example Fig. 6.4). In fact, the μ-disp loops for amplitudes below 5 mm have an elliptical shape with a slope that rapidly decreases with increasing in amplitude, and this corresponds to the first phase of the function $K'$; furthermore, the μ-disp loops after about 15 mm start to show the part of the steady-state rolling and this new shape will slowly lead $K'$ to tend to 0, since the steady-state condition is characterized by the absence of stiffness. These different phases seen for $K'$ *(amplitude)* are also well visible for the functions $\delta$ *(amplitude)* and $K^*$ *(amplitude)*, these being related to $K'$.
- For this reason, the plots from Fig. 6.16 to Fig. 6.19 present the interpolant equations for $K'$, $K^*$ and $\delta$ only up to 5 mm amplitude. In this way, these equations can predict well the value of the ELVFD parameters in this limited range of amplitude and could be used for an iterative analysis, updating the parameters of a Kelvin model, for the prediction of the vibrational behaviour of the RBRL device (see section 4.5 for a proposal of a simplified model based on ELVFD representation).
- The ELVFD representation gives a global description of the behaviour of the device, and hence does not capture some of the details seen before looking directly at the μ-disp loops; an example is the difference in the maximum value of friction between the 1st cycle and the following ones (see Fig. 6.1): as told above, $K'$ and $K''$ do not show significant dependence on the number of the cycle (see Fig. 6.16).

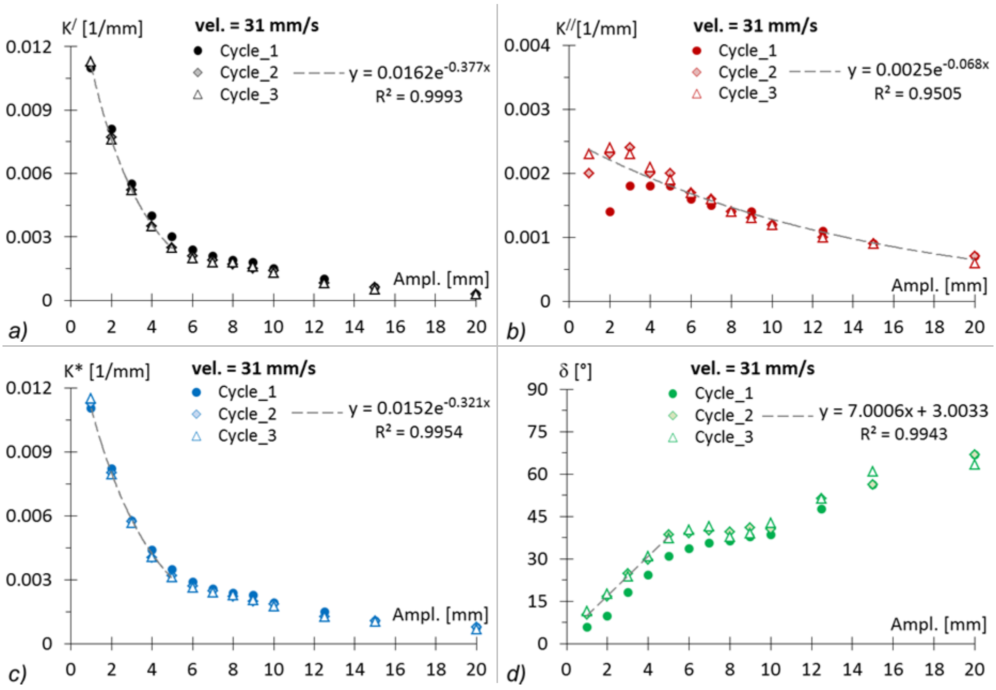

*Fig. 6.16 $K^{/}$, $K^{//}$, $K^{*}$, δ vs ampl. Rubber A, t=2mm, D=25mm, $W/ER^{2}$=1.2, constant velocity.*

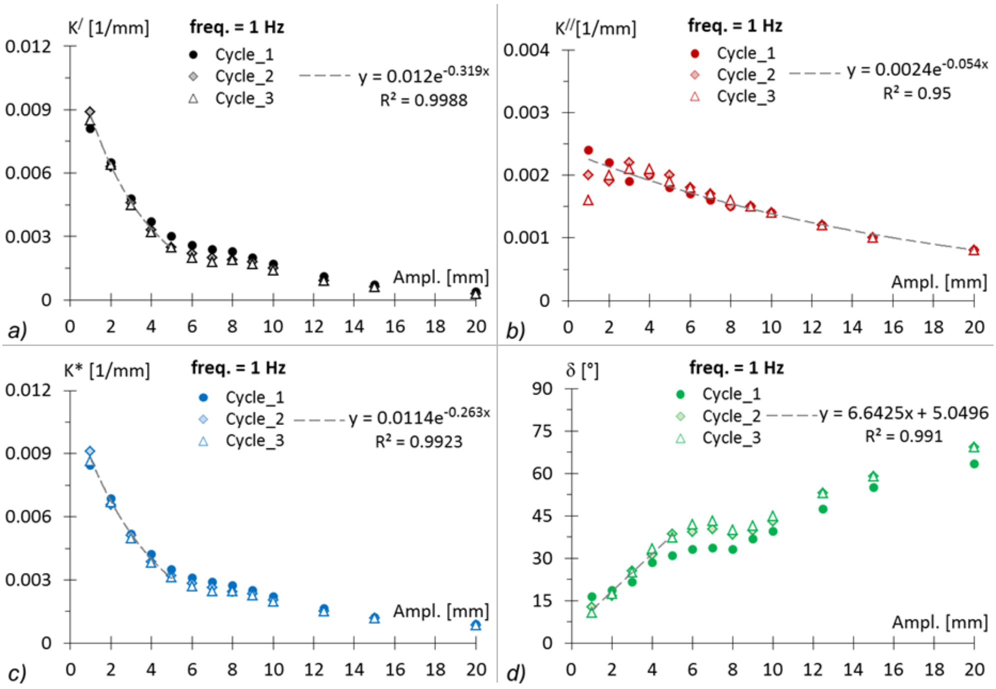

*Fig. 6.17 $K^{/}$, $K^{//}$, $K^{*}$, δ vs ampl. Rubber A, t=2mm, D=25mm, $W/ER^{2}$=1.2, constant frequency*

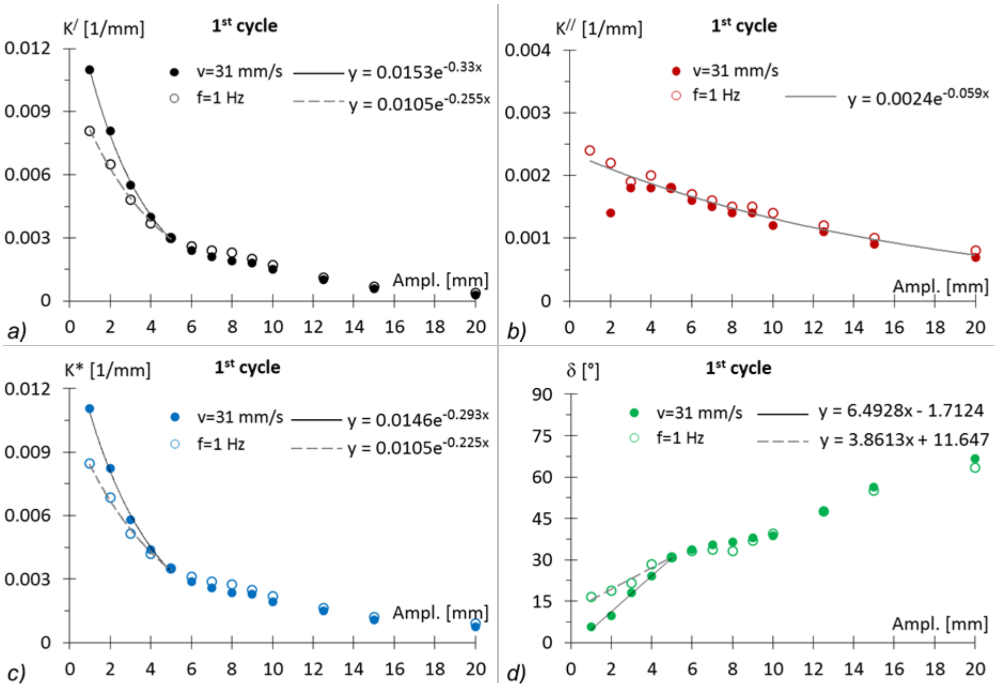

*Fig. 6.18 K$^{/}$, K$^{//}$, K*, δ vs amplitude. Rubber A, t=2mm, D=25mm, W/ER$^2$=1.2, 1$^{st}$ cycle.*

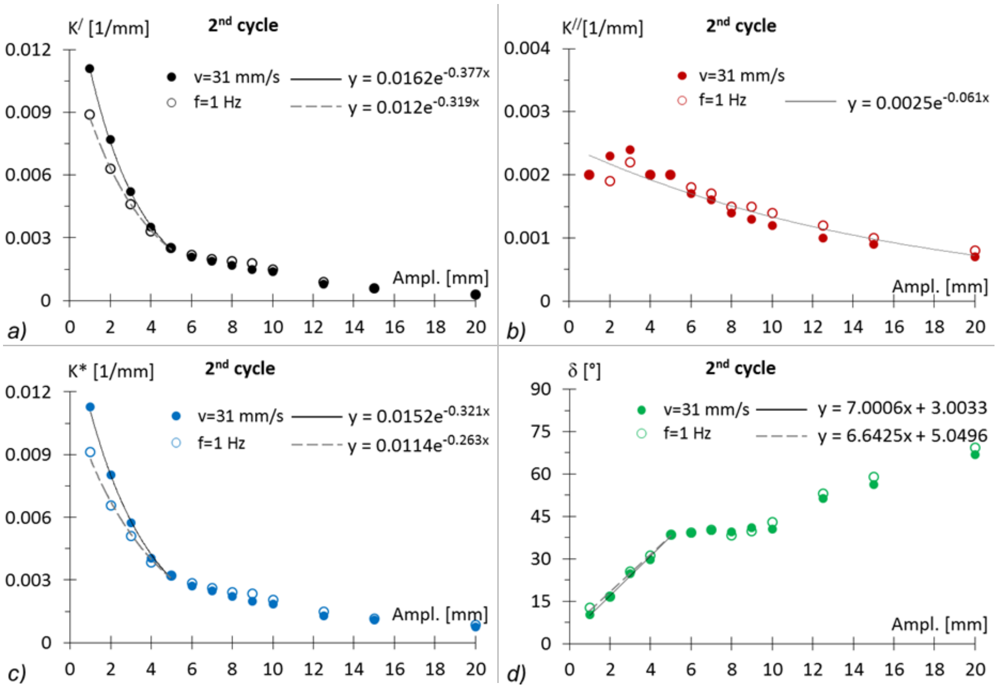

*Fig. 6.19 K$^{/}$, K$^{//}$, K*, δ vs amplitude. Rubber A, t=2mm, D=25mm, W/ER$^2$=1.2, 2$^{nd}$ cycle.*

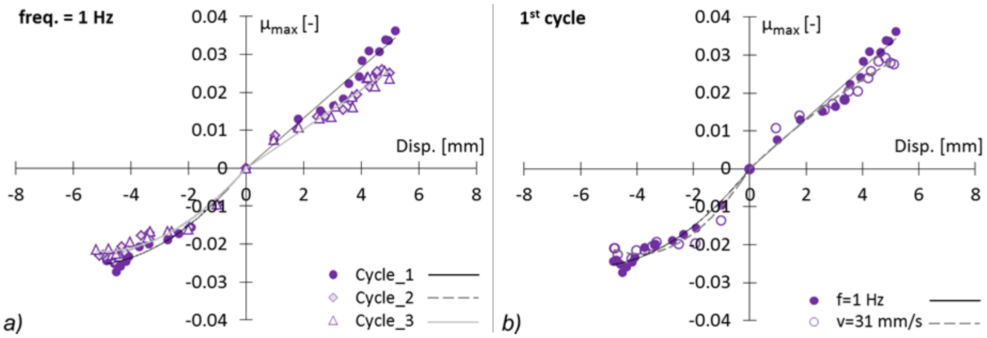

*Fig. 6.20 μ_max vs displacement. Rubber A, t=2mm, D=25mm, W/ER$^2$=1.2. a) Different cycles, all at 1 Hz; b) comparison of constant frequency (1 Hz) and velocity (31 mm/s) results for first cycles.*

Finally, Fig. 6.20 reports the maximum values of rolling friction, plotted versus the displacement of the top plate of the RBRL device, for the same test of reference and for the same comparisons seen above. In particular, the figure shows how the recovery time between the first cycle and the next ones (a) has a greater influence on $\mu_{max}$ than that given by the different velocities involved in the tests (b). The values of $\mu_{max}$ related to the roll-out of the balls after their return in the original position (see quadrant with negative values) show obviously smaller values than those associated with the first roll-out, due to recovery of the initial indentation. Fig. 6.20 gives also some indications about the deflection of the RBRL device corresponding to the realization of the peak force, thus about the position in which the phenomenon of the balls roll-out may be ideally identified, that is close to 5 mm for this case study.

Since the ELVFD parameters are not significantly influenced by the number of the cycle of the test, every case study presented in the comparisons from Fig. 6.21 to Fig. 6.24 is for the second cycle of each test. In these plots, the ELVFD parameters are compared for the various parameters investigated, which are: stress parameter W*, diameter D of the balls, thickness t of the rubber layer and type of rubber; these comparisons are shown separately for the cases of test with constant velocity (left) and test with constant frequency (right).

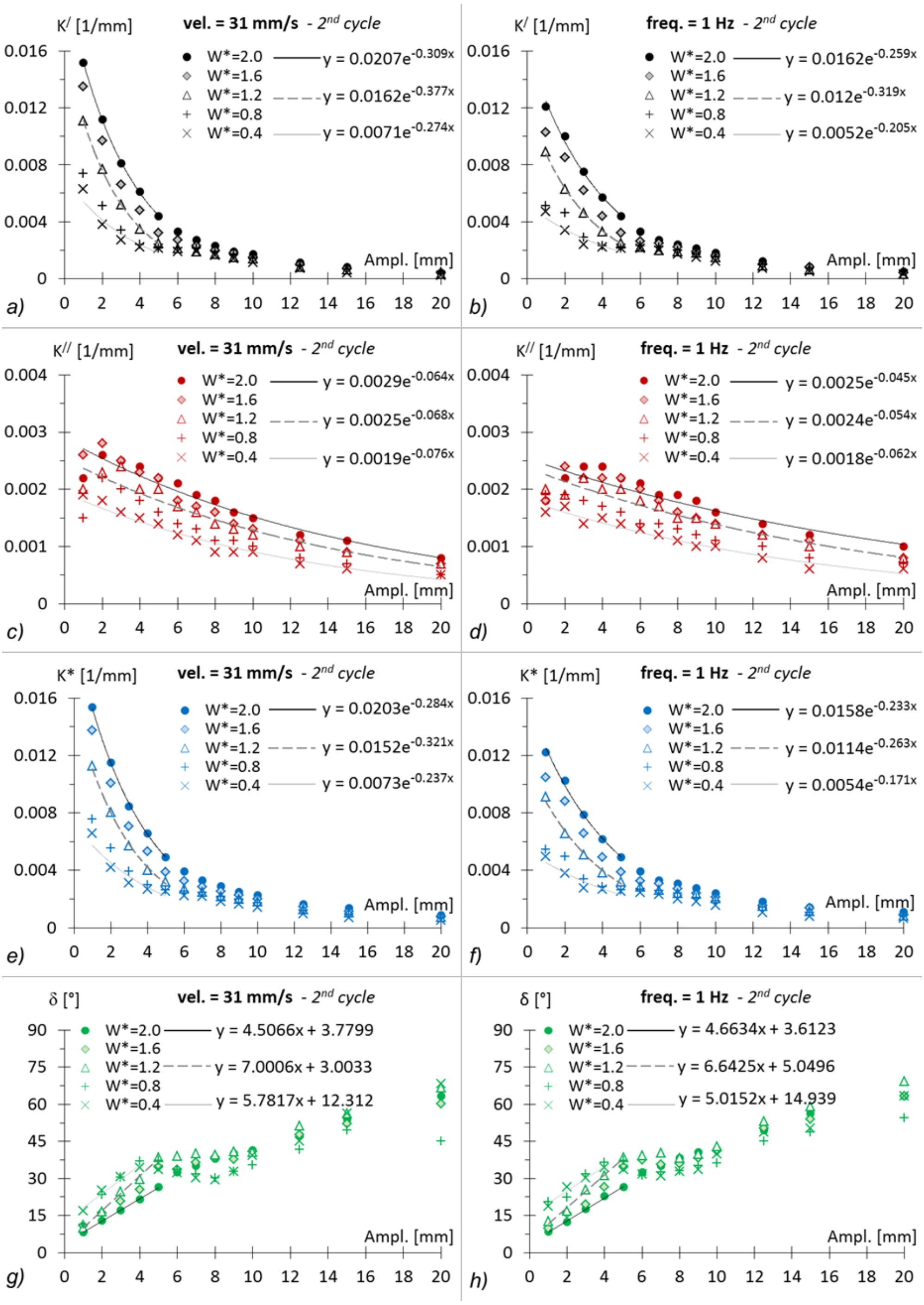

*Fig. 6.21 Comparison of K$^{/}$, K$^{//}$, K*, δ vs amplitude, for the values of the stress parameter W* analyzed. Case: rubber A, t=2mm, D=25mm _ 2$^{nd}$ cycle.*

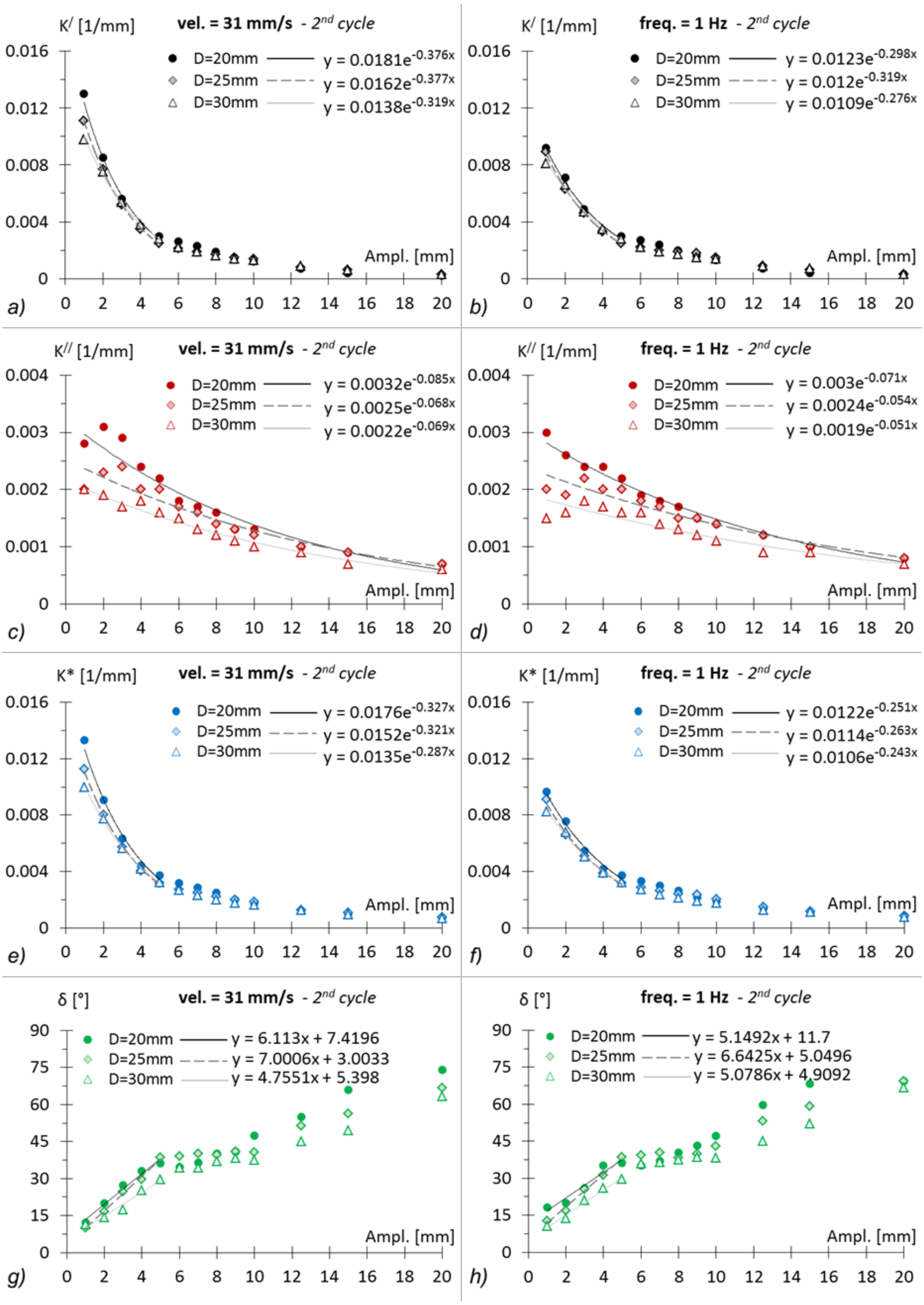

*Fig. 6.22 Comparison of K/, K//, K*, δ vs amplitude, for the values of the ball diameter D analyzed. Case: rubber A, t=2mm, W/ER$^2$=1.2 _ 2$^{nd}$ cycle.*

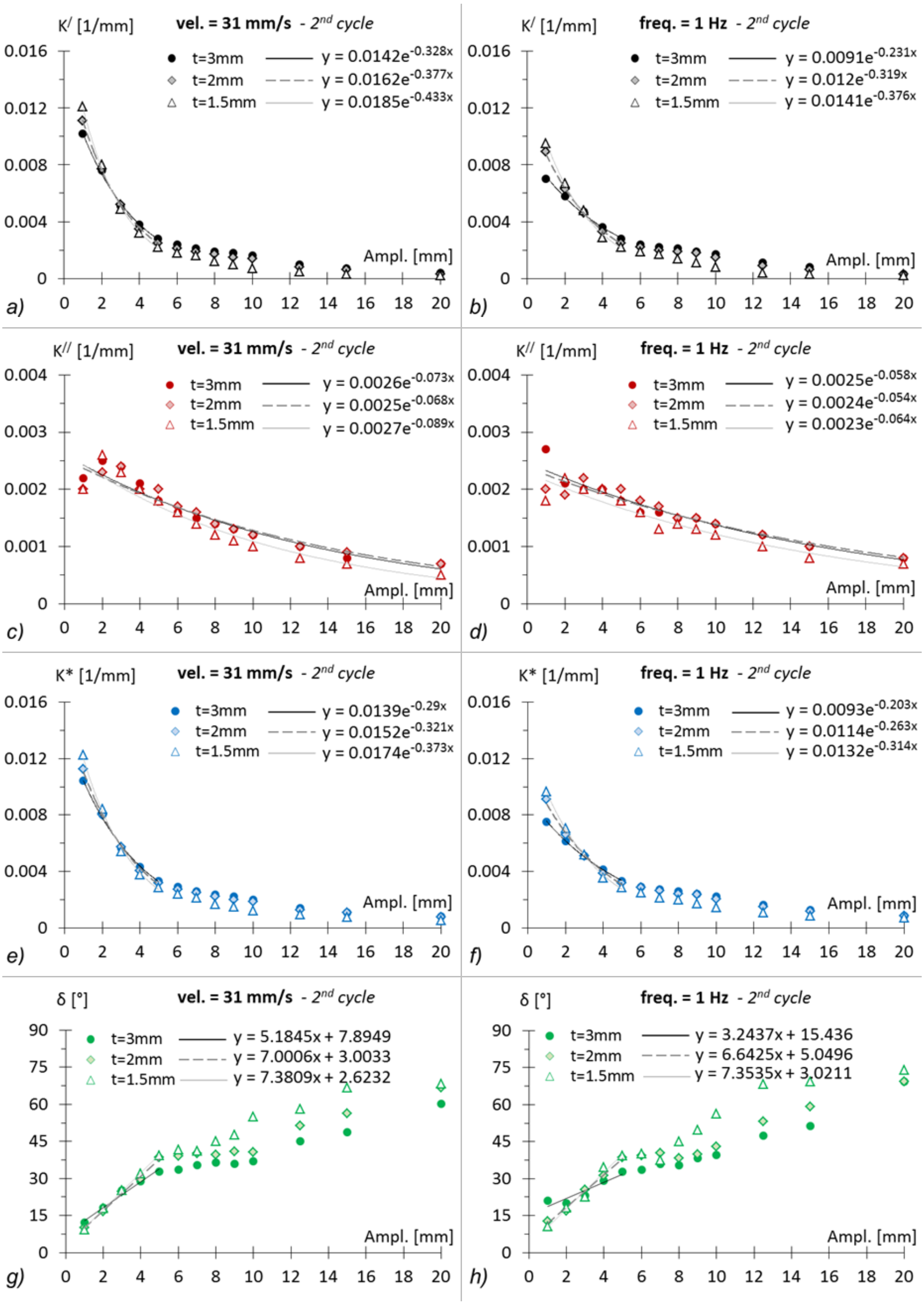

*Fig. 6.23 Comparison of $K^{/}$, $K^{//}$, $K^{*}$, δ vs amplitude, for the values of the rubber thickness t analyzed. Case: rubber A, D=25mm, $W/ER^2$=1.2 _ 2nd cycle.*

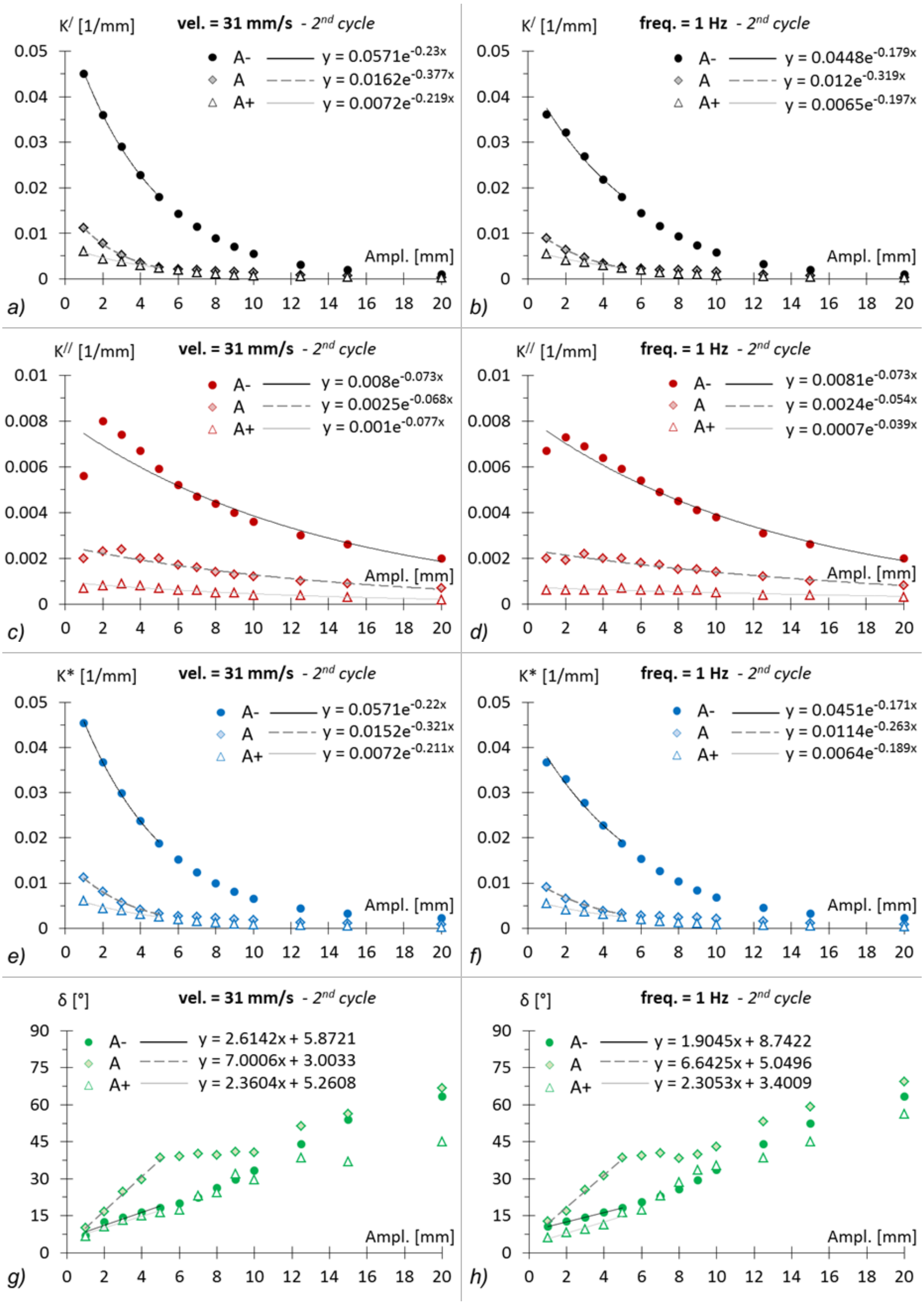

*Fig. 6.24 Comparison of $K^{/}$, $K^{//}$, $K^*$, δ vs amplitude, for the different rubbers (A-, A, A+) analyzed. Case: t=2mm, D=25mm, $W/ER^2$=1.2 _ 2nd cycle.*

Some brief remarks about the comparisons presented from Fig. 6.21 to Fig. 6.24 are listed below.

- Comparisons for the different stress parameters W* (see Fig. 6.21)

For a given rubber and within the investigated range of the parameters of the RBRL device, the stress level is the parameter most influential on the behaviour of the device.

$K^{/}$ and $K^{//}$ greatly increase with increase in W* for the smaller amplitudes and, for a given W*, vary with amplitude, in the same way as previously discussed for the reference case. The same influence is also visible for K*, it being related to $K^{/}$ and $K^{//}$ through the Eq. (6.1).

Concerning the loss angle, the results show an opposite trend: for the smaller amplitudes the highest values of W* are associated with the lowest values of δ and thus, considering Eq. (6.2), with the lowest values of the damping ratio $\zeta$. Significantly, for the small-deflections behaviour of the RBRL device, it could be advantageous to use very low stress levels, in such a way as to reach big values of the damping coefficient with minimal associated peak forces (i.e. with low values of $K^{/}$). However, from the theory of Muhr et al. (1997) we know that low values of W* lead to low values of the steady-state rolling friction, and are possibly inconsistent with provision of the desired energy dissipation at large deflections. The correct compromise between these situations has to be opportunely designed.

The same considerations made above are visible for both the cases of test with constant velocity and constant frequency, even if with a slightly different intensity for the parameters $K^{/}$ and K*. The figures for $K^{//}$ show instead the same comparison since, as already seen above, the loss stiffness does not significantly depend on the velocity. This last remark remains valid also for the next comparisons.

- Comparisons for the different balls diameter D (see Fig. 6.22)

All the ELVFD parameters increase with decrease in the value of D for the smaller amplitudes. However, this effect is smaller than the one seen before for the variation of W*, and is more visible for the tests with constant velocity, which correspond to the ones with higher velocity up to 5 mm amplitude.

- Comparisons for different rubber thicknesses t (see Fig. 6.23)

These comparisons show a very limited variation of the ELVFD parameters. Nevertheless a particular trend can be observed in the variation of $K^{/}$, also reflected by those of K* and δ: $K^{/}$ decreases with increasing t for amplitudes up to about 3 mm, after which it becomes bigger. Possibly this behaviour is related to the quasi-permanent strains in the centre of the indentation pit, described in the next section, that occur for higher stress parameter values and thinner layers of rubber. If the centre of the indentation is quasi-permanent, there would be no elastic recovery in the lee of the rolling contact to compensate for the force needed to apply increased elastic deformation at the advancing side of the contact: this results in increase of the elastic part of the resistance to small rocking deflections.

From the theory of Muhr et al. (1997) we know that increasing the rubber thickness results in increased rolling friction, and this is consistent with the increasing of $K^{/}$ for the small deflections of the RBRL device, bigger than about 3 mm (see Fig. 6.23 a): this is due to the deeper indentations produced by the balls on the thicker rubber sheet.

- Comparisons for the different type of rubber (see Fig. 6.24)

The characteristics of the rubber have obviously a determinant role for the behaviour of the RBRL device, thus have to be properly designed for the specific purpose.

Fig. 6.24 shows values of $K^{//}$ and $K^{/}$ for rubber A- that are respectively 3 or 4 times higher than those for rubber A. However, similarly to the comparisons of Fig. 6.21 between the stress parameters, although the values of $K^{/}$ and $K^{//}$ are the greatest ones, the associated values of loss angle δ and damping ratio $\zeta$ (see Eq. (6.2)) are smaller with respect to the case with rubber A. This means that the choice of a rubber too soft to provide high values of the damping coefficient could be not advantageous, at least for small excitations. For larger excitations than covered by Fig. 6.24 this consideration is not significant, because the effective stiffness is dominated by the auxiliary rubber springs and not by the behaviour of the balls rolling within a small distance of their initial position.

Rubber A+ shows the lowest values of $K^{/}$ and $K^{//}$, as is to be expected for the stiffest rubber since for it the indentation will be smallest, while it provides values of δ that are similar to those of the rubber A-.

Although rubber A is characterized by values of $K^{/}$ and $K^{//}$ that are intermediate respect to the other compounds, as expected, the results suggest a significantly higher loss angle for it than for the other rubbers for amplitudes up to 10 mm; it is not clear why this should be.

The plots from Fig. 6.25 to Fig. 6.28 present the maximum values of the rolling friction $\mu_{max}$ obtained by the 1st cycle of all the sinusoidal tests performed; these are plotted versus the displacement of the top plate of the RBRL device, and are presented through the same mode of comparison as used above for the ELVFD parameters.

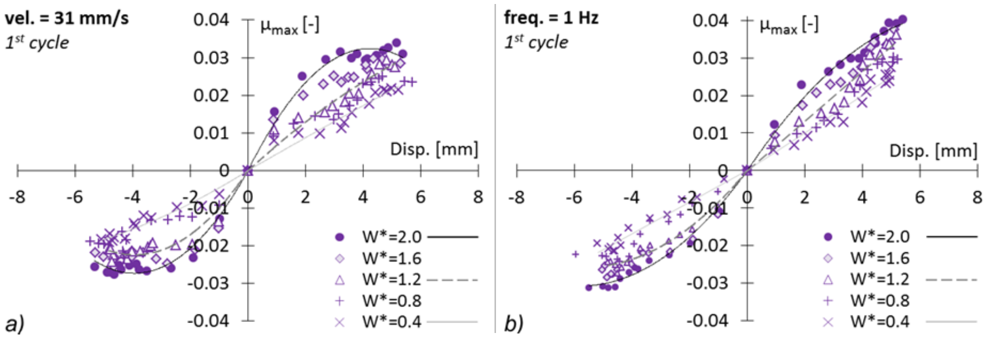

*Fig. 6.25 Comparison of $\mu_{max}$ vs displacement, for the values of the stress parameter W* analyzed. Case: rubber A, t=2mm, D=25mm _ 1st cycle.*

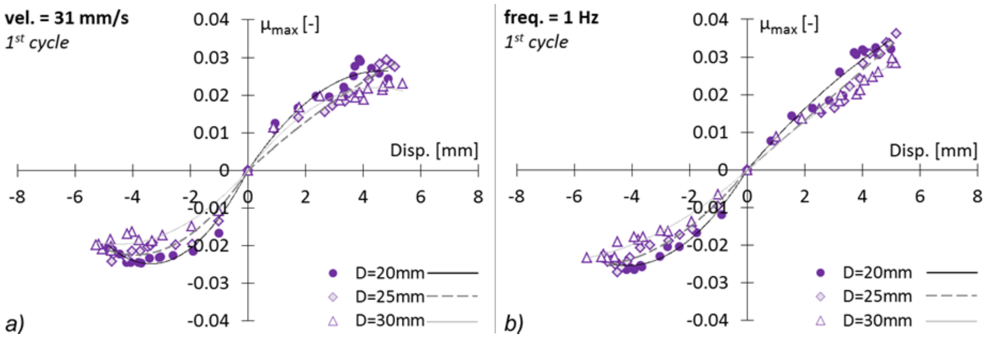

*Fig. 6.26 Comparison of $\mu_{max}$ vs displacement, for the values of the ball diameter D analyzed. Case: rubber A, t=2mm, $W/ER^2$=1.2 _ 1st cycle.*

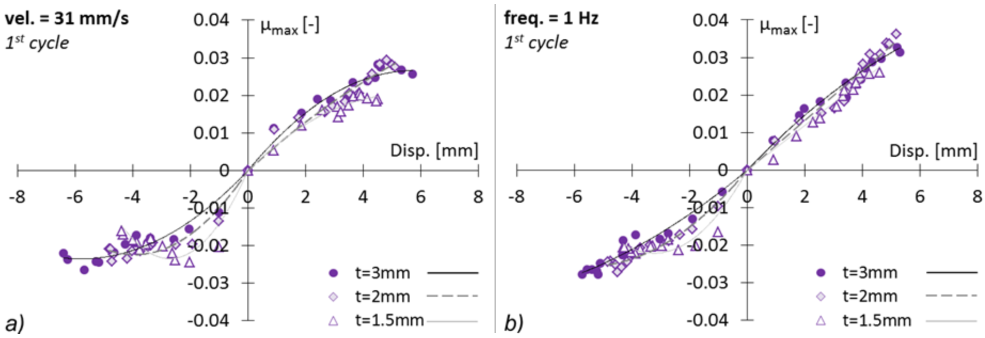

*Fig. 6.27 Comparison of $\mu_{max}$ vs displacement, for the values of the rubber thickness t analyzed. Case: rubber A, D=25mm, $W/ER^2$=1.2 _ 1st cycle.*

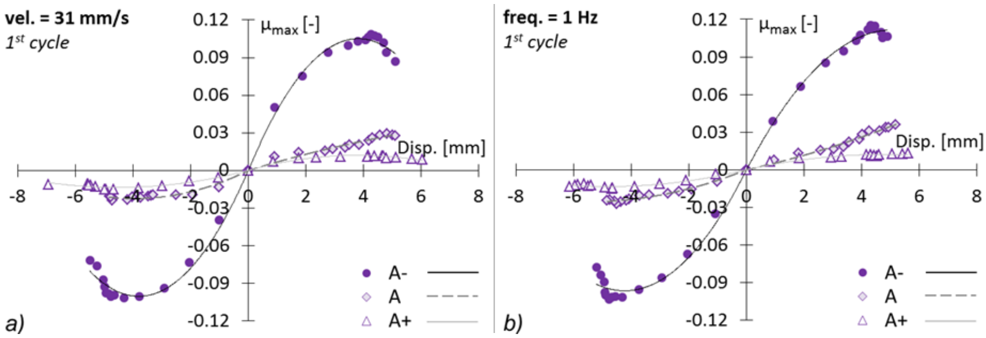

*Fig. 6.28 Comparison of $\mu_{max}$ vs displacement, for the different rubbers (A-, A, A+) analyzed. Case: t=2mm, D=25mm, $W/ER^2$=1.2 _ $1^{st}$ cycle.*

Some of the previous remarks are still valid for the results here presented.

It is worth considering how in the case of tests with constant frequency (see figures b) the values of $\mu_{max}$ increase quite linearly up to the peak value $\mu_{peak}$ (maximum μ for that case study), which generally corresponds to the $\mu_{max}$ of the loop of 20 mm amplitude. This is not always true for the case of tests with constant velocity (figures a), which generally present a more curvilinear shape. The trend of these values is not always very clear, due in part to an imperfect centring of the μ-disp loops about the vertical axis, especially for the ones of very small amplitude; however, this fact did not affect the value of the ELVFD parameters presented before, calculated through the Harmonic method.

For the rubber A- (see Fig. 6.28) a difference with respect to the other cases is easily identifiable: the $\mu_{max}$ related to the loop of 5 mm amplitude, corresponding to the fifth point from the origin of the axes, is very close to the $\mu_{peak}$, consistently with that already seen in Fig. 6.13 a) and b).

A last consideration regards the displacement $\Delta_{peak}$ corresponding to $\mu_{peak}$, which could be assumed to be the displacement at roll-out of the balls from their pits: this would seem to be related to the shape and to the magnitude of the indentation. This is visible looking at Fig. 6.28. The different rubber layer will present, under the balls loaded with the same stress level, pits with different curvature around the contact area: the more stiff the rubber the smaller the curvature, resulting in an increased displacement at roll-out (A+ > A > A-).

The dependence of $\Delta_{peak}$ on the parameters involved in this experimentation is better shown from Fig. 6.29 to Fig. 6.32, where the same dependence is also presented for the values of $\mu_{peak}$ and $K_{peak}$; $K_{peak}$ is the secant stiffness calculated by the ratio $\mu_{peak}/\ \Delta_{peak}$. The figures show these values, related to the peak force, comparing the cases of test with constant velocity and constant frequency; in addition, the same values are provided for the μ-disp loop of 5 mm amplitude, which ideally represents the last loop with balls rocking inside their pits.

In particular, the consideration made above about $\Delta_{peak}$ for different types of rubber is well recognizable in Fig. 6.32 c and d.

In the case of same rubber (A), Fig. 6.30 and Fig. 6.31 show respectively the

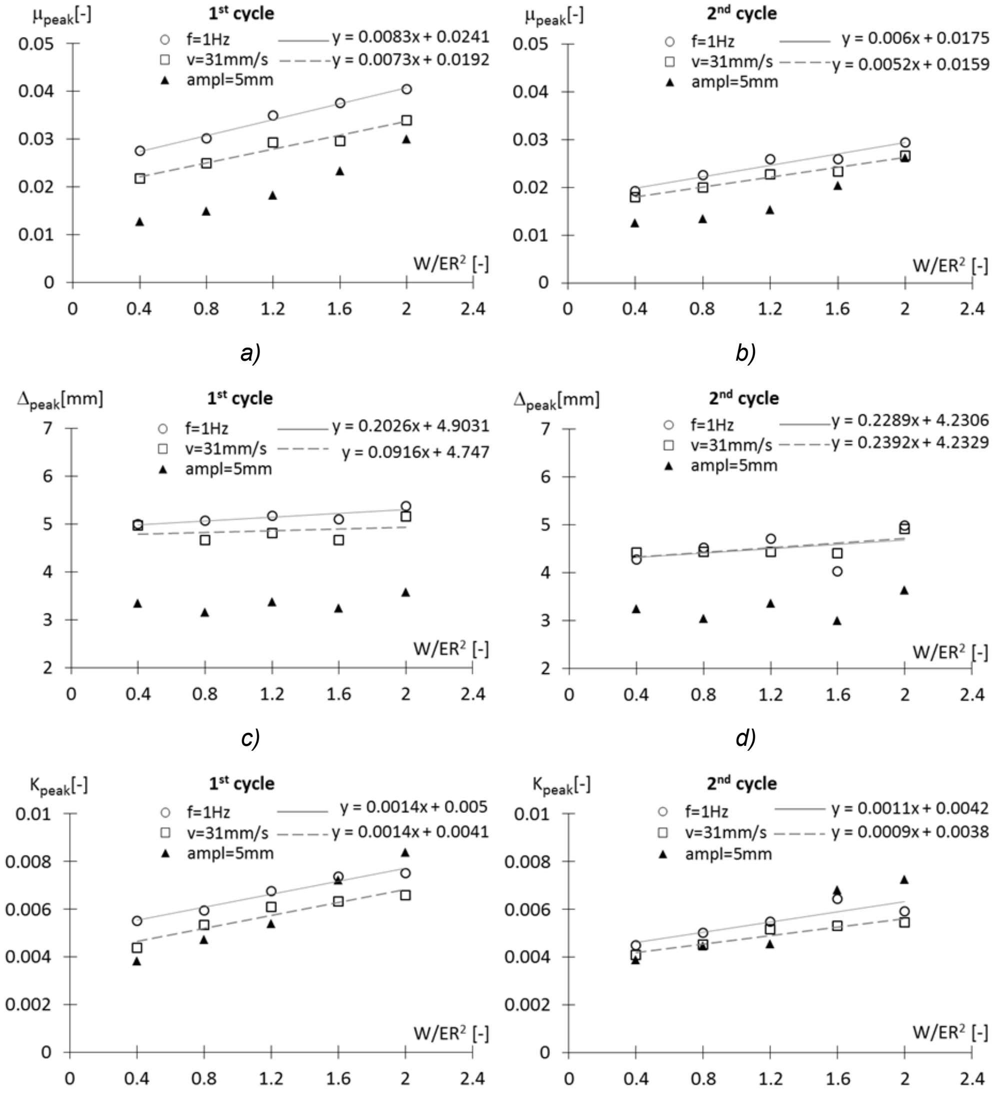

*a)* *b)*

*c)* *d)*

*e)* *f)*

*Fig. 6.29 $\mu_{peak}$, relative displacement $\Delta_{peak}$ and secant stiffness $K_{peak}$ plotted versus the stress parameter $W/ER^2$. Case: rubber A, t=2mm, D=25mm.*

influence of the ball diameter D and the rubber thickness t on $\Delta_{peak}$, which increases with increasing in the value of these parameters D and t. In addition, it is worth noting that while $\mu_{peak}$ increases with increasing in the thickness, it decreases with increasing in the diameter of the ball.

The dependence of these parameters on the stress level W* is also interesting (see Fig. 6.29): while $\mu_{peak}$ increases visibly with increasing in the value of W*, $\Delta_{peak}$ remains substantially constant or increases very slightly.

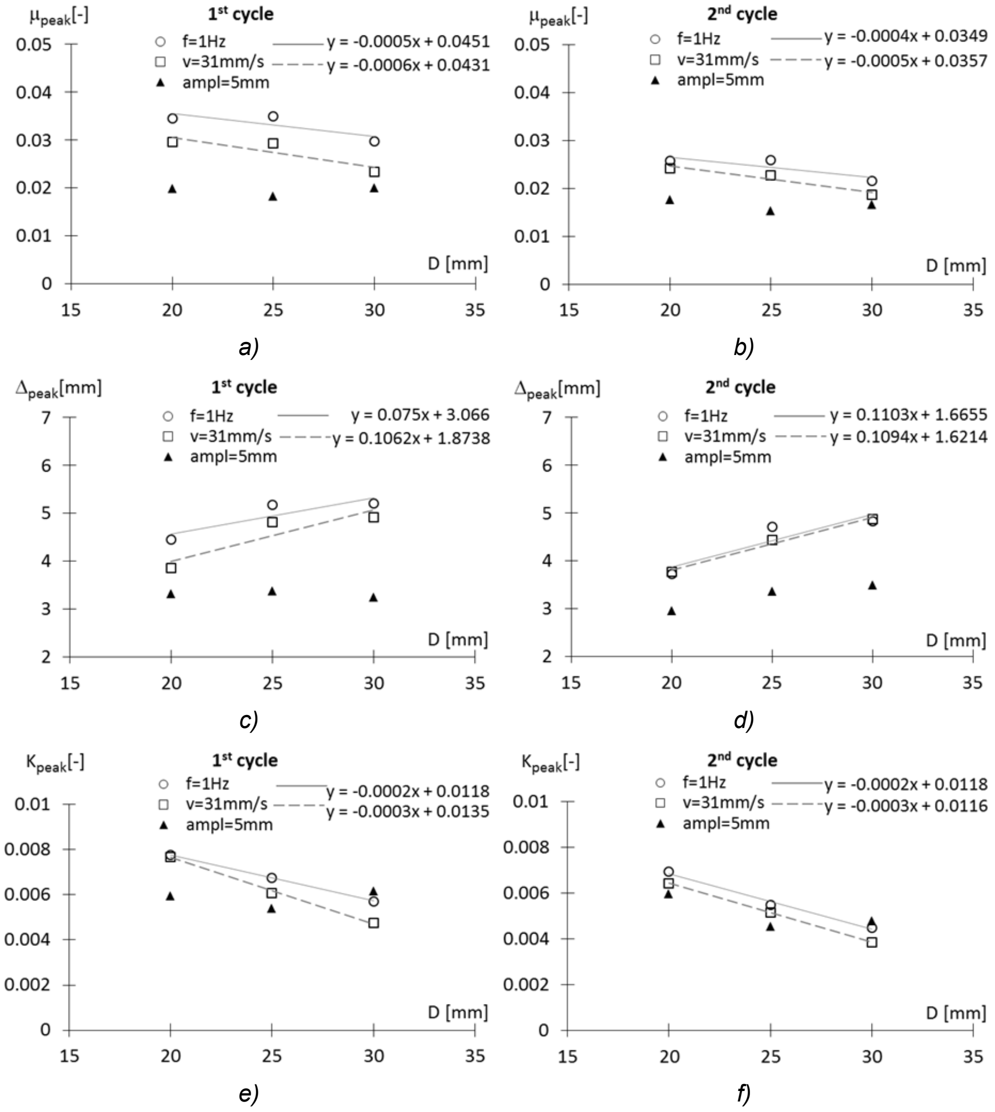

*a)* *b)*

*c)* *d)*

*e)* *f)*

*Fig. 6.30 $\mu_{peak}$, relative displacement $\Delta_{peak}$ and secant stiffness $K_{peak}$ plotted versus the diameter D of the ball. Case: rubber A, t=2mm, $W/ER^2$=1.2.*

These figures have an illustrative nature, and are intended to show the principal dependences of the peak phenomenon on the different test conditions analyzed. The values of $\mu_{peak}$, $\Delta_{peak}$ and $K_{peak}$ plotted for each type of test, being referred to the maximum value between the values of $\mu_{max}$ associated with that particular type of test, could be corresponding to μ-disp loops with different amplitude.

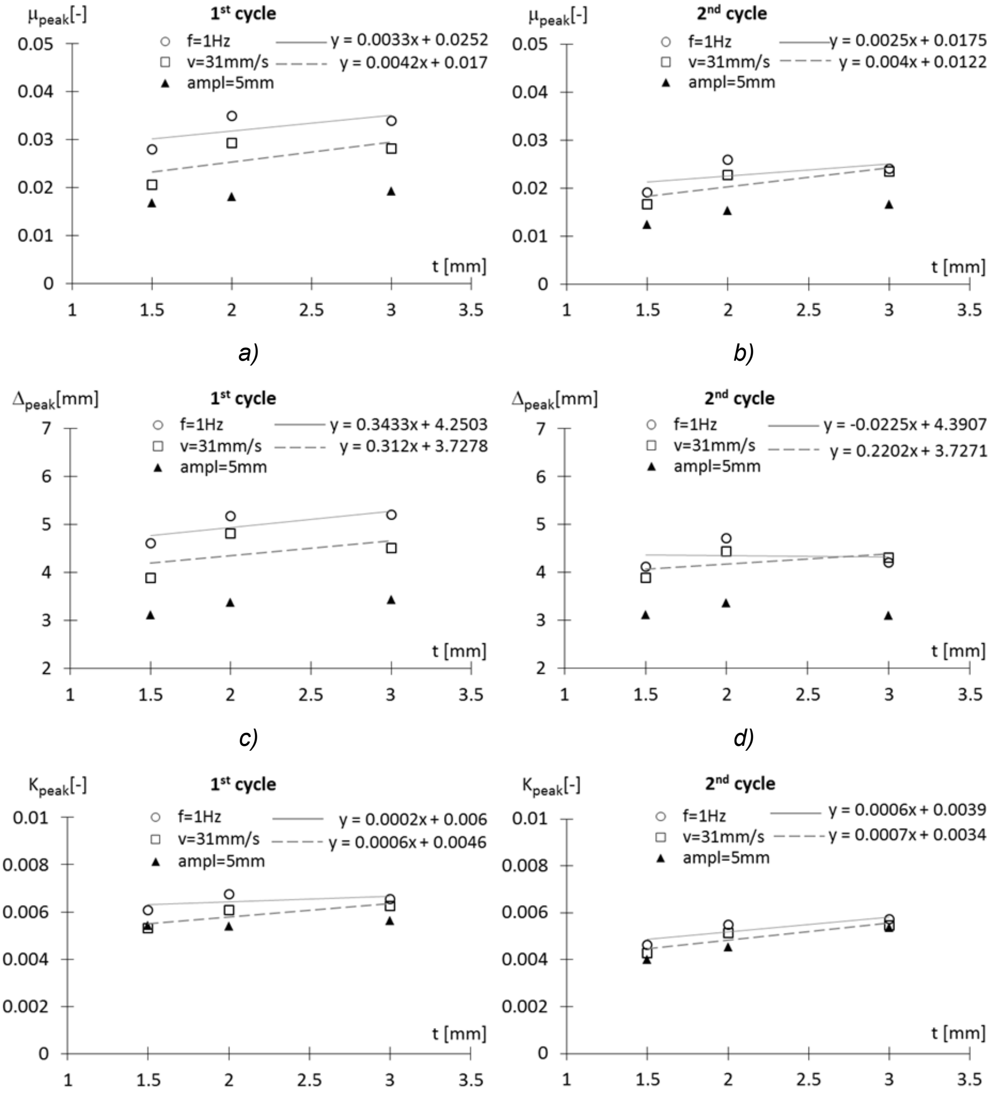

*a)* *b)*

*c)* *d)*

*e)* *f)*

*Fig. 6.31 $\mu_{peak}$, relative displacement $\Delta_{peak}$ and secant stiffness $K_{peak}$ plotted versus the thickness t of the rubber layer. Case: rubber A, D=25mm, $W/ER^2$=1.2.*

Further details about this, together with a different elaboration of these results, will be presented later with the aim to show the influence of $\mu_{peak}$ by the recovery time and by the distance of rolling of the balls from their initial pits.

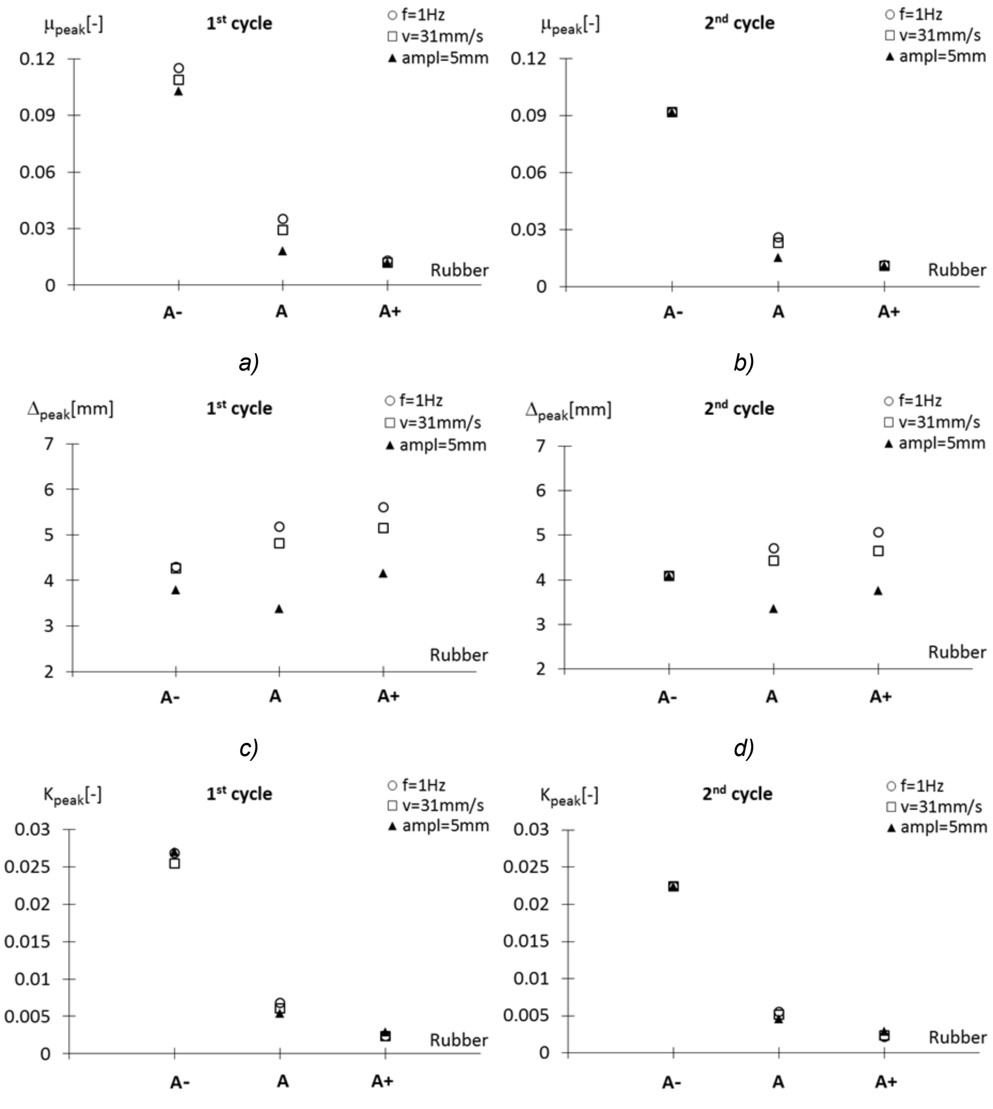

*a)* *b)*

*c)* *d)*

*e)* *f)*

*Fig. 6.32 $\mu_{peak}$, relative displacement $\Delta_{peak}$ and secant stiffness $K_{peak}$ plotted versus the type of the rubber. Case: t=2mm, D=25mm, $W/ER^2$=1.2.*

## 6.3 Tests for the measurement of the pit geometric profiles

### *6.3.1 Description of the tests*

The purpose of this experimentation is to investigate the residual indentation formed in a thin rubber layer, due to creep in the rubber, observed after an indenter (steel ball) has been removed following a period under static load. The results of such experimentation, together with the results of the previous tests, could be useful for a better comprehension of the small-deflections behaviour of the RBRL device, principally helping to define and predict the local effects - in particular the peak force phenomenon - of the balls roll-out from their pits.

The new samples of Fig. 6.33 have been realized for this experimentation, and consist of approximately 12x12 cm sheets of rubber directly moulded on steel circular plates, previously sandblasted and painted with Chemlok_220 as bonding agent. A procedure similar to the one adopted for the realization of the rubber layers for the RBRL devices (see Section 5.1) was used also in this case. The choice to perform the measurement of the geometric profiles of the pits on these new samples rather than on the bigger plates of the RBRL devices was made on the basis of testing. It has enabled these tests to be done independently of the other tests on the RBRL systems. The same rubber mixtures A, A+ and A-, mixed and employed for the RBRL devices previously tested, were used also for these samples. The characterization tests of rubber compounds, with their principal characteristics and parameters, are reported in Section 5.2.

The tests for each sample consisted of two principal phases:

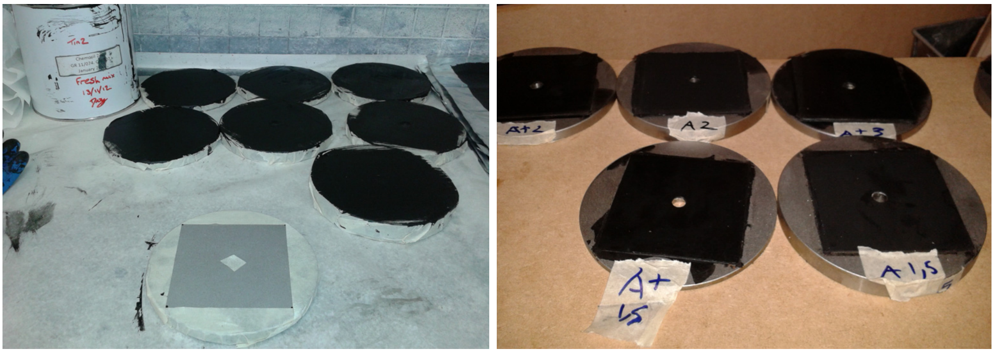

*a)* *b)*

*Fig. 6.33 Samples used to measure the geometric profiles of the pits: a) painting with Chemlok_220 (bonding agent) after sandblasting of the steel plates; b) samples finished.*

1) application of the load on two steel balls supported by the rubber layer of the sample, approximately for 25 hours, by means of another circular steel plate without rubber, placed over the balls, connected to a stud passing through the central holes of the steel plates, which ended with a support element for the application of the masses (see Fig. 6.34);

2) unloading of the sample and, within 10-15 minutes, measuring of the geometric profile of the depressions created by the steel balls on the rubber sheet, due to the load and its dwell time (see Fig. 6.35 and Fig. 6.36).

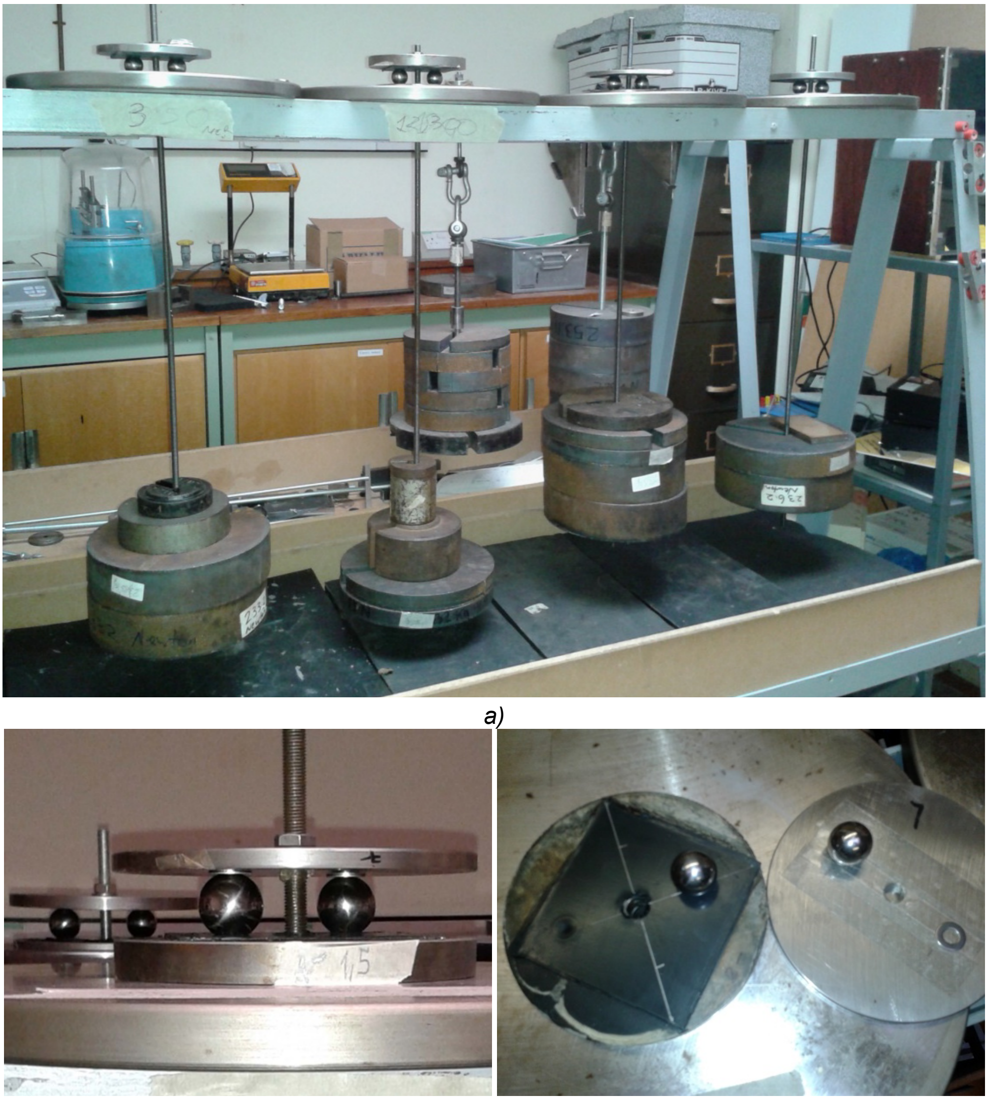
a)

b) c)

*Fig. 6.34 Setup for the first phase of the test: application of the load on the samples for 25h.*

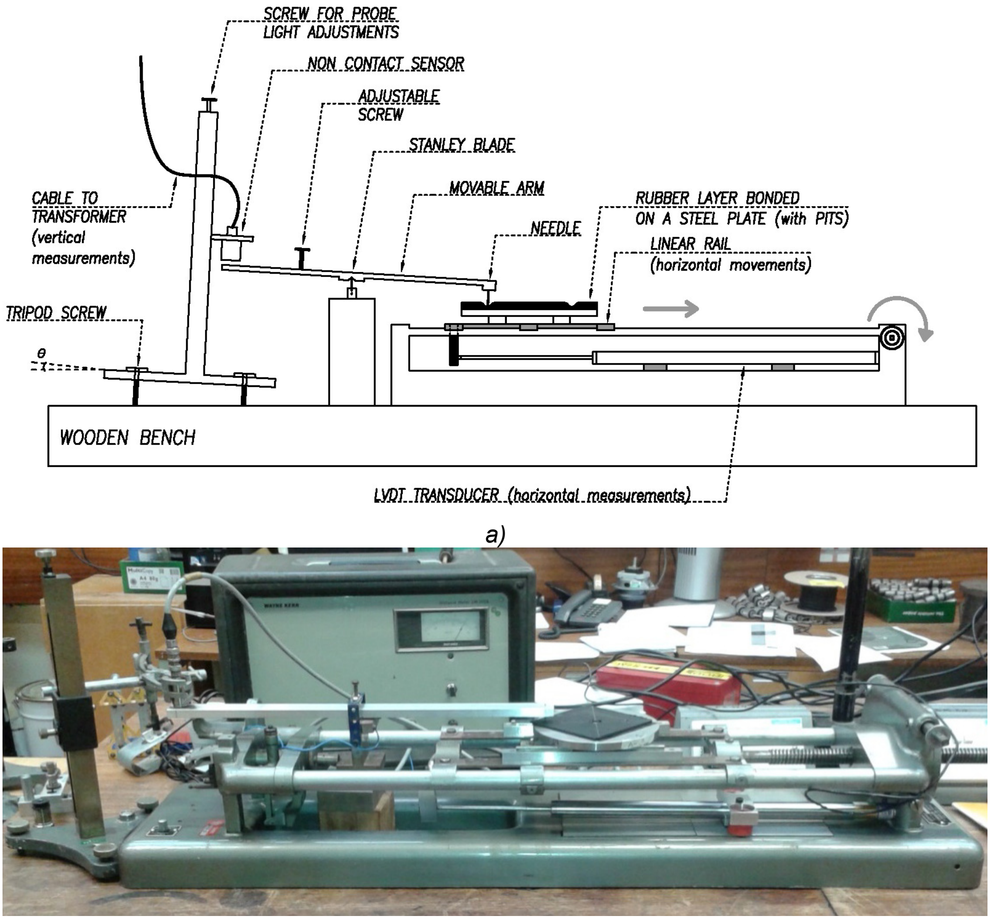
SCREW FOR PROBE LIGHT ADJUSTMENTS
NON CONTACT SENSOR
ADJUSTABLE SCREW
STANLEY BLADE
MOVABLE ARM
NEEDLE
RUBBER LAYER BONDED ON A STEEL PLATE (with PITS)
LINEAR RAIL (horizontal movements)
CABLE TO TRANSFORMER (vertical measurements)
TRIPOD SCREW
θ
WOODEN BENCH
LVDT TRANSDUCER (horizontal measurements)

a)

b)

*Fig. 6.35 a) Scheme and b) image of the setup for the measurement of the geometric profiles of the pits.*

The choice to use only two steel balls instead of three, that if not aligned define only one plane, is due to the lower vertical load to be applied to reach the target stress levels on the rubber (reported in Tab. 6.3). Two washers (see Fig. 6.34 b, c) were used to locate the balls properly relative to the top plate and together with a nut on the stud ensured the two steel plates remained parallel to each other, thus approximate equality was achieved between the loads on the balls. In this way every sample was also used for two tests, having every time undisturbed rubber for use in the second test, rotating the diametrically opposed placement of the balls by 90° (see Fig. 6.34 c).

The setup for the measurement of the pit profiles – after unloading and removing the balls – is shown in Fig. 6.35. It consists of a sledge on which the test plate was mounted, the sledge in turn being supported on an extensometer frame and moved horizontally with a lead screw. A LVDT transducer was opportunely placed to measure the horizontal displacement x of the sledge. The vertical profile y of the rubber surface was followed using the vertical motion of a needle probe mounted in an aluminium alloy bar, pivoted on a blade. The swing of the arm was measured using a non-contacting capacitance probe.

The 28 tests carried out are indicated in Tab. 6.3; these covered the following combinations of parameters:

- rubber: A, A+, A- ;
- thickness (*t*) of the rubber layer: 1.5 – 2 – 3 mm;
- diameter (*D*) of the steel balls: 15 – 20 – 25 – 30 mm;
- stress parameter ($W/ER^2 = W^*$): 1.2 – 2 – 3;

where R is the radius of the steel balls.

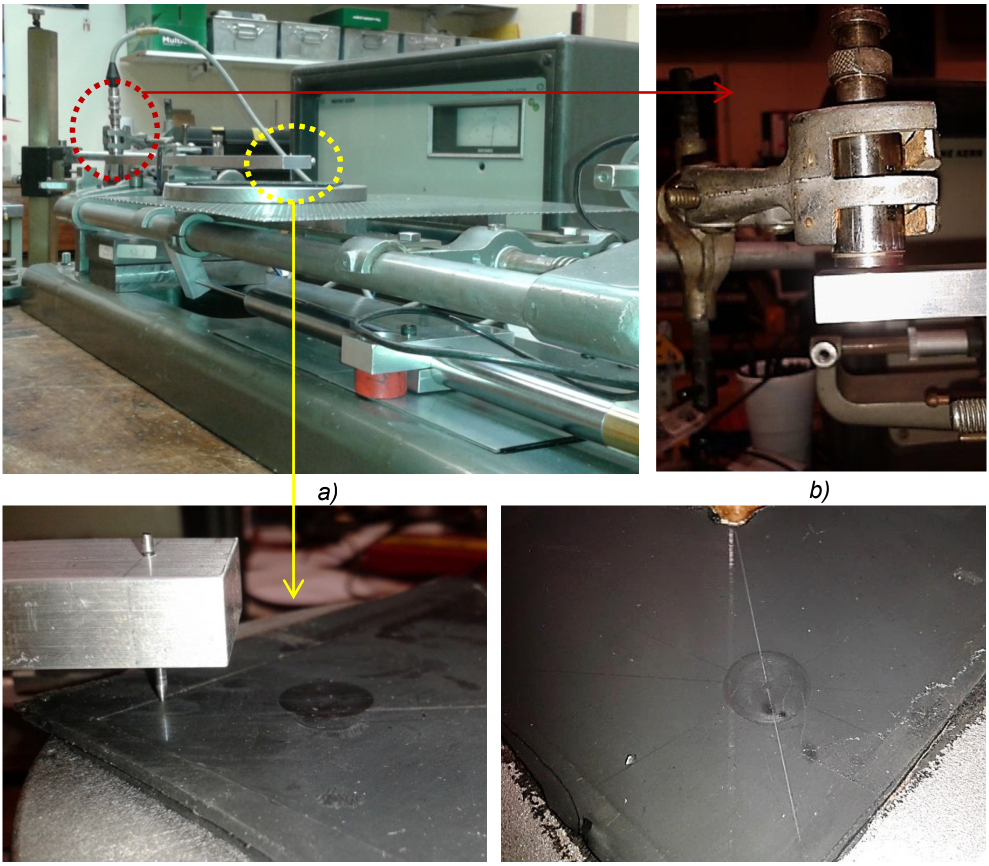

a) b)

c) d)

*Fig. 6.36 Details of the setup (a) for the measurement of the pit profiles: b) non-contacting capacitance probe and c) needle probe at the two ends of the aluminium alloy bar. d) View of a pit after some measures (the lines shown the measurement directions).*

More measures of the same pit were performed and both the pits of the same sample were analyzed. This was essential to reduce the error in the measurement and to have a more realistic mean value of the maximum residual indentation for each test. However, the time passed between unloading and measuring the profile has to be considered carefully: repetitions of the test on the same pit generally showed a slow reduction in indentation with time from unloading, due to the viscoelastic recovery of the rubber. So, when the first measure was considered good, also in relation to the following ones, this was assumed as the result for that test; otherwise, in the minority of the cases, an opportune mean value was taken between the following measures on the same pit or between the measures of the two pits created on the same sample.

| **Rubber** | **Name test** | **t_layer** (mm) | **D_balls** (mm) | **t/R** (-) | **W/ER$^2$** (-) |
|---|---|---|---|---|---|
| **A** | A_t1,5_D30_W1,2 | 1.5 | 30 | 0.10 | 1.2 |
| | A_t1,5_D25_W1,2 | 1.5 | 25 | 0.12 | 1.2 |
| | A_t2_D25_W1,2 | 2 | 25 | 0.16 | 1.2 |
| | A_t2_D20_W1,2 | 2 | 20 | 0.20 | 1.2 |
| | A_t3_D25_W1,2 | 3 | 25 | 0.24 | 1.2 |
| | A_t3_D15_W1,2 | 3 | 15 | 0.40 | 1.2 |
| | A_t1,5_D30_W2 | 1.5 | 30 | 0.10 | 2 |
| | A_t1,5_D25_W2 | 1.5 | 25 | 0.12 | 2 |
| | A_t2_D25_W2 | 2 | 25 | 0.16 | 2 |
| | A_t2_D20_W2 | 2 | 20 | 0.20 | 2 |
| | A_t3_D25_W2 | 3 | 25 | 0.24 | 2 |
| | A_t3_D15_W2 | 3 | 15 | 0.40 | 2 |
| | A_t2_D30_W3 | 2 | 30 | 0.13 | 3 |
| | A_t2_D25_W3 | 2 | 25 | 0.16 | 3 |
| | A_t2_D20_W3 | 2 | 20 | 0.20 | 3 |
| | A_t2_D15_W3 | 2 | 15 | 0.27 | 3 |
| **A+** | A+_t1,5_D25_W1,2 | 1.5 | 25 | 0.12 | 1.2 |
| | A+_t2_D25_W1,2 | 2 | 25 | 0.16 | 1.2 |
| | A+_t3_D25_W1,2 | 3 | 25 | 0.24 | 1.2 |
| | A+_t1,5_D25_W2 | 1.5 | 25 | 0.12 | 2 |
| | A+_t2_D25_W2 | 2 | 25 | 0.16 | 2 |
| | A+_t3_D25_W2 | 3 | 25 | 0.24 | 2 |
| **A-** | A-_t1,5_D25_W1,2 | 1.5 | 25 | 0.12 | 1.2 |
| | A-_t2_D25_W1,2 | 2 | 25 | 0.16 | 1.2 |
| | A-_t3_D25_W1,2 | 3 | 25 | 0.24 | 1.2 |
| | A-_t1,5_D25_W2 | 1.5 | 25 | 0.12 | 2 |
| | A-_t2_D25_W2 | 2 | 25 | 0.16 | 2 |
| | A-_t3_D25_W2 | 3 | 25 | 0.24 | 2 |

*Tab. 6.3 Characteristics of the tests carried out: combinations of the stress parameter W*, thickness t of the rubber layer and diameter D of the balls for the different rubber compounds.*

### *6.3.2 Results*

The results obtained by this experimentation are summarized here below from Fig. 6.37 to Fig. 6.46. In particular, some geometric profiles of the residual indentation after unloading are presented and compared to each other for different test conditions, i.e. for different values of stress parameter, thickness of the rubber layer and diameter of the balls. The profiles are plotted separately for each type of rubber (A, A+, A-) and, to better understand their real shape, they are singularly replicated together with the profile of the associated spherical indenter, although with different scales of representation in x and y axes.

The dependence of the maximum residual indentation $d_R$ on the parameters involved in this study is clear: $d_R$ increases with increasing in the stress level (Fig. 6.37), in the thickness of the rubber layer (Fig. 6.39) and in the diameter of the balls (Fig. 6.41). It is very influenced also by the viscoelastic properties of the rubber compound, as proved by its higher value for the rubber A- than the rubber A or A+ for the same load and geometry (compare Fig. 6.37 with Fig. 6.43 and Fig. 6.45).

An interesting observation, with reference to the shape of these geometric profiles, was made. Considering the case of rubber A, in particular Fig. 6.38 and Fig. 6.40, two different types of shape for the residual pit are visible: either presenting the central part with a curvature still compatible with the shape of the indenter (steel ball) or showing instead a higher value of this curvature. This latter case seems to happen for the higher values of the stress parameters and for the lower ones of the rubber layer thickness. This phenomenon might be the result of a different recovery velocity of the rubber, between the central part and the sides of the pit. In fact, the central part of the rubber depression is the one subjected to the highest stresses and thus, in presence of a relevant stress parameter and a thin rubber layer, this could be characterized by relaxation effects really greater than the ones in the lateral parts of the pit. This type of shape for the residual indentation was typical for the rubber A- (see Fig. 6.44) while it was never observed for the rubber A+ (Fig. 6.46). This obviously points to the viscoelastic properties of the rubber, which are much more pronounced in the case of rubber A-.

Fig. 6.47 shows photographs of these two different types of geometric profile.

***__Case: rubber A__***

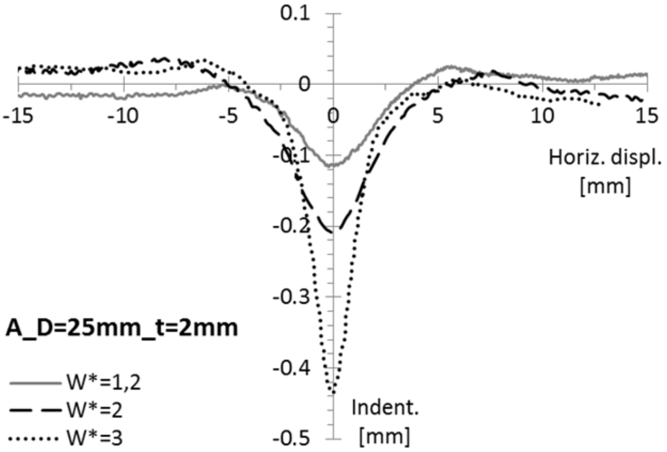

*Fig. 6.37 Comparison of the geometric profiles of the residual indentation for the case of rubber A, D=25mm, t=2mm, for different values of the stress level (W*=1.2, 2, 3).*

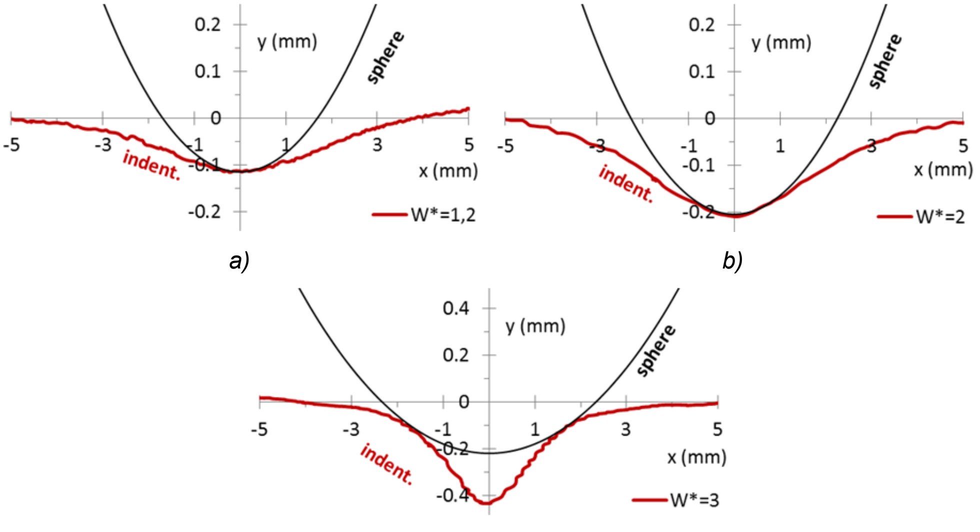

a)

b)

c)

*Fig. 6.38 Geometric profiles of Fig. 6.37 with the indication of the relative indenter.*

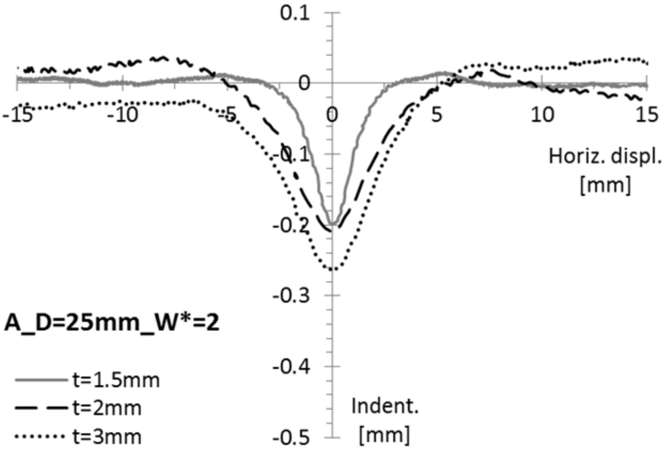

*Fig. 6.39 Comparison of the geometric profiles of the residual indentation for the case of rubber A, D=25mm, W*=2, for different thicknesses of the rubber layer (t=1.5, 2, 3 mm).*

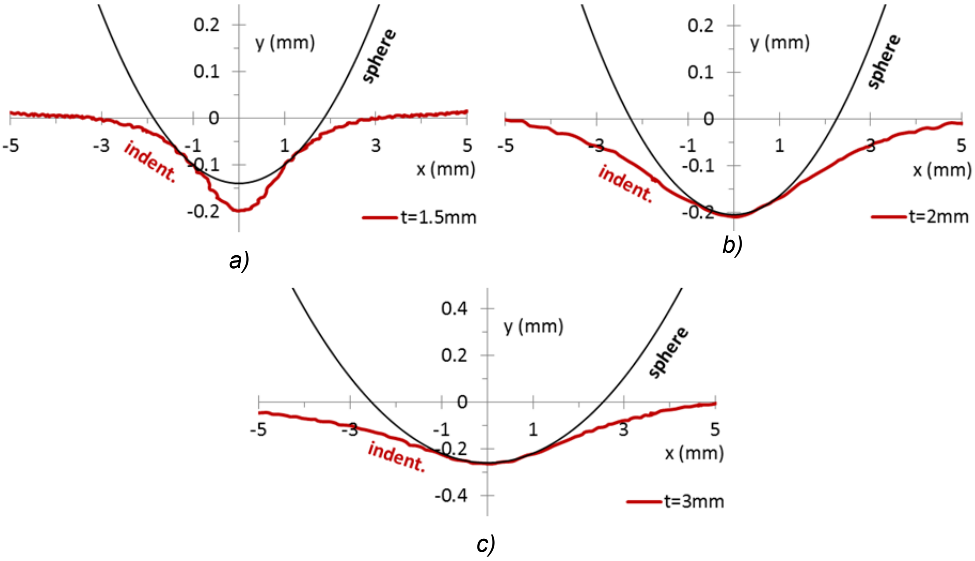

a)

b)

c)

*Fig. 6.40 Geometric profiles of Fig. 6.39 with the indication of the relative indenter.*

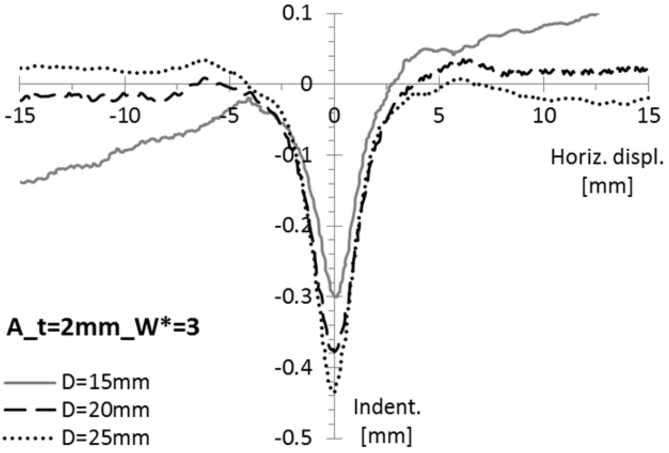

*Fig. 6.41 Comparison of the geometric profiles of the residual indentation for the case of rubber A, t=2mm, W*=3, for different values of the ball diameter (D=15, 20, 25).*

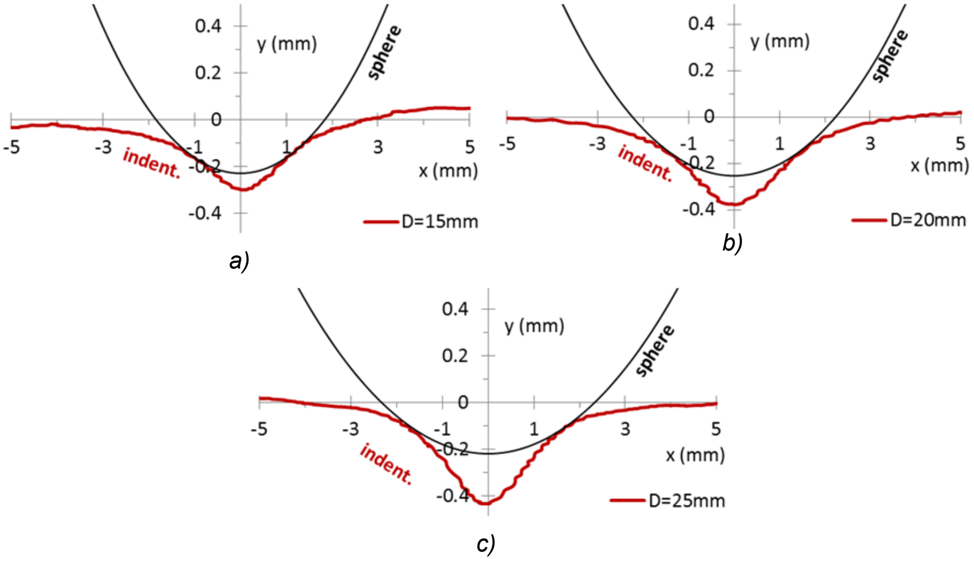

*Fig. 6.42 Geometric profiles of Fig. 6.41 with the indication of the relative indenters.*

## ***Case: rubber A+***

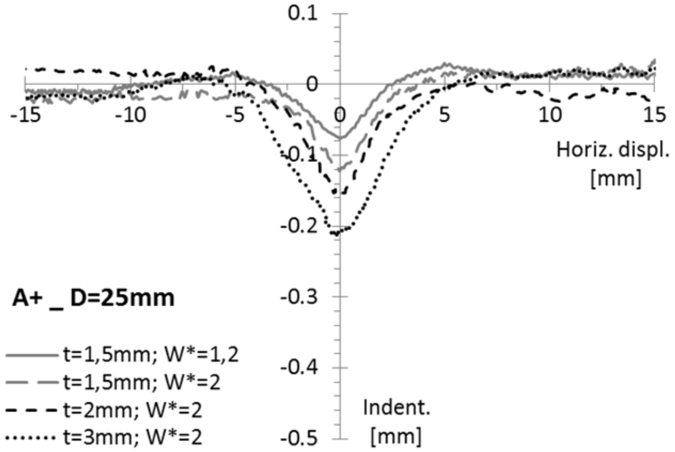

*Fig. 6.43 Comparison of the geometric profiles of the residual indentation for the case of rubber A+, D=25mm, for different combinations of stress level (W*=1.2, 2) and thickness of rubber layer (t=1.5, 2, 3 mm).*

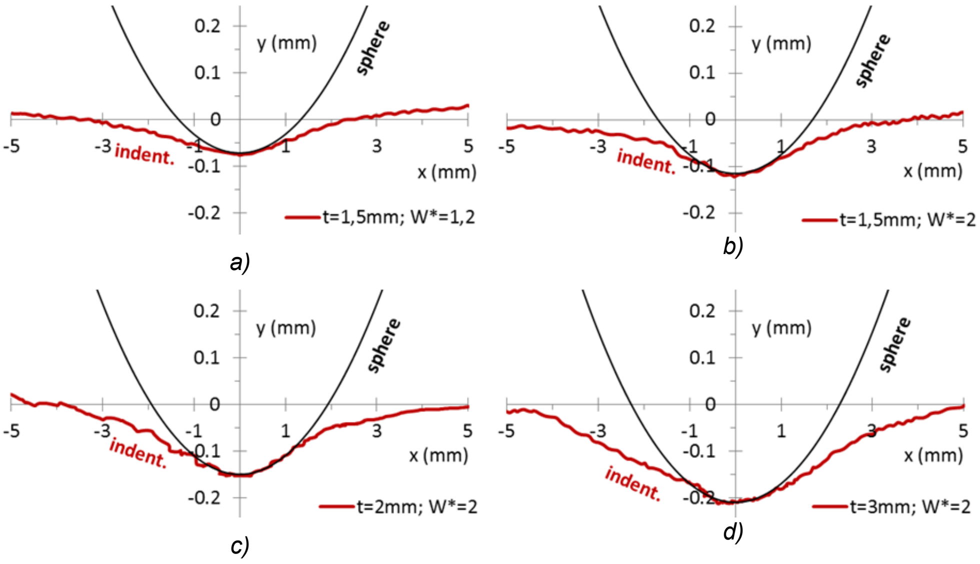

*Fig. 6.44 Geometric profiles of Fig. 6.43 with the indication of the relative indenter.*

### ***Case: rubber A-***

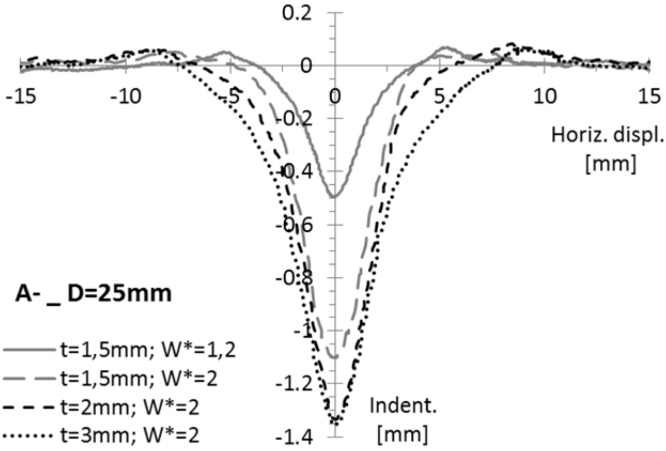

*Fig. 6.45 Comparison of the geometric profiles of the residual indentation for the case of rubber A-, D=25mm, for different combinations of stress level (W*=1.2, 2) and thickness of rubber layer (t=1.5, 2, 3 mm).*

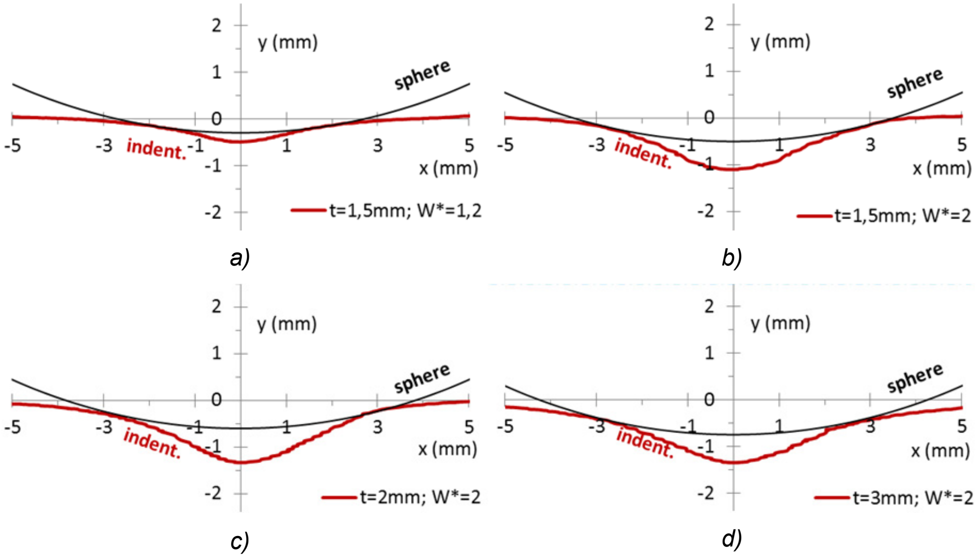

*Fig. 6.46 Geometric profiles of Fig. 6.45 with the indication of the relative indenter.*

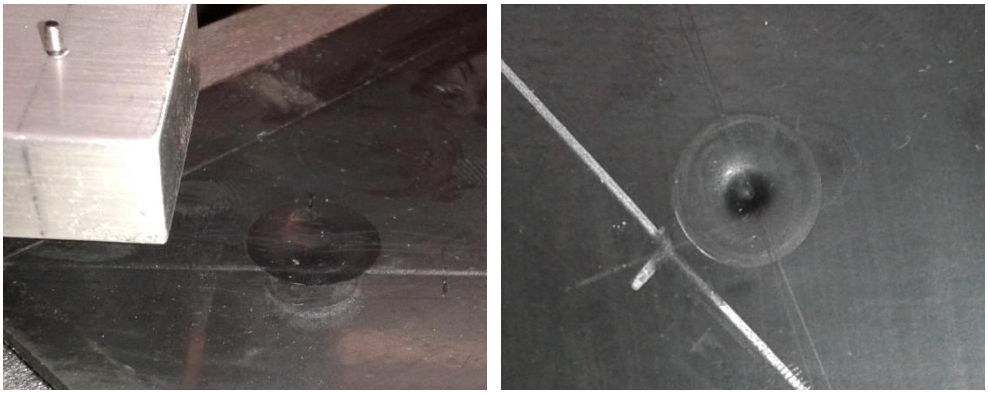

*a)* *b)*

*Fig. 6.47 Different shape of the profile of the residual indentation: a) recovery of the rubber at the same velocity (typical for rubber A+, and A with W*<2); b) recovery of the rubber with different velocities inside the pit, slower in the central part (typical for rubber A-).*

Fig. 6.48 and Fig. 6.49 present the maximum values of the residual indentation $d_R$ for all the tests performed; $d_R$ was defined as the distance from the lowest point in the pit to the plane of the undeformed rubber. The $d_R$ values are plotted against the ratio t/R and for different values of $W/ER^2$. As shown before, $d_R$ increases with increase of both the parameters t (thickness) and D (diameter), or radius R. For this reason and for the case of rubber A, these results were also reproduced separately for the different thicknesses of rubber analyzed (Fig. 6.48 b, c, d), in order to better visualize these dependencies.

In order to better define the local effects of the RBRL device when the balls roll-out from their pits, the definition of a theoretical relation (also empirical) between the maximum residual indentation and the parameters which influence it would be very important.

For this purpose, the Hertz's equations (see Section 3.1.4) for the indentation depth $d$ and the contact radius $a$, valid for an elastic half space of Young's modulus $E$, are once again shown here below (Timoshenko, 1934):

$$a = \left[ \frac{3}{4} WR \left( \frac{1-\nu^2}{E} \right) \right]^{\frac{1}{3}} = \left[ \frac{9}{16} \frac{WR}{E} \right]^{\frac{1}{3}} \tag{6.3}$$

$$d = \frac{a^2}{R} = \left( \frac{9}{16} \right)^{\frac{2}{3}} \left( \frac{W^2}{E^2 R} \right)^{\frac{1}{3}} \tag{6.4}$$

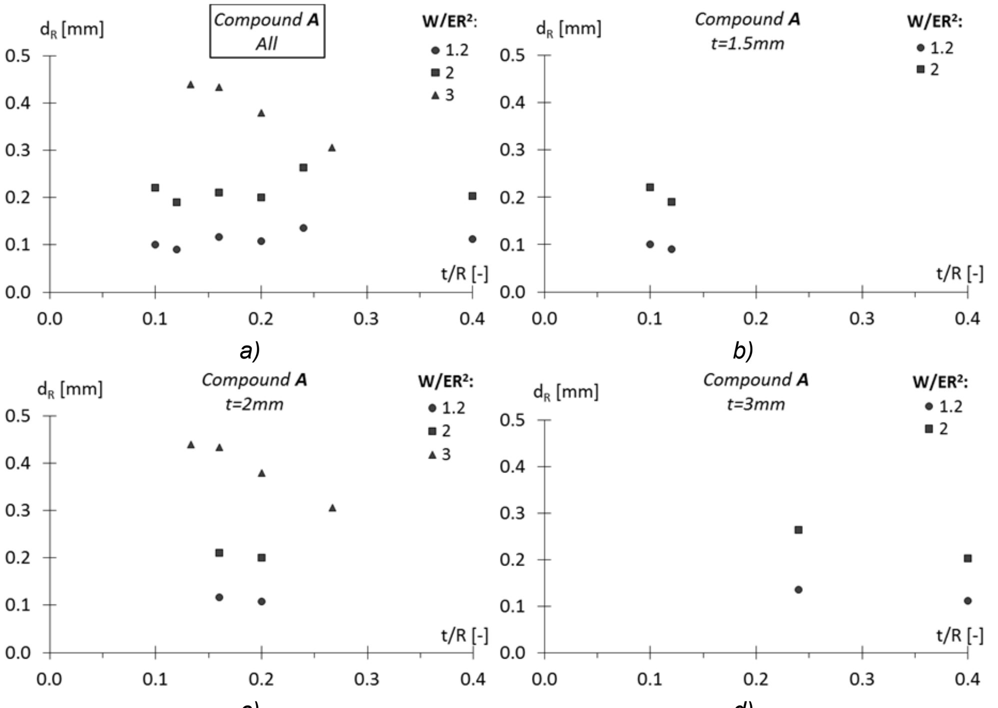

a) b)

c) d)

*Fig. 6.48 a) Maximum residual indentations by tests, after a dwell time of the load of 25 hours, for the case of rubber A and different values of t/R and W/ER$^2$. The same results are reproduced in the figures b), c), d) for the different values of rubber layer thickness analyzed.*

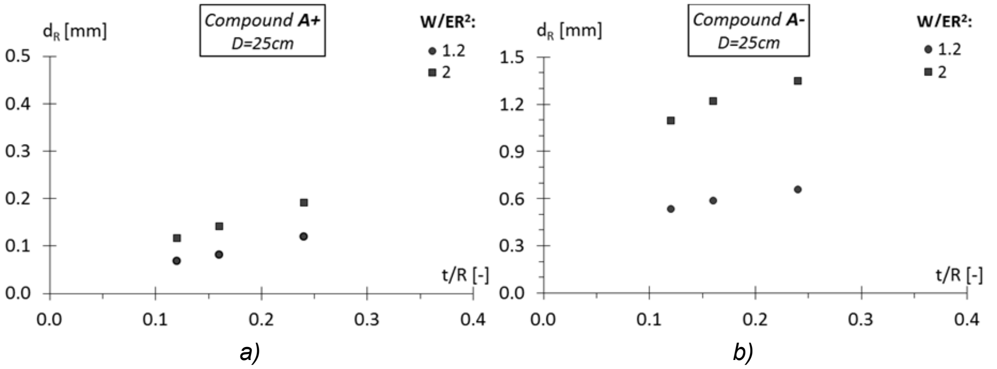

a) b)

*Fig. 6.49 Maximum residual indentations by tests, after a dwell time of the load of 25 hours, for different values of t/R and W/ER$^2$, and for the case of rubber A+ (a) and A- (b).*

in which $W$ is the vertical load, $R$ is the sphere radius and $\nu$ is the Poisson's ratio, which was set to 0.5, the material being rubber. An interesting experimentation performed by Waters (1965), on the influence of the thickness of the rubber layer on the indentation, has shown the possibility to relate the parameters $a$ and $d$ in the same way as in the Hertz theory:

$$a = \sqrt{dR} \tag{6.5}$$

even if $d$ is not the Hertzian value $d_\infty$ (related to a rubber layer of infinite thickness) but the one modified through the equation:

$$d = d_\infty f(t/a) = \left(\frac{9}{16}\right)^{\frac{2}{3}} \left(\frac{W^2}{E^2 R}\right)^{\frac{1}{3}} f(t/a) \tag{6.6}$$

where $t$ is the thickness of rubber layer and $f(t/a)$ is the following function empirically determined by Waters, true within the regime of small loads and indentations:

$$f(t/a) \simeq 1 - \exp(-At/a) \tag{6.7}$$

in which $A$ is a parameter for the boundary conditions at the back of the rubber layer, and is set 0.417 for the bonded condition.

The equations above represent also the base of the Muhr et al. theory (1997) about rolling friction coefficient on thin rubber layer, presented in the Section 3.1.4 and investigated through a parametric experimentation in the previous Chapter.

The indentation values calculated through the Eqs. (6.6) and (6.7) are reported in Fig. 6.50 and Fig. 6.51, for the different rubbers, ratios of t/R and values of $W/ER^2$ analyzed in this experimentation; these values are indicated with the symbol $d_W$ for convenience, where “$_W$” indicates Waters. In particular, two types of maximum indentation under load are shown in these figures: the one calculated using the elastic Young’s modulus E, and the one obtained considering the modulus $E'(t_{dw})$ relaxed after a time dwelling $t_{dw}$ of the load of 1500 minutes (consistent with the tests carried out). The relation between the moduli is:

$$\begin{aligned} E'(t_{dw}) &\simeq E - 3H_0 \cdot \ln(t_{dw}) \\ G'(t_{dw}) &\simeq G - \ H_0 \cdot \ln(t_{dw}) \end{aligned} \tag{6.8}$$

where G is the shear modulus and $H_0$ is the relaxation parameter of the rubber. The principal properties of the rubbers used in these tests (see Section 5.2) are reported again in Tab. 6.4 for more clarity; in particular, $H_0$ values were obtained considering the variation of the time in minutes, hence $t_{dw}$ has to be used is minutes.

| Rubber | G [MPa] | E [MPa] | tgδ [-] | $H_0$ [MPa] |
|---|---|---|---|---|
| **A+** | 0.56 | 1.68 | 0.010 | 0.00375 |
| **A** | 0.38 | 1.14 | 0.037 | 0.00412 |
| **A-** | 0.29 | 0.87 | 0.108 | 0.00827 |

*Tab. 6.4 Principal characteristics of the rubber compounds used in the tests.*

The results of the maximum indentation $d_W$, of Fig. 6.50 and Fig. 6.51, clearly show that the residual indentation $d_R$ measured by the tests does not correspond to the indentation increment, under load, due to the relaxation effects on the rubber and represented in these figures by the distance between the $d_W$ values associated with the same case study.

Anyhow, these results show a influence of the parameters t, R and $W/ER^2$ on the values of $d_W$ similar to the influence of the same parameters on $d_R$ (see Fig. 6.48 and Fig. 6.49). In particular $d_W$, as well as $d_R$, increases with increasing $W/ER^2$, t and R. This observation is significant for the purpose of devising an empirical relation able to predict the values of the residual indentation $d_R$, but it is not enough considering the following points:

- the values of the indentation $d_W$ under load show a magnitude similar for the different rubbers, justified by the use of a non-dimensional stress parameter instead of an absolute value of force, while the residual indentations $d_R$ are very different for the various compounds analyzed;

- the dependencies on the parameters t, R and $W/ER^2$ of the values of $d_W$ and $d_R$, although similar in the trend, show different intensities; this is visible, for example, comparing Fig. 6.48 a) to Fig. 6.50 a) and looking at the case study with stress parameter equal to 3: while for the indentation under load it presents values lower than the ones associated with a bigger thickness of rubber (3 mm), for the residual indentation it shows the greater values.

Considering all that seen so far, a possible empirical relation to predict the residual indentation $d_R$ has the following form:

$$d_R = \left( d_W \cdot \frac{\Delta G}{G} \right) \cdot f_{1(stress\ parameter)} \cdot f_{2(pit\ geometry)} \cdot f_{3(rubber)} \tag{6.9}$$

The idea was to consider the value of $d_w$, calculated with the Young's modulus, as the reference value for the indentation before unloading, and multiply this value for

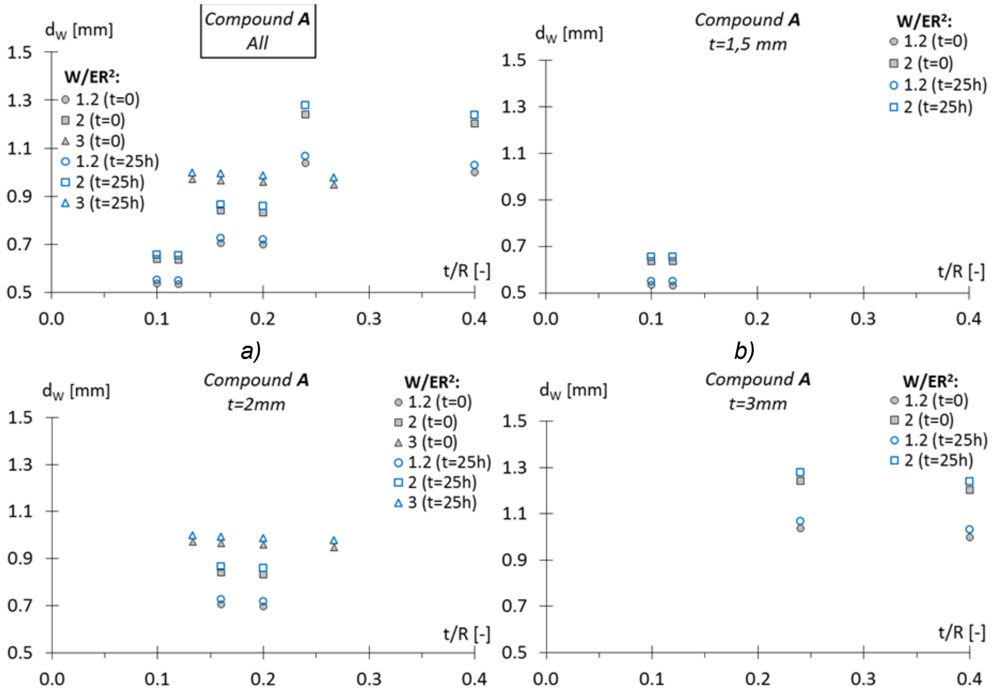

a) b) c) d)

*Fig. 6.50 a) Maximum indentations under load given by Waters' equations (Eqs. (6.6) and (6.7)), considering the Young's modulus (t=0) and the one relaxed after 25 hours (t=25h), for the case of rubber A and different values of t/R and W/ER$^2$. The same results are reproduced in the figures b), c), d) for the different values of rubber layer thickness analyzed.*

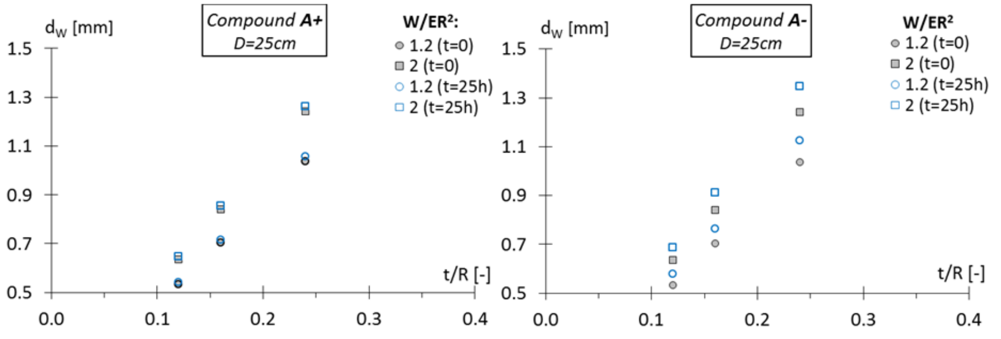

a) b)

*Fig. 6.51 Maximum indentations under load given by Waters' equations (Eqs. (6.6) and (6.7)), considering the Young's modulus (t=0) and the one relaxed after 25 hours (t=25h), for different values of t/R and W/ER$^2$, and for the case of rubber A+ (a) and A- (b).*

a fraction related to the instantaneous recover of the rubber, represented by the ratio ΔG/G, where ΔG is the part of the shear modulus G ideally lost for the relaxation phenomenon of the rubber:

$$\Delta G = H_0 \ln(t_{dw}) \tag{6.10}$$

$t_{dw}$ represents the dwell time of the static load on the rubber and, using $H_0$ reported in Tab. 6.4, it has to be considered in minutes (in these tests was 1500 min); the minimum value of $t_{dw}$ that can be considered is 1 minute. If the material is perfectly elastic the residual indentation after unloading is null, as in the case of an elastic spring pushed and then released; thus, ΔG/G ratio has a meaning of reduction of the elastic stiffness of the rubber needed to recover its deformation. If ΔG tends to 0, such as for an elastic material, $d_R$ also tends to 0, while if ΔG tends to G, such as in the case of a purely viscous material, $d_R$ tends to the value of indentation under load $d_W$, as might be expected. Furthermore, if $t_{dw}$ tends to its lower limit of 1 minute, and so the relaxation phenomenon of the rubber has not time to produce effects, consistently ΔG as well as $d_R$ will tend to 0.

However, the values obtained by multiplying $d_W$ by ΔG/G did not fit well enough the values of $d_R$ measured by the tests, although they were similar. Some corrective functions (see Eq. (6.11)) were thus used, considering the principal parameters involved in this study: this is consistent with the observations seen before, in particular with the one about the different influence of these parameters on the two types of indentation, $d_W$ and $d_R$. In fact, a same value of indentation $d_W$ under load can be obtained, for the same rubber type, using different combinations of the parameters $W/ER^2$, t and R (or contact radius *a* of the pit), which could influence in a different way the relaxation phenomenon of the rubber and thus the residual indentation; it follows that $d_W$ might not be sufficient to describe alone all the variability of $d_R$, also considering the same rubber and the same dwell time of the load for the pit creation.

Applying the corrective functions $f_1$ and $f_2$ of the Eq. (6.11) a good fitting with the experimental values of $d_R$ was obtained for the case of rubbers A and A+; the corrective function $f_3$ was finally added to consider the great dependence of $d_R$ on the viscoelastic properties of the rubber, and so to guarantee a good estimation of the residual indentation also for rubber A-: this function is approximately equal to 1 for the rubbers such as A and A+ with relatively low values of $H_0$ and loss angle.

$$\begin{aligned} f_{1(stress\ parameter)} &= \frac{W}{ER^2} \\ f_{2(pit\ geometry)} &= \frac{a}{t} \\ f_{3(rubber)} &= (1 + 1000 H_0 \delta) \end{aligned} \tag{6.11}$$

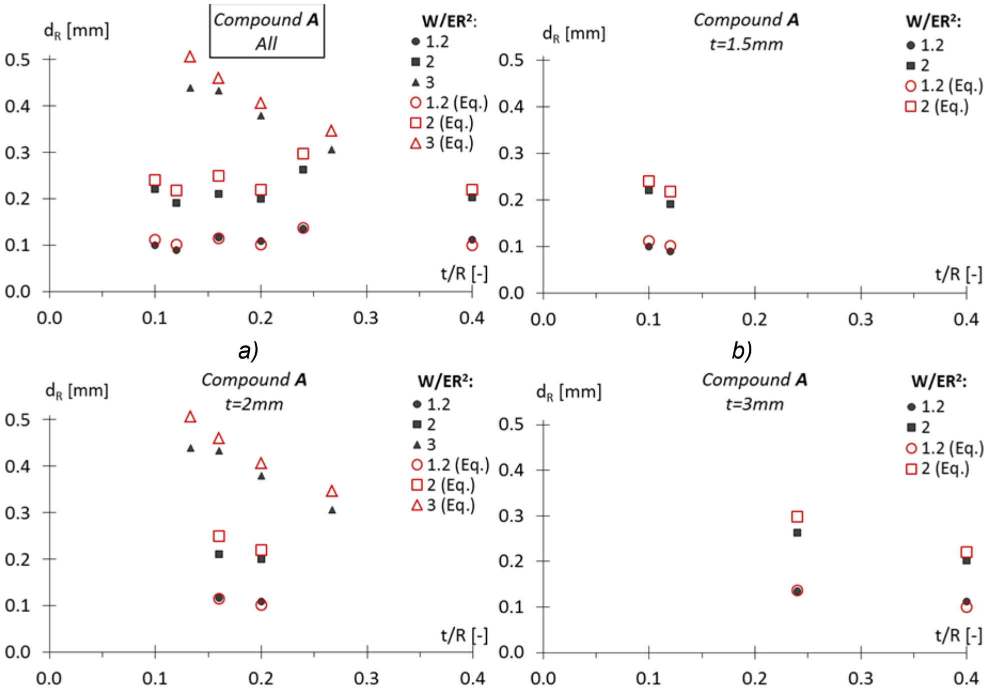

a) b)

c) d)

Fig. 6.52 a) Comparisons between test results and values calculated by Eq. (6.12) for the maximum residual indentation, for the case of rubber A and different values of t/R and W/ER$^2$. The same results are reproduced in the figures b), c), d) for the different values of rubber layer thickness analyzed.

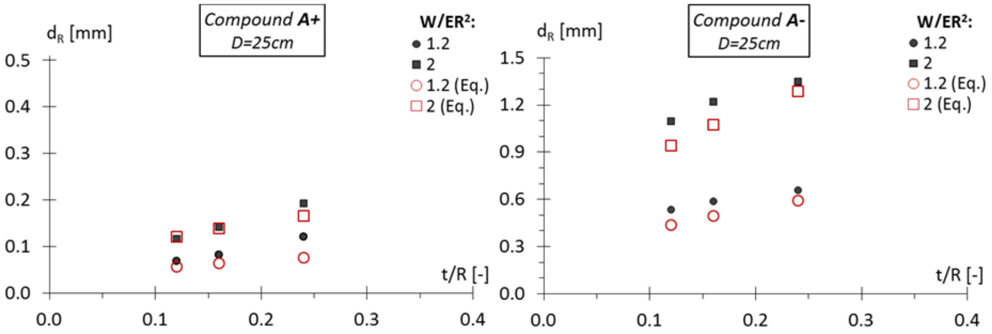

a) b)

Fig. 6.53 Comparisons between test results and values calculated by Eq. (6.12) for the maximum residual indentation, for different values of t/R and W/ER$^2$, and for the case of rubber A+ (a) and A- (b).

In conclusion, the empirical relation to estimate the residual indentation is reported in Eq. (6.12) and its efficacy is shown in Fig. 6.52 and Fig. 6.53, where the experimental values of $d_R$ are compared with the estimated ones.

$$d_R = \left( d_W \cdot \frac{\Delta G}{G} \right) \cdot \frac{W}{ER^2} \cdot \frac{a}{t} \cdot (1 + 1000 H_0 \delta) \tag{6.12}$$

Fig. 6.54, Fig. 6.55 and Fig. 6.56 give the estimates of the residual indentation $d_R$, according to Eq. (6.12) and after a dwell time of the load of 1500 minutes, for a certain range of t/R and for chosen values of the stress parameter and the ball diameter, separately for the three rubbers investigated.

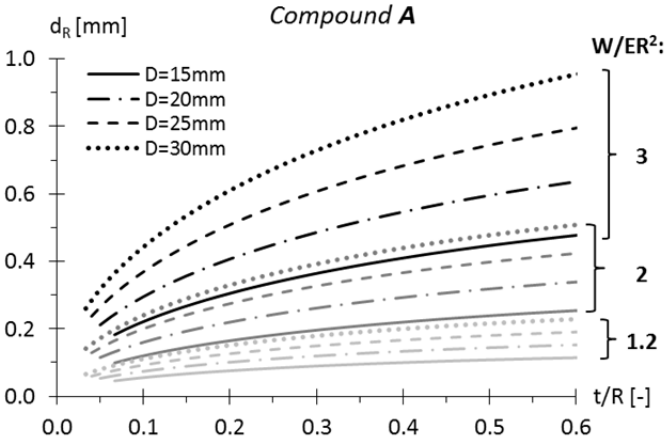

*Fig. 6.54 Estimate of the maximum residual indentation $d_R$ through the Eq. (6.12), after a dwell time of the load of 25 hours, for the rubber A and for a certain range of t/R and $W/ER^2$.*

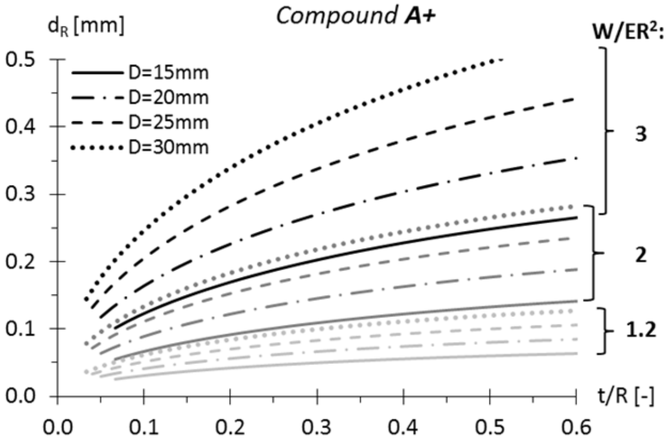

*Fig. 6.55 Estimate of the maximum residual indentation $d_R$ through the Eq. (6.12), after a dwell time of the load of 25 hours, for the rubber A+ and for a certain range of t/R and $W/ER^2$.*

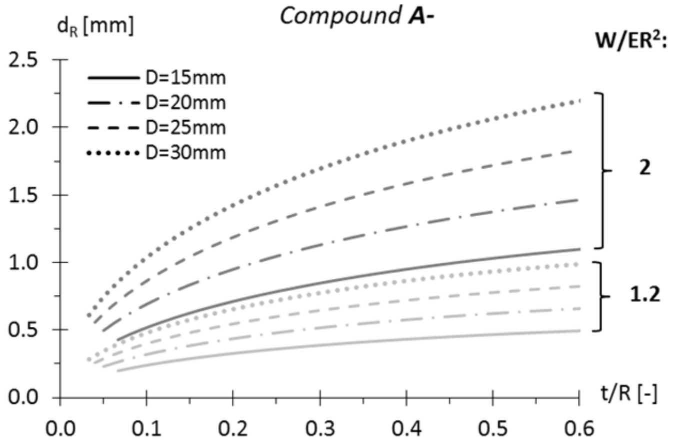

*Fig. 6.56 Estimate of the maximum residual indentation $d_R$ through the Eq. (6.12), after a dwell time of the load of 25 hours, for the rubber A- and for a certain range of t/R and $W/ER^2$.*

These results will be used later for some numerical elaborations with regard to the peak rolling forces due to the roll-out of the balls from their pits. In particular, the peak forces measured by the sinusoidal tests previously described, at small amplitudes, will be analyzed together with the information on the residual indentation to find a general relation for the prediction of the peak forces of the RBRL device: this is really important for the correct design of the device and for the modelling of its dynamic behaviour for assessing its efficacy.

## 6.4 Sinusoidal uniaxial tests on ECOEST-project devices: dwell time influence

### *6.4.1 Description of the tests*

In the ECOEST project (Guerreiro et al., 2007) the characterisation of the RBRL system was limited to a separate test for the recentering springs done at TARRC, and to sinusoidal accelerations of the mass-down configuration (see chapter 4) on A-A rubber tracks, together with the recentering springs, carried out on the ISMES shaking table at 5 Hz. For this reason, it was decided to perform more comprehensive monoaxial sinusoidal tests at TARRC, for the current project, considering all the types of rubber layer used in the ECOEST experimentation.

These tests, presented in Tab. 6.5, were carried out using the same test setup shown in section 5.3.1: a single shear configuration for one RBRL device with no recentering springs. In particular, three possible combinations of the rubber layers were tested: A-A, A-B and B-B (Guerreiro et al., 2007); for each of these combinations, two different values of load per ball were used, 150 N and 250 N, corresponding to values of the stress parameter of about 0.8 and 1.35 respectively. In addition, three different times $t_{dw}$ of dwelling of the load in its static configuration were tested for the cases with rubber tracks A-A: 6, 12 and 24 hours; for the other tests, only the dwell time of 24 hour was used.

The sinusoidal displacement excitations used for the tests are reported in Tab. 6.6 and Tab. 6.7. The first input (Tab. 6.6) consisted of sinusoidal cycles of small amplitude (balls inside their pits), from 1 to 5 mm, executed at different frequencies to keep the maximum value of velocity constant: three different maximum velocities were assumed, 31.4, 62.8 and 125.6 mm/s. The other three sinusoidal inputs (Tab. 6.7) involved sinusoidal cycles from 6 to 70 mm and were run separately for the three cases of maximum velocity. Each test included three sinusoidal cycles.

The reason for performing the tests with amplitudes from 1 to 5 mm, for all the velocities assumed, before the other tests with constant velocity and greater amplitudes, was to study the effect of the pits on the system behaviour, it being very influenced by the rubber recovery, which will take place in a time-dependent manner as soon as the balls have rolled far enough to escape their pits.

The effects of the velocity have been already shown and commented in detail in section 6.2, thus in this section will be given more space to other interesting results and comparisons.

| N° of test | Rubber Layers | Load/ball [N] | Dwell time [h] |
|---|---|---|---|
| 1 | A-A | 150 | 6 |
| 2 | A-A | 150 | 24 |
| 3 | A-A | 150 | 96 |
| 4 | A-A | 250 | 6 |
| 5 | A-A | 250 | 24 |
| 6 | A-A | 250 | 96 |
| 7 | A-B | 150 | 24 |
| 8 | A-B | 250 | 24 |
| 9 | B-B | 150 | 24 |
| 10 | B-B | 250 | 24 |

*Tab. 6.5 Tests performed on the devices used in the ECOEST project (1999).*

A final consideration concerns the age of the rubber tracks tested: these were moulded for the ECOEST project in 1999, thus 15 years before the new tests at TARRC.

| **Test Input 1** | | | |
|---|---|---|---|
| Amplitude [mm] | Frequency [Hz] | **Max. velocity** [mm/s] | N° cycles [-] |
| *1* | 5.00 | **31** | 3 |
| *1.5* | 3.33 | | |
| *2.5* | 2.00 | | |
| *5* | 1.00 | | |
| *1* | 10.00 | **63** | |
| *1.5* | 6.67 | | |
| *2.5* | 4.00 | | |
| *5* | 2.00 | | |
| *1* | 20.00 | **126** | |
| *1.5* | 13.33 | | |
| *2.5* | 8.00 | | |
| *5* | 4.00 | | |

*Tab. 6.6 First sinusoidal input, with amplitudes from 1 to 5 mm (corresponding to balls rocking inside their pits).*

| | **Test Input 2** | **Test Input 3** | **Test Input 4** | |
|---|---|---|---|---|
| | **Max vel. = 31 [mm/s]** | **Max vel. = 63 [mm/s]** | **Max vel. = 126 [mm/s]** | |
| Amplitude [mm] | Frequency [Hz] | Frequency [Hz] | Frequency [Hz] | N° cycles [-] |
| *6* | 0.83 | 1.67 | 3.33 | 3 |
| *7* | 0.71 | 1.43 | 2.86 | |
| *8* | 0.63 | 1.25 | 2.50 | |
| *9* | 0.56 | 1.11 | 2.22 | |
| *10* | 0.50 | 1.00 | 2.00 | |
| *12.5* | 0.40 | 0.80 | 1.60 | |
| *15* | 0.33 | 0.67 | 1.33 | |
| *20* | 0.25 | 0.50 | 1.00 | |
| *30* | 0.17 | 0.33 | 0.67 | |
| *40* | 0.13 | 0.25 | 0.50 | |
| *50* | 0.10 | 0.20 | 0.40 | |
| *70* | 0.07 | 0.14 | 0.29 | |

*Tab. 6.7 Sinusoidal inputs subsequent to the one of Tab. 6.6, with amplitudes from 6 to 70 mm.*

### *6.4.2 Results*

An example of the results gathered by these tests is reported in Fig. 6.57 and Fig. 6.58, respectively for the case of rubber tracks A-A and B-B.

The μ-disp loops here presented, for the amplitudes of displacement up to 20 mm, show substantially the same shapes as previously seen for the parametric experimentation on freshly moulded tracks presented in section 6.2. The only difference, visible comparing the loops up to 5 mm to the ones with bigger amplitude, is localized in the maximum value of the rolling friction $\mu_{max}$ and is due to the nature of the test input. In fact, the tests up to 5 mm for all the velocities were performed first, avoiding the effects of viscoelastic recovery of the pits; instead, these effects influenced the tests with bigger amplitudes, which allowed a some time for recovery before the balls returned to the pits.

A slight dependence on the velocity is visible for the steady-state rolling friction of the loops of Fig. 6.57 with amplitudes bigger than 20 mm. The same dependence is less visible for the case of rubber tracks B-B of Fig. 6.58, which shows very large loops, the rubber B being a high-damping compound (Guerreiro et al., 2007).

Fig. 6.59 and Fig. 6.61 give the Equivalent Linearized Viscoelastic Frequency-Domain representation of the behaviour of the RBRL devices tested, through the ELVFD parameters: storage stiffness $K^{/}$, loss stiffness $K^{//}$, complex stiffness K* and loss angle δ; the Harmonic method was again used to calculate these parameters.

In particular, Fig. 6.59 compares the different types of rubber track, A-A, A-B and B-B, for both the values of the load per ball analyzed, 150 and 250 N, and for a dwell time $t_{dw}$ of 24 hours. The case of the tracks B-B presents the highest values of $K^{/}$, $K^{//}$ and thus K*, as expected. However, the loss angle δ is similar for all the rubber tracks. As already mentioned (see section 4.3), in the case of modelling with a Kelvin model the value of δ is related to the critical damping ratio $\zeta$; therefore, the choice of a very high-damping compound, such as type B, might not be advantageous for this scope, but could lead to some unfavourable consequences, such as excessive peak values of rolling friction or semi-permanent deformations on the rubber layers (see Fig. 6.60).

Another useful consideration, from the results of Fig. 6.59, concerns the use of two different rubbers for the tracks of the RBRL device: this solution leads to intermediate results between those associated to the use of identical tracks for either type of rubber.

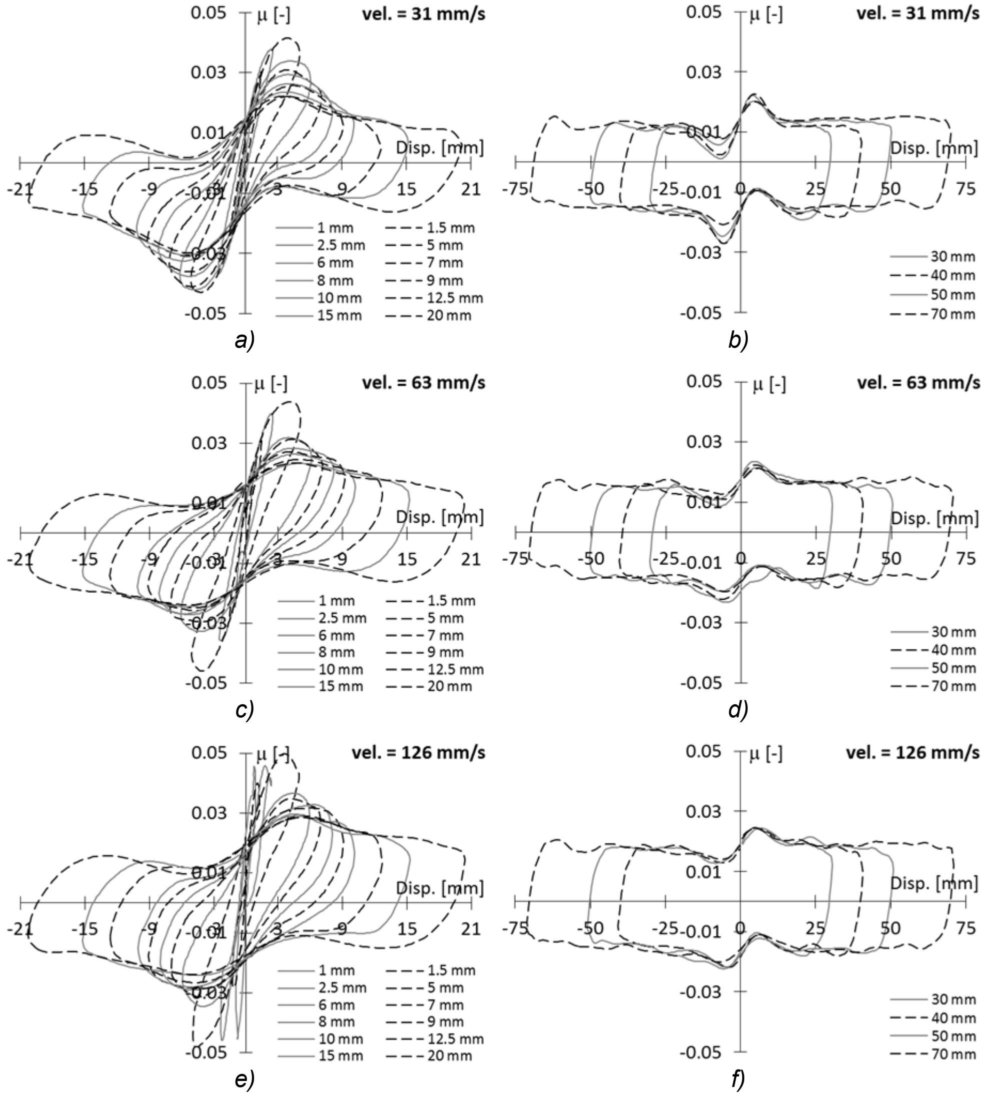

*a)* *b)*

*c)* *d)*

*e)* *f)*

*Fig. 6.57 μ-disp loops. Case: rubber tracks A-A, W = 250 N, $t_{dw}$ = 24 h, 2$^{nd}$ cycle.*

Fig. 6.61 compares the ELVFD parameters for the case with rubber tracks A-A and load per ball 250 N, for different dwell times. These comparisons were limited to the first amplitudes up to 5 mm, to avoid disturbance on the results because of the effects on the pits of the recovery of the rubber deformation, as explained above. While $K^{/}$ increases with increasing dwell time, $K^{//}$ remains substantially constant; therefore, in terms of μ-disp loop for the rocking of a ball inside its pit, the time of dwelling of the load seems to act only to increase the real stiffness of this loop, rather than its energy dissipation or area. The same results are presented in a different way in Fig. 6.62: the ELVFD parameters, together with the values of the maximum rolling friction $\mu_{max}$, are plotted versus the logarithm of the time for the different amplitudes. In addition to the previous remark, the dependence of these parameters on the dwell time can be here directly seen and quantified: the trend appears quite linear with the logarithm of the time.

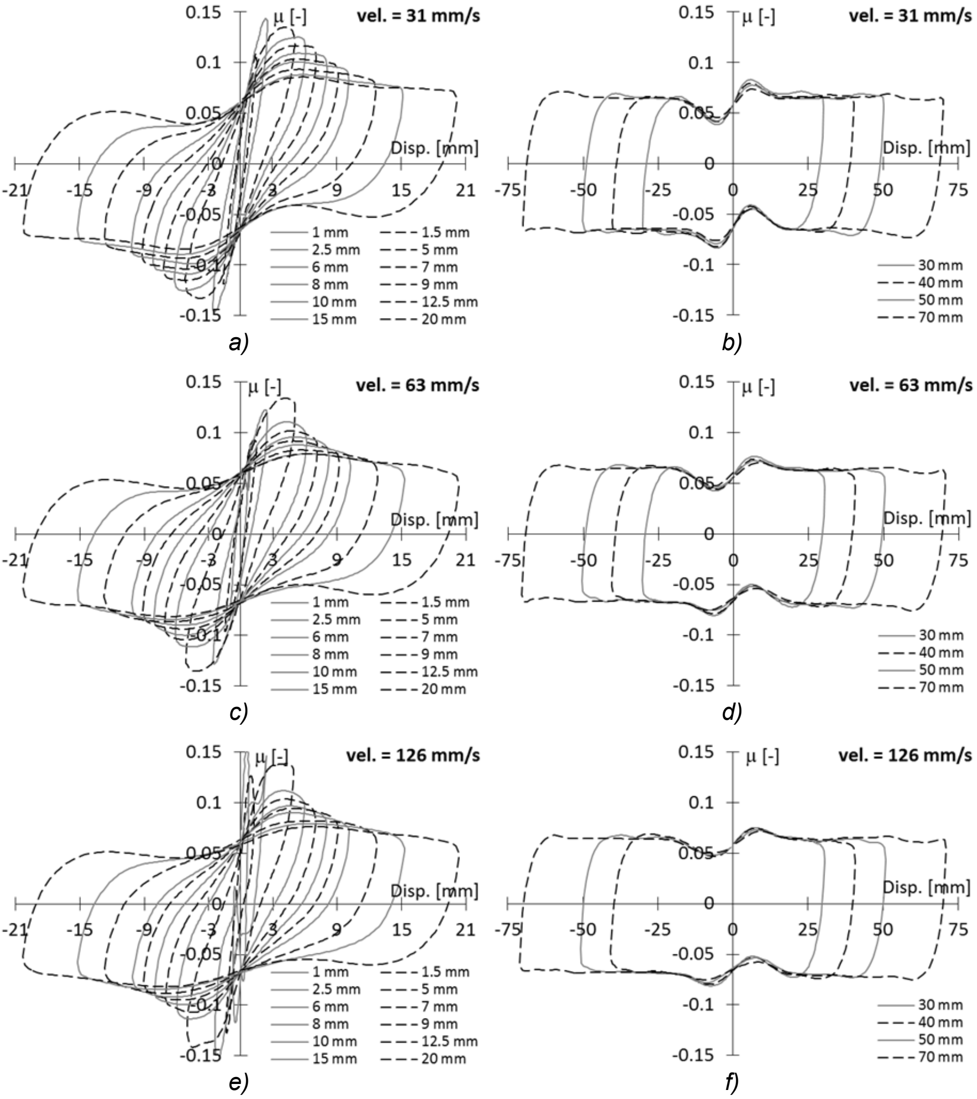

*Fig. 6.58 μ-disp loops. Case: rubber tracks B-B, W = 250 N, $t_{dw}$ = 24 h, $2^{nd}$ cycle.*

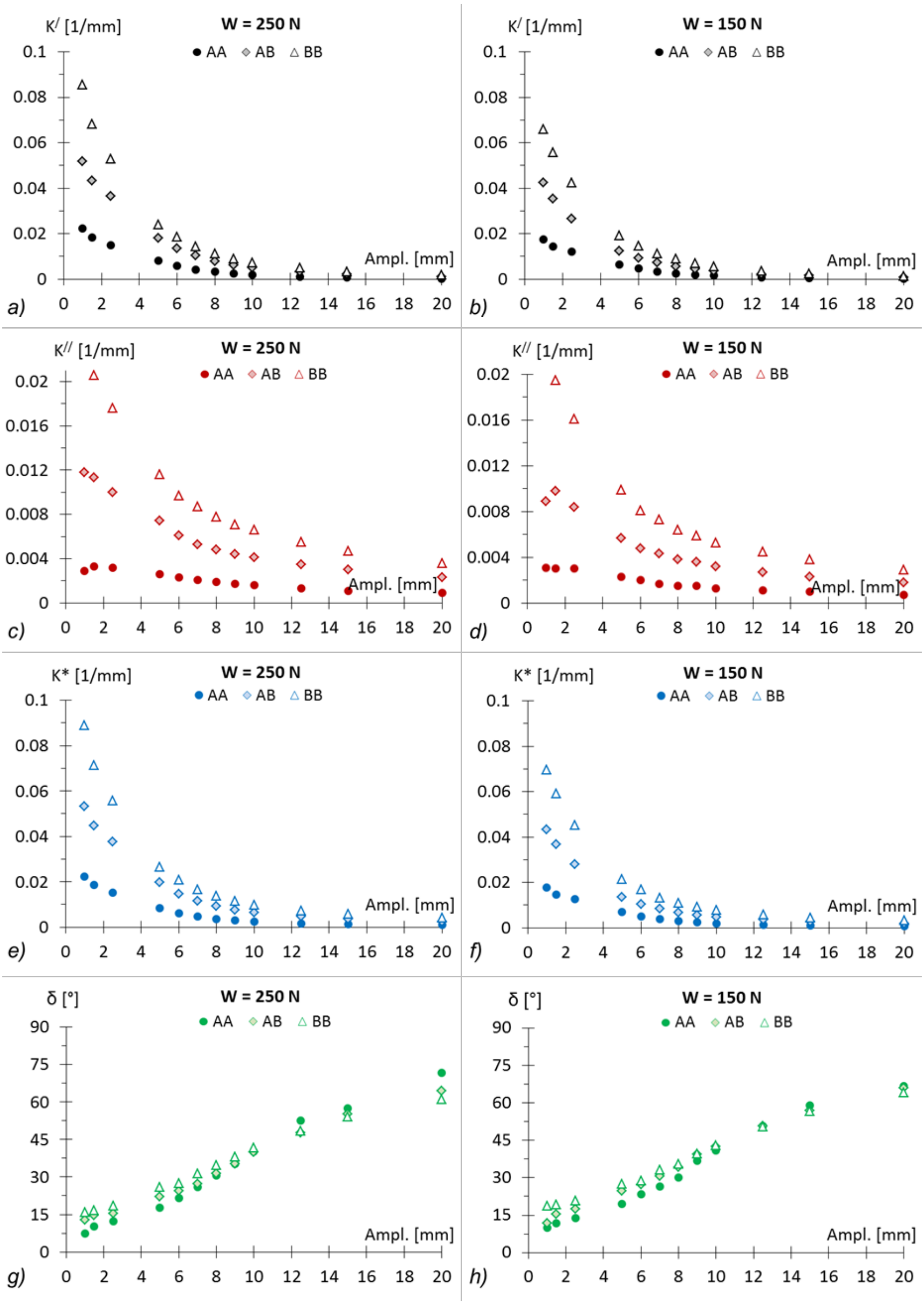

*Fig. 6.59 Comparison of $K^{/}$, $K^{//}$, $K^{*}$, δ vs amplitude, for the different rubber tracks considered: A-A, A-B and B-B. Case: $t_{dw}$ = 24 hours, max. vel. = 31 mm/s, $2^{nd}$ cycle.*

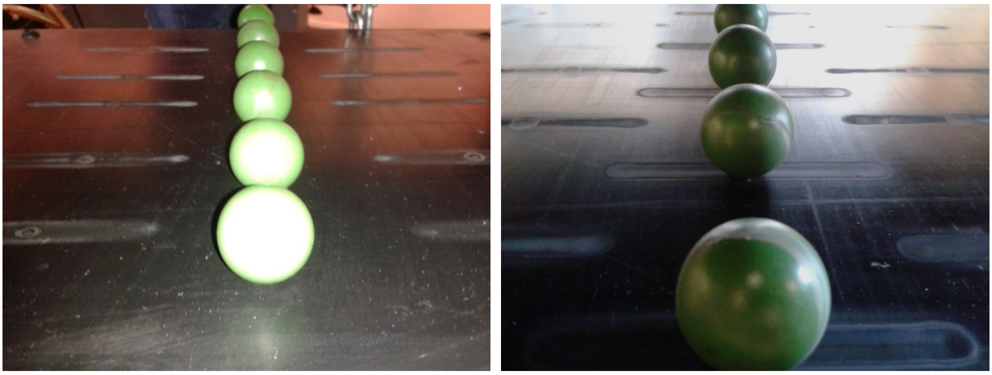

*a)* *b)*

*Fig. 6.60 Semi-permanent rolling tracks on the rubber layer B. Case B-B, $t_{dw}$=24 h, W=250 N: a) before the test (the semi-permanent rolling tracks visible derive from the previous test with W=150 N); b) afer the test.*

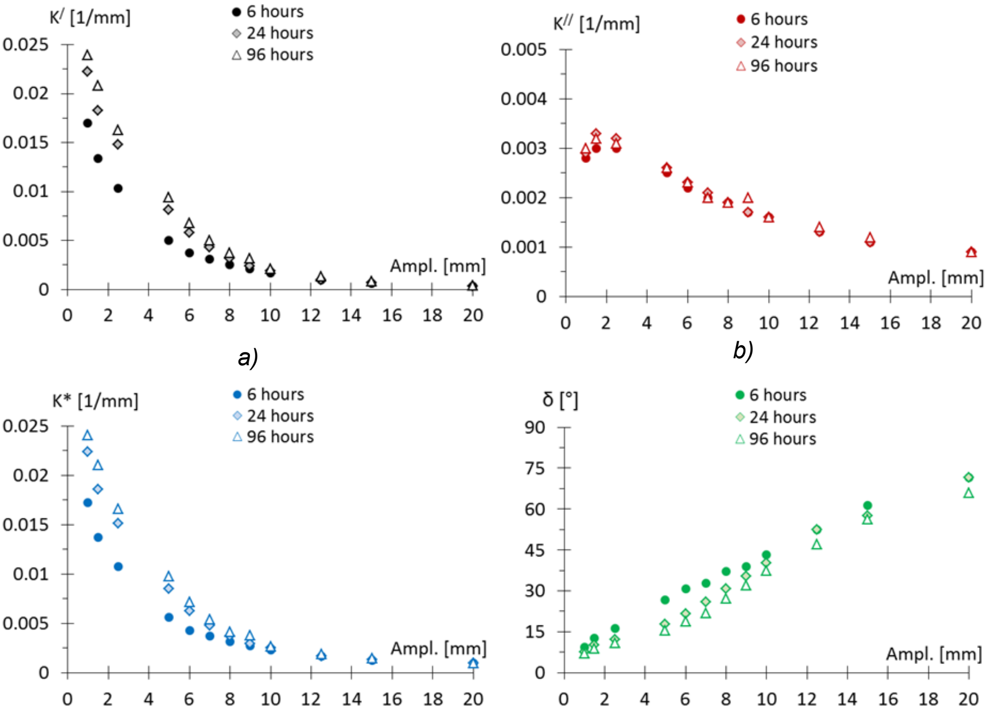

*a)* *b)*

*c)* *d)*

*Fig. 6.61 Comparison of $K^{/}$, $K^{//}$, $K^*$, $\delta$ vs amplitude, for the different dwell times of the load considered: 6, 24 and 96 hours. Case: tracks A-A, W = 250 N, max. vel.= 31 mm/s, 2$^{nd}$ cycle.*

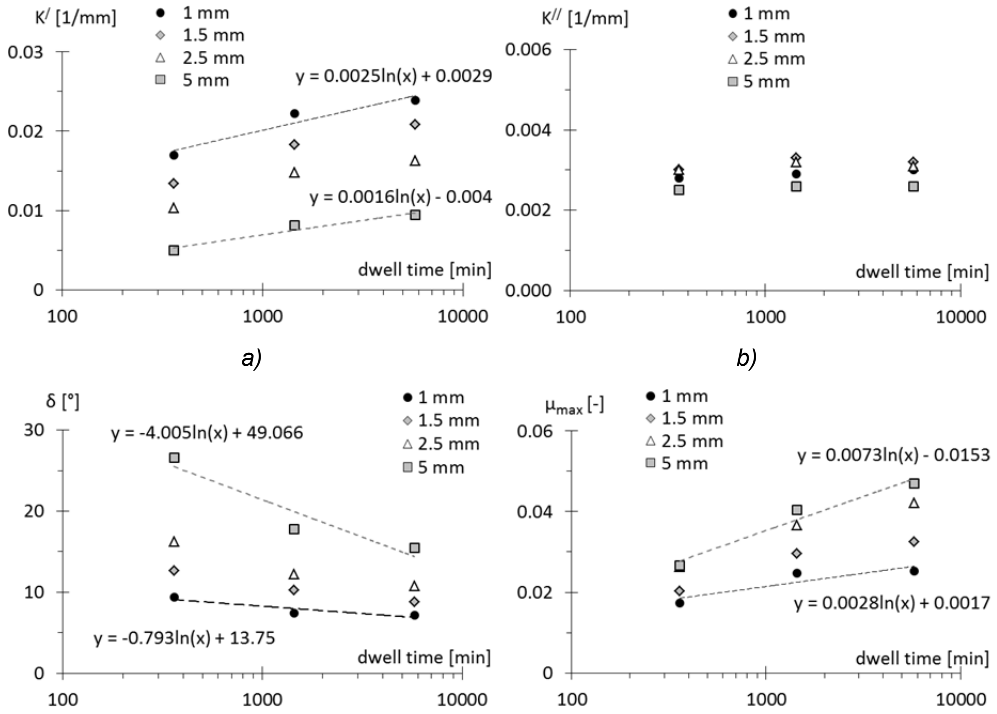

a) b)

c) d)

*Fig. 6.62 Dependence of $K^{/}$, $K^{//}$, δ and $\mu_{max}$ on the logarithm of the dwell time, for amplitudes up to 5 mm (balls inside pits). Case: tracks A-A, W = 250 N, max. vel.= 31 mm/s, 2nd cycle.*

Finally, Fig. 6.63 shows the values of $K^{/}$ and $K^{//}$, versus amplitude, referred to the following cases:

- 1) sinusoidal shaking-table test performed at 5 Hz during the ECOEST experimentation in 1999 (see Chapter 4), with a stress parameter W* of about 1.3;
- 2) new test performed at TARRC, for the current PhD project, on the same RBRL device used in the ECOEST test, with W* of about 1.35;
- 3) new test performed at TARRC on a new RBRL device, with W* equal to 1.2;
- 4) new test performed at TARRC on a new RBRL device, with W* equal to 1.6.

All these cases are characterized by the same type of RBRL device: rubber tracks A-A, t = 2 mm, D = 25 mm. Only for the ECOEST test were the recentering rubber springs included, but for very small amplitudes their effect can be neglected. From this comparison some interesting considerations can be done about the behaviour of the RBRL device after 15 years from its realization. Higher values of the real stiffness $K^{/}$ can be clearly noticed until 6 mm amplitude for the case 2) that, considering also the very similar results between the cases 1), 3) and 4), would lead to conclude that the rubber layers tend to provide, with their aging, a value of stiffness slightly greater for the first oscillation amplitudes of the balls inside their pits. For $K^{//}$, the various cases compared show approximately the same low values, even if a strong increasing of $K^{//}$ for the case 1) can be noticed below 3 mm amplitude. Other considerations more detailed might be done, but the difficulty in the reproducibility of the results, due to the different test conditions, test setup and other variables, suggest using this comparison more qualitatively. For example, the results of the new tests are for a dwell time of 24 hours, which is only supposed to be for the ECOEST test.

However, the tests presented in this section on the ECOEST devices confirm a very good behaviour of the RBRL system after 15 years from its manufacturing.

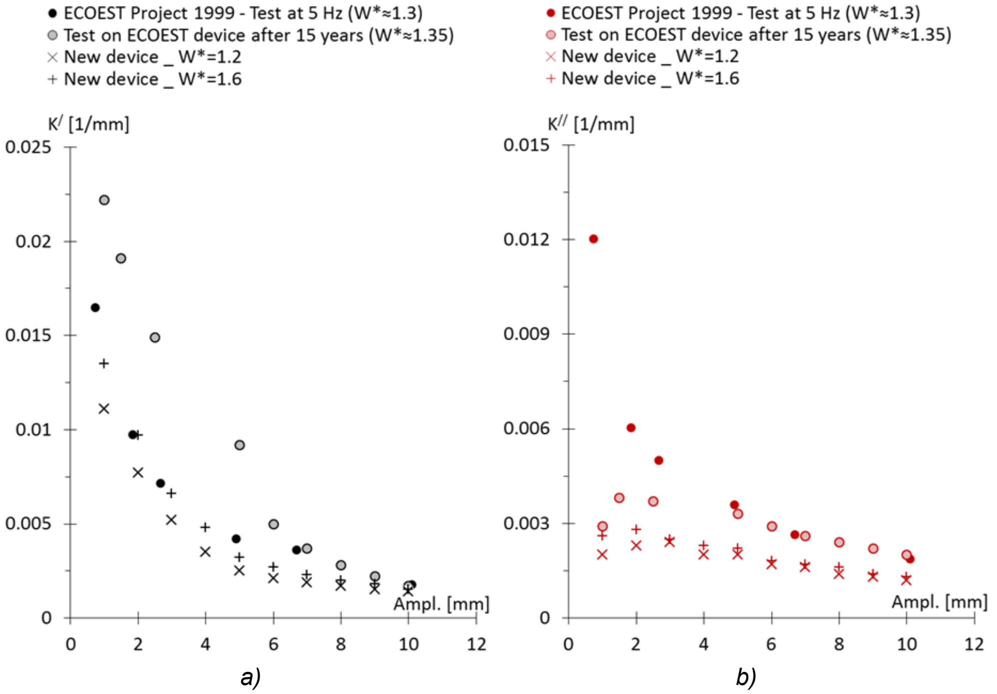

a) b)

*Fig. 6.63 Comparisons of $K^{/}$ and $K^{//}$ of the RBRL device with rubber A, t = 2mm, D = 25 mm between the cases of: sinusoidal shaking-table test performed at 5 Hz during ECOEST project (W* ≈ 1.3), new sinusoidal test on the same ECOEST device and with similar W* (after 15 years from its production), new sinusoidal tests on a new RBRL device (produced at TARRC for this PhD Project) with values of W* of 1.2 and 1.6.*

## 6.5 Prediction of the peak forces and of the recovery effects of the rubber

In this section is briefly presented a further elaboration of the experimental results already shown in section 6.2 (sinusoidal tests) and 6.3 (measures of the residual profile of the pits), with the aim to obtain some useful empirical relations to estimate $\mu_{peak}$ values, considering its dependence on the dwell time of the load and on the recovery of the rubber, as well as on the principal characteristics of the RBRL device, such as the type of rubber, the diameter D of the ball, the thickness t of the rubber layer and the stress parameter $W/ER^2$.

For this purpose the values of $\mu_{peak}$ from the sinusoidal tests with constant frequency were used rather than those from the tests with constant velocity. The starting point to obtain these relations was to consider the ratio $d_R/d_W$, between the residual indentation $d_R$ after unloading (calculated by Eq. (6.12)) and the elastic indentation under load $d_W$ (determined by Water's equations, see Eqs. (6.6) and (6.7)), as key parameter for the determination of the ratio $\mu_{peak}/\mu_{roll}$, which represents the increment of the steady-state rolling friction $\mu_{roll}$ because of the effects of the initial indentation. Thus, the following conceptual relations were considered:

$$\mu_{peak} \approx f(\mu_{roll}, viscous\ contribution) \tag{6.13}$$

$$\frac{\mu_{peak}}{\mu_{roll}} \propto \left[1 + f_a\left(\frac{d_R}{d_W}\right)\right] \tag{6.14}$$

The parameter $d_R$ carries with it the important information regarding the relaxation phenomenon of the rubber ("viscous contribution" of the Eq. (6.13)), through the parameter $H_0$ and the logarithm of the dwell time of the load which are used for its calculation.

Both $d_R$ and $d_W$ are then influenced by the parameters t/R and $W/ER^2$ of the RBRL device. Fig. 6.64 a) presents the dependence of the ratio $\mu_{peak}/\mu_{roll}$ on the parameter t/R: the values of $\mu_{peak}$ were obtained by tests with same stress level and rubber A presented in section 6.2; $\mu_{roll}$ was instead calculated by the theory of Muhr et al. (1997) calibrated as shown in Chapter 5. Approximately, the same dependence is visible in Fig. 6.64 b) for the ratio $d_R/d_W$. Therefore, this means that the dependence of $\mu_{peak}/\mu_{roll}$ on the parameter t/R is already correctly considered in the ratio $d_R/d_W$. Instead, Fig. 6.65 shows a dependence on the stress parameter that is opposite for the two ratios $\mu_{peak}/\mu_{roll}$ and $d_R/d_W$. This fact results in the necessity to

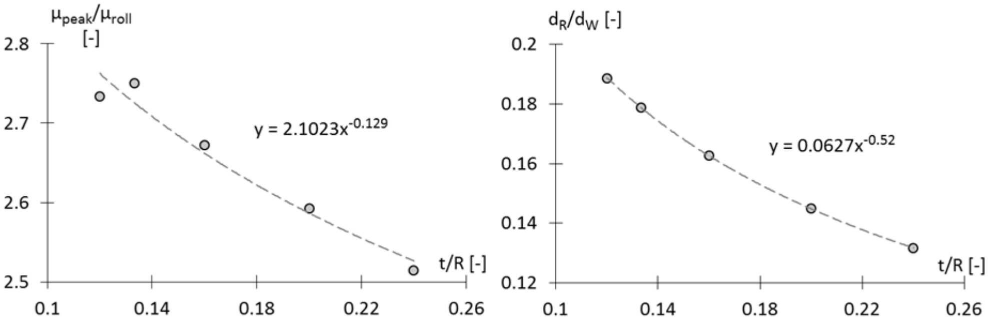

*a)* *b)*

*Fig. 6.64 Same dependence of the ratio $\mu_{peak}/\mu_{roll}$ (a) and $d_R/d_W$ (b) on the parameter t/R. The values of $\mu_{peak}$ were obtained by sinusoidal tests performed with same $W/ER^2$ and rubber A, presented in section 6.2.*

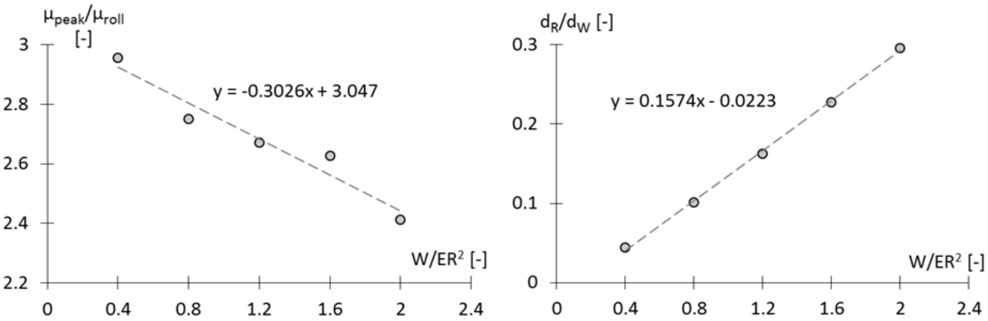

*a)* *b)*

*Fig. 6.65 Different dependence of the ratio $\mu_{peak}/\mu_{roll}$ (a) and $d_R/d_W$ (b) on the stress parameter $W/ER^2$. The values of $\mu_{peak}$ were obtained by sinusoidal tests performed on the same device with rubber A, t = 2 mm, D = 25 mm, presented in section 6.2.*

calibrate the right part of the Eq. (6.14) for the parameter $W/ER^2$, introducing the function $f_b(W\ /\ ER^2)$ as shown in Eq. (6.15).

$$\frac{\mu_{peak}}{\mu_{roll}} \simeq \left[1 + f_a\left(\frac{d_R}{d_W}\right) \cdot f_b\left(\frac{W}{ER^2}\right)\right] \tag{6.15}$$

At first, the function $f_a(d_R\ /\ d_W)$ was determined according to Eq. (6.16), considering the $\mu_{peak}$ of all those sinusoidal tests, presented in section 6.2, carried-out with the same value of $W/ER^2$ (= 1.2) and different rubbers and ratio t/R.

$$f_a\left(\frac{d_R}{d_W}\right) \equiv \left[\frac{\mu_{peak}}{\mu_{roll}} - 1\right] \Big/ f_b\left(\frac{W}{ER^2}\right) \tag{6.16}$$

where: $f_b\left(1.2\right) \equiv 1$.

The function $f_a$ fitting the experimental results is shown in Fig. 6.66. A power law for the interpolation line was assumed also for reasons of logical consistency: if the value of $d_R$ tends to 0, because the dwell time of the load tends to 0 or the rubber tends to respond elastically, also $f_a$ has to tend to 0, so that $\mu_{peak}$ could tend to $\mu_{roll}$.

The function $f_b$ was then obtained in accord to Eq. (6.17). For this scope, the values considered of $\mu_{peak}$ are the ones of the sinusoidal tests performed using the same RBRL device with rubber A and t = 2 mm, considering different t/R and obviously different $W/ER^2$. The choice to consider $\mu_{peak}$ associated with only one RBRL device was done with the aim to reduce as possible the sources of uncertainty.

$$f_b\left(\frac{W}{ER^2}\right) \equiv \left[\frac{\mu_{peak}}{\mu_{roll}} - 1\right] \Big/ f_a\left(\frac{d_R}{d_W}\right) \tag{6.17}$$

The function $f_b$ fitting the experimental results is shown in Fig. 6.67.

Finally, from the interpolating equations reported in Fig. 6.66 and Fig. 6.67 and through the Eq. (6.15), the following empirical relation can be provided for the prediction of the $\mu_{peak}$:

$$\mu_{peak} \simeq \mu_{roll}\left[1 + 3.2 \cdot \left(\frac{d_R}{d_W}\right)^{0.3} \cdot \left(\frac{W}{ER^2}\right)^{-0.54}\right] \tag{6.18}$$

The efficacy of such empirical relation is shown in Fig. 6.68 through the comparison of the experimental values of $\mu_{peak}$ with those calculated by the equation; this comparison was extended to all the sinusoidal tests presented in section 6.2.

Fig. 6.69 shows how the ratio $\mu_{peak}/\mu_{roll}$ and the function $f(d_R/d_W)$ (shown in Fig. 6.66) have the same dependence on the parameter t/R, consistently with what already seen at beginning in Fig. 6.64. The small difference in this comparison is due to the calibration of the function $f(d_R/d_W)$ for the different compounds (see Fig. 6.66), the values of $\mu_{peak}/\mu_{roll}$ being associated only to the rubber A (these values are the ones already presented in Fig. 6.64 a).

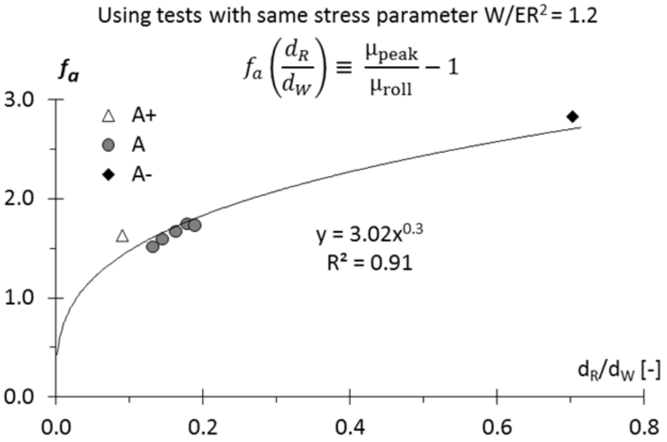

*Fig. 6.66 Interpolating function* $f_a$ *according to Eq. (6.16).*

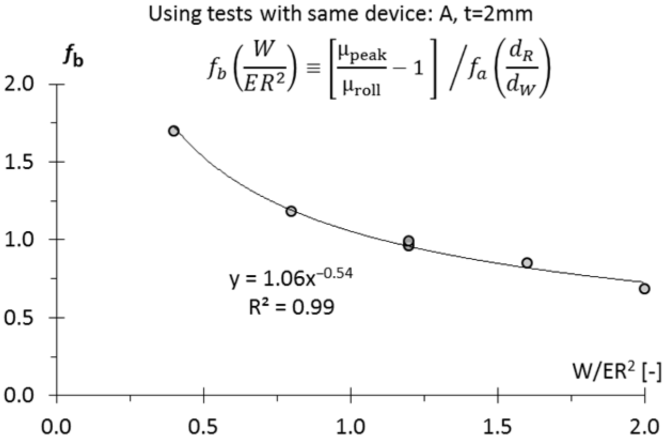

*Fig. 6.67 Interpolating function* $f_b$ *according to Eq. (6.17).*

Eq. (6.18) takes into account the dependence of $\mu_{peak}$ on the load dwell time through the parameter $d_R$ (see Eq. (6.12)). The estimated dependence of $\mu_{peak}$ on the dwell time is shown for three types of RBRL device in Fig. 6.70 (rubber A), Fig. 6.71 (rubber A-) and Fig. 6.72 (rubber A+), for a range of the stress parameter from 0.4 to 2.

The $\mu_{peak}$ values obtained by the sinusoidal tests presented in section 6.4, performed on the ECOEST device with rubber tracks A-A, t = 2 mm and D = 25 mm, are overlayed on the graph for the estimate of $\mu_{peak}$ in Fig. 6.70. For consistency, the experimental values considered are from sinusoidal loops of 20 mm amplitude and 1 Hz frequency; the tests were run after 6, 24 and 96 hours.

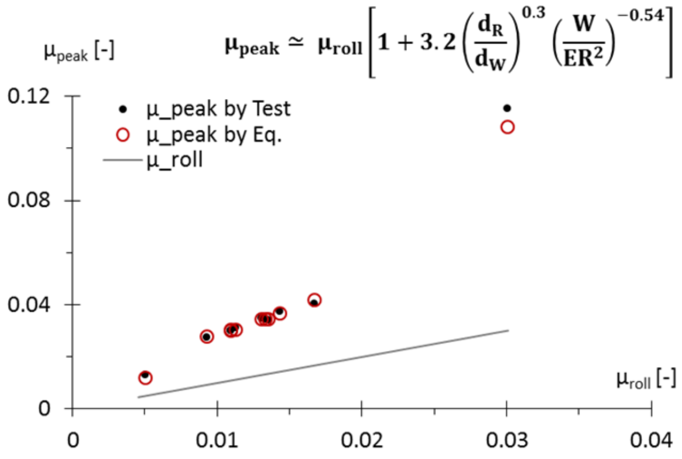

*Fig. 6.68 Estimate of $\mu_{peak}$ according to empirical Eq. (6.18) and comparison of the values with the experimental ones.*

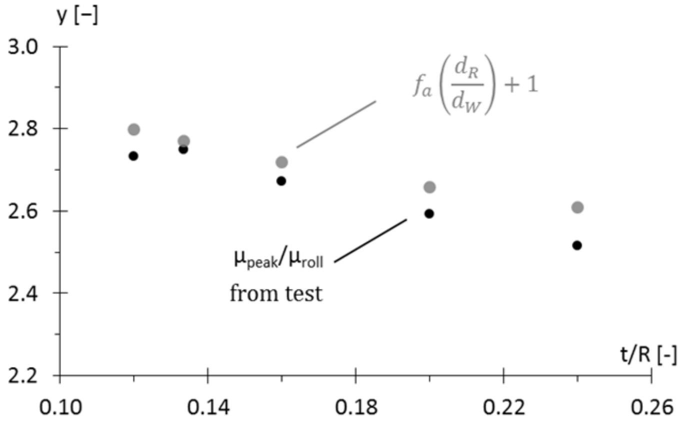

*Fig. 6.69 Comparison that shows the same dependence of the ratio $\mu_{peak}/\mu_{roll}$ and of the function $f_a$ (shown in Fig. 6.66) on the parameter t/R.*

The trend of the estimated values of $\mu_{peak}$ versus the dwell time is due also to the choice made for the interpolation law of the function $f_a$ (see Fig. 6.66). The resulting shape is quite linear with the logarithm of the dwell time after the first minutes, but shows a slight reduction of its slope with increasing in the dwell time. This seems to have a physical sense, since the increment of the force for the roll-out of the balls from their pits has to be a physical limit. A similar shape was already observed for the results presented in section 6.4, associated with sinusoidal tests of amplitude smaller than 5 mm and different dwell times (see Fig. 6.62): this is an evidence of the efficacy of the empirical relation here presented.

Finally, Fig. 6.73 shows that the estimated values of $\mu_{peak}$ do not change in the case of different combinations of the parameters W/ER$^2$ and t/R, which keep constant the value of $\mu_{roll}$ according to the theory of Muhr et al. (1997).

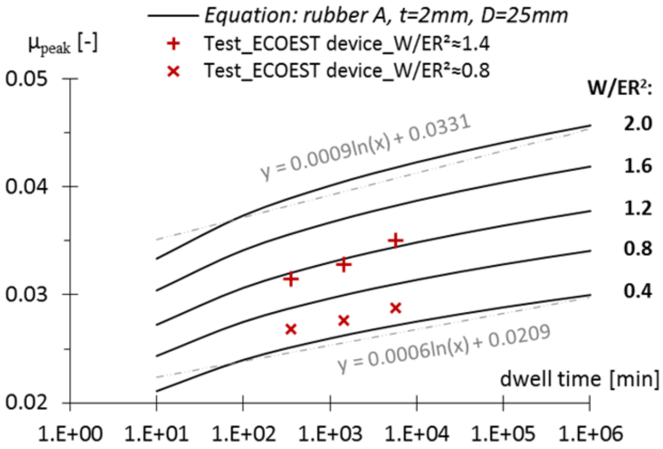

*Fig. 6.70 Dependence of the estimated values of $\mu_{peak}$ on the load dwell time, according to Eq.(6.18), for different stress levels and for the case of rubber A, t = 2 mm and D = 25 mm. Overlap of the $\mu_{peak}$ values gathered by the sinusoidal tests presented in section 6.4 on the associated ECOEST device (A, t = 2mm, D = 25 mm).*

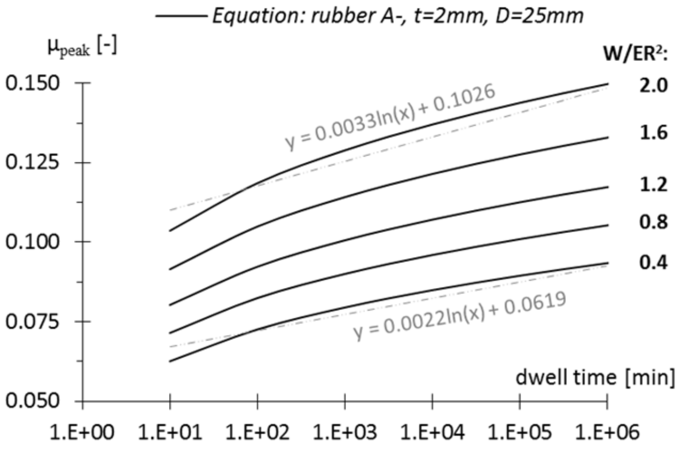

*Fig. 6.71 Dependence of the estimated values of $\mu_{peak}$ on the load dwell time, according to Eq.(6.18), for different stress levels and for the case of rubber A-, t = 2 mm and D = 25 mm.*

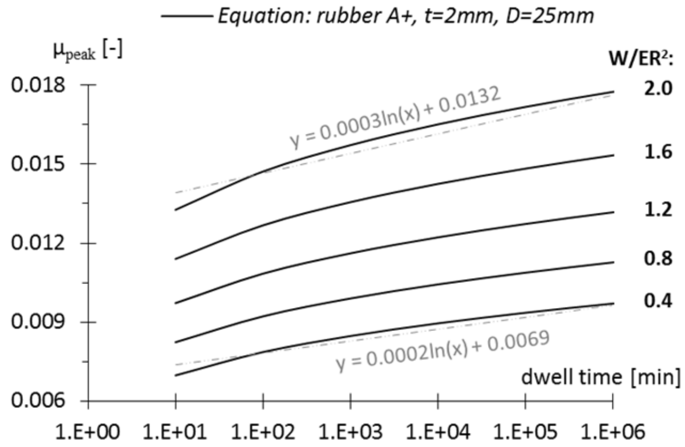

*Fig. 6.72 Dependence of the estimated values of $\mu_{peak}$ on the load dwell time, according to Eq.(6.18), for different stress levels and for the case of rubber A+, t = 2 mm and D = 25 mm.*

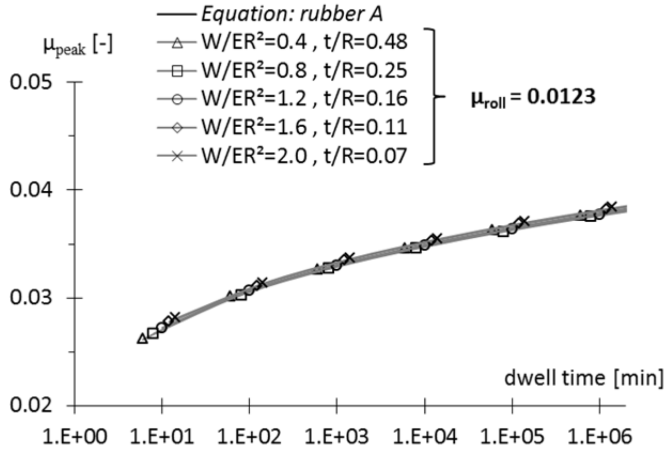

*Fig. 6.73 Estimate of $\mu_{peak}$, according to Eq.(6.18), for rubber A, D = 25 mm and different combinations of the parameters $W/ER^2$ and t/R. Each of these combinations is characterized by the same value of $\mu_{roll}$ according to the theory of Muhr et al. (1997).*

A last interesting elaboration about the maximum rolling friction $\mu_{max}$ is presented below. The intention was to find a relation between the maximum rolling friction $\mu_{max\_cycle1}$, associated with the first roll-out of the balls from their pits, and a generic $\mu_{max}$, associated with sinusoidal cycles subsequent to the first.

The choice to consider the values of $\mu_{max}$ from the sinusoidal tests performed at 1 Hz (see section 6.2) is very convenient for this new elaboration, since every sinusoidal cycle is completed in the same time of 1 second, independently of the amplitude of the test. This means that the ratio $\mu_{max}/\mu_{max\_cycle1}$, between the maximum rolling friction of the given cycle and of the first cycle, is consistent in terms of recovery time if compared within the series of tests with different amplitude. Therefore, some useful considerations can be made about the effects of the recovery of the rubber on $\mu_{max}$.

In particular, Fig. 6.74 shows these considerations for the reference case with rubber A, t = 2 mm, D = 25 mm and $W/ER^2 = 1.2$. Fig. 6.74 a) presents the ratios $\mu_{max}/\mu_{max\_cycle1}$ associated with roll-out of the balls from their pits near the beginning of each sinusoidal cycle and, furthermore, after the return of the balls in their original position at half of the first cycle; these ratios are presented for the amplitudes investigated greater than 5 mm, i.e. for the sinusoidal tests that involve the balls roll-out. Two types of dependence of $\mu_{max}$ are visible in this figure:

- dependence on the recovery time for the pits, shown by the presence of the different interpolation lines;
- dependence on the sinusoidal amplitude of the test, i.e. on the maximum distance reached by the balls relative to their pits, shown by the shape of the interpolation lines; this dependence is caused by the fact that the stress field around the pits decreases with increase in rolling distance of the balls, resulting in a different influence on the recovery phenomenon of the rubber.

The same dependences can be seen in Fig. 6.74 b), that shows the values of the ratio $\Delta\mu_{max}/\mu_{max\_cycle1}$ versus the logarithm of the recovery time, for the different amplitudes considered; $\Delta\mu_{max}$ is the difference between the maximum rolling friction of the first cycle and that of the given cycle, associated with the same sinusoidal test or amplitude.

The first elaboration undertaken was the determination of the function $f_1$(Ampl.), which describes the dependence of the ratio $\mu_{max}/\mu_{max\_cycle1}$ on the distance rolled by the balls. For this scope, a shift of the values of the ratio $\mu_{max}/\mu_{max\_cycle1}$, presented in Fig. 6.74 a), was applied to remove the dependence of this ratio on the recovery time. In particular the points belonging to the first interpolation line were moved together so that the first of these points reached the value 1; then, the points of the other interpolation lines were shifted upwards considering the average distance between these lines. The result of this procedure is presented in Fig. 6.74 c), in which the interpolating equation provided was assumed as function $f_1$(Ampl.).

Afterwards, this function was used to modify the values of $\mu_{max}$, according to Eq. (6.19), in such a way to recalculate the values of the ratio $\Delta\mu_{max}/\mu_{max\_cycle1}$ removing its dependence on the amplitude. The results so obtained, plotted in Fig. 6.74 d), show the only dependence on the recovery time, which has been referred as $f_2$(time).

$$\mu_{\max\_\mathrm{MODIFIED}} = \frac{\mu_{\max}}{f_1(Ampl.)} \tag{6.19}$$

Finally, the empirical relation to estimate the effects of the recovery of the rubber on $\mu_{max}$ is proposed in Eq. (6.20) and requires the knowledge of $f_1$(Ampl.) and $f_2$(time), obtained experimentally and given in Fig. 6.74 c) and d). The efficacy of this empirical relation is shown in Fig. 6.75.

$$\mu_{\max}(Ampl.,\ time) = \mu_{\max\_cycle1} \cdot \left[ f_1(Ampl.) - f_2(time) \right] \tag{6.20}$$

The same elaborations presented for the reference case, shown in Fig. 6.74 and Fig. 6.75, were also applied for the case with higher stress parameter, $W/ER^2=2$, and for the case with rubber A-, respectively presented in Fig. 6.76 - Fig. 6.77 and Fig. 6.78 - Fig. 6.79.

*Case: rubber A, t=2mm, D=25mm, W/ER$^2$=1.2*

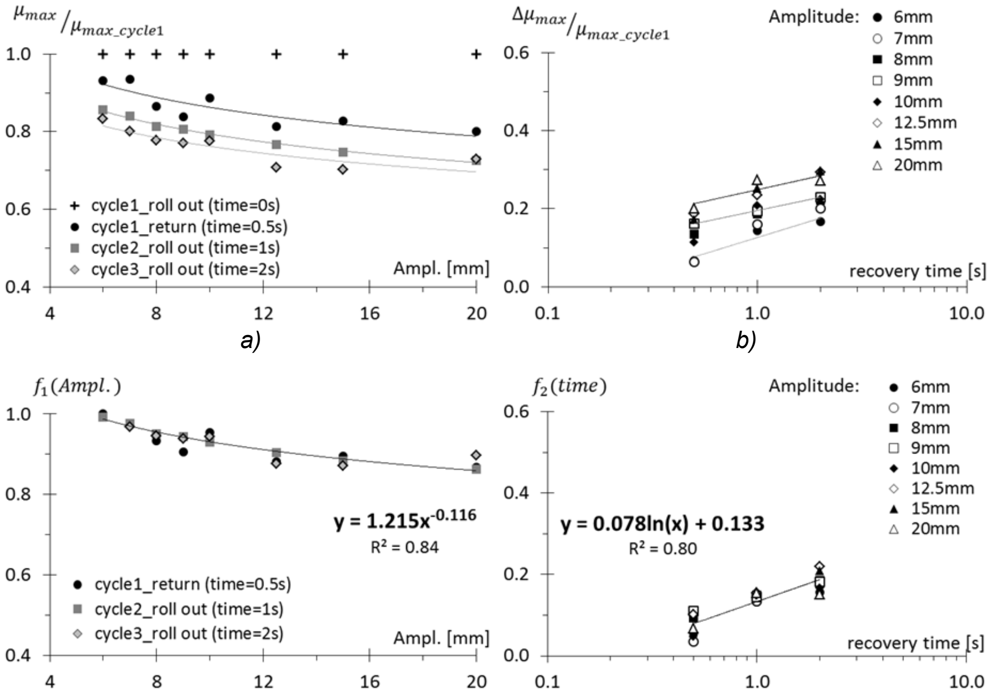

a) b)

c) d)

Fig. 6.74 a), b) Effects of the recovery of the rubber on the maximum rolling friction $\mu_{max}$ due to the roll-out of the balls from their pits. c), d) Interpolating equations for the functions $f_1$(Ampl.) and $f_2$(time) necessary to apply the equation Eq. (6.20).

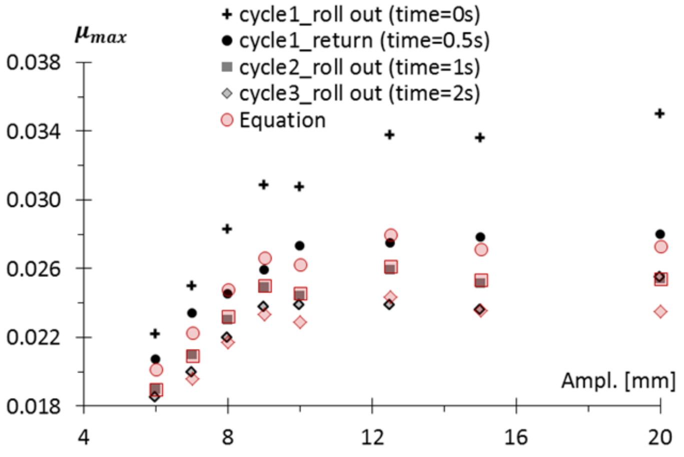

Fig. 6.75 Estimate of the recovery effects of the rubber on $\mu_{max}$, according to Eq. (6.20).

*Case: rubber A, t=2mm, D=25mm,* $W/ER^2=2$

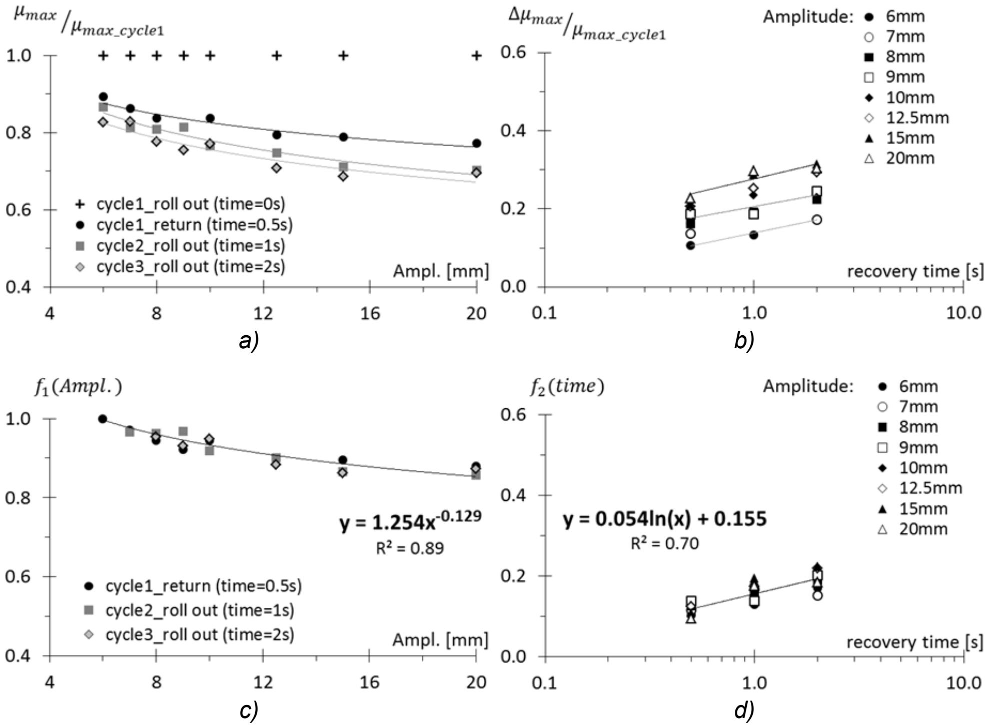

*Fig. 6.76 a), b) Effects of the recovery of the rubber on the maximum rolling friction* $\mu_{max}$ *due to the roll-out of the balls from their pits. c), d) Interpolating equations for the functions* $f_1$*(Ampl.) and* $f_2$*(time) necessary to apply the equation Eq. (6.20).*

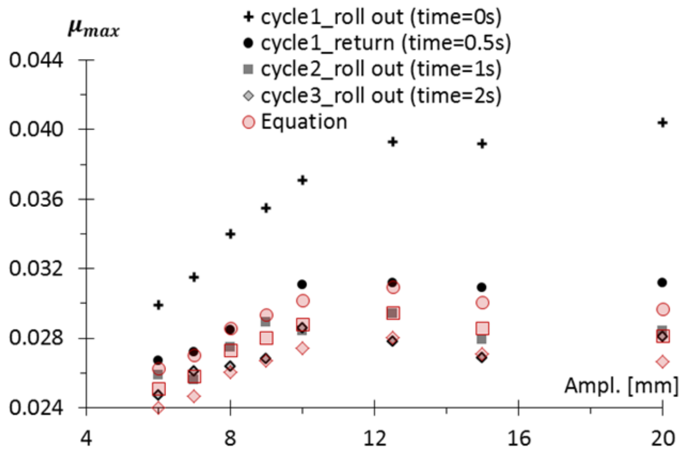

*Fig. 6.77 Estimate of the recovery effects of the rubber on* $\mu_{max}$*, according to Eq. (6.20).*

*Case: rubber A-, t=2mm, D=25mm, W/ER$^2$=1.2*

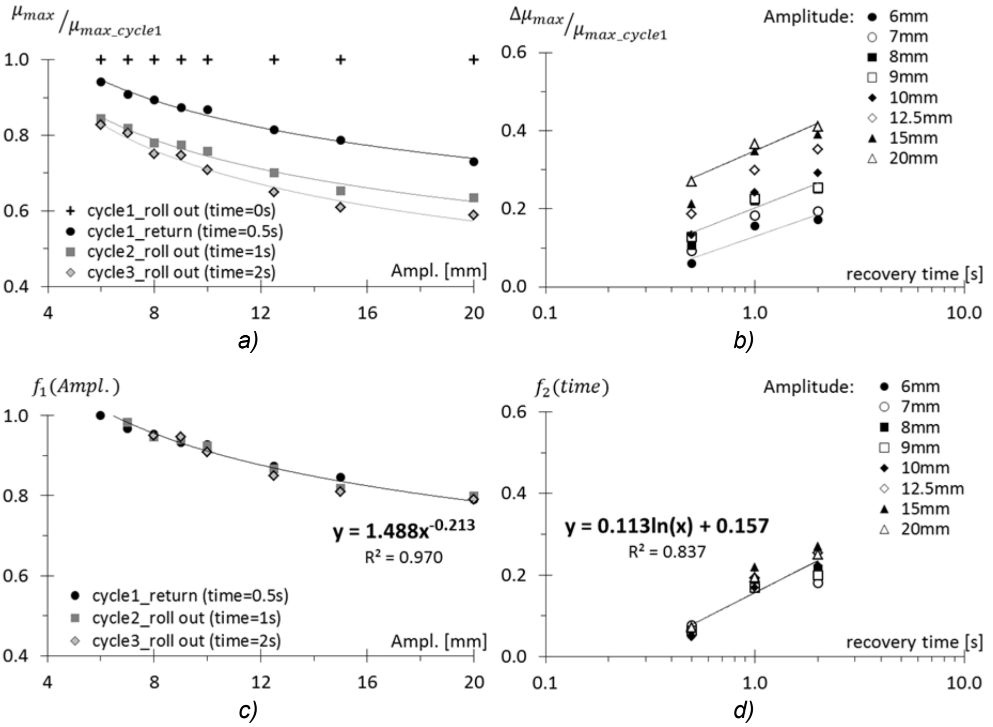

a) b)

c) d)

*Fig. 6.78 a), b) Effects of the recovery of the rubber on the maximum rolling friction $\mu_{max}$ due to the roll-out of the balls from their pits. c), d) Interpolating equations for the functions $f_1$(Ampl.) and $f_2$(time) necessary to apply the equation Eq. (6.20).*

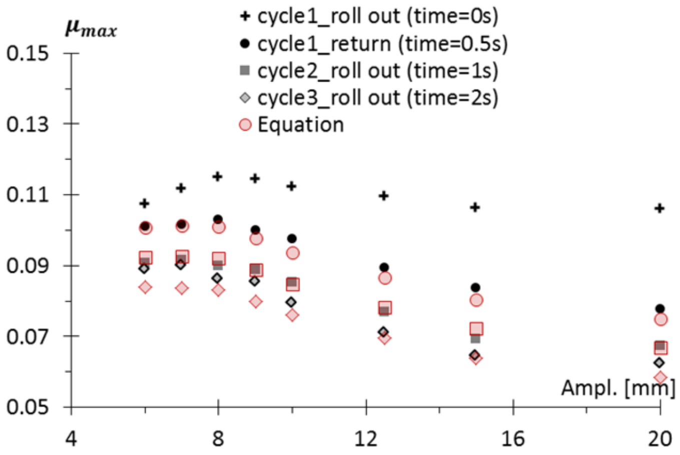

*Fig. 6.79 Estimate of the recovery effects of the rubber on $\mu_{max}$, according to Eq. (6.20).*

In conclusion, while Eq. (6.18) provides an estimate of the peak value $\mu_{peak}$ of the rolling friction for the RBRL device, with the Eq. (6.20) it is possible to keep into account the effects on the same $\mu_{peak}$ of the recovery of the rubber in the pits. These effects, due to the unloading of the pits for the previous roll-out of the balls and to the presence of a given recovery time, are reported above for some case studies or RBRL devices through the functions $f_1$(Ampl.) and $f_2$(time).

The empirical relations provided in this section are not able to fully describe in details all these complicated phenomena, but are aimed to give a general interpolation, interpretation and description for these problems, with some values of reference.

Further experimentation, focussed on the effects of the dwell time and recovery time on the residual indentation $d_R$ and on the $\mu_{peak}$ of the RBRL device, is needed to better deepen the study of these phenomena, obviously considering the results reached and presented in this chapter. It is worth noting that these experiments have to be characterized by a long time of test, the effects of the dwell and recovery time being approximately linearly dependent on the logarithm of the time. For this reason, additional numerical studies through the Finite Element Method (FEM) could be very useful to integrate the experimental results; some FEM models for these purposes were realized and compared to the test results, modelling the rubber with a Prony's series as explained in Ahmadi et al. (2008), but these results will be shown in a future publication, deciding to give space in this chapter only to the experimental studies and results.

## 6.6 Proposal of a new time-domain prediction model for the RBRL system

The RBRL isolation system, as seen before, presents three key types of behaviour, differentiated according to the magnitude of the displacements relative to the ground:

1) a small-deflection behaviour with balls rocking in their pits – giving almost elliptical force-displacement loops as for a viscoelastic material;
2) a large-deflection behaviour with balls rolling with a steady-state force of resistance – giving almost parallelogram-shaped loops with a slope given by the stiffness of the rubber recentering springs and a difference in force between loading and unloading paths equal to the rolling resistance;
3) a transition phase from 1) to 2) – very non-linear and complicate loops.

The principal elements of the RBRL that provide this behaviour are:

a) the steady-state rolling resistance of the balls on the rubber tracks;

b) the participation of the rubber spring;

c) the memory effects of the rubber-track surface-indentation, due to the ball pressure and to the viscoelastic properties of the rubber.

The effects of these three elements can be considered in parallel. In the following these effects are described in detail, finally arriving at a proposed time-domain model for describing the RBRL system force-displacement behaviour in a manner suitable for predictive time-history analyses of structures isolated on it.

a) Modelling of the steady-state rolling resistance

The rolling resistance can be characterized by means of a constant force model, as shown in Fig. 6.80 (as presented also in Guerreiro et al., 2007).

The theory of Muhr et al. (1997), considering its calibration presented in chapter 5, can be used to predict the value of the rolling friction μ that, multiplied by the vertical load applied on the isolation system, provides the rolling force. For clarity, the principal results obtained from the calibration of this theory (Fig. 5.22 and Tab. 5.11) are presented again below in Fig. 6.81 (all rubbers) and Tab. 6.8 (rubber A). Thus, from the knowledge of t/R and $W/ER^2$ the value of μ can be obtained.

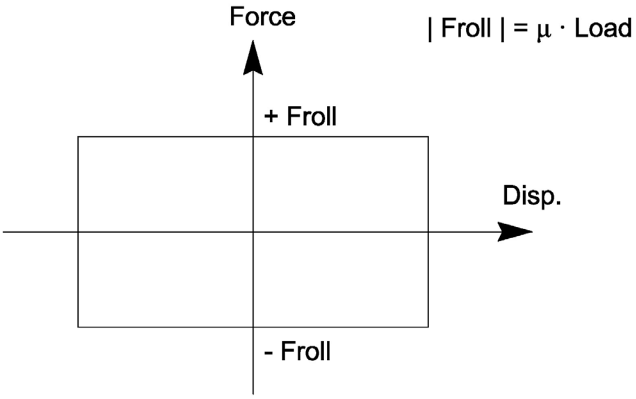

*Fig. 6.80 Modelling of the steady-state rolling resistance.*

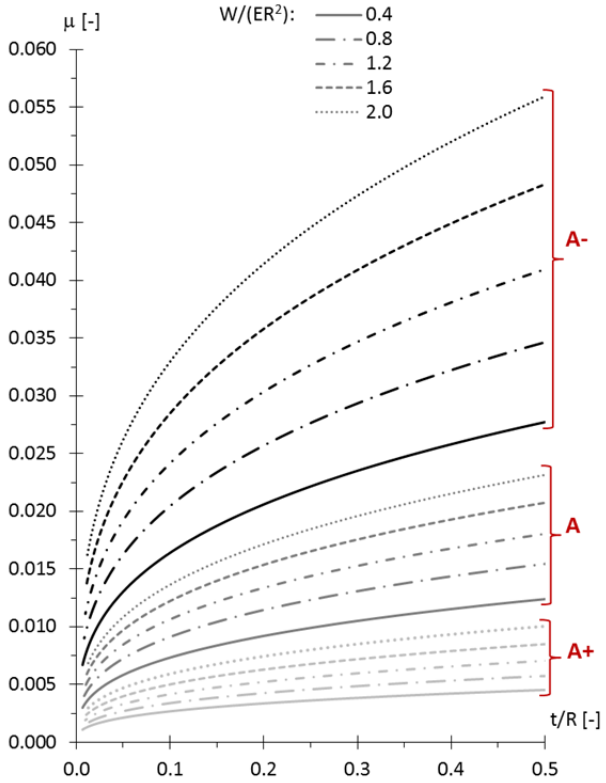

*Fig. 6.81 Theoretical μ values, calibrated through the experimentation (Ch. 5), for each compound (A+, A, A-) and stress parameter (W/ER$^2$) analyzed, for an adequate range of t/R.*

| | W/ER$^2$=0.6 | W/ER$^2$=0.8 | W/ER$^2$=1 | W/ER$^2$=1.2 | W/ER$^2$=1.4 | W/ER$^2$=1.6 |
|---|---|---|---|---|---|---|
| ***μ [-]*** | ***t/R [-]*** | | | | | |
| *0.008* | 0.09 | | | | | |
| *0.009* | 0.13 | 0.10 | | | | |
| *0.01* | 0.18 | 0.14 | 0.11 | | | |
| *0.011* | 0.23 | 0.18 | 0.14 | 0.11 | | |
| *0.012* | 0.31 | 0.24 | 0.19 | 0.15 | 0.12 | |
| *0.013* | 0.39 | 0.30 | 0.24 | 0.19 | 0.15 | 0.13 |
| *0.014* | 0.49 | 0.38 | 0.30 | 0.24 | 0.19 | 0.16 |
| *0.015* | 0.61 | 0.47 | 0.37 | 0.30 | 0.24 | 0.19 |
| *0.016* | 0.75 | 0.57 | 0.45 | 0.36 | 0.29 | 0.24 |
| *0.017* | 0.91 | 0.69 | 0.54 | 0.43 | 0.35 | 0.28 |
| *0.018* | | 0.83 | 0.65 | 0.52 | 0.42 | 0.34 |
| *0.019* | | 0.98 | 0.77 | 0.61 | 0.49 | 0.40 |
| *0.02* | | | 0.90 | 0.72 | 0.58 | 0.47 |
| *0.021* | | | 1.05 | 0.84 | 0.67 | 0.54 |
| *0.022* | | | | 0.97 | 0.78 | 0.63 |
| *0.023* | | | | 1.12 | 0.89 | 0.72 |
| *0.024* | | | | | 1.02 | 0.82 |
| *0.025* | | | | | | 0.93 |
| *0.026* | | | | | | 1.06 |

*Tab. 6.8 Theoretical μ values for rubber A, calculated for selected values of t/R and W/ER$^2$ using the theory of Muhr et al. (1997), experimentally calibrated.*

b) Modelling of the rubber springs behaviour

For the modelling of the behaviour of the rubber springs, a non-linear tangent stiffness should be used, according to the results presented and discussed in depth in chapter 5. Here below, Eq. (6.21) shows the formulation obtained for calculating the tangent stiffness:

$$K_{\tan}\left(\phi_{i,}D\right)=K_{init}^{/}\left(\phi_i\right)+\Delta K_{\tan}\left(D\right) \qquad (6.21)$$

where $D$ is the deflection of the rubber spring, $\phi_i$ is the diameter of the spring, $K_{init}^{/}\left(\phi_i\right)$ is the initial value of the storage stiffness (hence also of the tangent stiffness) and $\Delta K_{\tan}\left(D\right)$ is the deflection-dependent part of the stiffness.

The values of $K_{init}^{/}\left(\phi_i\right)$ and $\Delta K_{\tan}\left(D\right)$ can be approximately calculated by Eqs. (5.12) and (5.14) respectively (presented in chapter 5), generalizing the use of Eq. (6.21) for whatever spring diameter. If more accuracy is required, the values proposed again in Tab. 6.9 should be used, these being calibrated specifically for each diameter tested (in this case $\Delta K_{\tan}$ is considered dependent also on $\phi_i$ ).

All the results provided in this thesis about the rubber recentering springs are related to 1 spring only; thus, the final stiffness of the recentering system can be simply obtained by multiplying these values by the number of springs to be used.

The force-displacement loops obtained by tests, as well as the shape of the tangent stiffness (calculated using Eq. (6.21)) against spring deflection, are presented again for clarity in Fig. 6.82 and Fig. 6.83 respectively.

As already observed, the energy dissipation provided by the recentering system could be neglected, especially for the smaller spring diameters. However, the modelling of this dissipation might be easily done using a simple Kelvin model instead of a single non-linear stiffness, calibrating the Kelvin parameter *c* from the values of the loss stiffness $K^{//}$ provided in chapter 5, as already seen in section 4.5.

| $\phi_i$ [mm] | $K_{init}^{/}$ [N/mm] | $\Delta K_{\tan}(D)$ [N/mm] |
|---|---|---|
| 30 | 1.31 | $\Delta K_{\tan}(D) = -7.30\cdot 10^{-10}\cdot D^5 + 3.096\cdot 10^{-7}\cdot D^4 - 4.56\cdot 10^{-5}\cdot D^3 + {}$ $+ 2.47\cdot 10^{-3}\cdot D^2 - 8.19\cdot 10^{-3}\cdot D$ |
| 40 | 3.08 | $\Delta K_{\tan}(D) = -6.91\cdot 10^{-10}\cdot D^5 + 3.144\cdot 10^{-7}\cdot D^4 - 5.05\cdot 10^{-5}\cdot D^3 + {}$ $+ 3.10\cdot 10^{-3}\cdot D^2 - 2.41\cdot 10^{-2}\cdot D$ |
| 50 | 5.57 | $\Delta K_{\tan}(D) = -3.86\cdot 10^{-10}\cdot D^5 + 1.967\cdot 10^{-7}\cdot D^4 - 3.53\cdot 10^{-5}\cdot D^3 + {}$ $+ 2.37\cdot 10^{-3}\cdot D^2 - 1.18\cdot 10^{-2}\cdot D$ |

*Tab. 6.9* $K_{init}^{/}$ *and* $\Delta K_{\tan}(D)$ *for the various diameters* $\phi_i$ *of the rubber spring tested.*

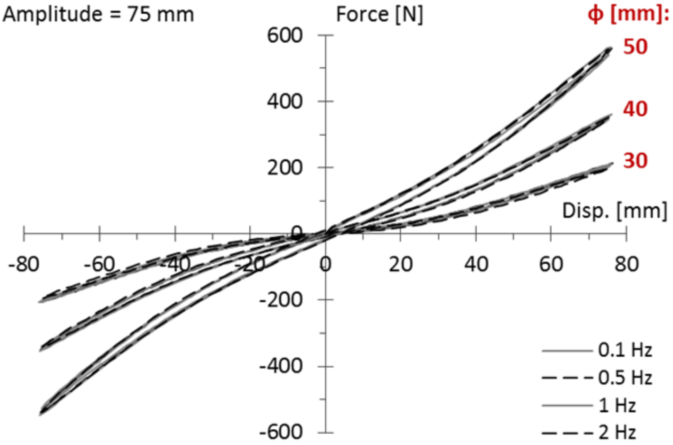

*Fig. 6.82 Hysteretic loops from the sinusoidal tests (Ch. 5) with same amplitude,75 mm, and different frequencies; diameters of the springs tested: 30, 40, 50 mm. Values for one spring.*

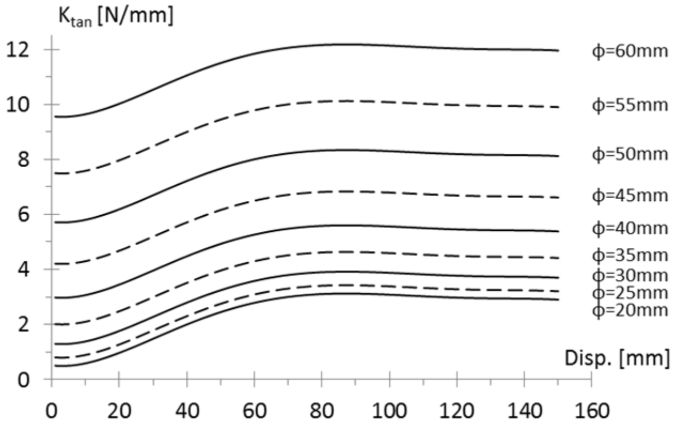

*Fig. 6.83 Prediction of the tangent stiffness* $K_{tan}$ *values using Eq. (5.15), proposed again in Eq.(6.21), for different diameters of the spring: 30, 40 and 50 mm.*

### c) Modelling of the pit effects

The initial viscoelastic indentations provide to the RBRL system, for small displacements, nonlinear force-displacement characteristics, with high damping and high stiffness, albeit the stiffness declining rapidly as the displacement amplitude increases. The nature of this behaviour could be considered as the sum of two principal effects:

- the rolling resistance of the steel balls on the rubber tracks;
- a non-linear elastic behaviour, consisting of an increment and of a subsequent decrement of force, for the roll-out of the balls from their depressions.

These observations, valid in general, are well visible in Fig. 6.84 and Fig. 6.85. These plots are related to the 1st cycle of a sinusoidal test performed at 0.5 Hz with 65 mm amplitude; the device tested is that of reference of section 6.2, with: rubber tracks A, t=2 mm, D=25 mm, $W/ER^2=1.2$.

Fig. 6.84 a) shows the non-linear elastic behaviour due to the pits, which corresponds to the mean values of rolling friction between the corresponding positive and negative μ values of the loop. Fig. 6.84 b) provides the values of the tangent stiffness $K_{tg\_PIT}$, calculated from the non-linear μ-disp behaviour of plot a). Tab. 6.10 reports the interpolating equations of the non-linear elastic behaviour and of the tangent stiffness plotted in Fig. 6.84, for both the first and second balls roll-out of the cycle. In particular, the peak force of the non-linear elastic behaviour, from which the force decrement starts, was found for a displacement of about 5 mm of the top plate; from this point the force decreases until about 15 mm, where the influence of the pits becomes negligible.

Fig. 6.85 shows instead the mean of the absolute magnitudes of the values of μ, i.e. approximately the values of rolling friction resistance $\mu_{\_PIT}$ inside and close to the pit. This friction shows a minimum value at the beginning of the μ-disp loop, then an increment until about 5 mm and finally a gradual reduction up to the steady-state rolling resistance (about 15 mm). This should be associated with the thickness of the rubber layers, variable from the initial position of the balls up to the undisturbed rubber, due to ball indentation. Another important consideration is that the effect of the pits on the rolling resistance seems considerable only for the first roll-out of the balls.

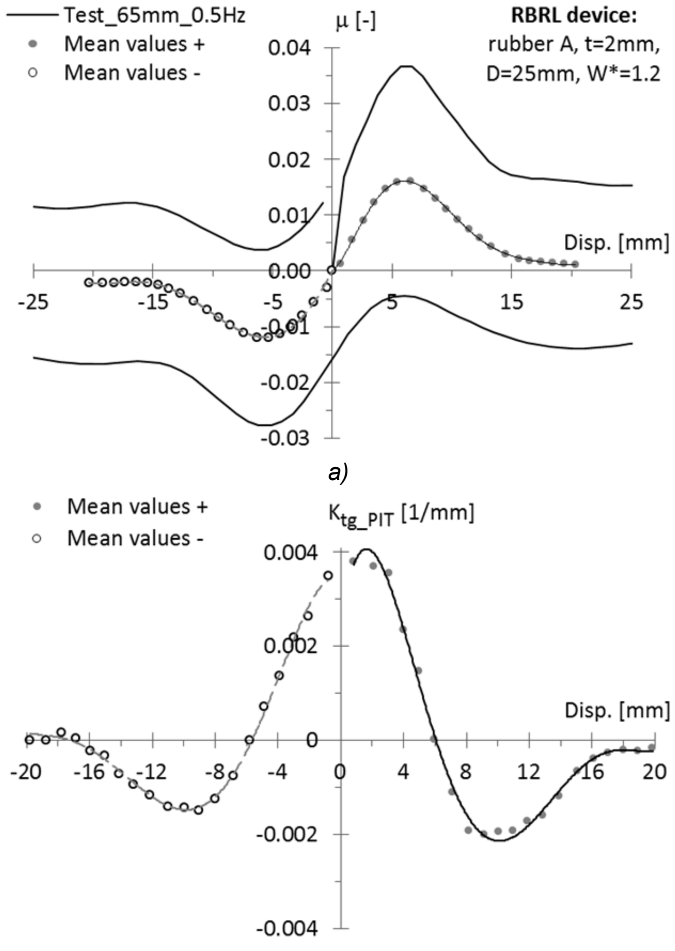

*a)*

*b)*

*Fig. 6.84 a) Non-linear elastic behaviour for the presence of the initial depression under the ball. b) Tangent stiffness calculated from the non-linear μ-disp behaviour of plot a). Results from a sinusoidal test performed at 65 mm amplitude and 0.5 Hz frequency, on the RBRL device assumed as reference (A, t=2mm, D=25mm, W*=1.2).*

| | |
|---|---|
| *A)* μ-disp behaviour (+) – 1st balls roll-out | $y = 2E\text{-}08x^6 - 1E\text{-}06x^5 + 3E\text{-}05x^4 +$<br>$- 0.0004x^3 + 0.0014x^2 + 0.0017x$ |
| *B)* μ-disp behaviour (-) – 2nd balls roll-out | $y = -1E\text{-}09x^6 - 1E\text{-}07x^5 - 5E\text{-}06x^4 +$<br>$- 4E\text{-}05x^3 + 0.0002x^2 + 0.0041x$ |
| *C)* Tangent stiffness (+) – 1st balls roll-out | $y = 7.226E\text{-}8x^5 - 4.451E\text{-}6x^4 + 9.740E\text{-}5x^3 +$<br>$- 8.571E\text{-}4x^2 + 2.091E\text{-}3x + 2.546E\text{-}3$ |
| *D)* Tangent stiffness (-) – 2nd balls roll-out | $y = -3.451E\text{-}8x^5 - 2.102E\text{-}6x^4 - 4.432E\text{-}5x^3 +$<br>$- 3.430E\text{-}4x^2 - 2.682E\text{-}4x + 3.393E\text{-}3$ |

*Tab. 6.10 Interpolating equations of the non-linear μ-disp behaviour and of the associated tangent stiffness plotted in Fig. 6.84.*

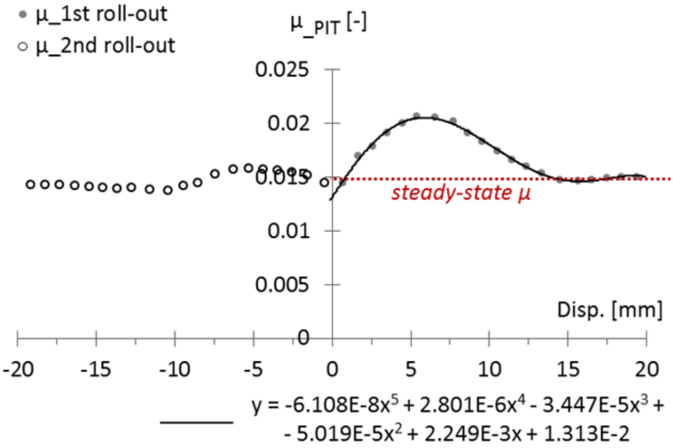

*Fig. 6.85 Influence of the pits on the rolling friction resistance for small displacements of the balls. Test at 65 mm and 0.5 Hz, on the reference RBRL device.*

Some interesting observations are reported below:

1)- The shape of the non-linear elastic μ-disp behaviour observed in Fig. 6.84 a) for positive displacements is very similar to that associated with negative deflections, only scaled by the ratio of the two peak rolling frictions.

This is again valid comparing tests with different sinusoidal velocities, as proposed in Fig. 6.86. Figure a) shows the envelopes, only for the positive displacements, of the sinusoidal tests on the reference RBRL device presented in section 6.2, for the cases of constant velocity (“v=31mm/s”) and constant frequency (“f=1Hz”). The non-linear μ-disp behaviour for positive displacements of Fig. 6.84 a) (for test “65mm”) was scaled by the ratio of the $\mu_{peak}$ values of the different tests, $\mu_{peak}$ (“v=31mm/s”)/ $\mu_{peak}$ (“65mm”) and $\mu_{peak}$ (“f=1Hz”)/ $\mu_{peak}$ (“65mm”): the results obtained show a good fitting between the non-linear μ-disp shapes scaled by that of test “65mm” and those directly calculated from the results of the tests “v=31mm/s” and “f=1Hz”. For clarity, Fig. 6.86 a) shows only the non-linear elastic μ-disp shapes obtained by scaling (indicated by the points), but the good fitting with the real ones is visible looking at the shape of the associated μ-disp envelopes. Figure b) shows instead the relative tangent stiffness $K_{tg\_PIT}$ .

2)- The minimum value of the rolling resistance at the beginning of the μ-disp loop, due to the effect of the pits, is better visible in Fig. 6.87, because of the higher number of points considered to describe the μ-disp loop of the cases shown; this figure compares the values of the rolling friction $\mu_{\_PIT}$, inside the pit, for the same tests of Fig. 6.86: “65mm”, “v=31mm/s” and “f=1Hz”. The minimum value of

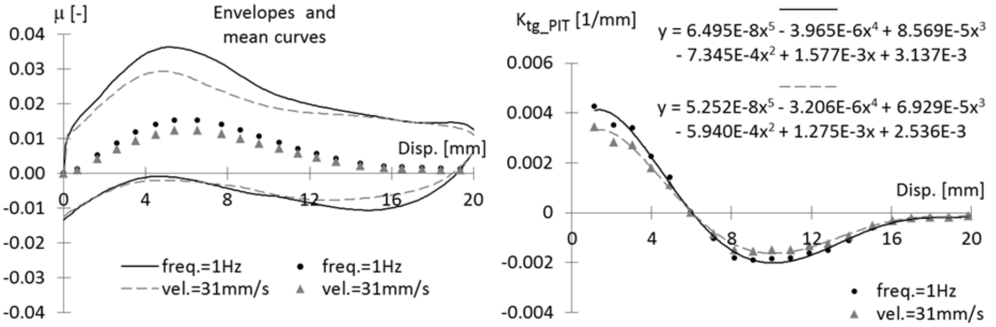

*a)* *b)*

*Fig. 6.86 a) Envelopes of the μ-disp loops of the tests with constant velocity (v=31mm/s) and constant frequency (f=1Hz), for the reference RBRL device, presented in section 6.2. The points represent the non-linear elastic μ-disp behaviour inside the pit, and were obtained by scaling the values of Fig. 6.84 a) by the ratio of the $\mu_{peak}$ values. b) Related tangent stiffnesses.*

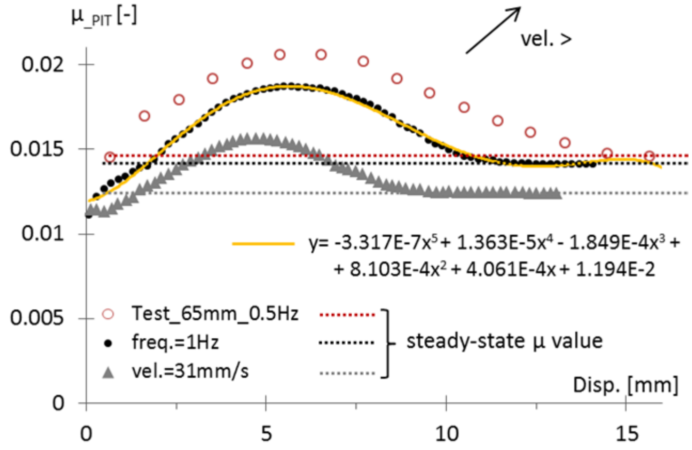

*Fig. 6.87 Influence of the pits on the rolling friction resistance for small displacements of the balls. Test at 65 mm and 0.5 Hz, on the reference RBRL device.*

friction seems to be again calculable from the theory of Muhr et al. (1997), considering a reduced value of thickness according to the empirical relation of Waters (1965) given in Eq. (3.18).

More important, a dependence of $\mu_{\_PIT}$ on the test velocity is also clearly visible.

3)- Finally, it is significant to consider that the effect of the pits is influenced by the dwell time of the load, the recovery of the indentations and the test velocity. The empirical results obtained in chapter 6 could be useful to take into account some of these effects, and a possible way to do this could be by finding some functions to appropriately scale the non-linear elastic behaviour in the pit, in accord to the different influence of dwell time, rubber recovery and velocity. However, the calibration of these influences is not considered herein, and needs further investigation.

Concluding, Fig. 6.88 presents the time-history model proposed for the efficacy prediction of the RBRL system through non-linear time-history analyses. For clarity, the pits effect on the rolling resistance is specifically indicated in Fig. 6.88 a) as an additional contribution ΔFroll(Disp.), a function of the displacement, to the steady-state rolling resistance Froll, which is constant; instead in Fig. 6.88 b), these two contributes of rolling resistance are included in the term Froll(Disp.). An additional and properly calibrated stiffness $K_{unloading}$, shown in Fig. 6.88 c), can be considered in series with the frictional element for modeling the unloading phase.

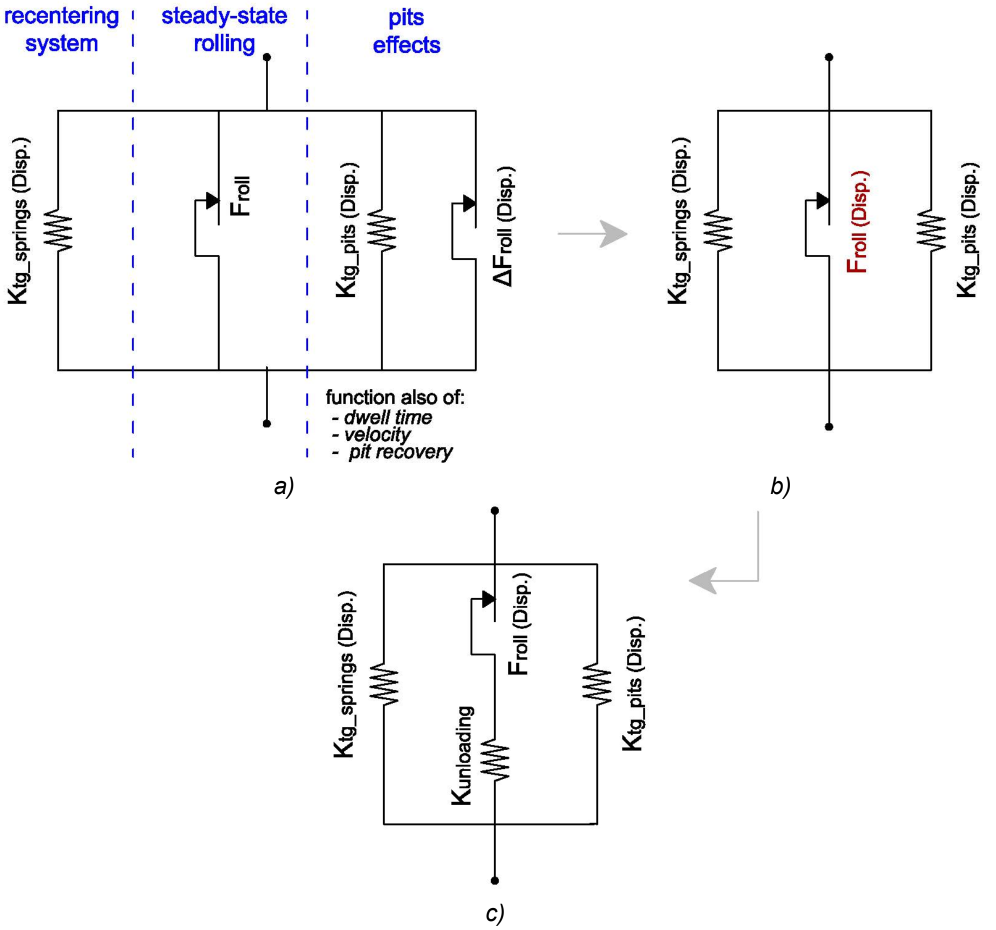
recentering system
steady-state rolling
pits effects
Ktg_springs (Disp.)
Froll
Ktg_pits (Disp.)
ΔFroll (Disp.)
function also of:
- dwell time
- velocity
- pit recovery
a)
Ktg_springs (Disp.)
Froll (Disp.)
Ktg_pits (Disp.)
b)
Ktg_springs (Disp.)
Froll (Disp.)
Kunloading
Ktg_pits (Disp.)
c)

*Fig. 6.88 Proposal of a time-domain model for the RBRL isolation system.*

### Verification of the correct prediction of the model for small-deflections

The principal reason for a new time-domain model, with respect to that presented by Guerreiro et al. (2007) and discussed in Chapter 4, is to improve the prediction of the small-deflections behaviour of the RBRL system.

Below, some numerical analyses performed in Opensees are presented for the evaluation of the model efficacy. The tests with constant sinusoidal frequency (f=1Hz) performed on the RBRL device of reference, presented in section 6.2, are used for comparison with the numerical behaviour prediction (see Fig. 6.89).

For this purpose, the model contribution due to rubber springs ($K_{tg\_springs}$) is not considered here, the tests being carried out without a recentering system. $K_{unloading}$ is set equal to 0.15 mm$^{-1}$. The remaining contributions to the model are Froll(Disp.) and $K_{tg\_pits}$(Disp.). For these, the previous results shown already provide the needed equations; in particular:

- equation of Fig. 6.87 was assumed for Froll(Disp.);
- equation of Fig. 6.86 b) was assumed for $K_{tg\_pits}$(Disp.).

The limits of applicability of such equations, in term of displacement, are shown in the related figures; after these limits:

- Froll(Disp.) becomes Froll in steady-state condition;
- $K_{tg\_pits}$(Disp.) becomes null.

A last consideration regards the contribution Froll(Disp.): as seen before, the effect of the pits is significant only for the first half of the loop, which involves the first roll-out of the balls; therefore, for the second half of the loop (second roll-out), the value of the rolling resistance was set to the steady-state one.

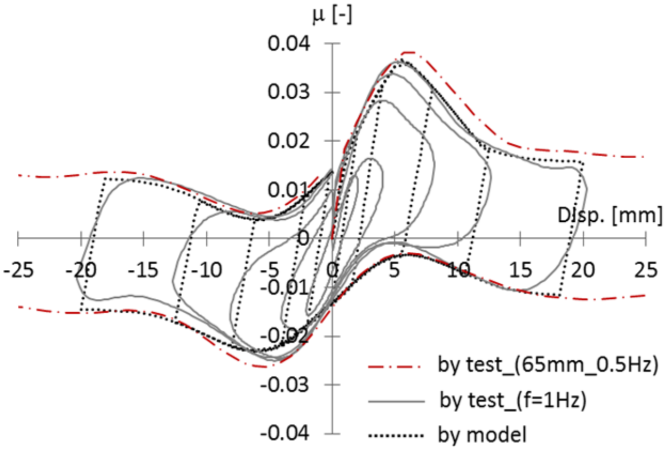

*Fig. 6.89 Comparison of the real μ-disp loops (no recentering springs) with those predicted by the model.*

## 6.7 Conclusions

1- The effects of the initial pits on the small-deflection behaviour of the RBRL system were investigated. The pit phenomenon, due to the viscoelastic properties of the rubber together with a certain dwell time of the load, provides high-damping and high stiffness behaviour for small displacements from the original reference position, and is responsible for the advantageous dynamic response of the system for small seismic intensities, if compared to an equivalent sliding isolation system. For this purpose three different experimentations carried out at TARRC are shown and discussed.

2- The first experimentation presented sinusoidal monoaxial parametric tests, performed on the new RBRL devices produced at TARRC for this Ph.D. project. The tests involved different displacement-imposed sinusoidal motions, covering the range of amplitudes from 1 to 20 mm, and diverse parameters of the isolation device. A dwell time of the load of 25 hours was considered before running each test, to allow the creation of the initial pits. Rolling friction-displacement (μ-disp) loops and ELVFD parameters were used to describe the performance of the RBRL device for small deflections.

a- Useful information was obtained regarding the shape of these loops, in particular for the transition phase from the rocking of the balls inside their pits to free rolling.

b- ELVFD parameters have shown that, for the smallest deflections, which are influenced by the effects of the initial indentation, velocity has a small effect on $K^{/}$ and negligible effect on $K^{//}$. The ELVFD representation provides an objective comparison of the dependences of the behaviour of the device on its principal parameters: the type of rubber and the stress level are the most influential parameters, for the ranges investigated for these parameters in this experimentation. Finally, the effects of recovery time on the initial pits, between subsequent sinusoidal cycles, are not clearly represented by the ELVFD parameters; thus, further plots are specifically proposed for the maximum rolling friction ratios (due to the roll-out of the balls from their pits) and for the associated values of displacement and secant stiffness, again comparing the different parameters investigated.

3- The second experimentation consisted of some measurements of the pit geometric profiles, immediately after unloading. Different values of the principal parameters of the RBRL device were investigated; consistent with the previous parametric sinusoidal tests, a dwell time of the load of 25 hours was used to create the residual indentation.

a- Some interesting observations were made about the shape of the pits; in particular, two shapes of residual indentation were identified, related to different types of rubber and stress level:

- the first shows a curvature still compatible with the associated indentor, indicating a uniform recovery of the rubber;
- the second presents a greater value of curvature with respect to that of the indentor, proving the recovery of the rubber is not uniform.

b- An empirical equation is finally proposed for the estimation of the maximum value of the residual indentation; this is based on the parameters of the test and on the viscoelastic properties of the rubber.

4- The third and last experimentation described is related to sinusoidal monoaxial tests carried out on the same RBRL devices as used in the ECOEST Project, thus with rubber tracks of type A, low damping, and B, high damping, moulded in 1999. Different dwell times of the load in its static configuration were considered.

a- Firstly, these tests proved the good performance of the RBRL device after 15 years from the moulding of the rubber tracks.

b- Secondly, the characterization of the behaviour of the RBRL device with rubber type B has led to the conclusion that the use of high-damping compounds for the tracks might not be advantageous.

c- Finally, an interesting quasi-linear dependence of the maximum force on the logarithm of the dwell time of the load was observed, for sinusoidal loops with amplitudes not larger than 5 mm.

5- Comparing the results of the first two experimentations, another useful empirical relation was provided between the peak force and the maximum residual indentation. Using this relation, the estimate of the peak force for different dwell times of the load shows a trend very similar to the one observed in the third experimentation on the ECOEST RBRL devices: this is an evidence of the efficacy of the empirical relation presented. Furthermore, some empirical relations are also provided to take into account the effects of the rubber recovery in the pits; in particular it was observed that the reduction in the value of the maximum force, due to the recovery of the initial indentation, is a function of the time of analysis as well as of the distance rolled by the balls from their pits. All these studies and empirical relations aim to provide useful tools for the calibration of a possible time-domain model for the RBRL system.

6- Finally a time-domain model is proposed for the prediction of the monoaxial non-linear behaviour of the RBRL system. This model gives a better representation of the system behaviour than the Guerreiro model (Guerreiro et al., 2007) and is based on the physical phenomena observed with the tests. The model can be adapted for different conditions of geometry and load, for different rubber layers and for different recentering rubber springs.

# 7 CONCLUSIONS AND FUTURE WORKS

## 7.1 General observations

This thesis focuses on the characterization studies of an innovative seismic isolation device, the RBRL (Rolling-Ball Rubber-Layer) system. The device, originally proposed by Prof. A.G. Thomas, was developed at TARRC (“Tun Abdul Razach Research Centre”) to enable isolation of low-mass (< 10 t) structures. It comprises: a rolling-based bearing system, which allows any displacements in the horizontal plane; two rubber layers bonded to the steel tracks, which give an adequate damping due to the rolling steel balls; some rubber springs, which ensure the recentering of the system through their elastic stiffness.

The system is very versatile, a great range of equivalent natural frequencies and coefficients of damping being achievable through the independent choice of rubber spring and rubber rolling track layer. It is suitable for isolating light structures and much more effective at low excitations than an equivalent sliding system would be.

The device assembly is relatively economical and is easy to tailor for the specific case, in terms of geometry and performance.

In particular, the latter consideration makes the RBRL isolation system very attractive for the protection of works of art in a museum, which are present in large quantity and characterized by very different shapes, dimensions and masses.

This research work was carried out within a collaboration between the University of Padova – Dept. of Civil, Architectural and Environmental Engineering – and TARRC, a Research and Promotion Centre of the Malaysian Rubber Board located in Hertford-UK.

The experimental campaign described in this work, together with the RBRL devices production, has been carried out at TARRC under the scientific guidance of Dr. Alan H. Muhr (Head of the Engineering Design Unit of TARRC).

## 7.2 Innovative aspects of the research

The principal innovative results achieved in this Ph.D. project are pointed below.

### 1- FREE ROLLING BEHAVIOUR

The theory of Muhr et al. (1997) was evaluated and applied by carrying out the requisite numerical integrations. This theory allows the calculation of the steady-state rolling friction, for the rolling of a steel ball on thin rubber layers, if the following parameters are known: load per ball, radius of the ball, thickness of the rubber layers, Young’s modulus and hysteresis parameter of the rubber. The theory proved useful when compared the results of a parametric monoaxial sinusoidal experimentation. This result could be important at two different levels:

- one more general, related to technological and scientific research in the rubber field, for which this theory could be a useful tool;
- one more specific, related to modelling of the rolling friction force for the RBRL device in steady-state conditions, for design purposes and for the device behaviour assessment.

### 2- EXPERIMENTAL DATABASE

A detailed and overall characterization of the non-linear dynamic behaviour of the RBRL system has been presented. This was reached using experimental data of a previous shaking-table test campaign (ECOEST project) and performing new experiments that have involved all the principal components of the isolation system.

3- OBSERVATION OF A NOVEL PHENOMENON

The theory of viscoelasticity, based on Boltzmann's idea of a fading memory of the effects of past deformations, has been found to be very useful for several aspects of rubber behaviour observed in this work. However, in the case of the depressions formed after a period of static load on a ball, it was found that only part of the deformation recovers in the expected time-dependent manner. For very high stresses, such as in the centre of the contact region between a thin layer of rubber and a highly loaded ball, a semi-permanent deformation – a "pit" - was observed. This is of considerable significance for the practical behaviour of the RBRL system, but is also an apparently unpublished phenomenon. It is akin to the "permanent set" seen after homogeneous deformations of some rubbers (in particular those containing a high loading of filler) to large strain, but here has been observed in unfilled natural rubber, which normally shows very low set. Also, the compression ratio of the set region appears to be very large, about 50% (≈ current thickness / initial thickness). This phenomenon calls for more detailed investigation, and may provide insight into molecular mechanisms for other behaviour – e.g. during fracture – that occur under extreme deformation.

4- SET OF EMPIRICAL RELATIONS

A set of empirical relations and numerical interpolation functions, fitted to the experimental data, have been given. These consider the principal effects on the system behaviour for the presence of the pits, such as the peak force and its reducing due to rubber recovery. These results may be used to design the system to meet specifications, and also to provide a framework for describing the behaviour that any model should capture.

5- DESIGN PROCEDURE

A design procedure for the RBRL isolation system is proposed. This procedure allows the determination of all the parameters that influence the system behaviour, for a specific design spectrum and vertical load, starting from the choice of isolation period and damping ratio.

6- TIME DOMAIN MODEL

A time-domain model is proposed for the prediction of the non-linear dynamic behaviour of the RBRL system. This model gives a better representation of the system behaviour than the one presented in Guerreiro et al. (2007), and it is based more on the physic phenomena observed with the tests. The model is adaptable for different geometric and load conditions, different rubber tracks and different recentering rubber springs. The model here presented is limited to the monoaxial case, but could be generalized for the biaxial analysis.

## 7.3 Future developments and recommendations for further research

- Further investigations are needed to establish whether the effects on the device behaviour related to the initial residual indentation could be understood from a viscoelastic model for the rubber, or whether the results – notably of a semi-permanent depression formed for the highest stresses in the centre of the contact patch on some thin rubber layers – falls outside the scope of theory currently established in rubber science. This local phenomenon is responsible of the advantageous behaviour of the RBRL device at low seismic excitations, which do not result in the roll-out of the balls from their pits. Despite this, the initial indentation effects have to be checked carefully, these being directly associated with the peak rolling friction. The dependence of these local effects on viscoelasticity implies the necessity to perform investigation tests over a wide range of time. Hence, a useful tool that might integrate the experimental results in an easier way is represented by FEM (Finite Element Method) analyses; for this purpose rubber might be modelled with a Prony's series, as explained in Ahmadi et al. (2008), for which the principal parameters are already reported in section 5.2.2 for the compounds analyzed in this Ph.D. project.
- A natural evolution of the work herein presented is the biaxial characterization of the device behaviour, this being more realistic than the monoaxial one. The observations done for each experimentation presented, about the test setup, test input and gathered results, could help to correctly address the new biaxial experimentations.
- Subsequently to these biaxial characterization tests, the time-domain model here proposed for the RBRL system could be extended to the biaxial domain.
- The detailed information and empirical relations here proposed, about the effects of the dwell time of the load and the rubber recovery of the pits on the small-deflections behaviour of the RBRL system, might be then added to the model if a more accurate representation is desired.

- Finally the issue of the vertical seismic actions should be investigated, even if the recentering rubber springs seem to provide a little help for such purpose. These effects, although of secondary importance, could be significant for those structures free to rock.

# REFERENCES

Achour N., Miyajima M., Kitaura M. and Price A., (2011), *Earthquake Induced Structural and Non-structural Damage in Hospitals*, Earthquake Spectra 27 (3), 617-634.

Agbabian M., Masri S., Nigbor R. and Ginell W., (1988). *Seismic damage mitigation concepts for art objects in museums*", Proceedings of the 9th World Conference on Earthquake Engineering, August 2–9, Tokyo–Kyoto, Japan.

Ahmadi H.R. and Muhr A.H., (1995), *Contribution of MRPRA to development of design guidelines for isolated structures*, Proceedings of Post-SMiRT Conference Seminar on Seismic Isolation, Passive Energy Dissipation and Control of Vibrations of Structures, Santiago, Chile.

Ahmadi H.R. and Muhr A.H., (1997), *Modelling dynamic properties of filled rubber*, Journal of Plastics, Rubber and Composites Processing and Applications, 26 (10), 451-461.

Ahmadi H.R. and Muhr A.H., (2011), *Dynamic properties of filled rubber. Part II - Physical basis of contributions to the model*, Rubber Chem. & Tech., 84, 24-40.

Ahmadi H.R., Kingston J.G.R. and Muhr A.H., (2008), *Dynamic properties of filled rubber*. *Part I – simple model, experimental data and simulated results*, Rubber Chem. & Tech., 81, 1-18.

Alessandri S., Giannini R., Paolacci F., Amoretti M. and Freddo A., (2014), A*ssessment of the seismic response of a base isolated HV circuit breaker with Steel Cable Dampers*, Proceedings of the Second European Conference on Earthquake Engineering and Seismology - 2ECEES, August 25-29, Istanbul, Turkey.

Al-Hussaini T.M., Zayas V.A. and Constantinou M.C., (1994), *Seismic Isolation of a Multi-Story Frame Structure Using Spherical Sliding Isolation System*, Report N° NCEER-94-0007, Buffalo, NY.

Aslam M., Godden W.G. and Scalise D.T., (1980), *Earthquake rocking response of rigid bodies*, Journal of the Structural Division ASCE, 106 (2), 377-392.

Augusti G. and Ciampoli M., (1993), *Protezione sismica degli oggetti d'arte: ulteriori studi sul moto di scivolamento con attrito*, Proceding of the 6th Italian Conference on Earthquake Engineering, October 13-15, Perugia, Italy.

Augusti G. and Ciampoli M., (1996), *Guidelines for Seismic Protection of Museum Contents*, Proceedings of the 11th World Conference on Earthquake Engineering - WCEE, June 23-28, Acapulco, Mexico, paper 1668. Available at: *http://www.iitk.ac.in/nicee/wcee/article/11_1668.PDF*.

Augusti G. and Sinopoli A., (1992), *Modelling the Dynamics of Large Blocks Structures*, Meccanica, 27 (3), 195-211.

Augusti G., Ciampoli M. and Airoldi L., (1992), *Mitigation of seismic risk for museum contents*: an introductory investigation, Proceedings of the 10th World Conference on Earthquake Engineering - WCEE, July 19-24, Madrid, Spain, Edited by A. Bernal, Balkema, Rotterdam, Netherlands, Vol. 9, 5995-6000.

Augusti G., Ciampoli M. and Sepe V., (1994), *Further studies on seismic behaviour and risk reduction for museum contents*, Proceeding of the 10th European Conference on Earthquake Engineering, Aug. 28 – Sept. 2, Vienna, Austria.

Baggio S., Berto L., Favaretto T. and Saetta A., (2013), *Mitigazione del rischio sismico per beni artistici mobili: un sistema di isolamento sismico*, Proceedings of the XV Italian Conference on Earthquake Engineering - ANIDIS, July 01-04, Padova, Italy (in Italian).

Berto L., Favaretto T. and Saetta A., (2013), *Seismic risk mitigation technique for art objects: experimental evaluation and numerical modelling of double* concave curved surface sliders, Bull Earthquake Eng, 11, 1817-1840.

Berto L., Favaretto T., Saetta A., Antonelli F. and Lazzarini L. (2012), *Assessment of seismic vulnerability of art objects: The "Galleria dei Prigioni" sculptures at the Accademia Gallery in Florence*, Journal of Cultural Heritage, 13, 7-21.

Bettinali F., Bellorini S., Bergamo G., Muhr A.H. and Diehl A., (2001), *Seismic Risk Mitigation of Light Structures by means of novel Rolling-Ball Rubber-Layer Systems*, Proceedings of 5th World Congress on Joints, Bearings and Seismic Systems for Concrete Structures, 7–11 October, Rome, Italy.

Borri A. and De Maria A., (2013 a), *Un indice per la ricognizione su larga scala della vulnerabilità sismica dei Beni Museali. Calibrazione e test*, Proceedings of the XV Italian Conference on Earthquake Engineering-ANIDIS, July 01-04, Padova, Italy (in Italian).

Borri A. and De Maria A., (2013 b), *Un indice per la ricognizione su larga scala della vulnerabilità sismica dei Beni Museali*, in: Sistema integrato di informazione tecnica, “Ingenio”, n.12, May (in Italian). Link: http://www.ingenio-web.it (http://www.ingenio-web.it/immagini/Articoli/PDF/X7gSvS1EcY.pdf).

Caldwell P., Gatscher J.A. and Littler S.R., (2007), *Essential Elements of Equipment Seismic Qualification to ASCE 7 by Shake Table Testing*, ASCE/SEI Structures Engineering Congress, May 16-19, Long Beach, CA.

Caliò I. and Marletta M., (2003), *Passive control of the seismic rocking response of art objects*, Engineering Structures, 25 (8), 1009-1018.

Caliò I. and Marletta M., (2004), *On the mitigation of the seismic risk of art objects: case-studies*, 13th World Conference on Earthquake Engineering, August 1-6, Vancouver, B.C., Canada, paper 2828.

Clemente P., (2010), *Dagli “strati di carbone e lana” ai moderni dispositivi antisismici*, Attività in campo sismico. Recenti studi e sviluppi futuri. Casaccia, December 2010 (in Italian). (http://old.enea.it/eventi/eventi2010/AttivitaCampoSismico201210/ClementeP.pdf)

Cook J., Muhr A.H., Sulong M. and Thomas A., (1997), *Rolling-ball Isolation System for Light Structures*, Proceedings of International Post-SMiRT Conference Seminar on Seismic Isolation, Passive Energy Dissipation and Active Control of Seismic Vibrations of Structures, 25-27 August, Taormina, Italy, 795-811.

Corradi L., (1993), *Meccanica delle strutture – Vol. 2: Le teorie strutturali e il metodo degli elementi finiti*, McGraw-Hill, Milano (*in Italian*).

Costantinou M.C., Mokha A. and Reinhorn A.M., (1988), *Teflon Bearings in Aseismic Base Isolation: Experimental Studies and Mathematical Modeling*, Report N. NCEER-88/0038, Buffalo, NY.

De Canio G. and Modena C., (2013), *Earthquake protection of movable and semi-movable cultural assets in their exposition sites*, Proceedings of the XV Italian Conference on Earthquake Engineering - ANIDIS, July 01-04, Padova, Italy.

De Canio G., (2012), *Marble devices for the Base isolation of the two Bronzes of Riace: a proposal for the David of Michelangelo*, Proceedings of the 15th World Conference on Earthquake Engineering - WCEE, September 24-28, Lisbon, Portugal.

Demetriades G.F., Constantinou M.C. and Reinhorn A.M., (1993), *Study of wire rope systems for seismic protection of equipment in buildings,* Engineering structures, 15, 321-334.

Derham C. J., Thomas A. G., Eidinger J. M. and Kelly J. M., (1977), *Natural Rubber Foundation Bearings for Earthquake Protection - Experimental Results*, NR

Technology, 39, 41 – 61 (reprinted: Rubber Chemistry and Technology, 1980, 53, 186 – 209).

Derham C.J., (1983), *Basic Principles of Base Isolation*, Proceedings of the International Conference on Natural Rubber for Earthquake Protection of Buildings and Vibration Isolation, 1982, Kuala Lumpur. Editor: Derham C.J., Malaysian Rubber Research and Development Board, 1983.

Derham C.J., Kelly J.M. and Thomas A.G., (1985), *Nonlinear Natural Rubber Bearings for Seismic Isolation*, Nuclear Engineering Design, 84 (3), 417-428.

Dimitrakopoulos E. and DeJong M. (2012), *Revisiting the rocking block: closed-form solutions and similarity laws*. Proceedings of the Royal Society A: Mathematical, Physical and Engineering Sciences, 468 (2144), 2294-2318. Doi:10.1098/rspa.2012.0026.

Dolce M., Cardone D., Nigro D. and Croatto F., (2003), *The effects of friction variability on the response of isolated bridges*, Proceeding of 8th World Seminar on Seismic Isolation, Energy Dissipation and Active Vibration Control of Structures, Yerevan, Armenia.

Dolce M., Ponzo F.C., Di Cesare A. and Arleo G., (2010), *Progetto di Edifici con Isolamento Sismico*, 2nd Edition, IUSS Press, Pavia, pp 215 (in Italian).

Donà M., Muhr A.H., Tecchio G., Dusi A. and Modena C., (2014), *Isolation of light structures with Rolling-Ball Rubber-Layer System - characteristics and performance*, Proceedings of the Second European Conference on Earthquake Engineering and Seismology - 2ECEES, August 25-29, Istanbul, Turkey, paper 1220.

EC8 - Comité Européen de Normalisation, (2004), *Eurocode 8-Design of Structures for Earthquake Resistance - Part 1: General Rules, Seismic Actions and Rules for Buildings*, EN 1998-1, CEN, Brussels, Belgium, 222 pp.

Erdik M., Durukal E., Ertürk N. and Sungay B., (2010), *Earthquake risk mitigation in Istanbul museums*, Nat Hazards, 53, 97-108.

Favaretto T. (2012), *Assessment and reduction of seismic vulnerability of art objects*. PhD Dissertation. University of Florence, T.U. Braunschweig.

FEMA E-74, Reducing the Risks of Nonstructural Earthquake Damage – A practical Guide, January 2011.

Ferry J.D., (1980), *Viscoelastic properties of polymers*, 3rd Edition, Wiley, New York, 1980.

FIP Industriale S.p.A., (2015), web site: http://www.fip-group.it.

Foti D. and Kelly J.M., (1996), *Experimental study of a reduced scale model seismically base-isolated with Rubber-Layer roller bearings*, Monograph IS-18, Monograph Series in Earthquake Engineering, ed. A.H. Barbat, International Center for Numerical Methods in Engineering, Barcelona, Spain.

Gent A.N. and Henry R.L., (1969), *Rolling Friction on Viscoelastic Substrates*, Trans. Soc. Rheol., 13, 255.

Gent A.N., (1962), *Relaxation processes in vulcanized rubber. I. Relation among stress relaxation, creep, recovery, and hysteresis*, Journal of Applied Polymer Science, 6(22), 433-441.

Giovannardi F. and Guisaso A., (2013), *Base isolation: dalle origini ai giorni nostri* (in Italian). Available at: http://lnx.costruzioni.net/wp-content/uploads/2013/09/Base-Isolation-dalle-origini-ai-giorni-nostri-1.pdf.

Goodno B.J., Gould N.C., Caldwell P. and Gould P.L., (2011), *Effects of the January 2010 Haitian Earthquake on Selected Electrical Equipment*, Earthquake Spectra, 27 (S1), S251-S276.

Greenwood, J.A., Minshall, H. and Tabor, D., (1961), *Hysteresis losses in rolling and sliding friction*, Proc. Roy. Soc. 259A, 480-507.

Guerreiro L., Azevedo J., Muhr A.H., (2007), *Seismic Tests and Numerical Modeling of a Rolling-ball Isolation System*, Journal of Earthquake Engineering, 11 (1), 49-66.

Gunn S.W.A., (1995), *Health effects of earthquakes*, Disaster Prevention and Management 4 (5), 6-10.

Housner G., (1963), *The behavior of inverted pendulum structures during earthquakes*. Bulletin of the Seismological Society of America, 53(2),403-417.

Ishiyama Y., (1984), *Motions of rigid bodies and criteria for overturning by earthquake excitations*. Bulletin of the New Zealand Society for Earthquake Engineering, 17 (1), 24-37.

ISO 8013:2012, (2012), Rubber, vulcanized -- Determination of creep in compression or shear.

Izumi M., (1988), *State-of-the Art Report. Base isolation and passive seismic response control*, Proceeding of 9th World Conference on Earthquake Engineering, August 2 – 9, Tokyo – Kyoto, Japan (Vol. VIII).

Kelly J.M. and Quiroz E., (1992), *Mechanical Characteristics of Neoprene Isolation Bearing*, Report N. UCB/EERC-92/11, Earthquake Engineering Research Center, Berkeley, CA.

Kelly J.M., (1990), *Base Isolation: Linear Theory and Design*, Earthquake Spectra, 6 (2), 223-244.

Kelly J.M., (1991), *Dynamic and Failure Characteristics of Bridgestone Isolation Bearings*, Report UCB/EERC-91/04, Earthquake Engineering Research Center, Berkeley, CA.

Kelly J.M., (1993), *Earthquake-Resistant Design with Rubber*, Publ. Springer-Verlag, London.

Kelly T.E., (1992), *Skellerup Industries Lead Rubber Isolation Bearings: Experimental Properties*, Holmes Consulting Group Ltd.

Kemeny Z.A. and Szidarovszky F., (1995), *Seismic isolation bearings with nonlinear gravity restoring*, Report No. MCEER VF01127, Multidisciplinary Center for Earthquake Engineering Research, Univ. at Buffalo, State Univ. of New York, Buffalo, N.Y.

Kesti M.G., Mowrtage W. and Erdik M., (2010), *Earthquake Risk Reduction of Structures by a Low-Cost Base Isolation Device: Experimental Study on BNC Bearing*, Proceedings of the 14th European Conference on Earthquake Engineering-ECEE, August 30 - September 03, Ohrid, Macedonia.

Kingston J.G.R. and Muhr A.H., (2011), *Effect of scragging on parameters in viscoplastic model for filled rubber*, Plastics, Rubber and Composites, 40, 4, 161-168.

Liberatore D. (editor), (2000), *Vulnerabilità dei beni archeologici e degli oggetti esibiti nei musei*. CNR-Gruppo Nazionale per la Difesa dai Terremoti, Roma, 118 pp (in Italian). Presentation available in internet: *http://apple.csgi.unifi.it/~restauro/Rischio%20sismico%20_%2008.pdf*.

Lowry M., Armendariz D., Farrar B.J. and Podany J., (2008), *Seismic Mount Making: A Review of the Protection of Objects in the J. Paul Getty Museum from Earthquake Damage,* in: Advances in the protection of museum collections from earthquake damage, symposium held at the J. Paul Getty museum at the Villa on May 3–4, 2006, J. Paul Getty Museum Trust, Los Angeles.

Lowry M., Farrar B.J., Armendariz D. and Podany J., (2007), *Protecting Collections in the J. Paul Getty Museum from Earthquake Damage,* Western Association for Art Conservation (WAAC) Newsletter, 29 (3), 16-23.

Martelli A., (2010), *Le moderne tecnologie antisismiche nell'adeguamento degli edifici storici*, Giornata di studio "Nuove idee per l'adeguamento sismico degli edifici storici”, ENEA, Roma, May 2010 (in Italian). (http://old.enea.it/eventi/eventi2010/AdeguamentoSismico110510/Martelli.pdf).

Martelli A., Clemente P., De Stefano A., Forni M. and Salvatori A., (2014), *Recent Development and Application of Seismic Isolation and Energy Dissipation and Conditions for Their Correct Use*, Perspectives on European Earthquake Engineering and Seismology - Geotechnical, Geological and Earthquake Engineering 34, Ansal A. (ed.). Chapter 14, 449 - 488.

Milne J., (1885), *Seismic Experiments*, Transactions of the Seismological Society of Japan, Vol. 8.

Muhr A.H. and Bergamo G., (2010), *Shaking Table Tests On Rolling-Ball Rubber-Layer Isolation System*, Proceedings of 14th European Conference on Earthquake Engineering (ECEE), 30 August – 03 September, Ohrid, Macedonian, paper 745.

Muhr A.H., Sulong M. and Thomas A.G., (1997), *Rolling-ball Rubber-layer Isolators*, Journal of Natural Rubber Research, 12 (4), 199-214.

Mullins L. and Tobin N. R., (1965), *Stress softening in rubber vulcanizates. Part I. Use of a strain amplification factor to describe the elastic behavior of filler-reinforced vulcanized rubber*, Journal of Applied Polymer Science, 9, 9, 2993–3009.

Naeim F. and Kelly J.M., (1999), *Design of Seismic Isolated Structures. From Theory to Practice*, John Wiley & Sons, Inc., New York, 1999.

Neurohr T. and McClure G., (2008), *Shake table testing of museum display cases*, Canadian Journal of Civil Engineering, 35 (12), 1353-1364.

Neurohr T., (2005), *Seismic Vulnerability of Art Objects: Literature Review Report,* Structural Engineering Series No. 2005-04, Department of Civil Engineering and Applied Mechanics, McGill University, Montréal, Canada.

Oikonomou K., Costantinou M.C., Reinhorn A.M. and Yenidogan C., (2012), *Seismic Isolation of Electrical Equipment “Seismic Table Simulation”*, Proceedings of the 15th World Conference on Earthquake Engineering – WCEE, September 24-28, Lisbon, Portugal.

Payne A.R., (1962), *The dynamic properties of carbon black-loaded natural rubber vulcanizates. Part I*, Journal of Applied Polymer Science, 6, 19, 57–63.

Priestley M.J.N., Evison J.J. and Carr A.J., (1978), *Seismic response of structures free to rock on their foundations*, Bulletin of the New Zealand National Society for Earthquake Engineering, 11 (3), 141-150.

Rivlin R.S. and Saunders D.W., (1949), *Cylindrical shear mountings*, Trans. Inst. Rubber Ind., 24, 296-306.

Robinson W.H., (1982), *Lead-Rubber Hysteretic Bearings suitable for protecting structures during earthquakes*, Earthquake Engineering and Structural Dynamics, 10 (4), 593-604.

Robinson W.H., Gannon C.R. and Meyer J., (2006), *The RoGlider – a sliding bearing with an elastic restoring force*, Bulletin of the New Zealand Society for Earthquake Engineering, 39, 1, 81-84.

Saadeghvaziri A.A. and Feng M.Q., (2001). *Experimental and Analytical Study of Base-Isolation for Electric Power Equipments*, MCERR Volume on Research Progress and Accomplishments, 29-40.

Schwanen W., (2004), *Modelling and identification of the dynamic behavior of a wire rope spring*, Technische Universiteit Eindhoven, The Netherlands, Report number: DCT-2004/28, Master Thesis, 2004.

Soong T.T. and Yao G.C., (1999), *Damage to Critical Facilities,* Preliminary Report from MCEER-NCREE Workshop, New York.

Soong T.T. and Yao G.C., (2000), *The Chi-Chi Taiwan Earthquake of September 21, 1999: Reconnaissance Report,* New York.

Symans M.D., (2004), *Seismic Protective Systems: Seismic Isolation.* Instructional Material Complementing FEMA 451, Design Examples, 2004.

Taghavi S. and Miranda E., (2003), Response Assessment of Nonstructural Building Elements, PEER Report 2003/05, University of California Berkeley.

Tyler R.G., (1977), *Dynamic Tests on PTFE Sliding Layers under Earthquake Conditions*, Bull. New Zealand National Society of Earthquake Engineering, 10 (3), 129-138.

Taylor A.W., Lin A.N. and Martin J.W., (1992), *Performance of Elastomers in Isolation Bearings*: a Literature Review, Earthquake Spectra, 8 (2), 279-304.

Thomas A.G., (1973), *Testing procedure for measurement of dynamic properties of rubber*, J. IRI, 7, 666-668.

Timoshenko S., (1934), *Theory of Elasticity*, McGraw Hill, New York.

Tsai C.S., (2012), *Advanced Base Isolation Systems for Light Weight Equipments,* Earthquake-Resistant Structures - Design, Assessment and Rehabilitation, Prof. Moustafa A. (Ed.), ISBN: 978-953-51- 0123-9, InTech. Available from: http://www.intechopen.com/books/earthquake-resistant-structures-design-assessment-and-rehabilitation/advanced-base-isolation-systems-for-light-weight-equipments.

Tsai C.S., Lin Y.C., Chen W.S. and Su H.C., (2010), *Tri-directional shaking table tests of vibration sensitive equipment with static dynamics interchangeable-ball pendulum system*, Earthq Eng & Eng Vib, 9, 103-112.

Tsai C.S., Lin Y.C., Chen W.S. Chen M.J. and Tsou C.P., (2006), *The material behavior and isolation benefits of Ball Pendulum System*, Cory J.F., The 2006 ASME Pressure Vessels and Piping Conference, Seismic Engineering, Vancouver, BC, Canada, Paper No. PVP2006-ICPVT11-93252.

Uang C.M. and Bertero V., (1990), *Evaluation of seismic energy in structures*, Earthquake Engineering and Structural Dynamics, 19, 77-90.

Ueda S., Enomoto T. and Fujita T., (2004), *Experiments and analysis of roller type isolation* device, Proceedings of the 13th World Conference on Earthquake Engineering - WCEE, August 01-06, Vancouver, B.C., Canada, paper 3362.

UNI EN-15129:2009, (2009), *Anti-seismic Devices*, European Committee for Standardization.

Waters N.E., (1965), The indentation of Thin Rubber Sheets by Spherical Indentors, Brit. J. Appl. Phys., 16, 557.

Whittaker A.S. and Soong T.T., (2003), *An overview of nonstructural components research at three U.S. Earthquake Engineering Research Centers*, Proceedings of Seminar on Seismic Design, Performance, and Retrofit of Nonstructural Components in Critical Facilities, Applied Technology Council Multidisciplinary Center for Earthquake Engineering Research, 29, 271-280.

Yim C., Chopra A. and Penzien J., (1980), *Rocking response of rigid blocks to earthquakes*. Earthquake engineering and structural dynamics, 8, 565-587.

Zayas V., Low S. and Mahin S., (1987), *The Friction Pendulum System (FPS) Earthquake Resisting System: Experimental Report* –Report N° UCB/EERC-87/01, Berkeley, California.

## Software used:

- Microsoft Office Excel 2010.
- MATLAB 7.5.0 (R2007b).
- Opensees – Open System For Earthquake Engineering Simulation, Pacific Earthquake Engineering Research Center – v. 2.4.5.
  (Free distribution: http://opensees.berkeley.edu/index.php)

# APPENDIX A:

The Matlab script used for numerical calculation of the integral $I(s)$ of Eq. (3.25) is reported below; this integral is needed for predicting of the steady-state rolling friction through the theory of Muhr et al. (1997).

```
% Definition of the Boundary Condition
% parameter A (Water, 1965)
%(A=0.417 bonded condition; A=0.67 lubricated condition)
A=0.417;

% Initialization and setting (see Muhr et al.,1997)
% s = integration variable
s_old=0.0;       % initial (then "previous") value of s
s_max=100.0;     % maximum value of s
ds=0.05;         % integration step for s
Int_old=0;       % initial (then "previous") value of I(s)
                 % integral to be calculated

% Number of integration steps
i_max=(s_max-s_old)/ds;

% Function to be integrated
syms s y
y=(((s^2)/(1-exp(-A/s)))^(3/2))*s;

% Integration Algorithm
for i=1:i_max
    s_new=s_old+ds;
    Int=double(int(y,s_old,s_new));
    Int_new=Int+Int_old;
    v(i)=Int_new;
    s_old=s_new;
    Int_old=Int_new;
end

% Results
v=v';
```